EVENT SHAPES IN $p\bar{p}$ COLLISIONS AT $\sqrt{s} = 1.96$ TeV

by

Scott Atkins, B.S., M.S.

A Dissertation Presented in Partial Fulfillment
of the Requirements for the Degree
Doctor of Philosophy

COLLEGE OF ENGINEERING AND SCIENCE
LOUISIANA TECH UNIVERSITY

August 2012

Replace this page with the Signature Page.

ABSTRACT

This dissertation presents the analysis of nine different event shapes measured in high energy $p\overline{p}$ collisions. An event shape can be defined as an event-based quantity that measures how the final energies are distributed in the final event. This analysis will test strong interactions as described by Quantum Chromodynamics (QCD), through their implementation in different Monte Carlo-based models. Each of the event shapes provides information about the flow of energy in QCD events and about the hadronic final states that occur in $p\overline{p}$ particle collisions, thus allowing the study of the dynamics of QCD multijet events. Any deviation of an event shape from zero will be indicative of higher-order effects, meaning that more than the two jets were produced in the event. For each of the event shapes, both normalized differential distributions ($\frac{1}{\sigma}\frac{d\sigma}{dX}$) and average event shapes ($\overline{X}$) were measured, where X is the event shape and σ is the cross section. This analysis uses $0.7\,\mathrm{fb}^{-1}$ of data taken between 2004 and 2006 by the DØ detector located at the Fermi National Accelerator Lab (Fermilab) in Batavia, IL, using $p\overline{p}$ collisions at a center-of-mass energy of $\sqrt{s} = 1.96$ TeV.

Replace this page with the approval for scholarly dissemination form.

DEDICATION

This dissertation is dedicated to my mother who has always been there for me through the laughter and the tears, who has always been supportive of me. This dissertation is as much for her as it is for me. I love you mom.

I am also dedicating this dissertation to my niece JoLee, who came into my life a little over three years ago. Uncle Scott loves you.

TABLE OF CONTENTS

LIST OF TABLES

LIST OF FIGURES

ACKNOWLEDGMENTS

I wish to thank all of those who have made this dissertation possible. This analysis would not have possible were it not for the hard work of everyone at the DØ collaboration. I would like to thank Ramu Ramachandran, who nominated me for the Board of Regents Graduate Fellowship, which I received. This allowed me more time to focus on my research. I would like to thank my Ph.D. committee members: Lee Sawyer, Markus Wobisch, Dick Greenwood, Jean Gourd, and Weizhong Dai. Jean Gourd and Weizhong joined my committee at the last minute when two members were no longer able to be on the committee. My advisors, Lee Sawyer and Markus Wobisch, guided me. They were very understanding and worked with me when I moved back home to care for my mother while she was going through cancer. I would like to thank my brother for the good times we had going to the movies and playing Nintendo Wii, although I could never beat him at most games. I would also like to thank the rest of my family, including my mom and my niece mentioned in the dedication. And lastly, thank you to anybody I may have missed.

CHAPTER 1

INTRODUCTION

Starting in the mid 1940s, the number of "elementary" particles began to explode. Many of these new particles behaved very strangely in that they were produced very quickly but decayed rather slowly, about 1000 times slower than they were created. In 1961, Murray Gell-Mann developed a particle classification scheme called the Eightfold Way [1], in an effort to organize all of these "elementary" particles in much the same way that Mendeleev came up with the periodic table of elements.

Similarly to Mendeleev, Gell-Mann and others did not know why the Eightfold Way worked; they just knew that it did. Three years later, in 1964, Gell-Mann and Zweig proposed that all of the particles of the Eightfold Way were not actually elementary after all, but were made up of even more elementary particles that Gell-Mann called *quarks* [1]. Their model was called the *quark model*. At the time there were three kinds (or flavors) of quarks postulated to exist: u for up, d for down, and s for strange.

All of the particles in nature that contain quarks are called *hadrons* which can be classified into one of two groups, depending upon how many quarks they contain: *baryons* (made up of three quarks, qqq) and *mesons* (made up of a quark-antiquark pair, $q\overline{q}$). There are some baryons that are made up of two or three quarks of the

same flavor in the same state – *e.g.* the Δ^{++} is made up of three u quarks in the same state. Many physicists objected to the quark model because it appeared to violate the Pauli exclusion principle. In 1964, Greenberg proposed a new quantum number for quarks that he called *color* [1]. There are three different color charges, designated green, blue, and red in analogy to the primary colors. Quarks have color; antiquarks have anticolor. The *color hypothesis* states that all particles in that are observed in nature are colorless – either $q\overline{q}$, where $\overline{q}$ has the anticolor of q, or qqq, where each quark has a different color.

In 1969, Feynmann proposed a model to describe the behavior of hadrons in collisions of very high energies. He called the elementary particles of his model *partons* [1]; thus, Feynmannn's model is called the *parton model*. The basic assumption of this model was that the partons inside a hadron are free. To explain the binding of partons to form hadrons, all that is needed is the parton distribution function (PDF) which describes how a hadron's momentum is apportioned. The number of partons that are seen by a particle scattering off a hadron depends upon the energy: more energy means more partons are seen. At low energies the scattering particle sees the three partons or a parton-antiparton pair: these are called the *valence* partons. This is the picture that is seen in the quark model. At higher energies the scattering particle sees the *sea partons*. It is now recognized that the valence partons are the same as the quarks in the quark model, and that the sea partons are made up of virtual quark-antiquark pairs and gluons.

The force between interacting partons is called the *strong force*. It exists between two objects with color charge just as the electromagnetic force exists between

two objects with electric charge. There are three color charges (the aforementioned red, green, and blue) versus two electromagnetic charges (+ or −). Color charge must be conserved in any interaction just as electric charge is. The theory that describes the interactions of color charged objects (objects that feel the strong force) is called *quantum chromodynamics* (QCD). The mediator of the strong force is the *gluon*. According to the symmetry of the special unitary group of size three for color ($SU(3)_c$), which serves as a basis for QCD, there are eight independent gluons, forming a color octet, which exist in states of different combinations of color and anticolor. Because the gluons have color charge, they are affected by the strong force: the gluons can interact with each other. This is different from photons which do not carry an electric charge and thus do not interact with one another.

In addition to the gluonic color octet states of $SU(3)_c$, there is also an unphysical gluonic colorless singlet state which is a combination of equal parts of $r\overline{r}$, $g\overline{g}$, and $b\overline{b}$. The difference between the octet and singlet states is that the singlet state is left unaffected by transformations in $SU(3)_c$. Some of the states in the octet are colorless. Using this information a more appropriate definition of the previously mentioned *color hypothesis* is that *all particles in that are observed in nature are color singlet states*: this accounts for the fact that the colorless gluons in the octet are not observed on their own. All color singlet states are colorless, but not all colorless states are singlets.

No free quark or gluon has ever been observed. It is an important axiom of QCD that they cannot be observed. The quarks and gluons are said to be confined inside the hadron of which they are a member: this is called *confinement*. There is

no analytical reason for this, but the color hypothesis gives an intuitive explanation. Individual quarks and gluons are not color singlet states; only color singlet states can be observed; therefore, free quarks and gluons will not be observed.

During a high energy collision free quarks or gluons are initially created. However, because of confinement they cannot exist on their own. The color force is strong enough that it is energetically favorable to create quark-antiquark pairs out of the vacuum. The creation of quark-antiquark pairs continues until there is no longer enough energy left in the color field. Each one of the quarks or gluons (which decay into quark-antiquark pairs) created during the collision combines with some of the quarks or antiquarks created from the vacuum to form a separate group of hadrons: this process is called *hadronization* or *fragmentation*. The group of hadrons formed from each quark or gluon initially created in the collision is called a *jet*.

In 1969, at the Stanford Linear Accelerator (SLAC) [2], experiments were done in which high energy electrons were fired at protons in order to see if the proton had any internal structure. These deep inelastic scattering (DIS) experiments, as they were called, are similar to the one Rutherford performed in the early 1900s to discover that the atom had a dense nucleus located at the center of the atom. The results of the DIS experiments showed that the proton had three scattering centers.

More direct evidence of quarks can also be obtained by studying e^+e^- collisions. One of the possibilities is that the two particles will annihilate each other, part of the time producing a quark-antiquark pair. According to QCD, these two quarks will form two jets. In 1975, at SLAC [3] jets were observed for the very first time, thus providing strong evidence that quarks exist. The authors calculated the quantity they

called *sphericity*[1]:

$$S \;=\; \frac{3(\sum_i |\vec{p}_{\perp i}|^2)_{min}}{2\sum_i |\vec{p}_i|^2} \;=\; \frac{3}{2}\,\frac{\min\limits_{\hat{n}} \sum_i |\vec{p}_i \times \hat{n}|^2}{\sum_i |\vec{p}_i|^2}\,, \tag{1.1}$$

where $\vec{p}_{\perp i} = \hat{n} \times (\vec{p}_i \times \hat{n})$; the second equation is an alternative form that makes the minimization more transparent. The $\hat{n}$ that minimizes S is called the sphericity axis. The number of events versus sphericity ($N\,vs.\,S$) was plotted for data, for a jet model with $\langle \vec{p}_\perp \rangle = 315$ MeV, and for a phase-space model. It was found that the data matched the jet model. They used an event shape to observe jets for the first time, and in the process provide strong evidence for quarks.

Evidence of the existence of the gluon can be obtained in a similar fashion to that for finding quarks. Since it is known that in e^+e^- collisions only two quarks are produced and that these two quarks will form two jets of particles, then discovery of events with a third jet, which must be a gluonic jet, will provide strong evidence for the existence of the gluon. In 1979 the TASSO experiment at PETRA [4] performed such an experiment and found a third jet, thus discovering the gluon. TASSO used the event shapes sphericity and aplanarity. These two event shapes are derived in a similar fashion to the sphericity used in this dissertation (see section 3.5.3) except that the momentum tensor used here is three-dimensional and that the sums are over individual particles not jets as is done in this dissertation. There will be three eigenvalues with $\lambda_1 \geq \lambda_2 \geq \lambda_3$. With i running over all particles in the event, sphericity (S) and aplanarity (A) are defined, respectively, by,

$$S = \frac{3}{2}\frac{\lambda_3 + \lambda_2}{\sum_i |\vec{p}_i|^2} \qquad \text{and} \qquad A = \frac{3}{2}\frac{\lambda_3}{\sum_i |\vec{p}_i|^2}\,. \tag{1.2}$$

[1]The terminology has evolved; sphericity used here is more closely related to event shape spherocity used in this dissertation

Having established that quarks and gluons exist inside of hadrons, one can infer the properties of the initiating quarks and gluons by measuring the properties of jets. Event shapes were used to provide detailed measurement of the properties of jets produced in high energy events. Drawing from the experience of previous experiments, a number of event shapes can be defined, all of which can provide information about how the final state energy is distributed. In [5] event shapes were described that are useful for studying high energy collisions in proton-antiproton colliders. In [6] two of those event shapes, thrust and thrust minor, were used to study events at the CMS (Compact Muon Solenoid) detector located at the LHC (Large Hadron Collider). This dissertation represents the first time that all nine event shapes defined in [5] are measured in a single analysis.

The nine event shapes are thrust, thrust minor, sum of masses, heavy mass, total broadening, wide jet broadening, F-parameter, sphericity, and spherocity; they will be defined in Chapter 3. These nine different event shapes will be studied in two different ways: both differential normalized distributions ($\frac{1}{\sigma}\frac{d\sigma}{dX}$), and average event shapes ($\overline{X}$), where X is the event shape. Each of the event shapes provides information about the flow of energy in QCD events and about the hadronic final states that occur in particle collisions, thus allowing the study of the dynamics of QCD multijet events. Any deviation of an event shape from zero will be indicative of higher-order effects, *i.e.* that more than the two jets existed in the event. These event shapes will be used to test different models of jet production in hadron colliders.

In the next chapter the theoretical background that is needed for this dissertation will be given, including discussions of how two different Monte Carlo (MC)

generators implement perturbative and nonperturbative elements of QCD, and of the jet finding algorithm used. In Chapter 3, the definition of the nine event shapes that are being studied along with phase space definitions needed for the analysis will be given. The accelerator complex that is located at Fermi National Accelerator Lab and the DØ detector which collected the data used in this dissertation are described in Chapter 4. The results of the analysis are presented and discussed in Chapter 5. A summary of the results and any conclusions drawn from said results are the topic of chapter 6.

CHAPTER 2

THEORETICAL BACKGROUND

This chapter will cover some background material that will be needed to study the event shape analysis. First, Feynman diagrams will be discussed. After that pertubative effects in Quantum Chromodynamics (QCD) and how they relate to the two Monte Carlo event generators SHERPA [7] and PYTHIA [8] will be discussed. Some nonperturbative effects of QCD and how those are implemented in SHERPA and PYTHIA will be discussed. Finally, the jet finding algorithm used by DØ will be discussed.

2.1 Feynman Diagrams

Feynman diagrams were originally invented by Richard Feynman while working on Quantum Electrodynamics (QED) [9]. They are a graphical representation of the scattering amplitudes for particle reactions. For example, if one wanted to know the probability of the the reaction $e^-e^+ \rightarrow \mu^-\mu^+$, one would first draw all possible Feynman diagrams that have an incoming electron (e^-) and positron (e^+), as in the sample diagram given in Figure 2.1. For each diagram that is drawn, the scattering amplitude is calculated using specific rules, called the Feynman rules. Then all of these amplitudes are added, and then the sum is squared. This squared sum multiplied by appropriate phase space factors gives the probability of the reaction.

There are actually an infinite number of Feynman diagrams for any particular reaction to all different orders. The order of a Feynman diagram is given by the number of vertices that the diagram has, a vertex being a point where any three lines in the diagram come together. The diagram in Figure 2.1 has two vertices; therefore, its order is two.

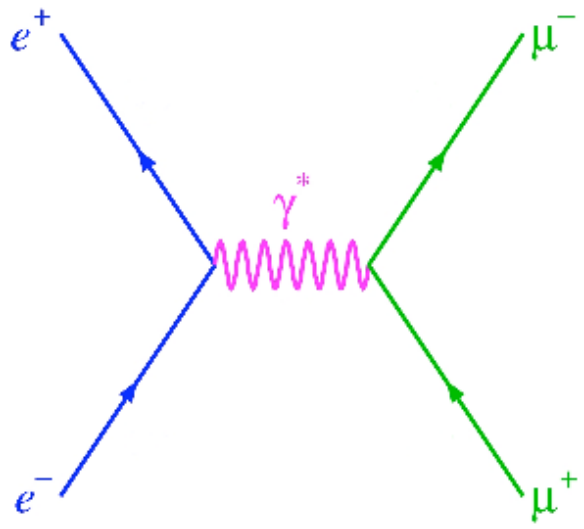

Figure 2.1: Sample Feyman diagram for creation of $\mu^-\mu^+$ from e^-e^+.

As was mentioned earlier, Feynman originally derived the rules and diagrams for QED, deriving these by using the Lagrangian for QED. However, Feynman diagrams and rules can be derived for any quantum field theory – for example, Quantum Chromodynamics (QCD) – using its Lagrangian. The fundamental diagrams (*i.e.* those from which all other diagrams can be made) for QCD are given in Figure 2.2.

The lowest order diagrams that can be derived are ones in which two of the fundamental diagrams are combined as if fitting two puzzle pieces together: matching two quark lines, two antiquark lines, or two gluon lines. All of the possibilities for

combining two fundamental diagrams are shown in Figure 2.3. Each of the two outgoing particles will create a jet of particles.

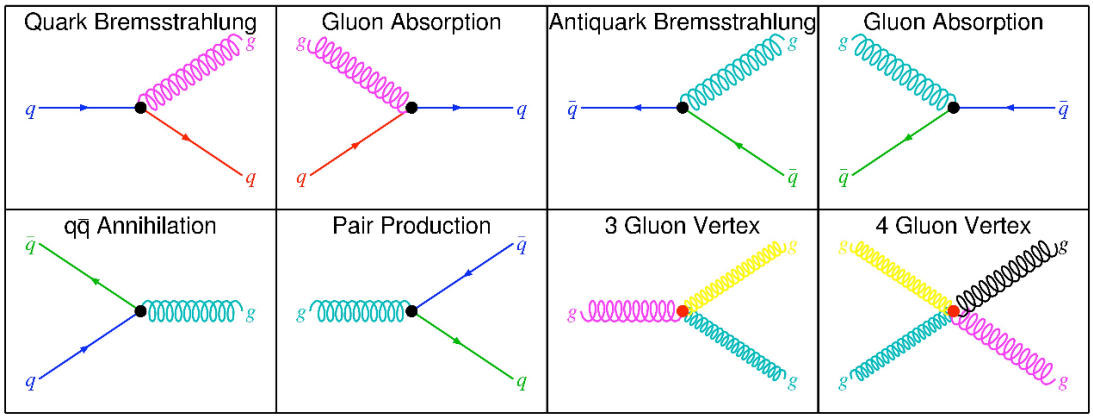

Figure 2.2: Fundamental vertices in QCD Feynman diagrams. Time runs from left to right. Quarks are represented by arrows that point to the left. Antiquarks are represented by arrows that point to the right. Gluons are represented by curly lines.

The Feynman diagrams in Figure 2.3 are the leading order diagrams for two-jet production. An extra gluon can be added to any of the diagrams in Figure 2.3 in two ways: as an internal gluon (meaning neither end of the gluon is free) or as an external gluon (one end of the gluon is attached and one end is free). The internal gluon picture will contribute to the two-jet creation; the external gluon will contribute to the three-jet picture. Sample of these differences is shown in Figure 2.4.

2.2 Perturbative Calculations

As was mentioned earlier, the order of a Feynman diagram is given by the number of vertices that the diagram has. Each vertex contributes one $\sqrt{\alpha_S}$ to the scattering amplitude, where α_S is the strong coupling constant. Each process in Figure 2.3 has two vertices; therefore, the scattering amplitude is $\propto \alpha_S$. Most of

the time what is measured is a cross section which is proportional to the scattering amplitude squared; thus, the cross section is $\propto \alpha_S^2$.

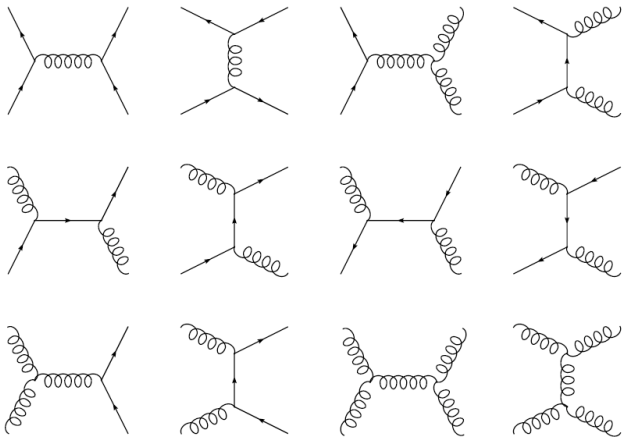

Figure 2.3: Leading order Feynman diagrams for creation of two jets [10]. Time runs from left to right. If time is taken to run up instead of to the right, more leading order 2-jet diagrams can be obtained – most of these will be repeats of time-running-to-the-right Figures.

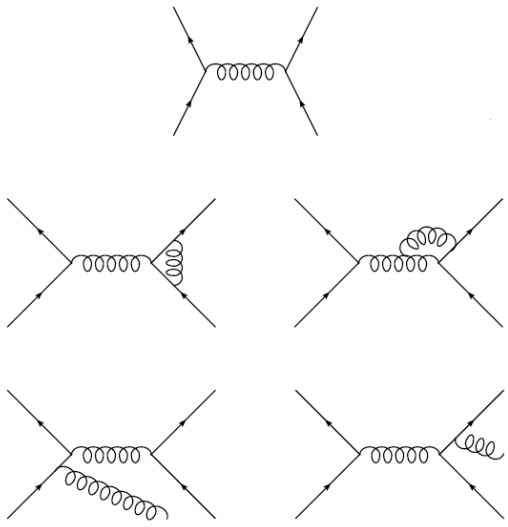

Figure 2.4: The top row shows a sample leading order Feynman diagram for creation of two jets; the middle row shows sample next-to-leading order Feynman diagrams for creation of two jets; and the bottom row shows sample leading order Feynman diagram for creation of three jets [10].

The strong coupling constant is not actually constant but varies with energy: the higher the energy, the weaker the coupling constant. For example at 1 GeV $\alpha_S \approx 1$; while at 91.2 GeV, $\alpha_S \approx 0.118$. If the energy is large enough, then calculating the scattering amplitudes can be done as a perturbative expansion in powers of α_S. In many cases only a few orders will be needed to get an accurate enough result. In the following two subsections, a brief discussion will be given about the different processes ($2 \to 2$, $2 \to 3$, etc) that are implemented by PYTHIA and SHERPA .

2.2.1 Pythia

PYTHIA [8] is an MC-based event generator that implements a number of high-energy final states. It has several parameters that can be varied which allow the model to be tuned to perform specific analyses. Of particular interest to this dissertation is how $2 \to n$ processes are simulated in PYTHIA: $2 \to 2$ plus parton showers.

In the beginning two particles are approaching each other (p and $\overline{p}$ for this dissertation). Each of these particles is characterized by a parton distribution function, which defines the substructure of the particle. One parton from each beam particle is taken as a shower initiator.

Each of these initiators showers by way of an iterative sequence of $1 \to 2$ branchings starting with $a \to bc$, where a is called the mother and b and c the two daughters. Each of the daughters is now free to branch. Define z as the fraction of energy and momentum of the mother a taken by daughter b, and the fraction $1z$ as the same for daughter c. A cut-off on the allowed range of z is introduced to avoid

problems that occur with the production of too many very soft gluons (*i.e.* gluons with very low transverse momentum). This is called an *initial-state shower*.

Once this branching is completed, one parton from each of the two showers enters the hard process as one of the tree-level, $2 \to 2$ processes shown in Figure 2.3. Any partons from the branching that are not part of the hard interaction are considered *initial-state radiation*; the first diagram in the third line of Figure 2.4 gives an example of initial-state radiation. No higher-order loop corrections like those in the second line of Figure 2.4 are explicitly included. The outgoing partons then branch in a similar fashion to construct a final-state shower that includes diagrams like the second diagram in the third line of Figure 2.4. The initial- and final-state showers allow for the possibility of more than two jets.

2.2.2 Sherpa

Sherpa[1] [7] is an another MC-based event generator that also generates many high-energy final states. Of particular interest to this dissertation is how $2 \to n$ processes are simulated in Sherpa: $2 \to 2$, $2 \to 3$, $2 \to 4$, and $2 \to 5$, plus a parton shower.

The idea used by Sherpa is to divide the phase space into two regimes – one of jet production, described by appropriate matrix elements ($2 \to 2$, $2 \to 3$, $2 \to 4$, and $2 \to 5$), and one of jet evolution, described by parton showering. The parton configurations of the matrix elements are studied. In this process a pseudo-shower configuration is created. Using this the matrix elements are reweighted[2]. After the

[1] Sherpa stands for Simulation of High-Energy Reactions of PArticles

[2] This is not to be confused with the reweighting of Sherpa used in this analysis; they are separate issues.

reweighting is done, the parton shower is performed starting with the previously mentioned pseudo-shower constructed.

The parton shower is only used to generate those jets which are not produced by the matrix elements. Only the softest jets (jets with the lowest transverse momenta) are generated by the parton shower.

2.3 Nonperturbative Calculations

There are processes in QCD that cannot be described using the perturbative approach discussed in the previous section. The two processes that will be discussed here are the *underlying event* involved in a particle collision, and the *hadronization* (or *fragmentation*) of partons into jets.

2.3.1 Underlying Event

The underlying event consists of beam remnants, multiple interactions, and pile-up. A beam remnant for a (anti-)proton beam consists of those constituents of the (anti-)proton which were not involved in the hard interaction but which are possibly color connected to one of the final-state particles.

Up to this point it has been assumed that one hard interaction occurs for each event, *i.e.* that only one parton from each incoming particle (proton or antiproton) takes part in hard interactions, and that everything else goes through unaffected. However, because the proton and antiproton both contain multiple partons, the probability of several interactions occuring at once during the same event need not be negligibly small.

In high-luminosity colliders such as the Tevatron, there is a small chance that a single bunch crossing[3] will have several separate $p\overline{p}$ collisions, which is called pile-up. From the standpoint of the DØ detector, pile-up can also occur because the calorimeter electronics may not be able to cope with rate at which events are happening: thus there will be energy left behind from the previous bunch crossing.

For most Monte Carlo event generators, the description of pile-up is poor. To obtain a good description of pile-up in experiments, minimum bias events[4] are overlaid on top of the output of the event generator.

2.3.2 Hadronization

There is no first-principles approach to hadronization that yields any quantitative results. Therefore, phenomenological models are used by Monte Carlo generators to simulate the hadronization. Pythia uses the Lund fragmentation model and Sherpa uses the cluster hadronization model.

The cluster hadronization model [12] uses the assumption that quantum numbers on the hadron level are intimately connected to the flow of quantum numbers on the parton level. The spectrum of masses of the emerging color-neutral clusters is governed by masses close to that of typical hadrons. Therefore, these clusters can be thought of as hadronic matter. Clusters are composed of flavor constituents, *i.e.* quarks or diquarks (two quarks bound together) or the like for antiquarks. Because of this gluons must decay into a quark-antiquark pair. Light clusters are taken directly

[3]The beams of protons and antiprotons are not continuous but are each grouped in bunches which circle the Tevatron in opposite directions. It is called a bunch crossing when these bunches intersect at DØ.

[4]Events triggered by the luminosity monitor, indicating an inelastic collision.

as light hadrons; heavier clusters either are taken as heavy hadrons or decay into lighter clusters which then are taken as light hadrons.

The Lund fragmentation model [13] treats all but the highest-energy gluons as field lines. These field lines are attracted to one another because gluons interact with other gluons and thus form narrow tubes called strings. The final state hadrons are created when the strings break.

2.4 Jets

The jet algorithm that will be described in this section can be used to reconstruct jets in each of the three separate regimes given in Figure 2.5.

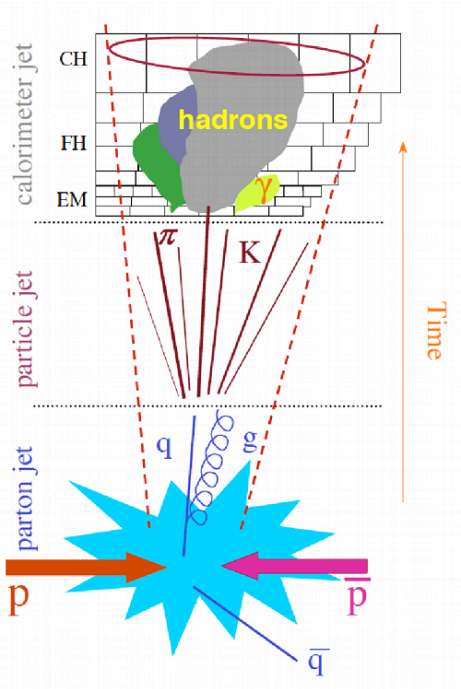

Figure 2.5: Parton, particle, and calorimeter jets.

The reconstruction of parton jets occurs using information either from fixed-order perturbative calculations or from parton showering models, depending upon

which Monte Carlo generator is used. The reconstruction of particle jets occurs after the partons have hadronized, using information from a Monte Carlo generator. Detector jets are reconstructed from either calorimeter cells or towers. This can be done for data or for a Monte Carlo simulation of the detector.

A jet algorithm should be fully specified, with all kinematic variables and features, such as preclustering and splitting/merging, well-defined. It should be independent of the detector and of how the jets are ordered (true for parton, particle, and detector jets). It must be efficient in the use of computing resources, straightforward to implement, and easy to calibrate. It must be infrared safe[5], collinear safe[6], and invariant under longitudinal boosts.

At various stages of the jet finding algorithm, items will need to be combined. The scheme used by DØ to combine objects is the *E-scheme*: two objects that are within a certain distance of each other are combined by adding their four momenta, where $P = (E, p_x, p_y, p_z)$ gives the four momentum of each object.

The first step in the jet finding algorithm used by DØ is to form preclusters from lists of items – calorimeter towers for detector jets and simulated particles, generated in Monte Carlo-based models, for parton or particle jets – that are ordered by decreasing transverse momemtum (p_T). The list of items is looped over until there are no individual items with $p_T^I > 500$ MeV left. What is left are a group of items called *preclusters* with $p_T^P > 1$ GeV. A flowchart showing the algorithm for

[5]Infrared safety means that the number of jets in the event does not change when a soft parton (parton with low transverse momentum) is added.

[6]Collinear safety means that the number of jets in the event does not change when one parton is split into two collinear ones.

preclustering is shown in Figure 2.6. The parts of the algorithm that are indicated by "applied for towers only" are parts that only apply to detector jets.

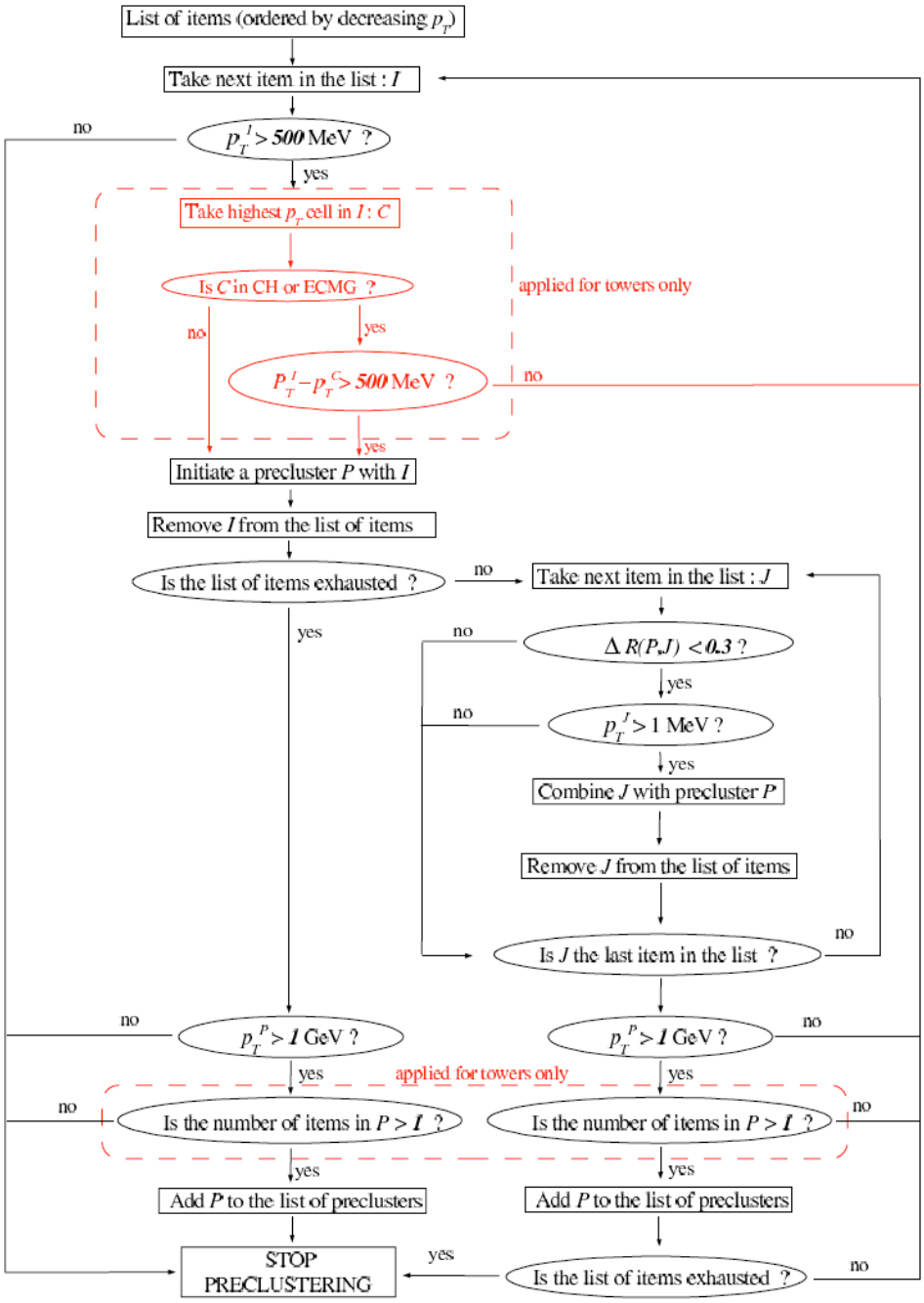

Figure 2.6: Flowchart describing the preclustering step of the jet reconstruction algorithm used by DØ, taken from [11]

The clustering phase of the jet finding algorithm (see Figure 2.7 for a flowchart of the clustering phase) takes two lists as inputs: the list of preclusters from the precluster phase and the list of items (calorimeter towers or cells).

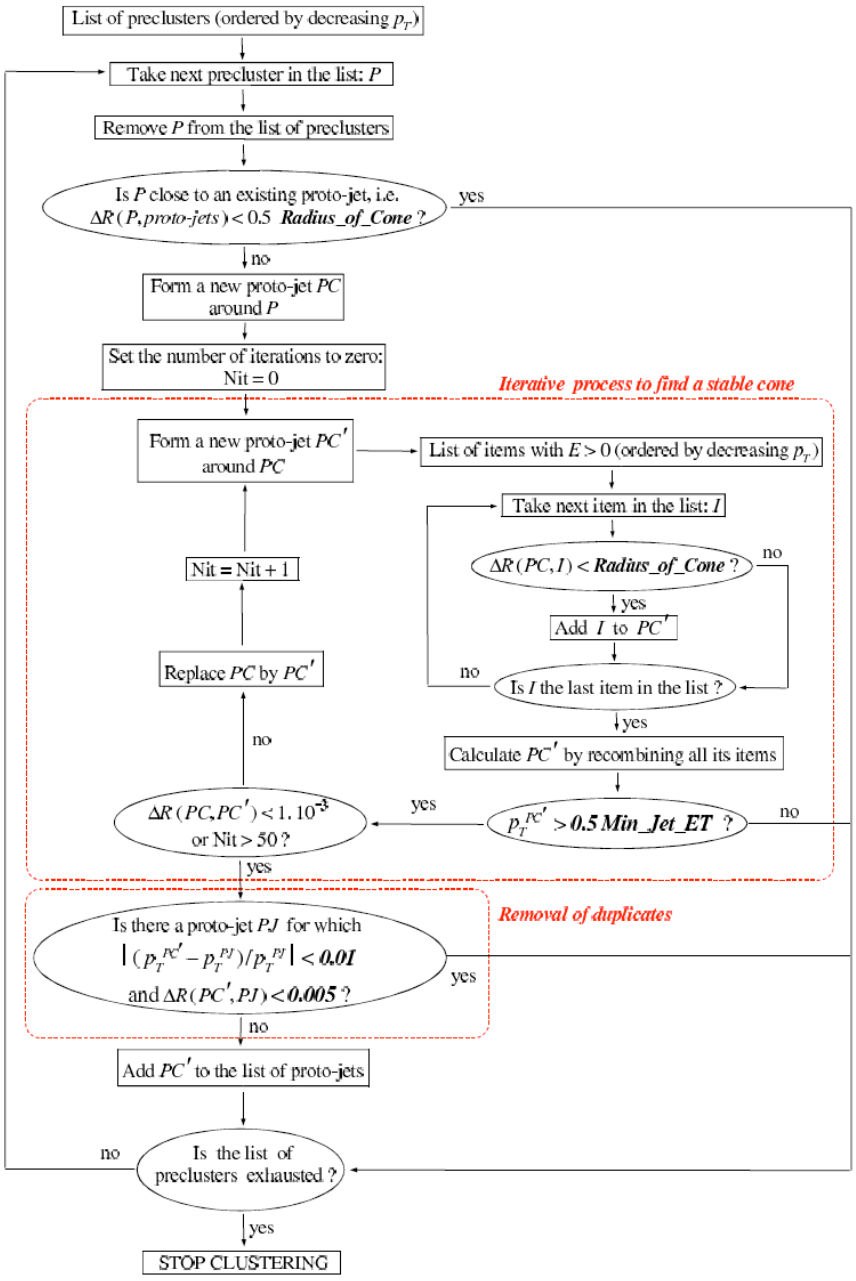

Figure 2.7: Flowchart describing the clustering step of the jet reconstruction algorithm used by DØ, taken from [11].

The list of preclusters ordered by decreasing transverse momemtum (p_T) is looped over until there are no preclusters left. Each precluster is either used as a seed for a protojet (stable cone) or discarded if it is too close to a pre-existing protojet. For each precluster that is a seed, all of the items are looped over to determine which items are within a distance ΔR (defined in Table H.1) of the protojet. For each item that is within the distance $\Delta R = 0.5 R_{cone}$, where $R_{cone} = 0.7$ for this dissertation, that item is added to the protojet using the E-scheme, updating the protojet. This process is iterated until the current protojet is within a tolerance of 0.001 of the previous iteration, or the number of iterations reaches the maximum of 50. The "removal of duplicates" step makes sure that the protojet is not already in the list of protojets.

As it stands the clustering algorithm is not infrared safe. To alleviate this problem, midpoints are formed from all combinations of two protojets that are within a distance range $R_{cone} < \Delta R < 2 * R_{cone}$ of each other, where R_{cone} is the radius of the cone. For this analysis $R_{cone} = 0.7$. Using the list of midpoints in place of the preclusters, the clustering algorithm in Figure 2.7 is run, excluding the duplicate checking step. A list of protojets is obtained from this step.

Often the protojets obtained from the preclusters and the ones from the midpoints share items. In order to avoid the double counting of the energy of these items, a merge/split algorithm needs to be performed (see Figure 2.8). The combined list of protojets from midpoint and preclustering, ordered by decreasing p_T, and the list of items are taken as input. The combined list is looped over, starting with the highest p_T protojet, until it is exhausted. Merging occurs if a protojet with a higher

p_T shares at least 50% of the p_T of a lower p_T protojet; splitting occurs when they share less than 50%. Once this step is completed, the calculation of the jet variables is done.

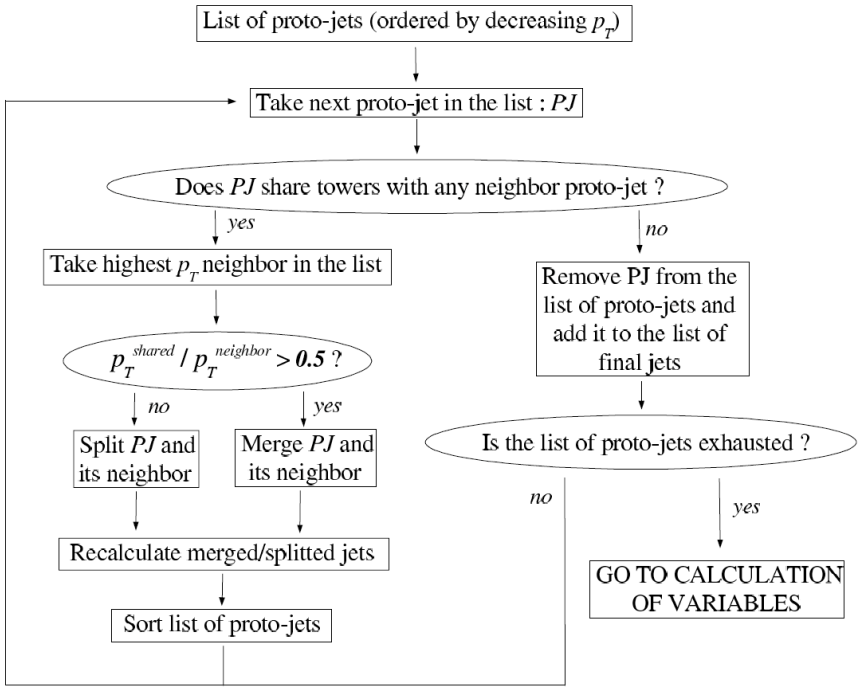

Figure 2.8: Flowchart describing the merge/split step of the jet reconstruction algorithm used by DØ.

CHAPTER 3

EVENT SHAPES

Event shapes measure how the energy of the final particles are distributed in the events. They provide information about the flow of energy in QCD events and about the hadronic final states that occur in particle collisions, thus allowing the study of the dynamics of QCD multijet events. This analysis will concentrate on jet-based event shapes, measured in the transverse plane in $p\overline{p}$ collisions. The event shapes, which are defined later in this chapter, are thrust, thrust minor, sum of masses, heavy mass, total broadening, wide jet broadening, F-parameter, sphericity, and spherocity.

These event shapes distinguish between massless back-to-back $2 \rightarrow 2$ and $2 \rightarrow 2+$ "anything else" processes; for this dissertation "anything else" means that there are extra jets beyond the two leading jets. These event shapes are constructed such that they vanish in the limit of a massless back-to-back $2 \rightarrow 2$ process; as will be seen later in this chapter, for some event shapes vanishing occurs in configurations that differ from massless back-to-back $2 \rightarrow 2$ processes. Another way to look at it is that the event shapes determine to what degree an event deviates from an exclusive massless dijet event.

3.1 Generic Event Shape

Generic event shape will refer to any of the event shapes being studied. There are one of three possible configurations for a generic event shape (see Figure 3.1): two back-to-back massless jets, two back-to-back massive jets, or two back-to-back massive jets with activity outside the jet.

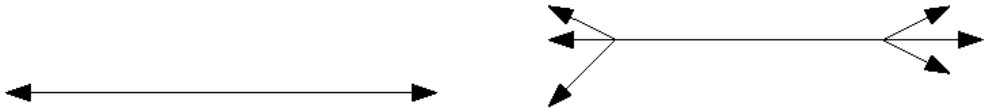

(a) Two massless back-to-back jets

(b) Two massive back-to-back jets

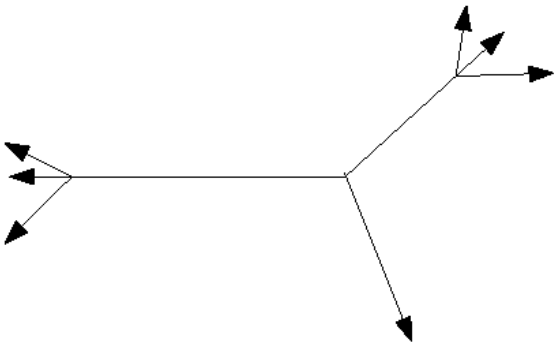

(c) Two massive jets with activity outside jets

Figure 3.1: Different jet configurations

For the configuration given in Figure 3.1c, the activity outside the jet could be anything that is not a part of the two jets; however, for this dissertation it is taken as extra jets. These extra jets have two possibilities: either unreconstructed jets (jets that do not meet the minimum criteria to be reconstructed) or reconstructed jets that have momenta below the momentum cutoff for the analysis. There can also be a combination of both: for example, a third reconstructed jet could be below the cutoff and any other jets could be unreconstructed.

As was mentioned in the introduction to this chapter, all of the event shapes go to zero for Figure 3.1a. For Figure 3.1b any of the event shapes but the sum of

masses and the heavy mass will go to zero. For Figure 3.1c there is the possibility that the total broadening and the wide jet broadening could be zero if there is activity outside the two jets that is below the momentum threshold for inclusion; all other event shapes are nonzero. The situation in Figure 3.1a is a subset of the situtation in Figure 3.1b – take the mass of the jets to be zero. The situation in Figure 3.1b is in turn a subset of the situation in Figure 3.1c – take the activity outside the two jets to be zero. Therefore, if an event shape is zero for a certain configuration, then it will be zero for any less general configuration. For which configuration in Figure 3.1 each of the event shapes being studied goes to zero will be shown in the sections that follow in this chapter.

3.2 Phase Space Cuts and Various Definitions

Each of the event shapes being studied is defined for a plane transverse to the beam axis, where the beam axis is taken as the z-axis. At least two jets are required to be in the event, also called a dijet event, in order for the event to be included in the study being presented in this dissertation. The first two jets, where jets are ordered by momentum in the transverse plane (p_T), must satisfy the following conditions:

$$\begin{aligned} y^* < y^*_{max} \qquad &\text{and} \qquad |y^{boost}| < y^{boost}_{max}\,, \\ p_{T1} > p_{T,threshold} \qquad &\text{and} \qquad p_{T2} > p_{T,threshold}\,, \end{aligned} \tag{3.1}$$

where

$$y^{boost} = \frac{y_1 + y_2}{2} \qquad \text{and} \qquad y^* = \frac{|y_1 - y_2|}{2}\,, \tag{3.2}$$

where y_1 and y_2 are the rapidities of the two leading jets and p_{T1} and p_{T2} are the transverse momenta of the two leading jets, and where $y^*_{max} = 0.5$, $y^{boost}_{max} = 1.0$, and

$p_{T,threshold} = 30$ GeV. In addition all jets in the dijet event that are to be included in the present study must belong to a set C defined in the dijet center-of-mass (CM) frame with a minimum p_T threshold as

$$C = \{p_{Ti} > p_{T,threshold}\ |y_i - y^{boost}| < (y^*_{max} + \delta y)\}\,, \tag{3.3}$$

where i refers to the jet, y_i is the rapidity of jet i, p_{Ti} is the transverse momentum of jet i, and $\delta y = 1.0$. From the requirements on the two leading jets, it can be seen that they are automatically members of set C.

The quantity H_T, which is needed in the definitions of seven of the nine event shapes and for defining analysis regions, is

$$H_T = \sum_{i \in C} p_{Ti}\,, \tag{3.4}$$

where i runs over all jets in C and

$$p_T = |\vec{p}_T|\ . \tag{3.5}$$

In addition to the aforementioned requirements, the p_T of the leading jet (p_{T1}) must be greater than $\frac{H_T}{3}$, *i.e.* $p_{T1} > \frac{H_T}{3}$. This requirement is added to improve the trigger turnons (see appendix C for the trigger turnon studies). This cut removes only a small portion of the physics content in the leading tail of the efficiency curves, which is where the inclusive jet triggers are not fully efficient anyway (see appendix C for what the inclusive jet triggers are).

3.3 Event Shapes Based upon the Thrust Axis, I

First, two event shapes based upon the thrust axis, the thrust and thrust minor, will be defined in this section.

3.3.1 Thrust

The thrust is defined by the following:

$$T_{T,C} \equiv \max_{\hat{n}_T} \frac{\sum_{i \in C} |\vec{p}_{Ti} \cdot \hat{n}_T|}{H_T}\,, \tag{3.6}$$

where the $\hat{n}_T$ lies in the transverse (xy) plane. The value of $\hat{n}_T$ that maximizes the *thrust* ($\hat{n}_{T,max}$) is called the *thrust axis*. The thrust axis and the beam direction form what is called the event plane.

The thrust is an important event shape in its own right. It is a measure of the energy flow in the event plane. In addition the determination of the thrust axis is needed in order for five other event shapes to be defined: thrust minor (subsection 3.3.2), sum of masses and heavy mass (subsection 3.4.1), and total broadening and wide jet broadening (subsection 3.4.2).

When one minus thrust goes to zero

For the thrust the quantity being studied is $1 - T_{T,C}$. It will be shown when $1 - T_{T,C}$ goes to zero. Assume two back-to-back jets – i.e. $\vec{p}_{T2} = -\vec{p}_{T1}$. With this and the definition of H_T:

$$1 - T_{T,C} = 1 - \max_{\hat{n}_T} \frac{|\vec{p}_{T1} \cdot \hat{n}_T| - |\,\vec{p}_{T2} \cdot \hat{n}_T|}{p_{T1} + p_{T2}} = 1 - \max_{\hat{n}_T} \frac{|\vec{p}_{T1} \cdot \hat{n}_T|}{p_{T1}}\,. \tag{3.7}$$

The $\hat{n}_T$ that maximizes the right-hand term must be $\hat{n}_{T,max} = \pm\vec{p}_{T1}/p_{T1}$ – $\hat{n}_{T,max}$ is along the direction of one of the two jets. This $\hat{n}_{T,max}$ will give $1 - T_{T,C} = 0$.

3.3.2 Thrust Minor

The *thrust minor* is a measure of the energy flow out of the event plane. It is defined by the following:

$$T_{m,C} \equiv \frac{\sum_{i \in C} |\vec{p}_{Ti} \times \hat{n}_{T,max}|}{H_T}\,, \tag{3.8}$$

where $\hat{n}_{T,max}$ is the $\hat{n}_T$ that maximizes the thrust in 3.3.1.

When the thrust minor goes to zero

It will be shown when the thrust minor goes to zero. Assume that there are two back-to-back jets, *i.e.* $\vec{p}_{T2} = -\vec{p}_{T1}$. In this case $\hat{n}_{T,max} = \pm\vec{p}_{T1}/p_{T1}$. Without loss of generality $\hat{n}_{T,max} = \vec{p}_{T1}/p_{T1}$ will be assumed. With these assumptions and the definition of H_T the thrust minor becomes

$$T_{m,C} = \frac{|\vec{p}_{T1} \times \hat{n}_{T,max}| + |\vec{p}_{T2} \times \hat{n}_{T,max}|}{p_{T1} + p_{T2}} = \frac{|\vec{p}_{T1} \times \hat{n}_{T,max}|}{p_{T1}} = \frac{|\vec{p}_{T1} \times \vec{p}_{T1}|}{p_{T1}^2} = 0\,. \tag{3.9}$$

For the thrust and thrust minor to obtain a zero value, two back-to-back massive jets with equal but opposite transverse momenta are needed – the case of Figure 3.1b.

3.4 Event Shapes Based upon the Thrust Axis, II

Additional event shapes based upon the thrust axis – sum of masses, heavy mass, total broadening, and wide jet broadening – will be defined in this section. The jets in the event first need to be separated into two groups – an up region (U) and a

down region (D) – defined in terms of the thrust axis ($\hat{n}_{T,max}$) by

$$\begin{aligned} C_U &: \ \vec{p}_{Ti} \cdot \hat{n}_{T,max} > 0 \ \ (i \in C_U) \,, \\ C_D &: \ \vec{p}_{Ti} \cdot \hat{n}_{T,max} < 0 \ \ (i \in C_D) \,. \end{aligned} \tag{3.10}$$

3.4.1 Sum of Masses and Heavy Mass

The normalized, squared invariant mass for each of the regions is defined as

$$\rho_{X,C} \equiv \frac{1}{H_T^2} \left(\sum_{i \in C_X} p_i \right)^2 \,, \tag{3.11}$$

where $X = U, D$ and where $p_i = (E_i, -p_{xi}, -p_{yi}, -p_{zi})$ is the four momentum of the jet i. The sum gives the total four-momentum for each region:

$$\begin{aligned} P_{tot}^{(X)} = \sum_{i \in C_X} p_i &= \left(\sum_{i \in C_X} E_i, -\sum_{i \in C_X} p_{xi}, -\sum_{i \in C_X} p_{yi}, -\sum_{i \in C_X} p_{zi} \right) \\ &= \left(E_{tot}^{(X)}, -p_{x,tot}^{(X)}, -p_{y,tot}^{(X)}, -p_{z,tot}^{(X)} \right) \,. \end{aligned} \tag{3.12}$$

Squaring the sum (dotting the four-vector into itself) gives

$$\left(P_{tot}^{(X)} \right)^2 = \left(E_i^X \right)^2 - \left(p_{x,tot}^X \right)^2 - \left(p_{y,tot}^X \right)^2 - \left(p_{z,tot}^X \right)^2 = \left(m_{tot}^{(X)} \right)^2 \,. \tag{3.13}$$

Using this shows that calling $\rho_{X,C} = \left(\sum_{i \in C_X} p_i \right)^2 / H_T^2 = \left(m_{tot}^{(X)} \right)^2 / H_T^2$ a normalized square mass was justified, where $\rho_{U,C}$ is for the up region and $\rho_{D,C}$ is for the down region. Using these definitions for $\rho_{U,C}$ and $\rho_{D,C}$, the sum of masses ($\rho_{S,C}$) and the heavy mass ($\rho_{H,C}$) are defined as

$$\begin{aligned} \rho_{S,C} &= \rho_{U,C} + \rho_{D,C} \,, \\ \rho_{H,C} &= \max \left(\rho_{U,C}, \rho_{D,C} \right) \,. \end{aligned} \tag{3.14}$$

When the masses go to zero

It will be shown when the sum of masses and the heavy mass go to zero. Assume that there are two back-to-back jets: one in the up region and one in the down region. Taking jet 1 to be in the up region and jet 2 in the down region, the normalized masses for the up and down regions are

$$\begin{aligned} \rho_{U,C} &= \frac{E_1^2 - p_{x1}^2 - p_{y1}^2 - p_{z1}^2}{H_T^2} = \frac{m_1^2}{(p_{T1} + p_{T2})^2}\,, \\ \rho_{D,C} &= \frac{E_2^2 - p_{x2}^2 - p_{y2}^2 - p_{z2}^2}{H_T^2} = \frac{m_2^2}{(p_{T1} + p_{T2})^2}\,. \end{aligned} \tag{3.15}$$

With this the sum of masses and heavy mass are

$$\begin{aligned} \rho_{S,C} &= \rho_{U,C} + \rho_{D,C} = \frac{m_1^2 + m_2^2}{(p_{T1} + p_{T2})^2}\,, \\ \rho_{H,C} &= \max\left(\rho_{U,C}, \rho_{D,C}\right) = \frac{\max\left(m_1^2, m_2^2\right)}{(p_{T1} + p_{T2})^2}\,. \end{aligned} \tag{3.16}$$

In order to have the sum of masses and the heavy mass be zero for this two jet event, $m_1 = m_2 = 0$. Therefore, the masses are both zero for the case of Figure 3.1a.

3.4.2 Total Broadening and Wide Jet Broadening

To define the broadenings, the pT-weighted average values of the rapidity ($y_{X,C}$) and the azimuthal angle ($\phi_{X,C}$) for the up and down regions ($X = U, D$) first need to be defined as

$$y_{X,C} \equiv \frac{\sum_{i \in C_X} p_{Ti} y_i}{\sum_{i \in C_X} p_{Ti}} \qquad \text{and} \qquad \phi_{X,C} \equiv \frac{\sum_{i \in C_X} p_{Ti} \phi_i}{\sum_{i \in C_X} p_{Ti}}\,. \tag{3.17}$$

Using these weighted average values, the broadenings for the up and down regions are

$$B_{X,C} \equiv \frac{1}{2H_T} \sum_{i \in C_X} p_{Ti} \sqrt{\left(y_i - y_{X,C}\right)^2 + \left(\phi_i - \phi_{X,C}\right)^2}\,, \tag{3.18}$$

where $X = U, D$. With the values for the broadenings of the up and down regions ($B_{U,C}$ and $B_{D,C}$), the values for the total broadening and the wide jet broadening are

$$\begin{aligned} B_{T,C} &= B_{U,C} + B_{D,C}\,, \\ B_{W,C} &= \max\left(B_{U,C}, B_{D,C}\right)\,. \end{aligned} \tag{3.19}$$

When the broadenings go to zero

It will be shown when the total broadening and the wide jet broadening go to zero. Assume that there are two jets (with all other activity in the event below the momentum threshold for inclusion) – one in the up region and one in the down region. These two jets do not necessarily have to be back-to-back. Taking jet 1 to be in the up region and jet 2 in the down region, the weighted average values of the rapidity and the azimuthal angle are

$$\begin{aligned} y_{U,C} &= \frac{p_{T1} y_1}{p_{T1}} = y_1 \qquad \text{and} \qquad \phi_{U,C} = \frac{p_{T1}\phi_1}{p_{T1}} = \phi_1\,, \\ y_{D,C} &= \frac{p_{T2} y_2}{p_{T2}} = y_2 \qquad \text{and} \qquad \phi_{D,C} = \frac{p_{T2}\phi_2}{p_{T2}} = \phi_2\,. \end{aligned} \tag{3.20}$$

The broadenings for the up and down regions are then

$$\begin{aligned} B_{U,C} &= \frac{1}{2H_T}\, p_{T1} \sqrt{\left(y_1 - y_{U,C}\right)^2 + \left(\phi_1 - \phi_{U,C}\right)^2} = 0\,, \\ B_{D,C} &= \frac{1}{2H_T}\, p_{T2} \sqrt{\left(y_2 - y_{D,C}\right)^2 + \left(\phi_2 - \phi_{D,C}\right)^2} = 0\,. \end{aligned} \tag{3.21}$$

The total broadening and the wide jet broadening are then both zero. Therefore, the broadenings are both zero for the case of Figure 3.1c, assuming that all other activity in the event is below the momentum threshold.

3.5 Event Shapes Independent of the Thrust Axis

The event shapes discussed in this section – F-parameter, sphericity, and spherocity – are independent of the thrust axis.

3.5.1 Spherocity

The spherocity is defined by the following:

$$S_{T,C}^{phero} = \frac{\pi^2}{4} \min_{\hat{n}} \left(\frac{\sum_{i \in C} |\vec{p}_{Ti} \times \hat{n}|}{H_T} \right)^2 . \tag{3.22}$$

When the spherocity goes to zero

It will be shown when the spherocity goes to zero. Assume that there are two back-to-back jets – i.e. $\vec{p}_{T2} = -\vec{p}_{T1}$. With this assumption the spherocity becomes

$$S_{T,C}^{phero} = \frac{\pi^2}{4} \min_{\hat{n}} \left(\frac{|\vec{p}_{T1} \times \hat{n}| + |\vec{p}_{T2} \times \hat{n}|}{H_T} \right)^2 = \frac{\pi^2}{2} \min_{\hat{n}} \left(\frac{|\vec{p}_{T1} \times \hat{n}|}{H_T} \right)^2 . \tag{3.23}$$

Since $H_T > 0$ and $|\vec{p}_{T1} \times \hat{n}| \geq 0$, the minimum in the spherocity definition will be zero, which occurs at $\hat{n} = \pm \vec{p}_{T1}/p_{T1}$, the direction of either of the two jets.

3.5.2 F-parameter

To define the F-parameter the following is needed

$$M^{lin} = \sum_{i \in C} \frac{1}{p_{Ti}} \begin{pmatrix} p_{xi}^2 & p_{xi}p_{yi} \\ p_{xi}p_{yi} & p_{yi}^2 \end{pmatrix} , \tag{3.24}$$

where M^{lin} is the linearized version of the transverse momentum tensor. This matrix has two eigenvalues, λ_1 and λ_2, with $\lambda_1 \geq \lambda_2$, found by using the trace (T) and determinant (D) of M^{lin}:

$$\lambda_1 = \frac{T + \sqrt{T^2 - 4D}}{2} \qquad \text{and} \qquad \lambda_2 = \frac{T - \sqrt{T^2 - 4D}}{2} . \tag{3.25}$$

The F-parameter is then the ratio of these two eigenvalues:

$$F_C = \frac{\lambda_2}{\lambda_1}\,. \tag{3.26}$$

When the F-parameter goes to zero

It will be shown when the spherocity goes to zero. Assume that there are two back-to-back jets – i.e. $\vec{p}_{T2} = -\vec{p}_{T1}$. With this assumption M^{lin} becomes

$$\begin{aligned} M^{lin} &= \frac{1}{p_{T1}} \begin{pmatrix} p_{x1}^2 & p_{x1}p_{y1} \\ p_{x1}p_{y1} & p_{y1}^2 \end{pmatrix} + \frac{1}{p_{T2}} \begin{pmatrix} p_{x2}^2 & p_{x2}p_{y2} \\ p_{x2}p_{y2} & p_{y2}^2 \end{pmatrix} \\ &= \frac{2}{p_{T1}} \begin{pmatrix} p_{x1}^2 & p_{x1}p_{y1} \\ p_{x1}p_{y1} & p_{y1}^2 \end{pmatrix}. \end{aligned} \tag{3.27}$$

The trace and determinant become

$$T = \frac{2}{p_{T1}}\,(p_{x1}^2 + p_{y1}^2) = 2p_{T1} \qquad \text{and} \qquad D = 0\,. \tag{3.28}$$

The eigenvalues are then

$$\lambda_1 = \frac{T + \sqrt{T^2 - 4D}}{2} = 2p_{T1} \qquad \text{and} \qquad \lambda_2 = \frac{T - \sqrt{T^2 - 4D}}{2} = 0\,. \tag{3.29}$$

Using these values for the eigenvalues, the F-parameter is then zero.

3.5.3 Sphericity

To define the sphericity the following is needed

$$M_{x,y} = \sum_{i \in C} \begin{pmatrix} p_{xi}^2 & p_{xi}p_{yi} \\ p_{xi}p_{yi} & p_{yi}^2 \end{pmatrix}, \tag{3.30}$$

where $M_{x,y}$ is the transverse momentum tensor. This matrix has two eigenvalues, λ_1 and λ_2, with $\lambda_1 \geq \lambda_2$, found by using the trace (T) and determinant (D) of $M_{x,y}$:

$$\lambda_1 = \frac{T + \sqrt{T^2 - 4D}}{2} \qquad \text{and} \qquad \lambda_2 = \frac{T - \sqrt{T^2 - 4D}}{2}\,. \tag{3.31}$$

The sphericity is then

$$S_{T,C}^{pheri} = \frac{2\lambda_2}{\lambda_1 + \lambda_2}\,. \tag{3.32}$$

When the sphericity goes to zero

It will be shown when the spherocity goes to zero. Assume that there are two back-to-back jets – i.e. $\vec{p}_{T2} = -\vec{p}_{T1}$. With this assumption $M_{x,y}$ becomes

$$M_{x,y} = \begin{pmatrix} p_{x1}^2 & p_{x1}p_{y1} \\ p_{x1}p_{y1} & p_{y1}^2 \end{pmatrix} + \begin{pmatrix} p_{x2}^2 & p_{x2}p_{y2} \\ p_{x2}p_{y2} & p_{y2}^2 \end{pmatrix} = 2\begin{pmatrix} p_{x1}^2 & p_{x1}p_{y1} \\ p_{x1}p_{y1} & p_{y1}^2 \end{pmatrix}\,. \tag{3.33}$$

The trace and determinant become

$$T = 2(p_{x1}^2 + p_{y1}^2) = 2p_{T1}^2 \qquad \text{and} \qquad D = 0\,. \tag{3.34}$$

The eigenvalues are then

$$\lambda_1 = \frac{T + \sqrt{T^2 - 4D}}{2} = 2p_{T1}^2 \qquad \text{and} \qquad \lambda_2 = \frac{T - \sqrt{T^2 - 4D}}{2} = 0\,. \tag{3.35}$$

Using these values for the eigenvalues, the sphericity is then zero.

For all of the events shapes in this section (spherocity, F-parameter, and sphericity) to obtain a zero value, two back-to-back massive jets with equal but opposite transverse momenta are needed – the case of Figure 3.1b.

CHAPTER 4

EXPERIMENTAL SETUP

The analysis performed in this dissertation is done with data collected by the DØ detector. This chapter describes the experimental apparatuses – Fermilab accelerator complex and the DØ detector – that are involved in the generation and collection of said data. In addition the specifics of the data collection will be discussed.

4.1 Fermilab Accelerator Complex

The Fermi National Accelerator Laboratory (Fermilab) accelerator complex (see Figure 4.1) accelerates protons and antiprotons to energies of 980 GeV each, producing collisions in the DØ detector at center-of-mass energy of 1.96 TeV. The acceleration is done in stages using several different accelerators.

The first stage is the pre-accelerator stage, which consists of a hydrogen ion (H^-) source and Cockcroft-Walton accelerator, which accelerates the H^- ions to an energy of 750 KeV. These H^- ions are then injected into a linear accelerator (linac) similar to the one in Figure 4.2.

In Figure 4.2 the H^- ions are represented by the little balls. As the H^- ions leave the Cockcroft-Walton (or any other ion source), they are attracted to the first drift tube (in the lower image of Figure 4.2) because the drift tube is oppositely charged from the H^- ion.

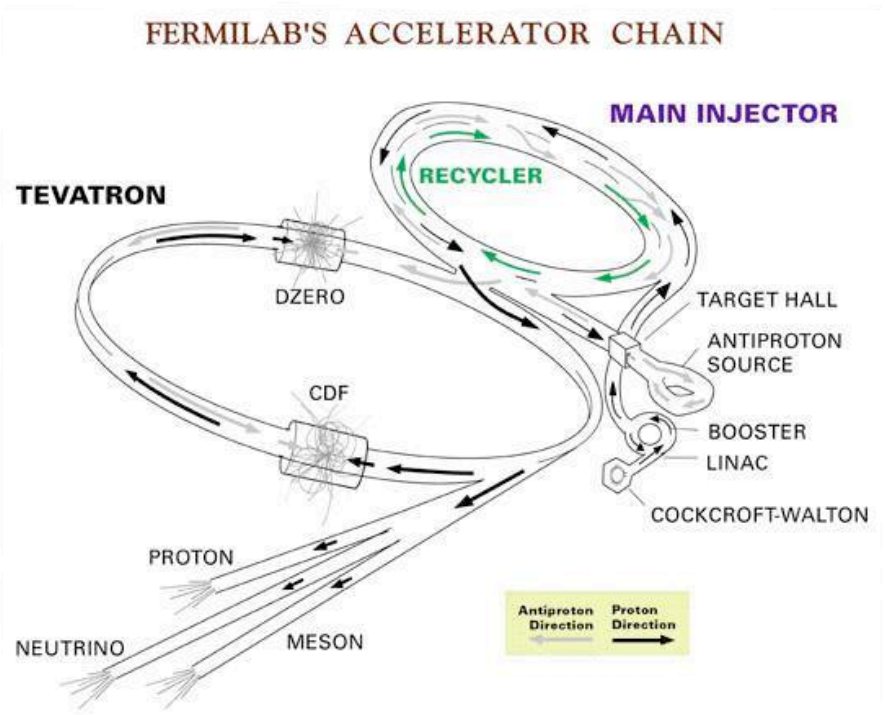

Figure 4.1: Layout of the Fermilab accelerator complex, including location of the two detectors – DØ and CDF.

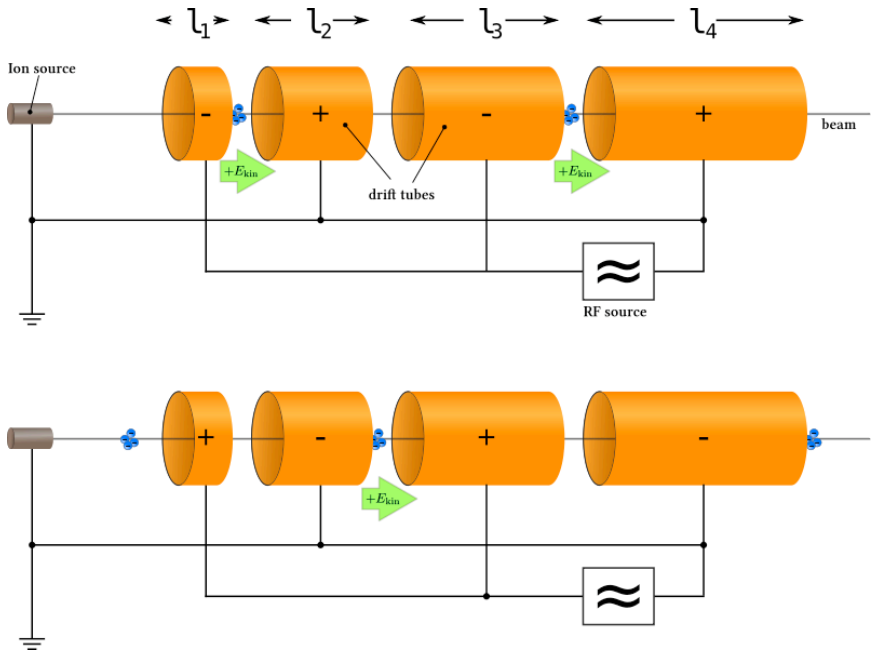

Figure 4.2: Generic linac

Once inside the drift tube there is no electric force on the H^- ion, so that the drift tube acts like a Faraday cage (inside which there is no electric field). Once outside the first drift tube the radio frequency (RF) oscillator changes the polarity of all of the drift tubes (upper image in Figure 4.2). When the H^- ion is outside the second drift tube, the polarity is switched again (lower image in Figure 4.2). This oscillation between the polarities continues until the H^- ion reaches the end of the linac, where the ion reaches its maximum energy. The linac at Fermilab accelerates the H^- ions from 750 KeV to 400 MeV.

After exiting the linac, the H^- ions are collided with a carbon foil that strips the electrons off the ion leaving the hydrogen nucleus (the proton). The rest of the accelerations of the protons (and later the antiprotons) are completed using several synchrotron accelerators, similar to the one in Figure 4.3. The synchrotron in Figure 4.3 works by having the particles (in Fermilab's case protons or antiprotons) injected into the accelerating cavity, which is similar to a linac. After being accelerated in the cavity, the particle is bent in a circular path by equally spaced magnets. Once the particle reaches the cavity, it is accelerated again. The magnetic field has a corresponding increase in magnitude to keep the particle moving in a cirlce of the same radius. The magnetic field is synched with the acceleration increase. This process of increasing the magnetic field just after the particle has been accelerated in the cavity is continued until the particle has reached the desired energy, at which point the particles are extracted and either sent to another accelerator or directed to a collision.

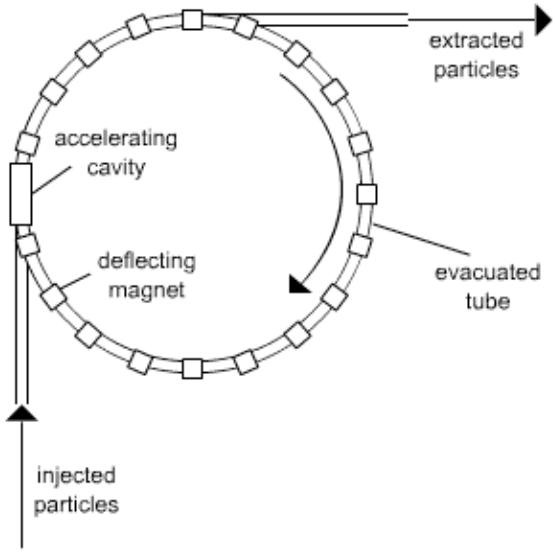

Figure 4.3: Generic synchrotron

The synchrotrons at Fermilab each have multiple acceleration cavities that are equally spaced around the circular path. The first such synchrotron that is reached after the H^- ions have been stripped of their electrons is the Booster which accelerates the protons from 400 MeV to 8 GeV. The protons are then sent to the Main Injector.

The Main Injector accelerates protons from 8 GeV to two different energies depending upon what is needed – 120 GeV used by the antiproton source, and 150 GeV injected into the Tevatron. The 120 GeV protons are sent slamming into a nickel target located in the Target Hall (see Figure 4.1). Some of the particles produced in these collisions are antiprotons. After separation 8 Gev antiprotons are gathered and stored in the Accumulator (located at the Antiproton Source in Figure 4.1) until enough have been collected for insertion into the Main Injector. The antiprotons are accelerated from 8 GeV to 150 GeV by the Main Injector.

The 150 GeV protons and antiprotons are inserted into the Tevatron which accelerates them both to 980 GeV. After this energy has been reached, the protons and antiprotons are directed to collide at two points along the Tevatron, the locations of the DØ and CDF detectors. A typical cycle of proton and antiproton collisions lasts approximately 24 hours. After this time the proton and antiproton beams are dumped and any remaining antiprotons are sent to the Recycler (see Figure 4.1) to be stored for the next cycle of collisions.

4.2 DØ Detector

The DØ detector is a large multielement, general purpose detector (see Figure 4.4) used for the study of high energy proton-antiproton ($p\overline{p}$) collisions which are generated by the Fermilab accelerator complex. See [14] for a very detailed description of the DZero detector. This section describes the subdetector components of the DØ detector: the tracking system, the calorimeter, the muon system, and the luminosity detector.

4.2.1 Tracking

Tracking is the second most important subdetector for the study of jets. A good tracking detector allows for the reconstruction of the primary interaction vertex (where the proton and antiproton were located when they collided) which is necessary for the proper measurement of a particle's energy and momentum. This information is in turn used by the jet reconstruction algorithm (see subsection 2.4) for the reconstruction of jets. The tracking system at DØ consists of two separate detectors,

the Silicon Microstrip Tracker (SMT) and the Central Fiber Tracker (CFT), and a solenoid magnet (see Figure 4.5).

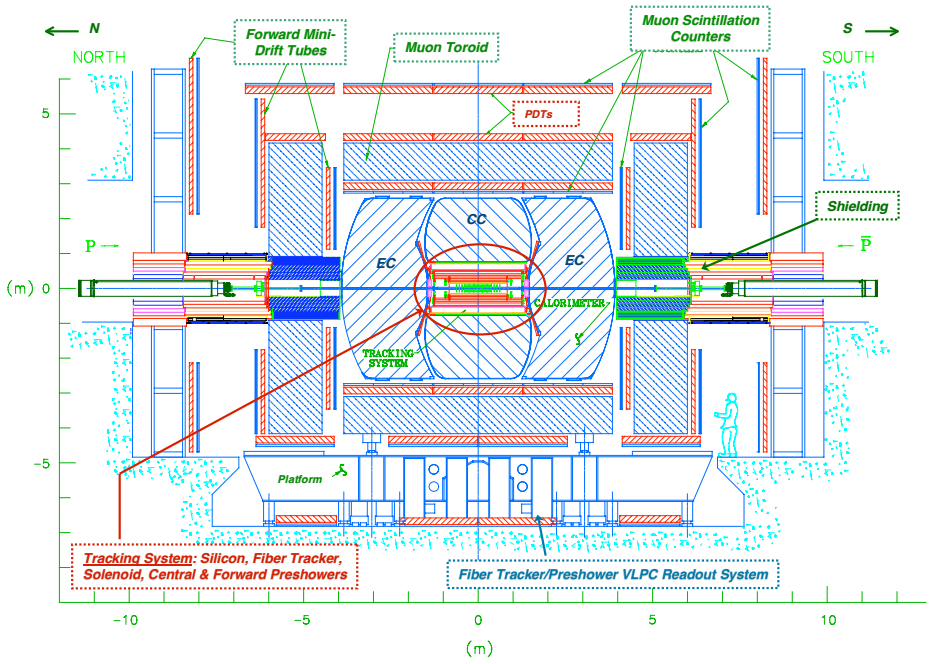

Figure 4.4: Schematic cross section of the DØ detector

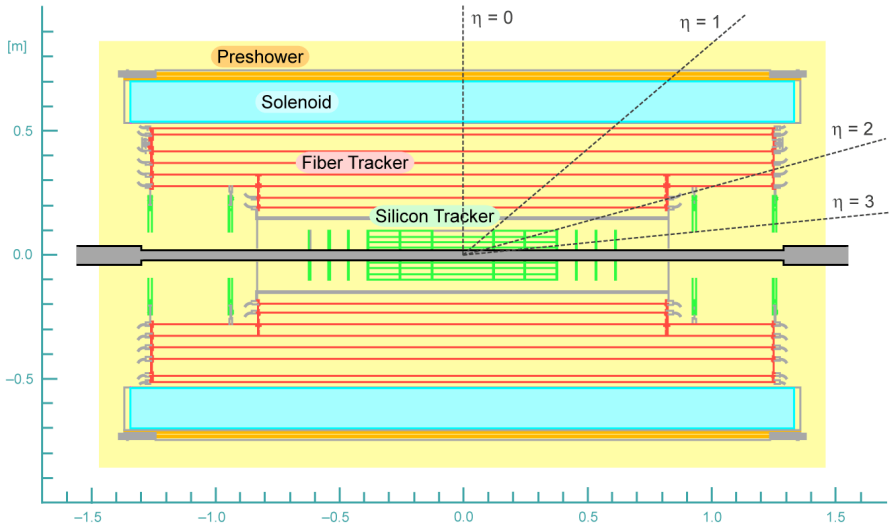

Figure 4.5: DØ tracking system. The silicon tracker (SMT) is closest to the beam pipe, followed by the fiber tracker (CFT).

The SMT detector consists of six barrels, 12 F-disks, and four H-disks of single or double sided silicon detectors (see Figure 4.6). Surrounding the SMT detector is the CFT detector which consists of a total of 200 km of scintillating fiber mounted on eight concentric cylinders. These two detectors work in concert with one another to determine the above-mentioned primary interaction vertex. Both of these detectors are surrounded by a solenoid magnet (see Figure 4.5) which provides a constant 2 T magnetic field. This allows the momentum of a charged particle to be determined since the amount of curvature of the particle in constant magnetic field is proportional to the momentum – $p = 0.3Br$, B in Telsa, r in meters, and p in GeV/c.

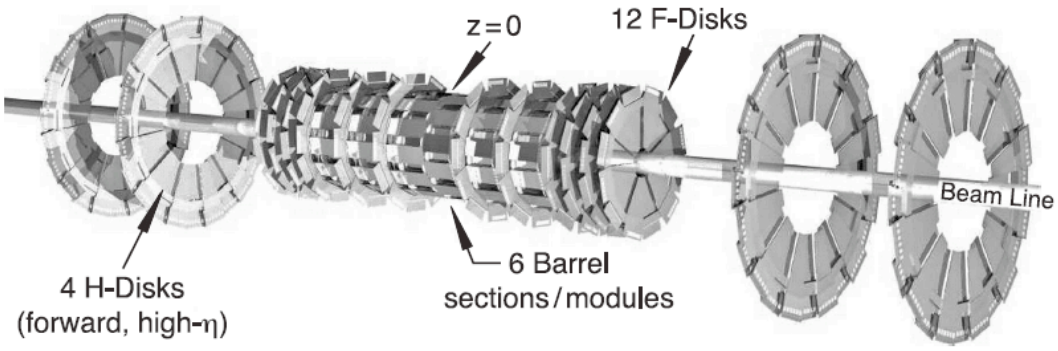

Figure 4.6: Isometric view of the SMT detector.

4.2.2 Preshower

The main purpose of the preshower detectors is to aid in electron and photon identification and background rejection during both triggering and offline reconstruction. They function as both calorimeters and tracking detectors, aiding in the matching between tracks and calorimeter showers. They are also used to correct the electromagnetic energy measurements of the central and end calorimeters for

losses caused by dead material, such as the solenoid, cables, and supports. The preshower measurements of energy and position are fast enough to allow the preshower information to be included as part of the Level 1 trigger.

The preshower detectors consist of the central preshower (CPS) and the forward preshower (FPS) detectors. The CPS is located between the solenoid and the central calorimeter, and the FPS is located between the luminosity monitor and the Intercryostat detector (see Figure 4.7).

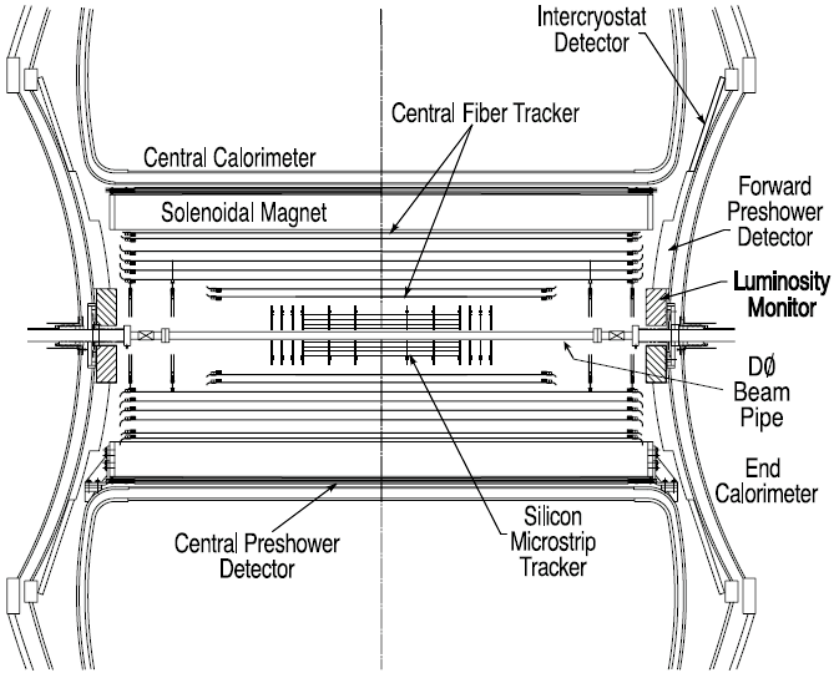

Figure 4.7: The preshower detectors as well as some of the other components of the DØ detector.

4.2.3 Calorimeter

The calorimeter is the most important subdetector for the measurement of jets. Figure 4.8 shows the layout of the DØ calorimeter. It is used to measure the energy of the particles traversing it, as all particles other than neutrinos and

muons are stopped inside of it. The calorimeter is designed in pseudoprojective towers (see Figure 4.10) pointing back to the origin; therefore, it provides some level of position information. The calorimeter is divided into three separate parts: the central calorimeter (CC) and two endcap calorimeters (EC). In each of these parts the calorimeter is further divided into three separate sections (listed from the interaction point radially outwards): electromagnetic (EM), fine hadronic (FH), and course hadronic (CH).

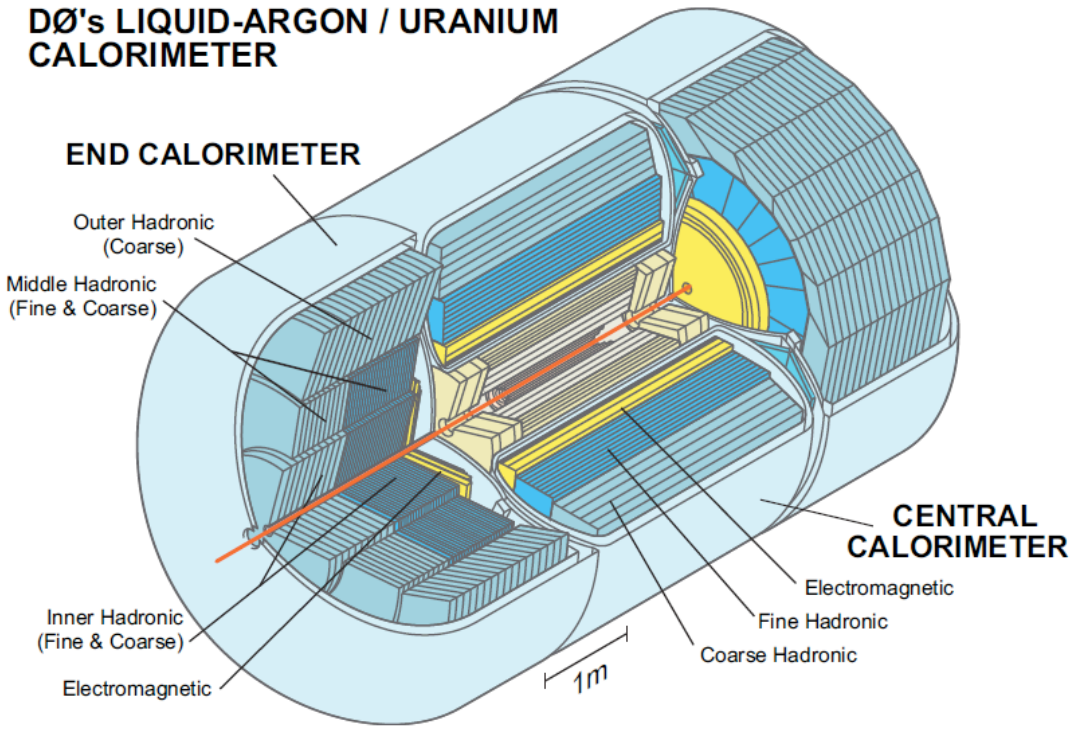

Figure 4.8: DØ calorimeter

DØ uses a sampling calorimeter. These types of calorimeters are ones in which the material that produces a particle shower (the material that the incoming particle interacts with) and the material that measures the deposited energy alternate with one another. This has the advantage that each material can be specialized to its task;

e.g. very dense material can be used to produce the shower which evolves quickly (useful if space is limited), even if this material is not suitable for measuring the energy deposited by the shower. A schematic view of a calorimeter unit used by DØ is shown in Figure 4.9.

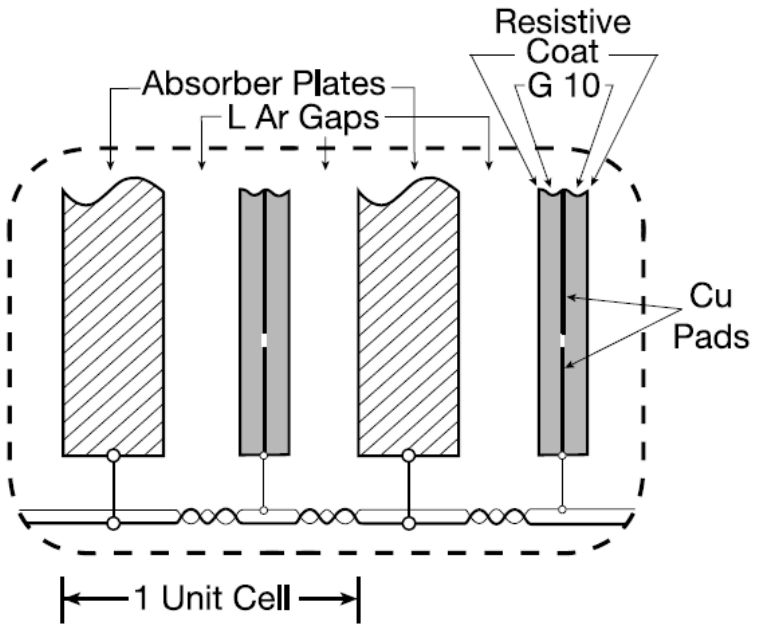

Figure 4.9: Schematic view of an individual calorimeter unit.

When an incoming particle interacts with the absorber plates, a particle shower is initiated. These particles ionize the liquid argon (LAr) that is in between the absorber plates. An electric field collects the free electrons to the surface of the copper pads which are the signal boards. The LAr and the copper pads together are what measure the deposited energy. The absorber plates are construsted of differing materials depending upon where one is in the calorimeter: the EM section has plates that are made of almost pure depleted uranium, the FH section has plates made of a uranium-niobium alloy, and the CH section has plates that are made of

copper (in the CC region) and stainless steel (in the EC regions). These individual calorimeter units are placed in such a way at different levels within the calorimeter that a pseudoprojective calorimeter tower can be formed, as shown in Figure 4.10.

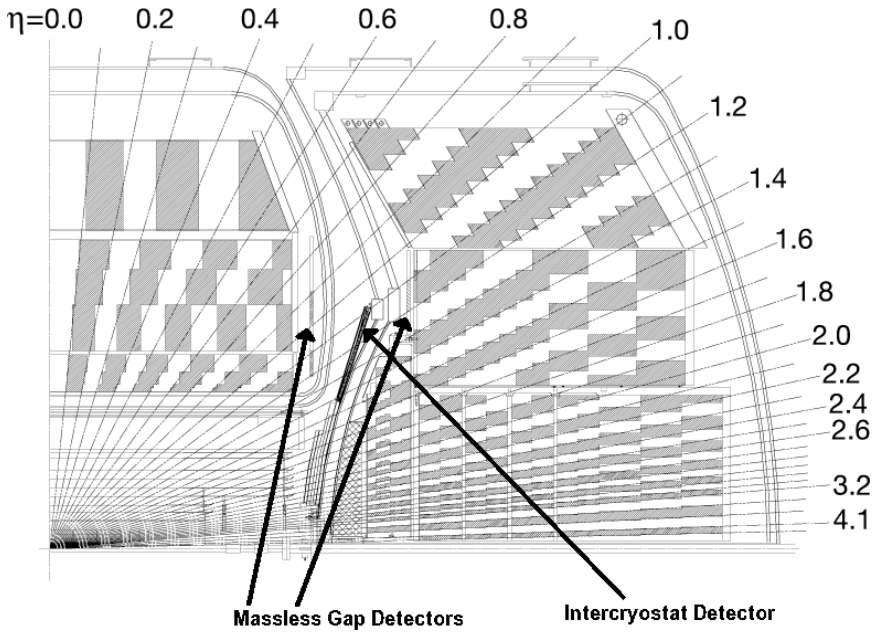

Figure 4.10: Side view of DØ detector showing the pseudoprojective towers.

The fact that liquid argon was chosen means that each of the three parts (one CC, two EC) has to be housed in its own cryostat to keep the argon in liquid form. This leads to areas in between the CC and two EC where there is no instrumentation, which reduces the energy resolution. To alleviate this problem, there are three additional sampling layers between the CC and each of the EC: two massless gap detectors (one just inside the CC and the other just inside the EC) and the inter cyrostat detector (ICD) attached to the outside of the EC. These three additional layers are indicated by arrows in Figure 4.10. The massless gap detectors are readout boards added into the liquid argon in the space near the cryostat wall.

The ICD is a different technology based upon scintillator tiles, fiber optic readout, and photomultiplier tubes.

4.2.4 Muon System

The outermost part of the DØ detector is the muon detector system which consists of the the muon scintillation counters, proportional drift tubes (PDTs), and the forward mini-drift tubes (MDTs) as shown in Figure 4.4. This detector system is used to find muons which are one of two particles that penetrate all the way through the calorimeters, the other being neutrinos.

The muon detector system is divided into three layers, progressively farther away from the calorimeter – A, B, and C. Each layer consists of drift tubes (PDT and MDT) and muon scintillation counters. Layer A lies between the calorimeter and the muon toroid; layers B and C lie outside the muon toroid. Layer A's scintillation counters are called Aϕ scintillation counters, which are used to identify the muon and to reject any backscatter from the forward sections. Layers B and C are called cosmic cap and bottom scintillation counters which are linked to the Tevatron clock that provides timing information that is used to reject any muons originating in cosmic rays, since these muons will be out of sync with any bunch crossing.

4.2.5 Luminosity

The luminosity monitor (LM) provides an accurate measurement of the luminosity ($\mathcal{L}$) for the DØ interaction region, which is needed for any measurement. The LM consists of two arrays with 24 plastic scintillation counters with PMT (photo

multiplier tube) readout: one located just inside of each of the end cap calorimeters (see Figure 4.11), at approximately $|z| = 140cm$.

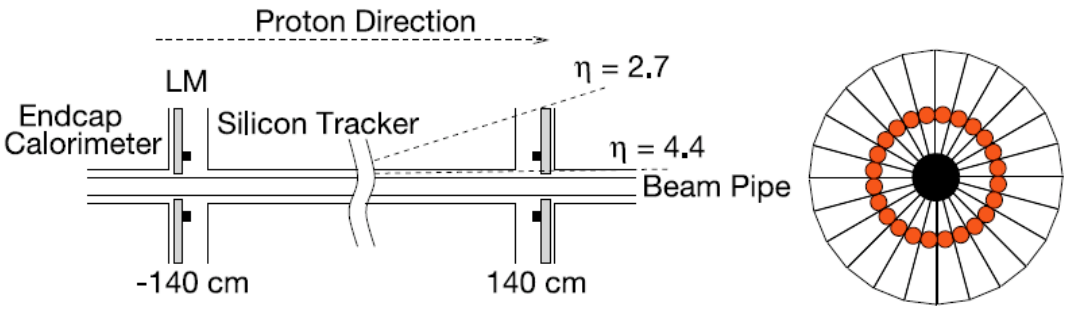

Figure 4.11: The Luminosity Monitor, shown from the side and along the beamline. The black boxes in the side view and the dots in the front view are the photomultiplier tubes.

The luminosity is determined using

$$\mathcal{L} = \frac{f\overline{N}_{LM}}{\sigma_{LM}}, \tag{4.1}$$

where f is the beam crossing frequency (how often the beams protons and antiprotons cross at DØ), $\overline{N}_{LM}$ is the average number of inelastic $p\overline{p}$ interactions per beam crossing, and σ_{LM} is the effective cross section of the luminosity monitor, which accounts for the acceptance and efficiency of the monitor. As determining $\overline{N}_{LM}$ with the LM alone is very difficult, $\overline{N}_{LM}$ is found by using Poisson statistics and the number of beam crossings with no $p\overline{p}$ collisions.

4.3 Trigger System and Data Acquisition

In this section the trigger and data acquisition system [14] will be explained. Particle collisions at DØ occur at a rate of 1.7 MHz: this is equivalent to the 396 ns between bunch crossings[1]. This is far too high of a rate for every event that

[1]The proton and antiproton beams are not continuous but occur in bunches that are 396 ns apart

occurs to be recorded. To reduce this incoming data rate from 1.7 MHz to a more manageable 50 Hz (frequency at which data is recorded to tape), a three-level trigger and data acquisition system is used to select appropriate events. Figure 4.12 presents a schematic of how data flows in the system.

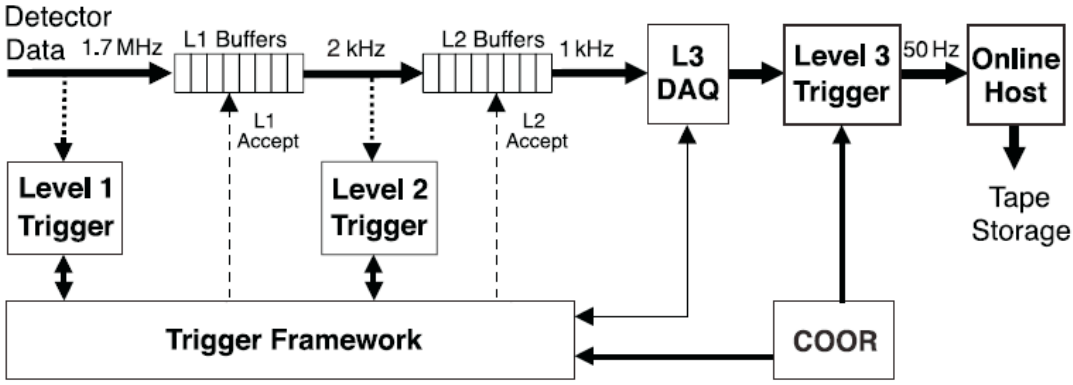

Figure 4.12: Schematic of the data flow in the trigger and data acquisition system.

The Level 1 (L1) stage is a hardware trigger. It has 3.5 μs to make a trigger decision, which is approximately 9 times longer than the time between bunch crossings. To alleviate this, the detector data is queued in the L1 buffer, giving the L1 trigger time to make a decision about whether or not to pass the event along as accepted. If the event is accepted, it is passed to the Level 2 (L2) stage; if it is not accepted it is dumped. Because of the small amount of time available for L1, the trigger decision is based upon very rough information from the various detector subsystems. The flow of information from the various subdetectors through to the L2 stage is shown in Figure 4.13. The rate of data flow coming out of the L1 stage into the L2 stage is 2 kHz.

The L2 trigger stage consists of a combination of hardware triggers and embedded microprocessors. The L2 trigger combines data from L1 as well as directly from

some detector components (see Figure 4.13) to form more complex physics objects. These objects are transmitted to L2 Global for a more informed trigger decision. If the event is accepted, then it is passed onto the Level 3 (L3) stage at a rate of 1 kHz.

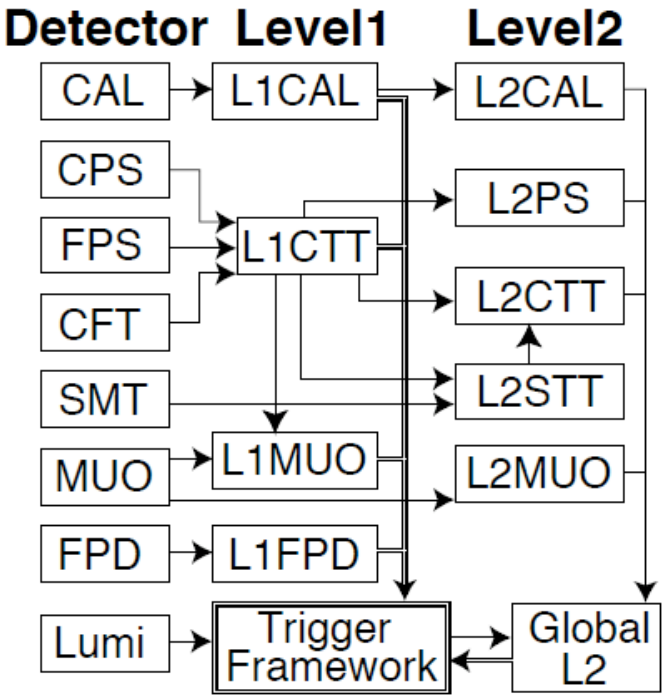

Figure 4.13: Schematic of the Level 1 and Level 2 trigger systems.

The L3 trigger system is a software based trigger level that runs on a computer processor farm. It makes a decision based on physics objects that were passed from L2 and any relations that exist between these objects. An event that is accepted by L3 is recorded to tape at rate of 50 Hz.

Also, the Trigger Framework applies a set of prescales at the L1 level. The prescale is a number that tells the system to fire on this type of event one out of N times for a particular trigger, where N is the prescale number. Prescale sets are used to balance the rates of more common triggers with those of rarely occuring triggers.

These prescales are based on luminosity. The more luminous the beam conditions, the higher N is. There are some cases where a trigger is unprescaled, so that every event is recorded.

CHAPTER 5

ANALYSIS

In this analysis nine different event shapes will be studied in two ways: by computing normalized differential distributions of event shapes ($\frac{1}{\sigma}\frac{d\sigma}{dX}\,vs\,X$) and by computing average event shapes ($\overline{X}\,vs\,H_T$), where X is any one of the nine event shapes used in this analysis. The normalized differential distributions will be defined in four H_T regions given in GeV: $180 \leq H_T < 300$, $300 \leq H_T < 450$, $450 \leq H_T < 675$, and $675 \leq H_T$.

The data set and event selection will be defined. There are then separate sections relating to the normalized differential distributions and to the average event shapes. In each of these sections the analysis bins will be defined followed by a comparison of the uncorrected data with reweighted SHERPA and PYTHIA. Both of these use the reweighting from the ongoing DØ measurement of the ratio of three-jet and dijet cross sections ($R_{3/2}$) [16]. Using the reweighted SHERPA, correction factors for the data and the relative uncertainty on the data will be determined. Corrected data will then be compared with unweighted SHERPA and PYTHIA.

As was seen in Chapter 2, PYTHIA implements the lowest-order (LO) matrix elements for $2 \to 2$ scattering plus parton showering; SHERPA implements all the LO matrix elements for $2 \to 2$, $2 \to 3$, $2 \to 4$, and $2 \to 5$ plus parton showering. It has

been shown in Chapter 3 that all of the event shapes go to zero for the $2 \to 2$ process. Therefore, what will be tested by the event shape analysis is (1) the radiation that comes from the parton shower for PYTHIA and (2) the contributions that come from the matrix elements for $2 \to 3$, $2 \to 4$, and $2 \to 5$ processes and to a lesser extent the parton shower for SHERPA.

5.1 Data Set and Event Selection

This analysis uses approximately $0.7 fb^{-1}$ of data from what is refered to as RunIIA[1]. After the data was recorded, it was processed offline into a usable form. The data is then analyzed using ROOT, a common histogramming program that uses an interpreter which uses a C++ syntax (see [15]).

Event quality cuts are imposed to make sure that no "bad" data are included. The data is required to pass these selection criteria: official RunIIA data quality cuts that include cuts on bad LBNs (Luminosity Block Numbers) and bad runs; the `calfail` flag is set to false (removes events where there was a problem in the calorimeter); $\frac{\not\!\!E_T}{p_T^{leading}} < 0.7$ (cuts out signals caused by cosmic rays hitting the detector); at least one primary vertex ($n^{vtx} \geq 1$); $|z^{vtx}| < 50$ cm (interaction vertex is within 50 cm of the center of the detector); and $n_{trks} \geq 3$ (number of tracks needed to reconstruct interaction vertex, removes fake vertices).

The variable $p_T^{leading}$ is the transverse momentum of the leading jet, with jets being ordered by decreasing p_T. The $\not\!\!E_T$ is the missing transverse energy which measures the total imbalance in the energy in the transverse direction (perpendicular

[1] RunIIA consists of runs 191000 - 213064 taken from 2004 to 2006

to the particle beam), which is caused by particles such as the muon or neutrino that leave little or no energy in the calorimeter.

In addition to these event quality cuts, all jets that are used in the analysis are required to be "good" jets by requiring that they pass the standard jet ID quality cuts that can be found in [19]. These cuts are designed to remove any overlap between jets and EM objects (such as electron or photons), noisy jets from the coarse hadronic calorimeter, and jets formed out of noise from the precision readout.

In addition to the event and jet quality cuts, there are also phase space cuts which specify what type of events are needed for the study being performed in this analysis. These cuts were given in section 3.2.

5.2 Normalized Differential Distributions

5.2.1 Analysis Bins

This section will describe how the analysis bins were chosen for the normalized differential distributions, $\frac{1}{\sigma}\frac{d\sigma}{dX}\, vs\, X$, where X is any of the nine event shapes that are being studied.

In the normalized differential distributions events are triggered by the inclusive jet triggers JT45, JT65, JT95, and JT125[2]. For each of the four regions of H_T, a single inclusive jet trigger is used. The one chosen is the highest trigger which is fully efficient in the corresponding H_T region.

The plot of number of events $N\, vs\, H_T$ is measured for all four jet triggers, separately for two-jet and three-jet events: an n-jet event has at least n jets in the

[2]The inclusive jet triggers include information from the L1, L2, and L3 stages of the data collection process. They are symbolized by JTxx, where at least one jet passes this trigger with $p_T \geq xx$.

event, maybe more. To obtain the cross section plots $\sigma\, vs\, H_T$, each bin in $N\, vs\, H_T$ is divided by the product of integrated luminosity and vertex efficiency $\sigma = \frac{N}{\mathcal{L}\epsilon_{vertex}}$. The integrated luminosity is the cumulative total of particle collisions recorded for each jet trigger; the vertex efficiency is a measure of how accurately the vertex (position of the interaction) is determined. These numbers are both listed in Table 5.1.

Table 5.1: Luminosity and vertex efficiency for jet triggers.

trigger name	integr. lumi $[pb^{-1}]$	vertex eff.
JT45	17.176	0.919
JT65	72.997	0.915
JT95	507.72	0.924
JT125	707.25	0.928

Trigger efficiencies are determined by taking the ratios of the cross section plots $\sigma\, vs\, H_T$ of subsequent triggers, *e.g.* $\frac{\sigma_{JT65}}{\sigma_{JT45}}$. See appendix C for the details of the trigger study. To obtain a reliable estimate of the H_T values at which the triggers become 99% efficient, the efficiency curves are fitted with

$$F(p) = 0.5 * \left[1 + Erf\left(\frac{p-a}{b + c * log(p)}\right)\right], \tag{5.1}$$

where $p = \frac{H_T}{1GeV}$; a, b, and c are the fit parameters; and Erf is the error function. The H_T values are those at the bin centers. The fitted efficiency plots are shown in Figures 5.1 and 5.2.

To determine the H_T value at 99% efficiency, set $F(p) = 0.99$ and use Steffensen's method [18] to solve for p. The 99% efficiency values for each trigger region (for both two- and three-jet events) are listed along with the values actually used by the analysis in Table 5.2.

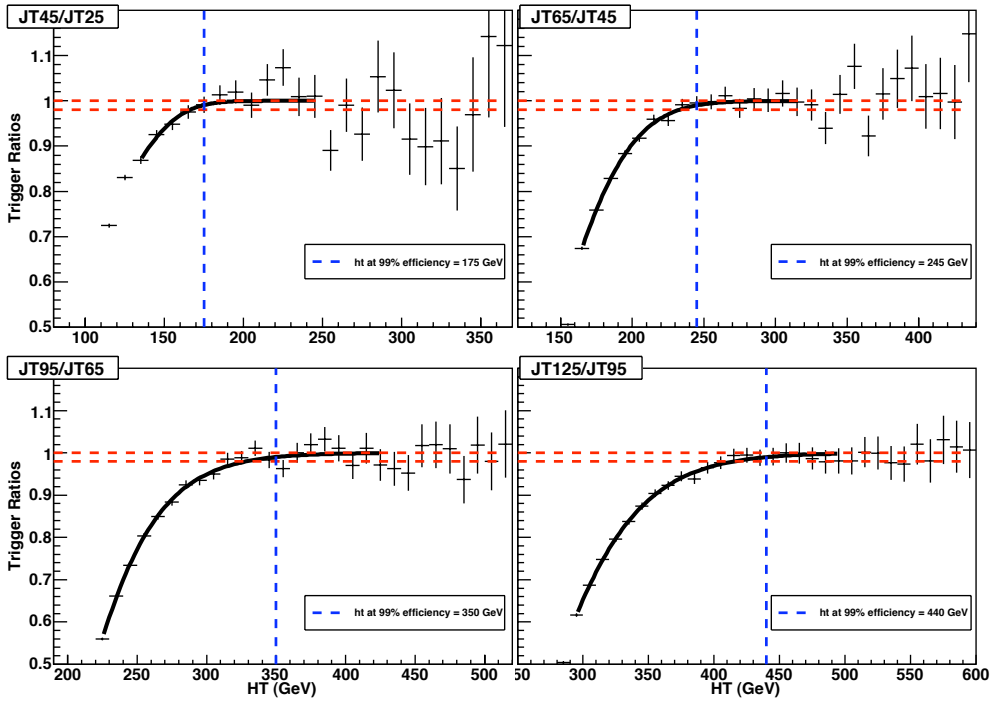

Figure 5.1: Trigger turnon curves fitted to determine the 99% efficiency value, for 2 jet events

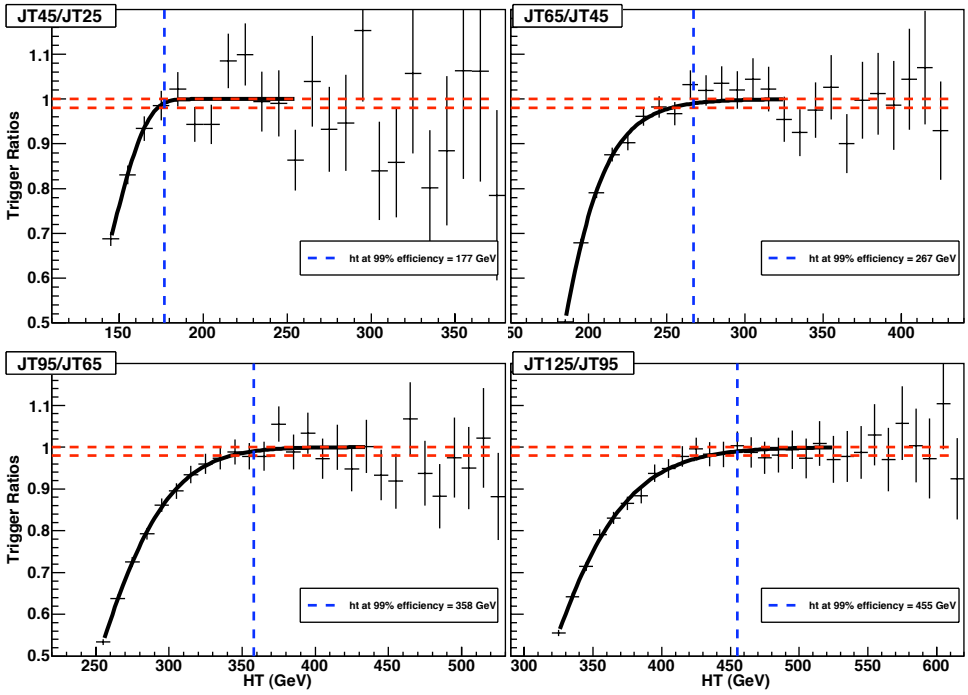

Figure 5.2: Trigger turnon curves fitted to determine the 99% efficiency value, for 3 jet events

All of the event shapes go to zero for a $2 \rightarrow 2$ massless process. To obtain values of an event shape that are greater than zero, one needs to have a third jet. Therefore, one needs to know when the three-jet turnon is. The values for the three-jet turnon are higher than the two-jet turnon because the trigger studies were done using H_T. The values chosen for use in the analysis had to be greater than the three-jet values because of the above-mentioned need for a third jet.

Table 5.2: Summary of the H_T values GeV at 99% efficiency for 2-jet and 3-jet events. The last columns give the actual values used for the normalized differential distributions analysis.

Trigger	2-jet turnon	3-jet turnon	Turnon used
JT45	175	177	180
JT65	245	267	300
JT95	350	358	450
JT125	440	455	675

Once the trigger studies were completed, the H_T regions for each trigger were chosen in the following way. The lower bound is the trigger turnon for the corresponding jet trigger; the upper bound is the trigger turnon for the next highest jet trigger. These regions are shown in Table 5.3.

Table 5.3: Summary of the H_T regions (in GeV) that are used for the normalized differential distribution analysis.

Trigger	Lower bound	Upper bound
JT45	180	300
JT65	300	450
JT95	450	675
JT125	675	none

Once this was done a migration study was performed to determine the binning that gave the optimal balance between purity and efficiency for the normalized differential distribution analysis. See appendix F.2 for the details of this study. At this point all event shapes had a minimum value of zero and a maximum value of one. However, in order to have enough statistics to perform the analysis, a value had to be set on the minimum number of events that occurred in a bin of data. This was chosen to be 20 events. See appendix G for the study that chose the minimum binning.

5.2.2 Comparison of Data and Jetsim with Sherpa and Pythia

It first should be mentioned that the particle generation done by Pythia and Sherpa (or any MC generator for that matter) stops after the partons have hadronized. In order to form any possible jets out of these particles, the DØ jet finding algorithm, given in Chapter 2, is applied to the results of Sherpa and Pythia. These results are then used as input for JetSim [20], a simulation of the response of DØ detector for jet measurements. JetSim takes these jets (which are at particle-level) and simulates the detector effects, generating the detector-level jets. It then computes the value of the observable (which can be tailored for a particular analysis), for particle-level jets, detector-level jets, and also for all variations of the detector effects within their uncertainties. For the rest of the section on normalized differential distributions when Sherpa and Pythia are mentioned, it is understood that JetSim has been used.

It also needs to be noted that throughout this section and the rest of the dissertation reference will be made to reweighted Sherpa (Pythia) or unweighted

SHERPA (PYTHIA). Reweighted SHERPA (PYTHIA) has been reweighted to describe the data, so that it will be useful in determining the correction factors. Unweighted SHERPA (PYTHIA) is what will be tested against the corrected data.

Plots of $\frac{1}{\sigma}\frac{d\sigma}{dX}$ *vs* X are first generated for data, which is uncorrected at this point, and for reweighted SHERPA and PYTHIA. These plots are then overlayed with one another so as to enable a comparison to see which Monte Carlo (MC) best describes the data. Results are given in Figures 5.3 - 5.6 for each of the four H_T regions.

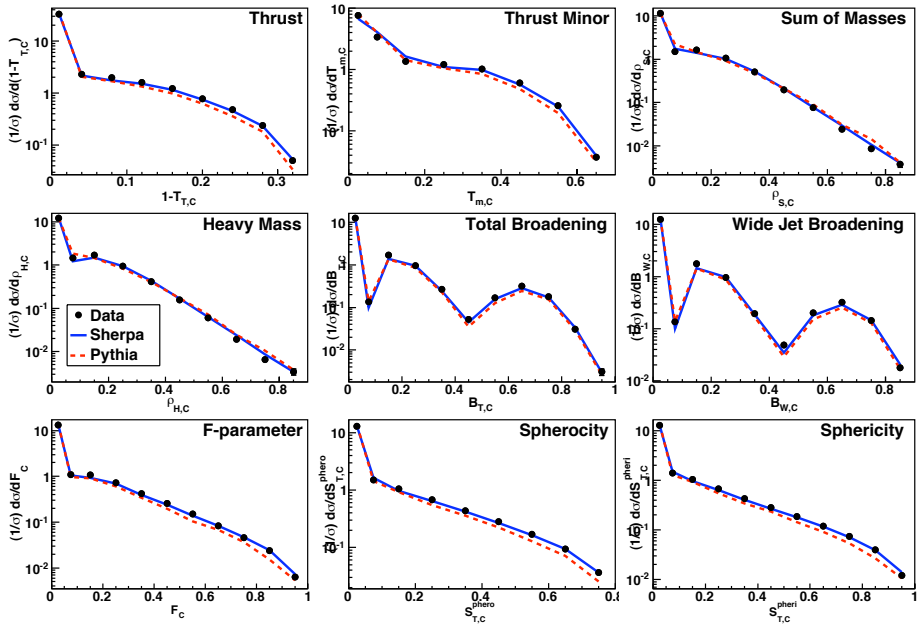

Figure 5.3: Differential normalized distributions for $180 \leq H_T < 300$ GeV.

In order to be sure that the MC describes the data well, control plots for 15 different quantities were generated, and the results for the reweighted MC and data were compared. See Appendix D for all of the control plots. These control plots are independent of any specific analysis that uses the reweighting that was obtained in

the $R_{3/2}$ analysis – *i.e.* the results of the control plots can also be used for the average event shape analysis as well.

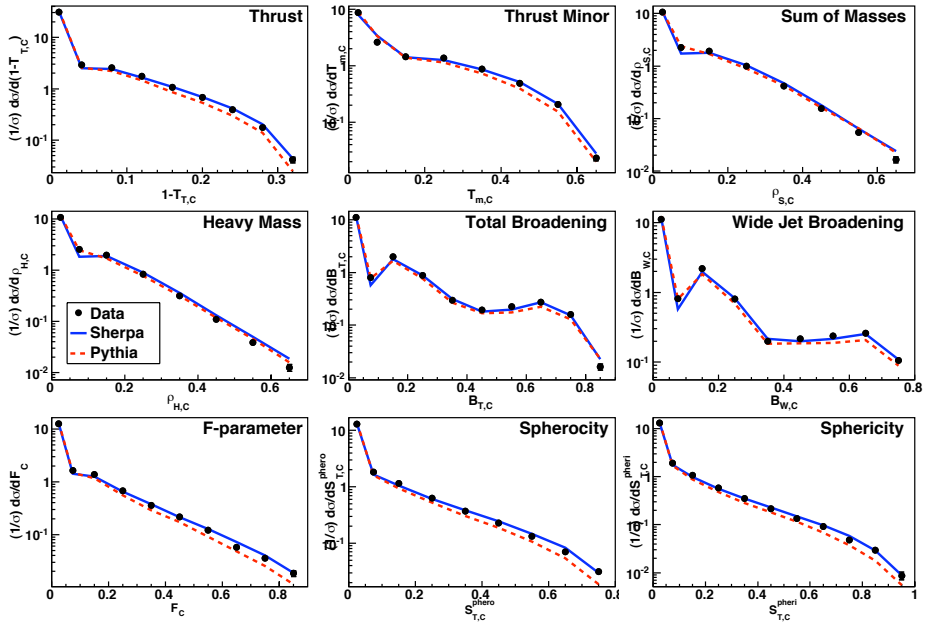

Figure 5.4: Differential normalized distributions for $300 \leq H_T < 450$ GeV.

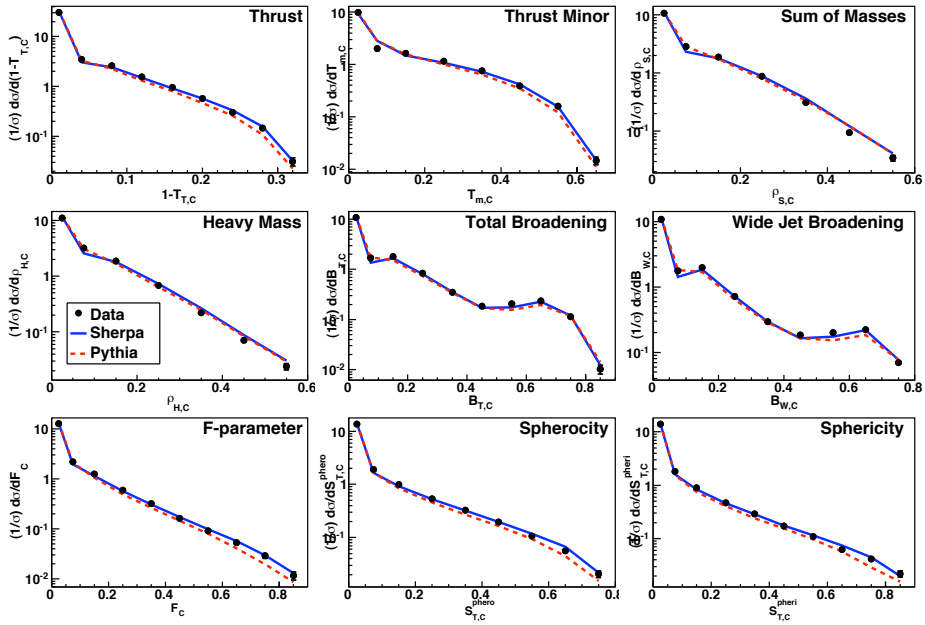

Figure 5.5: Differential normalized distributions for $450 \leq H_T < 675$ GeV.

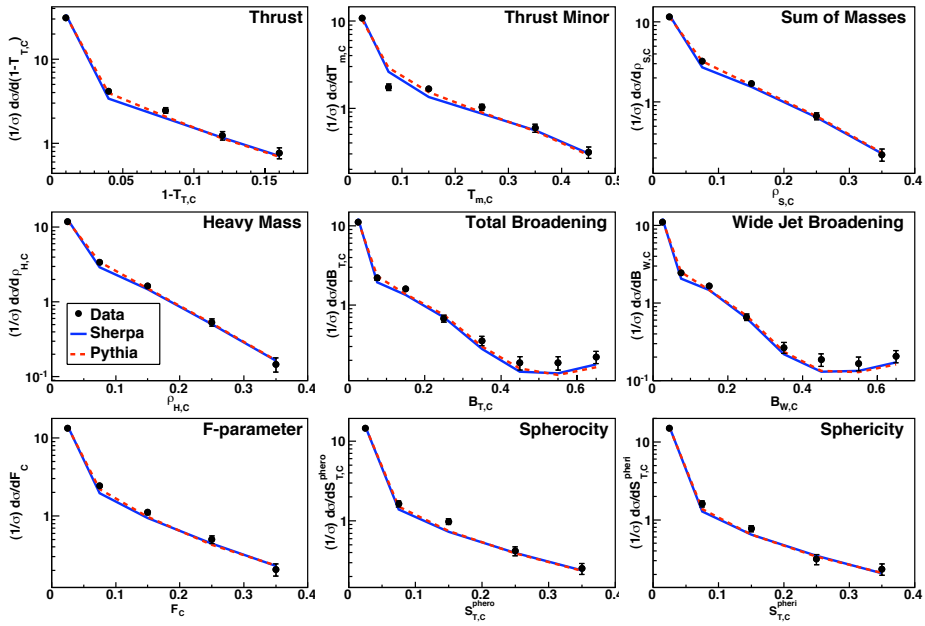

Figure 5.6: Differential normalized distributions for $H_T \geq 675$ GeV.

From these comparison, it is seen that in general SHERPA does a better job of describing the data that does PYTHIA. Therefore, SHERPA will be used to determine the correction factors as well as the uncertainties. PYTHIA will be compared to SHERPA to determine the model dependence uncertainty.

5.2.3 Corrections

The reweighted SHERPA was determined in the section 5.2.2 to give the best description of the uncorrected data. Therefore, it will be used to correct the data back to particle-level by multiplying the data by $\frac{PL}{DL}$, where DL is the detector-level histogram and PL is the particle-level histogram. The correction factors for each event shape are given in Figures 5.7 - 5.10 for each of the four H_T regions. In general, the correction factors range from 0.9 to 1.1.

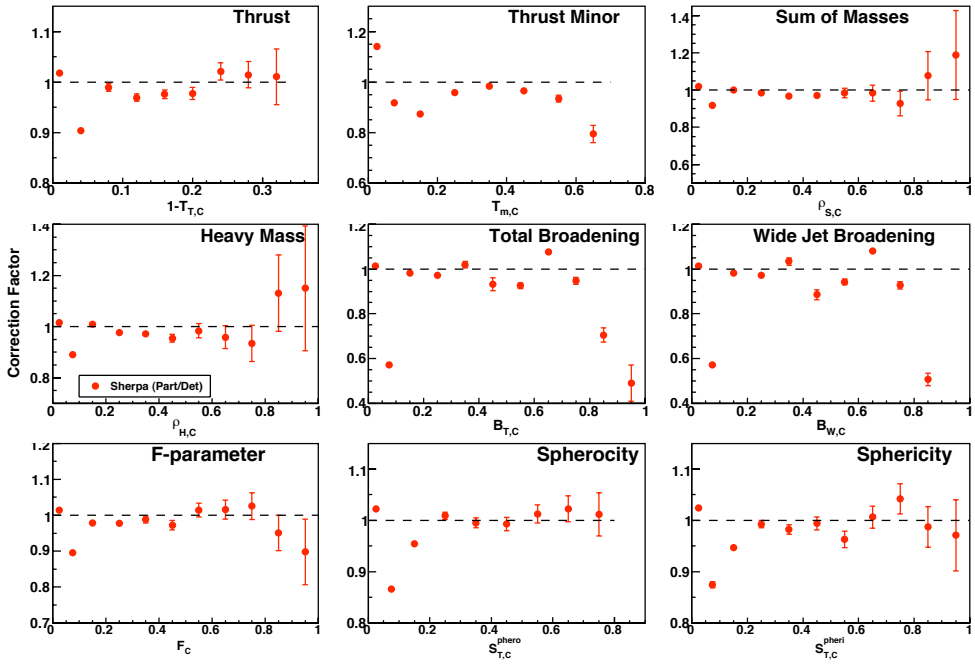

Figure 5.7: Correction factors for the differential normalized distributions for $180 \leq H_T < 300$ GeV

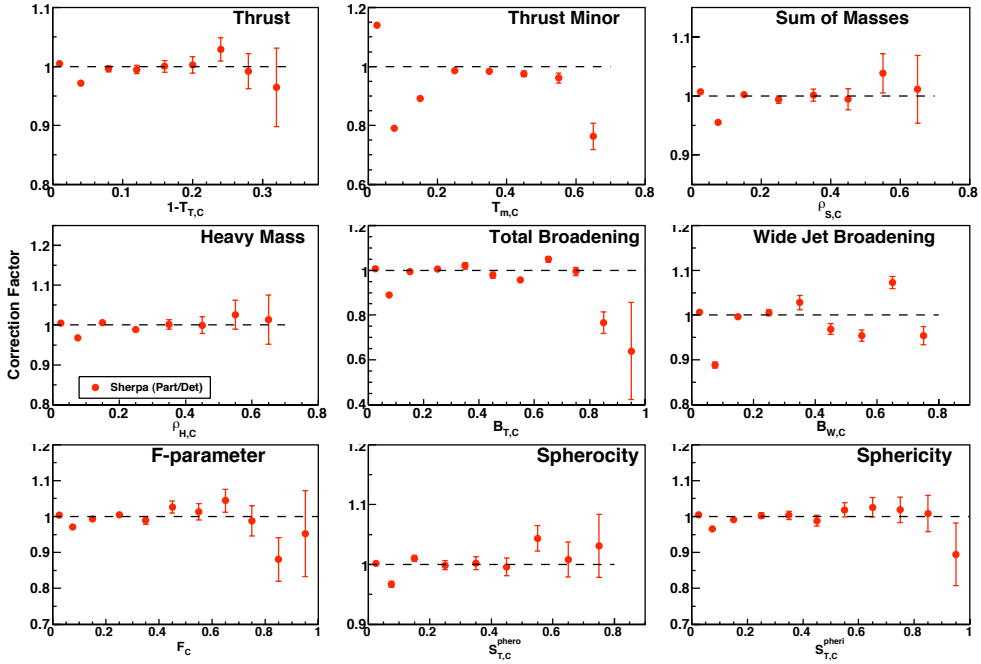

Figure 5.8: Correction factors for the differential normalized distributions for $300 \leq H_T < 450$ GeV.

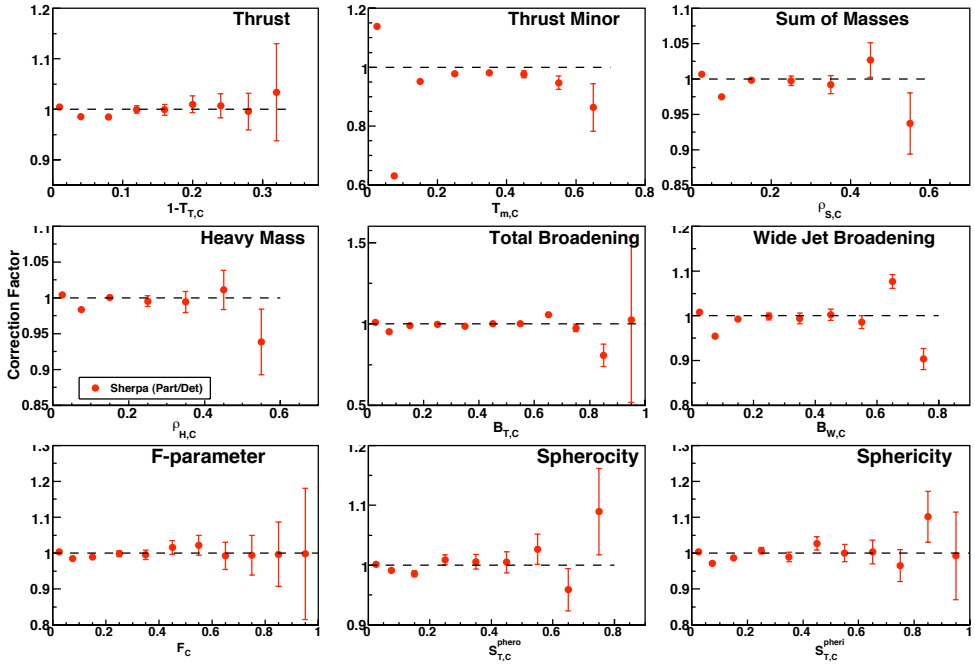

Figure 5.9: Correction factors for the differential normalized distributions for $450 \leq H_T < 675$ GeV.

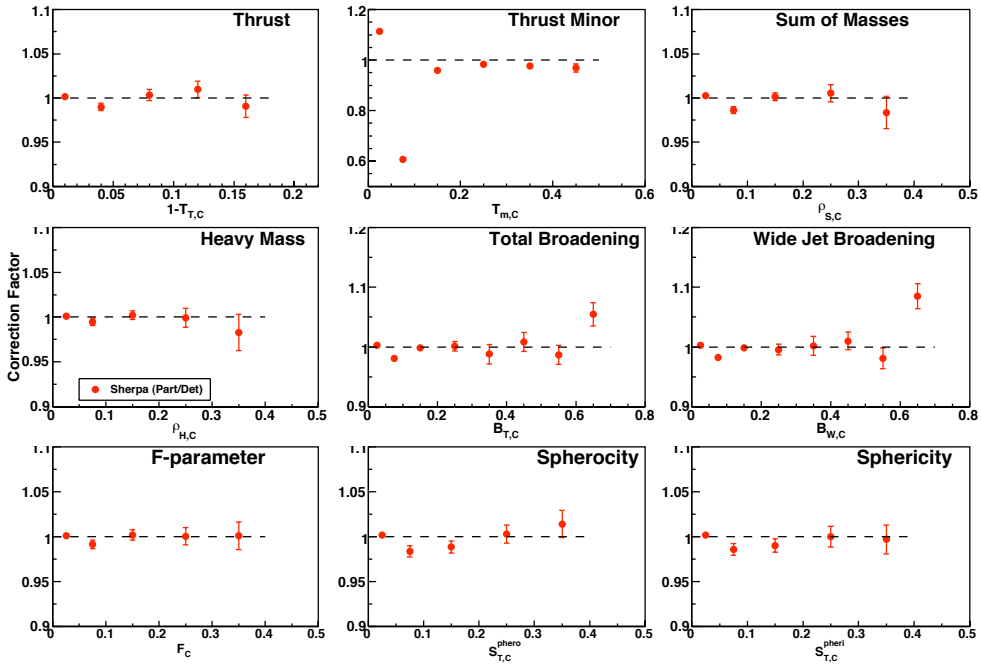

Figure 5.10: Correction factors for the differential normalized distributions for $H_T \geq 675$ GeV.

5.2.4 Uncertainties

The reweighted SHERPA was determined in the section 5.2.2 to give the best description of the uncorrected data. Therefore, it will be used to determine the relative uncertainties on the data. There are eight uncertainty sources in this analysis: jet p_T resolution, JES, jet η bias, jet η resolution, jet ϕ resolution, jet ID efficiency, modeling the shape of the z-vtx distribution, and the model dependence of the correction factors. All of these uncertainty sources are added in quadrature to obtain the overall relative uncertainty on the data. The relative uncertainty is given by $\frac{M-S}{S}$, where S is the reweighted SHERPA that has already been discussed and M is the reweighted SHERPA for which a given detector effect has been varied within its uncertainties. Plots of the relative uncertainty are shown in Figures 5.11 - 5.14 for each of the four H_T regions.

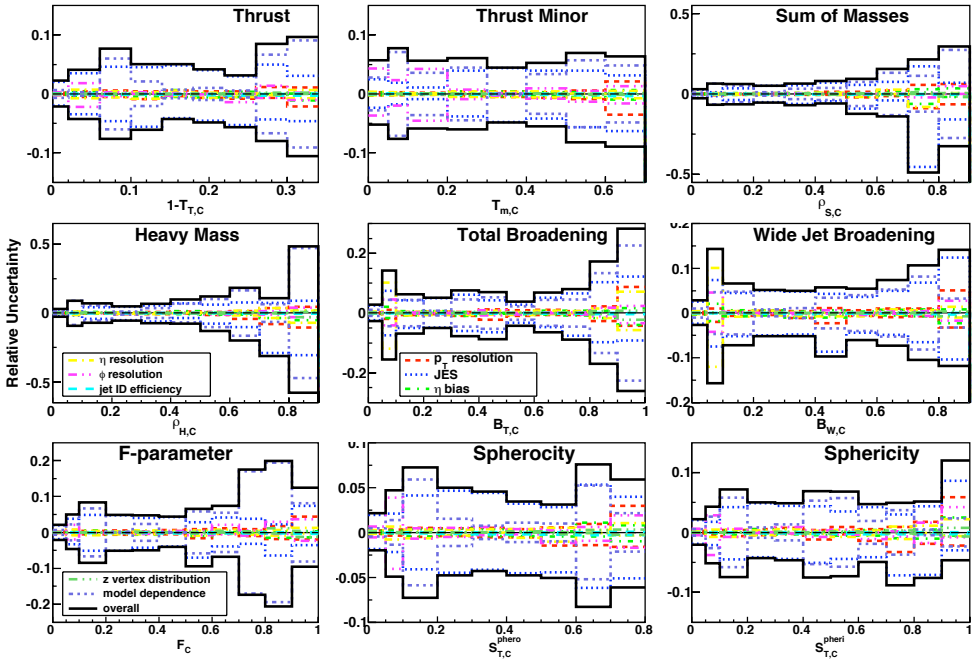

Figure 5.11: Relative uncertainties for $180 \leq H_T < 300$ GeV.

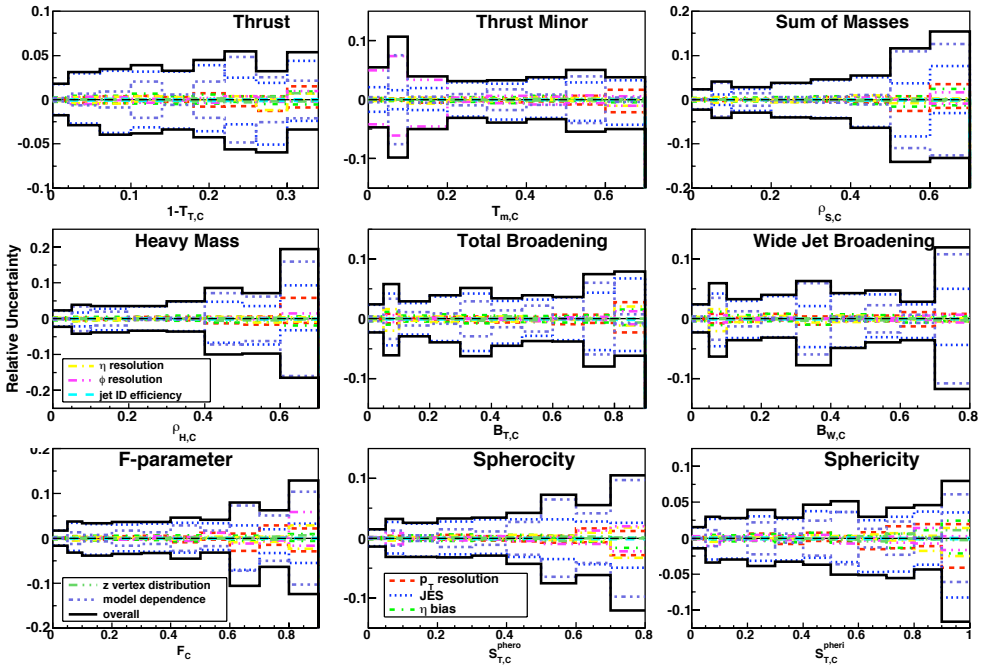

Figure 5.12: Relative uncertainties for $300 \leq H_T < 450$ GeV.

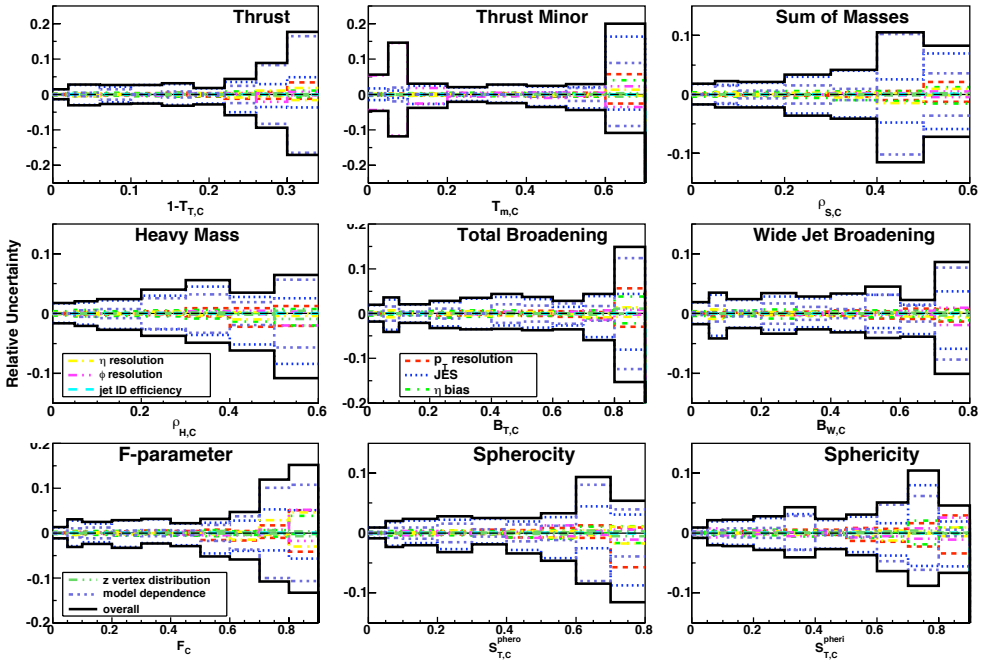

Figure 5.13: Relative uncertainties for $450 \leq H_T < 675$ GeV.

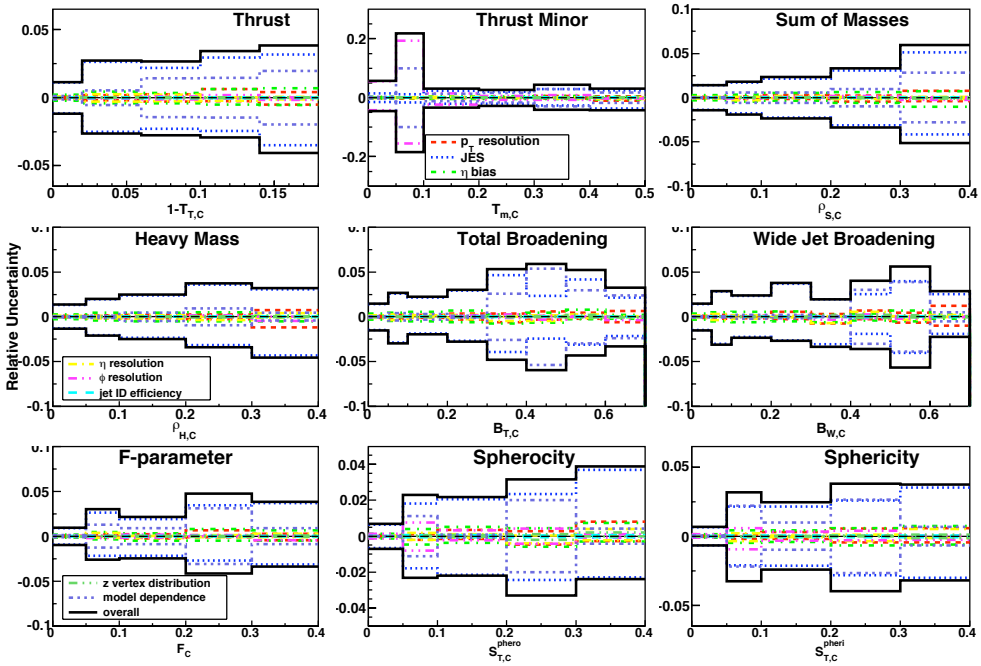

Figure 5.14: Relative uncertainties for $675 \leq H_T$ GeV.

The p_T resolution has 15 individual uncertainty sources; the JES has 49 individual uncertainty sources. See appendix E for a list of the the sources of uncertainty for JES and p_T resolution. To obtain the uncertainty for p_T resolution, all of the individual uncertainties are added in quadrature; similarly for the JES uncertainty.

5.2.5 Results

The data have been corrected, and the uncertainties have been determined. The uncertainties determined in the previous section are called the systematic uncertainties and are added in quadrature with the statistical uncertainties on the data. Now the unweighted SHERPA and PYTHIA are tested to see how well they describe the data. This is done by creating plots of (1) corrected data overlayed with unweighted SHERPA and PYTHIA, and (2) Data/MC for both SHERPA and PYTHIA. Figures 5.15,

5.17, 5.19, and 5.21 show the corrected data overlayed with unweighted MC. Figures 5.16, 5.18, 5.20, and 5.22 show the ratio of corrected data with unweighted MC.

The results show that in general SHERPA does a better job of describing the data than does PYTHIA, although there are some instances (combination of region and event shape) where PYTHIA does a better job – *e.g.* the thrust in region $180 \leq H_T < 300$ (see Figure 5.16). In order for SHERPA (or PYTHIA) to give an adequate description of the data, the uncertainty bars on the ratios of data with SHERPA (or PYTHIA) need to encompass the line at one, which is where the ratio would be if SHERPA (or PYTHIA) gave a perfect description of data. It is shown in Figures 5.16, 5.18, 5.20, and 5.22 that it depends upon which region and event shape one is looking at whether an adequate description of the data is given by either SHERPA or PYTHIA.

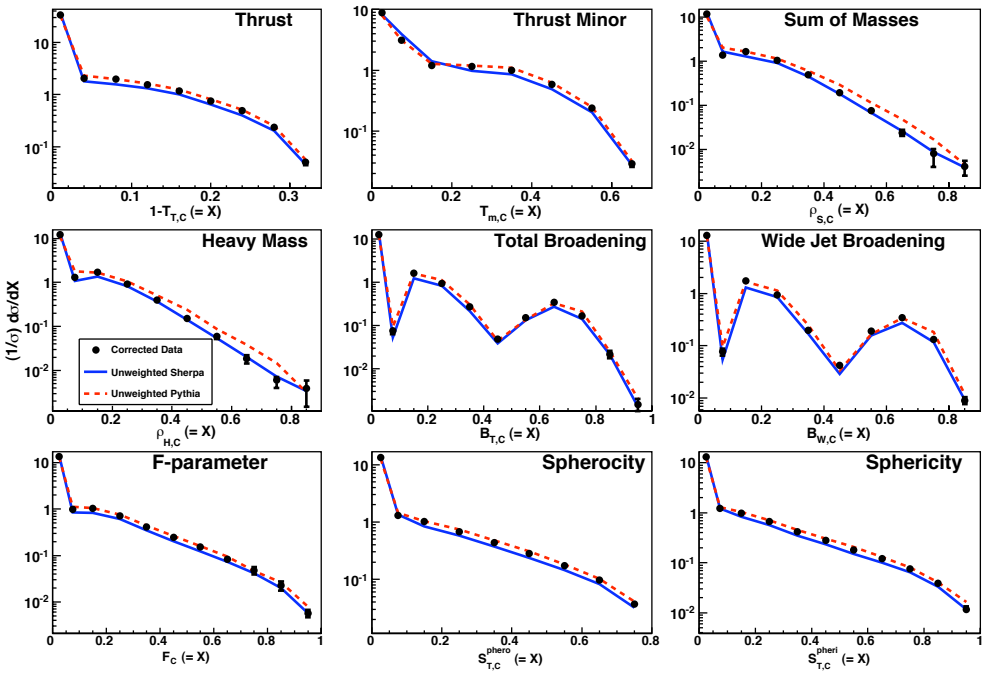

Figure 5.15: Comparison of corrected data with unweighted MCs for $180 \leq H_T < 300$ GeV.

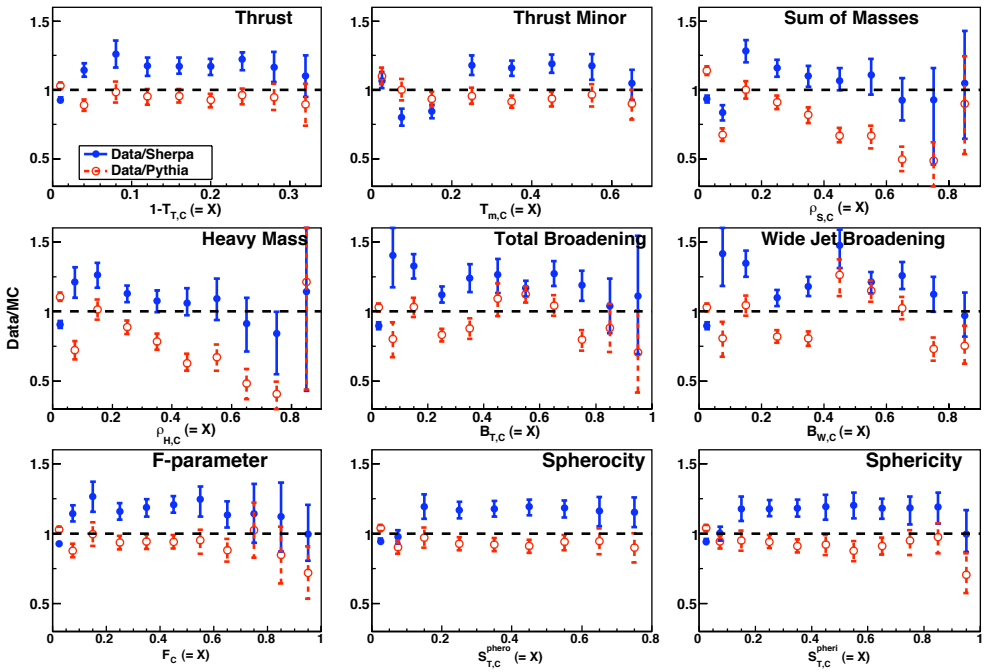

Figure 5.16: Data/MC for $180 \leq H_T < 300$ GeV, using data and MC from Figure 5.15.

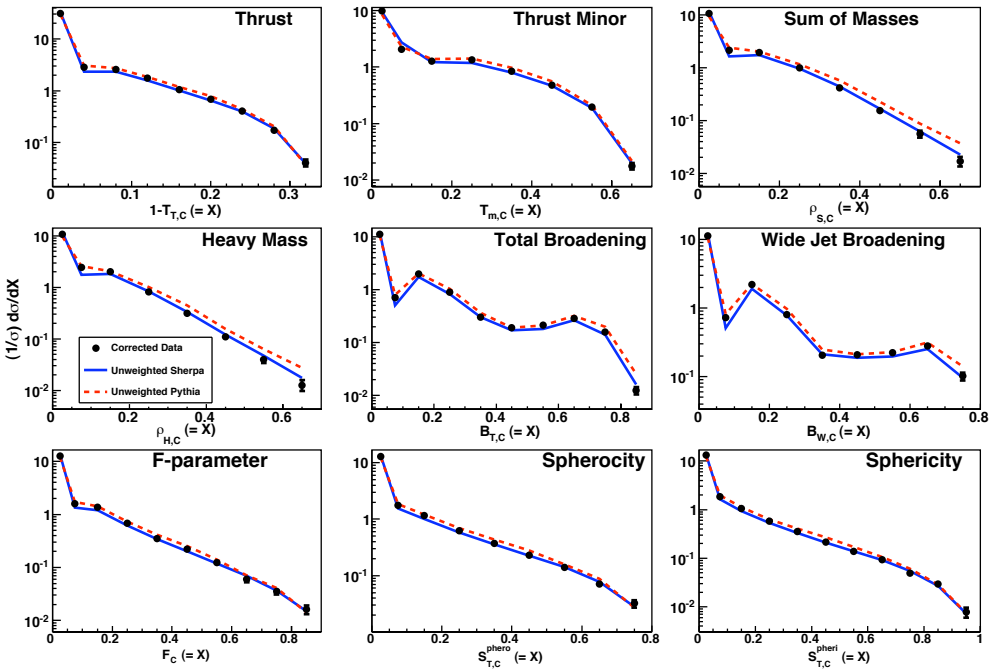

Figure 5.17: Comparison of corrected data with unweighted MCs for $300 \leq H_T < 450$ GeV.

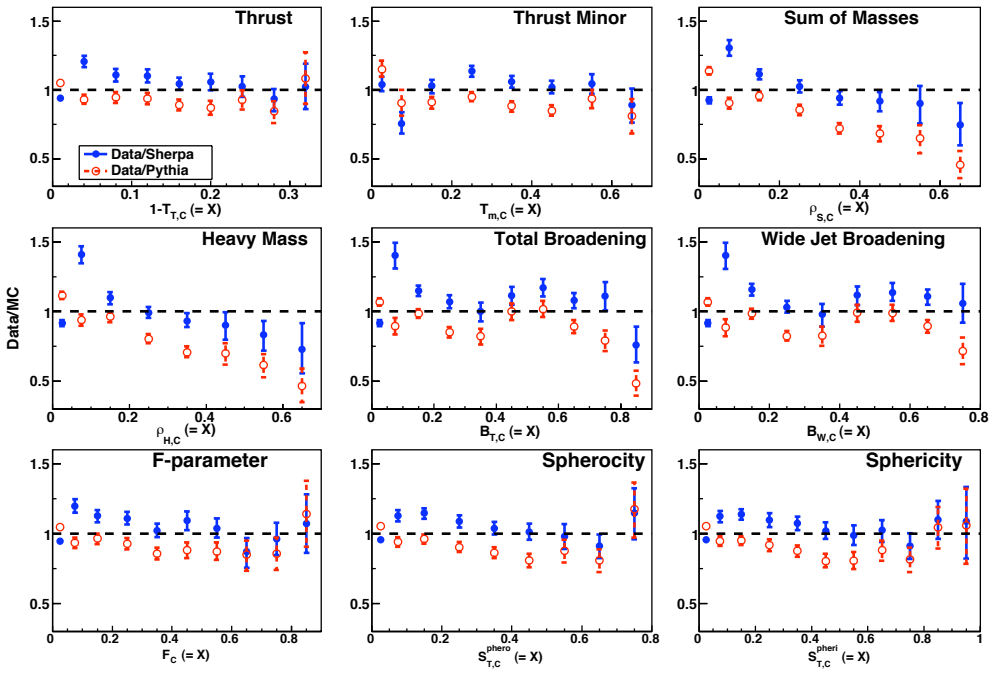

Figure 5.18: Data/MC for $300 \leq H_T < 450$ GeV, using data and MC from Figure 5.17.

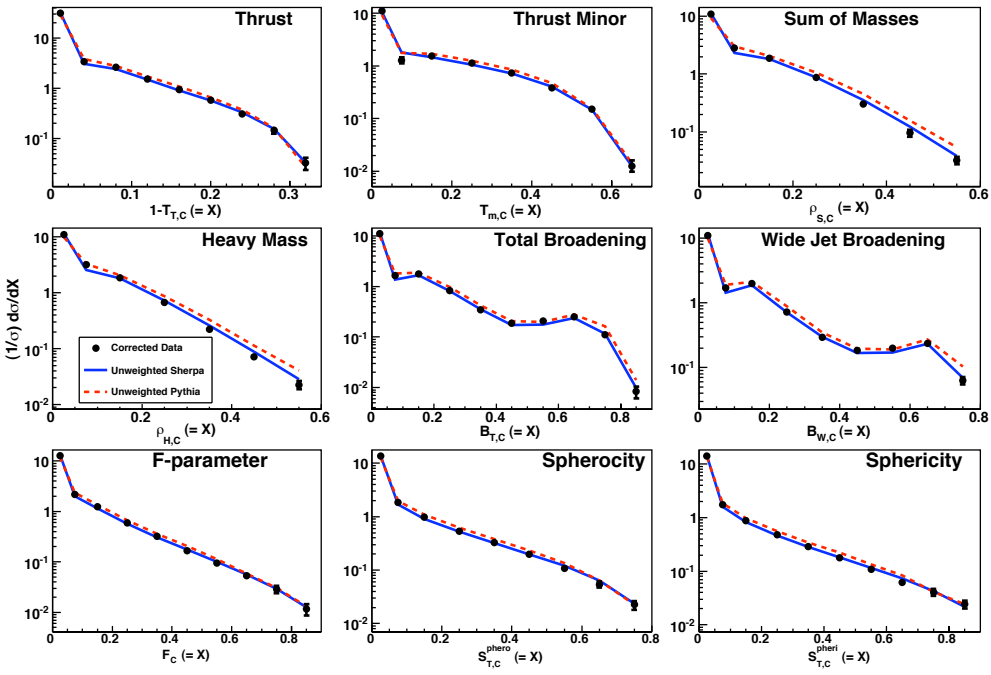

Figure 5.19: Comparison of corrected data with unweighted MCs for $450 \leq H_T < 675$ GeV.

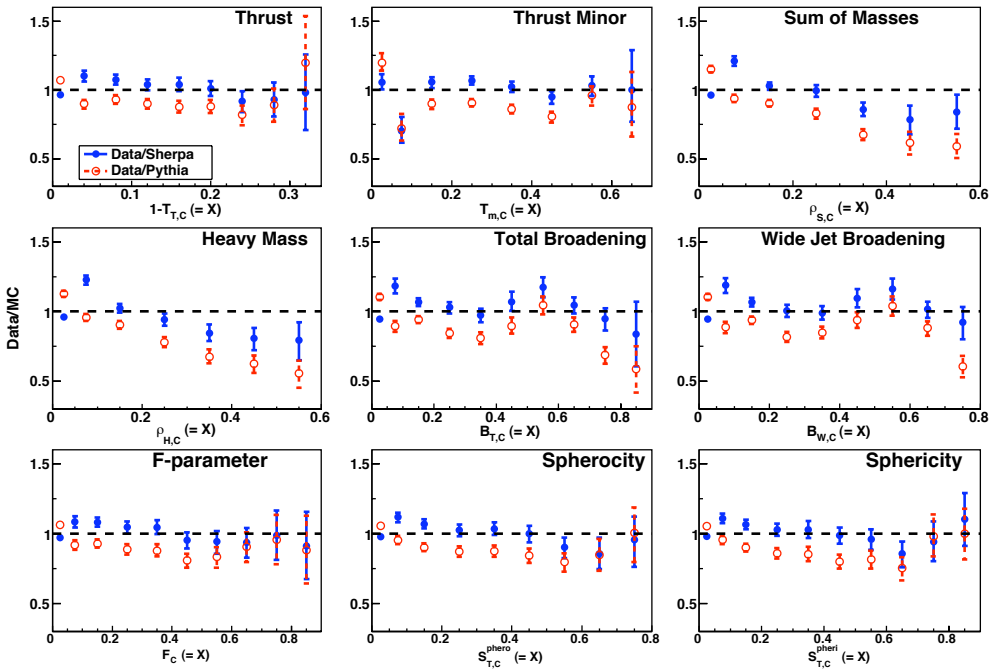

Figure 5.20: Data/MC for $450 \leq H_T < 675$ GeV, using data and MC from Figure 5.19.

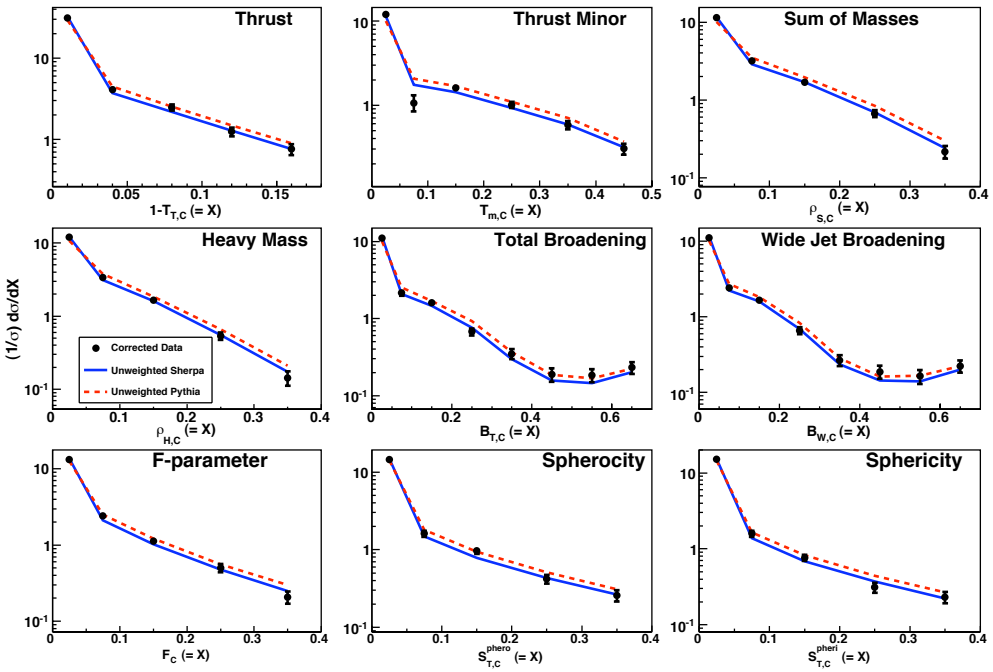

Figure 5.21: Comparison of corrected data with unweighted MCs for $H_T \geq 675$ GeV.

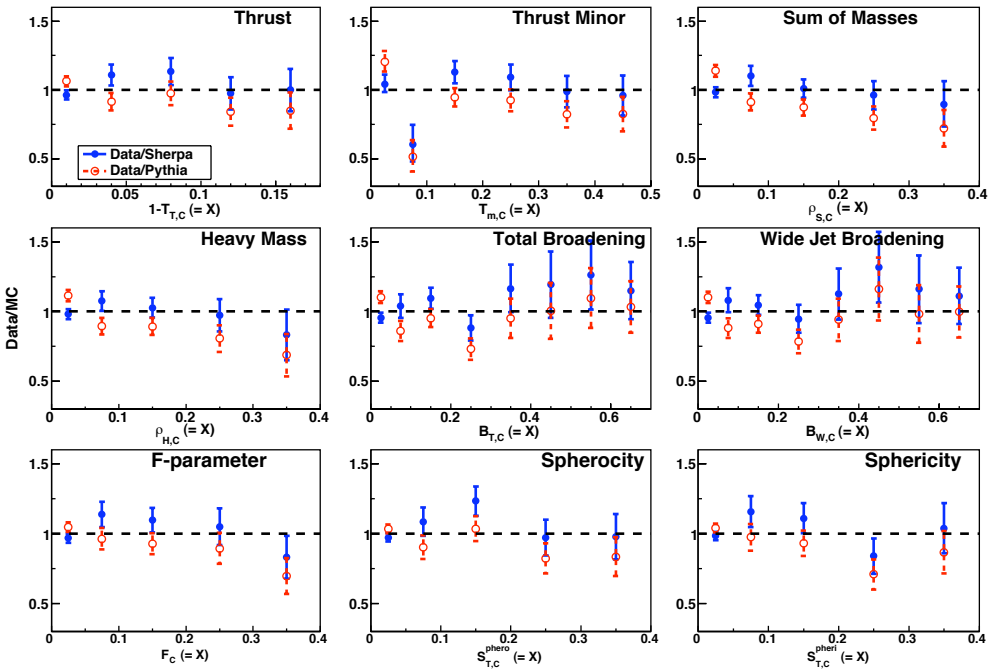

Figure 5.22: Data/MC for $H_T \geq 675$ GeV, using data and MC from Figure 5.21.

5.3 Average Event Shapes

5.3.1 Analysis Bins

This section will describe how the analysis bins were chosen for the average event shapes, $\overline{X}\,vs\,H_T$, where X will be any of the nine event shapes that are being studied.

Initially, the binning in H_T for the average event shapes was taken to be the same as in a recent DØ study of azimuthal decorrelations [17]. What needs to be determined here is the range of H_T that corresponds to each of the four jet triggers – JT45, JT65, JT95, and JT125. The same trigger study that was used to determine the H_T regions for the normalized differential distributions was used to determine the ranges for the jet triggers. These ranges are shown in Table 5.4. The upper bound for a jet trigger was chosen as the lower bound for the next higher jet trigger. The

upper bound for the JT125 trigger region was chosen as 1000 GeV since there will not be much data beyond this point.

Table 5.4: Summary of the H_T ranges (in GeV) that are used for the average event shape analysis.

Trigger	Lower bound	Upper bound
JT45	180	310
JT65	310	415
JT95	415	530
JT125	530	1000

5.3.2 Comparison of Data and Jetsim with Sherpa and Pythia

Plots of $\overline{X}$ *vs* H_T are first generated for data, which is uncorrected at this point, and for reweighted SHERPA and PYTHIA, analgously to section 5.2. The results are given in Figure 5.23.

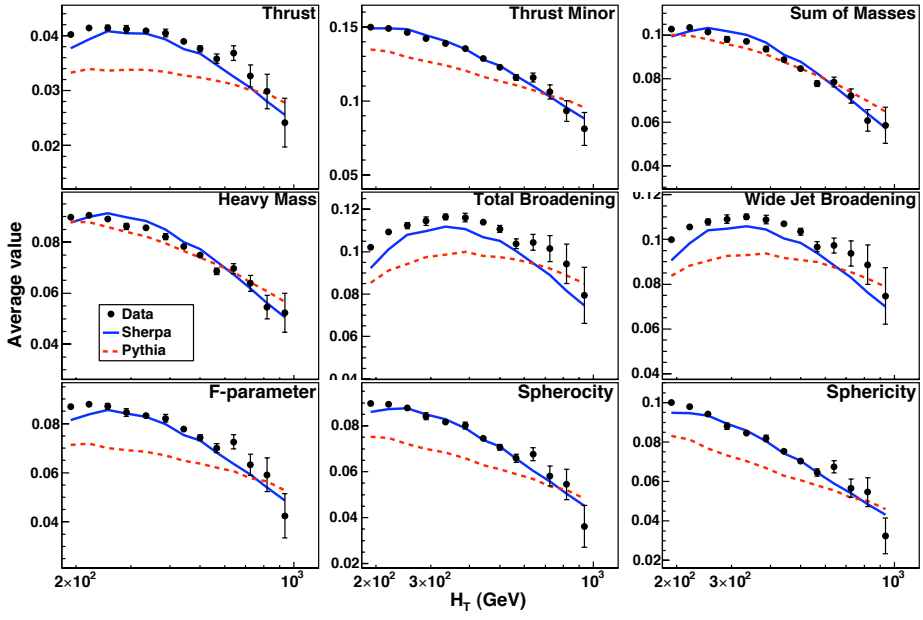

Figure 5.23: Uncorrected data with reweighted MC for average event shapes.

From a comparison of these plots, it is seen that in general SHERPA does a better job of describing the data that does PYTHIA. Therefore, SHERPA will be used to determine the correction factors as well as the uncertainties. PYTHIA will be compared to SHERPA to determine the model dependence uncertainty.

5.3.3 Corrections and Uncertainties

The reweighted SHERPA was determined in the section 5.3.2 to give the best description of the uncorrected data. Therefore, it will be used to correct the data back to particle-level and to determine the uncertainties on the data. Correcting back to particle-level involves multiplying the data by $\frac{PL}{DL}$, where PL is the particle-level histogram and DL is the detector-level distribution. These correction factors are given in Figure 5.24. A discussion of the eight uncertainty sources is given in section 5.2.4. Plots of the relative uncertainty are shown in Figure 5.25.

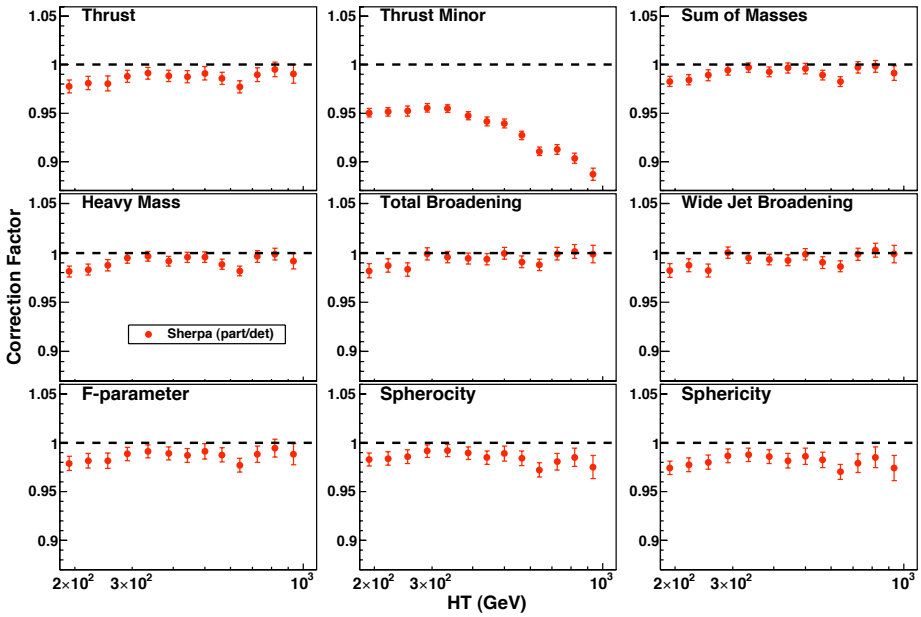

Figure 5.24: Correction factors for data for average event shapes.

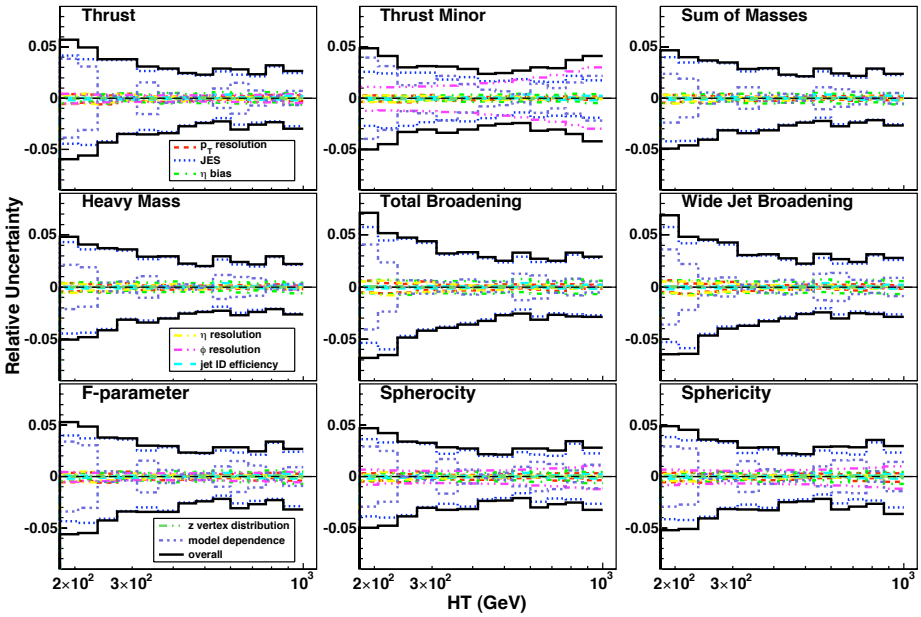

Figure 5.25: Relative uncertainties for data for average event shapes.

5.3.4 Results

The data has been corrected, and the uncertainties have been determined. These uncertainties are added in quadrature with the statistical uncertainties. To test SHERPA and PYTHIA, plots are created of (1) data overlayed with SHERPA and PYTHIA (see Figure 5.26), and (2) Data/SHERPA and Data/PYTHIA (see Figure 5.27).

In general SHERPA gives a better description of the data than does PYTHIA, except at low H_T values on some of the event shapes – *e.g.* the F-parameter in Figure 5.27. Analogously to section 5.2.5, the uncertainty bars on the ratios of data with SHERPA (or PYTHIA) need to encompass the line at one in order for SHERPA (or PYTHIA) to give an adequate description of the data. It is shown in Figure 5.27 that it depends upon the H_T value and the event shape one is looking at as to whether an adequate description of the data is given by either SHERPA or PYTHIA.

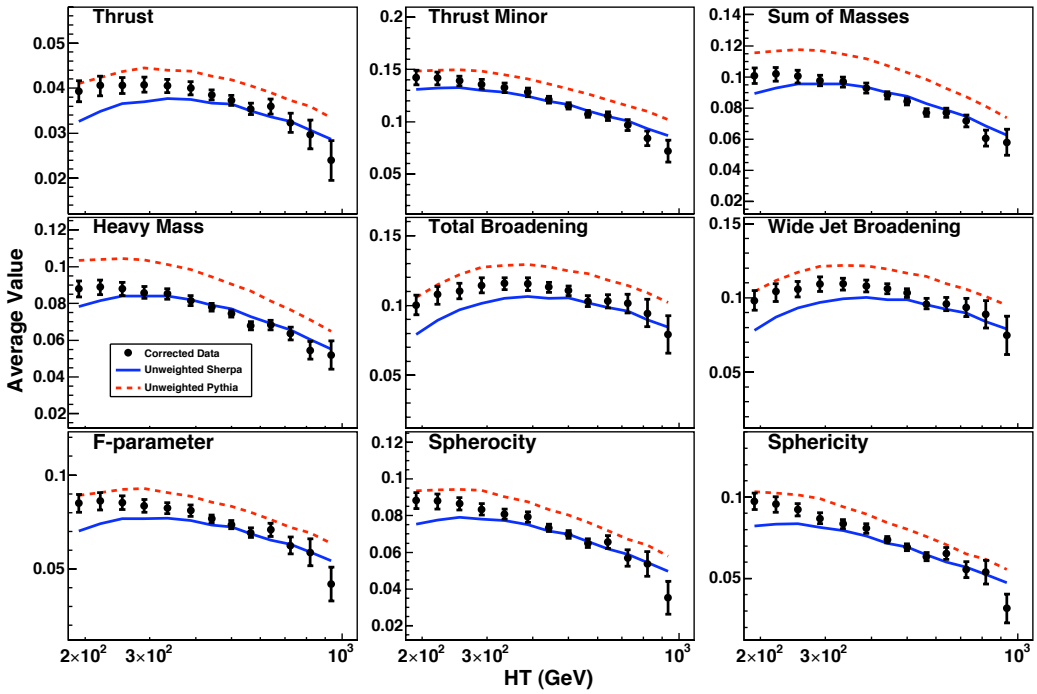

Figure 5.26: Comparison of corrected data with unweighted MCs for average event shapes.

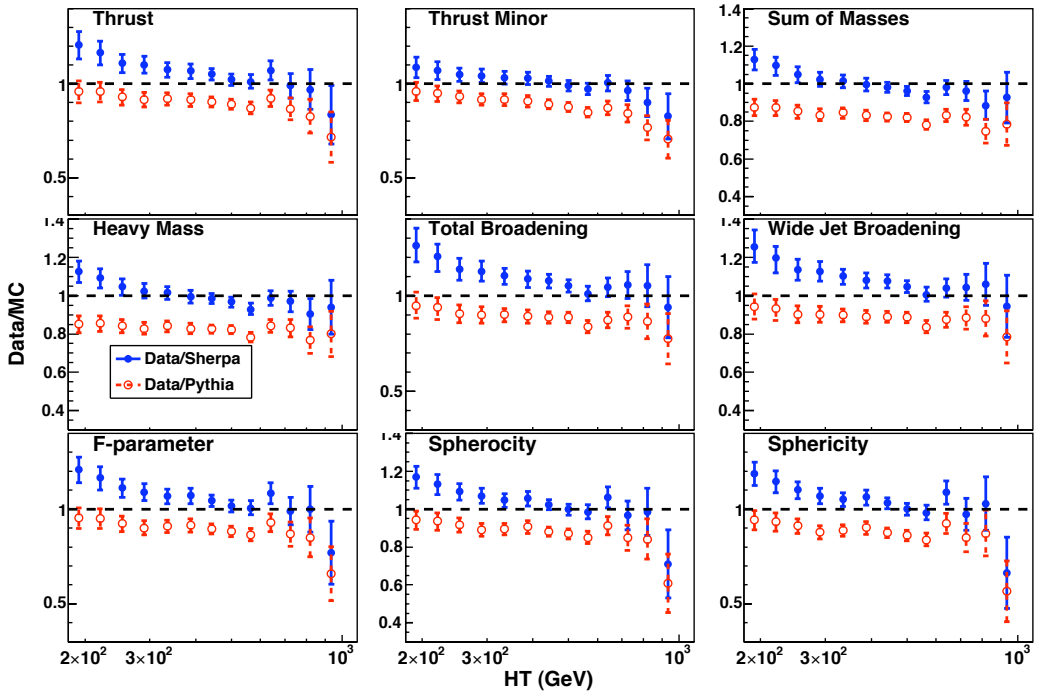

Figure 5.27: Data/MC for average event shapes, using data and MC from Figure 5.26.

5.3.5 Dip in Average Event Shapes

In performing this analysis an interesting issue arose: all of the average event shapes had a dip in them at around $H_T = 600$ GeV. This only occured in data. In order to study this effect the bins from Figure 5.23 were each divided into four equally-sized bins (± 1 GeV) – see Figure 5.28 for the finer-binned data overlayed with the normal-binned MC. The results of the finer binning showed some small little bumps at the first two boundaries and in the middle of the first region. However, one can still see the dip at around $H_T = 600$ GeV.

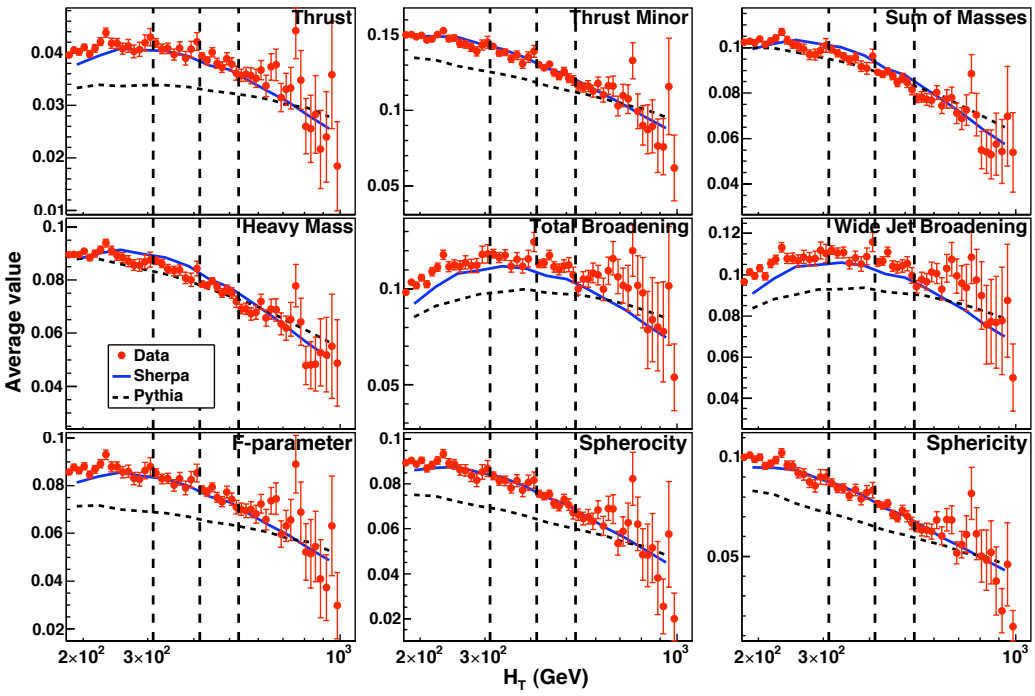

Figure 5.28: Average event shape plot with 4x finer binning. The vertical lines define the boundaries for the four trigger regions given in Table 5.4.

As a possible explanation for the bumps in the finer-binned data and for the dip, in each H_T bin plots were made of the rapidity differential cross section ($\frac{d\sigma}{dy}$) and

rapidity normalized differential cross section ($\frac{1}{\sigma}\frac{d\sigma}{dy}$) for each jet that enters the bin – see appendix I for these plots. No out of the ordinary behavior was found in these plots.

CHAPTER 6

SUMMARY AND CONCLUSIONS

This dissertation presented the study of nine different event shapes – thrust, thrust minor, sum of masses, heavy mass, wide jet broadening, total broadening, F-parameter, spherocity, and sphericity – for high energy $p\overline{p}$ collisions. The analysis tested strong interactions as described by Quantum Chromodynamics (QCD) by way of how these are implemented in two different Monte Carlo models: SHERPA and PYTHIA. Each of the event shapes provided information about the flow of energy in QCD events and about the hadronic final states that occur in $p\overline{p}$ particle collisions, thus allowing the study of the dynamics of QCD multijet events. Any deviation of an event shape from zero is indicative of higher-order effects – *i.e.* more than the two jets existed in the event.

To test the strong interactions, two different quantities were measured for each event shape: the normalized differential distribution ($\frac{1}{\sigma}\frac{d\sigma}{dX}\,vs\,X$) in four different H_T regions and the average event shape ($\overline{X}\,vs\,H_T$), where X is any of the nine event shapes. Both of these quantities were used to analyze how well the two different unweighted Monte Carlo models (SHERPA and PYTHIA) describe the data that has been corrected to particle level.

The results for both the normalized differential distributions and the average event shapes showed that in general SHERPA gives a better description of the data than does PYTHIA, although there are some places where PYTHIA gives a better description of the data. There are cases where the uncertainties on the ratio of Data/MC (for PYTHIA or SHERPA) do not encompass the value one, which means that the MC does not give an adequate enough description in those cases.

These results could mean one of three things: (1) unweighted SHERPA and PYTHIA do not give an ideal description of the data, (2) the reweighting from the $R_{3/2}$ analysis is not completely applicable for the event shape analysis, or (3) there is an uncertainty source that was not included.

In the process of studying the average event shapes an obvious dip was noticed at around $H_T = 600$ GeV. To study this dip, each of the bins in H_T was made four times finer. However, in doing this bumps were then noticed in the data. As a possible explanation for the bumps in the finer-binned data and for the dip, for each bin in H_T plots were made of $\frac{d\sigma}{dy}$ and $\frac{1}{\sigma}\frac{d\sigma}{dy}$, where y is the rapidity, for each jet that enters the bin: these plots are presented in appendix I. No out of the ordinary behavior was found in these plots.

APPENDIX A

JET ENERGY SCALE

A.1 Overview

DØ measures jets at the calorimeter level; theory computes jets at the parton level (see Figure A.1). In order to compare experiment with theory a common ground needs to be chosen: at DØ the common ground is chosen as the particle jets. The goal of the Jet Energy Scale (JES) is to correct, on average, the jet energy from calorimeter level E_{caljet} to the particle level $E_{ptcljet}$, using the formula:

$$E_{ptcljet} = \frac{E_{caljet} - E_{offset}}{R \cdot S} \cdot k_{bias} \,. \tag{1.1}$$

The offset energy E_{offset} includes any additional energy not associated with the original proton-antiproton collision: it includes effects from detector noise and pile-up from previous interactions and from multiple interactions within the same bunch crossing in the accelerator. The response R is the average fraction of measured calorimeter energy for particles inside the particle jet cone. The showering S corrects for the net energy flow across the boundary of the cone used for the jet: this net energy flow comes from particles showering into the jet cone that are not part of the jet or from particles that are part of the jet cone but whose energy is not completely contained in the cone. k_{bias} corrects for any biases that are introduced by the previously mentioned corrections.

A.2 Offset

As was seen earlier, E_{offset} includes any additional energy not associated with the original proton-antiproton collision. There are two contributions to this additional energy: multiple interactions (MI) and noise and pileup (NP).

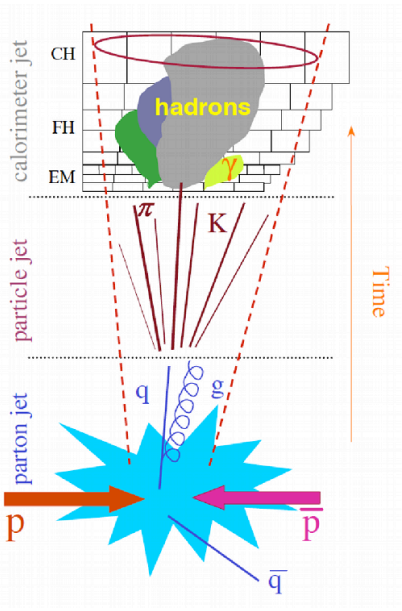

Figure A.1: Parton, particle, and calorimeter jet.

During any beam crossing, there may be more than one collision which will deposit energy in the calorimeter. To determine MI portion of the offset, minbias (MB) events are used. These events require hits on the luminosity monitors (LMhit), indicating an inelastic collision, in addition to coincident timing with the beam crossing. The energy for MB events with $N_{pv} = 1$ is subtracted from the energy for MB events with $N_{pv} > 1$ to obtain the MI portion of E_{offset}.

Pile-up can occur because the calorimeter electronics may not be able to cope with rate at which events are happening: thus there will be energy left behind from the previous bunch crossing. There is also noise that comes from electronics or the depleted uranium of the calorimeter. To detemine the NP portion of the offset, zero bias (ZB) events are used. These events require $N_{pv} = 0$ and no luminosity hits (LMveto) in addition to coincident timing with the beam crossing. The energy of these ZB events is the NP portion of E_{offset}.

The offset correction is calculated for a cone with a specific η by adding all the calorimeter towers in ϕ together. The formula for the E_{offset} is

$$E_{offset} = E_{MI}(N_{pv}, LMhit) - E_{MI}(N_{pv} = 1, LMhit) + E_{NP}(N_{pv} = 0, LMveto) \quad (1.2)$$

where N_{pv} is the number of primary vertices and L_{inst} is the instantaneous luminosity. Figure A.2 shows the amount of offset energy for NP plus MI with several different values of N_{pv}.

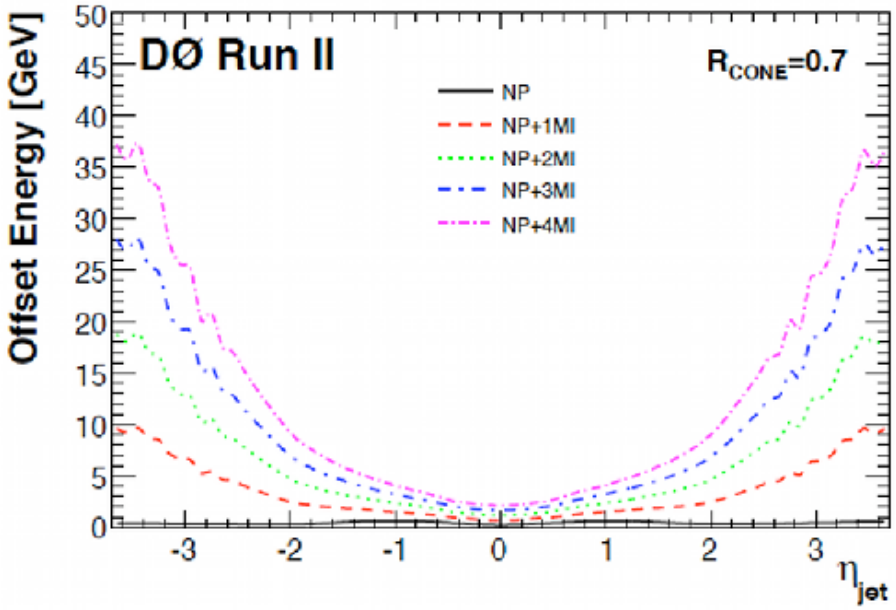

Figure A.2: Final offset correction for several different vertex multiplicities.

A.3 Response Correction

The response R can be broken into two pieces, which can be determined separately, in the following way: $R(\eta) = R_{CC}\, F_\eta$, where R_{CC} is the absolute response (or response in the central calorimeter); F_η is the relative response (or eta-dependent response).

A.3.1 Missing E_T Projection Fraction (MPF) Method

Consider X + *hadronic recoil*, where X ($= \gamma$, Z , or *jet*) is called the "tag object". The tag object and the hadronic recoil respond differently in a real calorimeter, *i.e.* $R_{tag} \neq R_{recoil}$. This following relation exists between the transverse momenta of the tag object and the hadronic recoil:

$$\vec{p}^{\,meas}_{Ttag} + \vec{p}^{\,meas}_{Trecoil} = -\vec{\not{E}}^{\,meas}_{T} \,, \tag{1.3}$$

where $\vec{\not{E}}^{\,meas}_{T}$ is the missing energy in the transverse direction. The two measured momenta are defined in terms of the actual momenta as

$$\vec{p}^{\,meas}_{Ttag} = R_{tag}\vec{p}_{Ttag} \qquad \vec{p}^{\,meas}_{Trecoil} = R_{recoil} \,, \tag{1.4}$$

where $\vec{p}_{Ttag} + \vec{p}_{Trecoil} = 0$. After dotting both sides of equation 1.3 with $\hat{n}_{Ttag}$ and performing a little algebra, the relation for $\frac{R_{recoil}}{R_{tag}}$ is

$$\frac{R_{recoil}}{R_{tag}} = 1 + \frac{\vec{\not{E}}^{\,meas}_{T} \cdot \hat{n}_{Ttag}}{|\vec{p}^{\,meas}_{Ttag}|} \tag{1.5}$$

By requiring the hadronic recoil to consist of one reconstructed jet (probe object) that is back-to-back with the tag object (angle between tag and probe is > 3 radians), the approximation can be made that $R_{recoil} \simeq R_{jet}$. As the MPF method gives an approximation, R^{sample}_{MPF} will be used to indicate a response derived with this method, where sample refers to the data sample used in deriving the response.

A.3.2 Absolute Response

For the absolute response the tag object is taken as a photon, $tag = \gamma$. Assuming that this measured photon transverse momentum $p^{meas}_{T\gamma}$ has been corrected to the particle level by the EM energy scale corrections, $R_{tag} = R_\gamma = 1$. In this case

equation 1.5 becomes

$$R_{MPF}^{\gamma^{meas}+jet} = 1 + \frac{\vec{\not{E}}_T^{meas} \cdot \hat{n}_{T\gamma}}{|\vec{p}_{T\gamma}^{meas}|}\,, \tag{1.6}$$

where $\gamma^{meas}+jet$ means the measured $\gamma+jet$ sample. This sample has a non-negligible dijet contamination where a jet mimicks a photon. The response measured in this sample, $R_{MPC,CC}^{mixture} = R_{MPF}^{\gamma^{meas}+jet}$, needs to be corrected for this contamination as well as for photon energy scale:

$$R_{MPF,CC}^{\gamma+jet} = R_{MPC,CC}^{mixture}\, k_{R,CC}^{\gamma}\,, \tag{1.7}$$

where $k_{R,CC}^{\gamma}$ is the correction factor that takes account of the two previously mentioned corrections, and $R_{MPF,CC}^{\gamma+jet}$ is the proper response for the pure $\gamma + jet$ sample.

The jet energy resolution being poor will introduce a bias in the response. In order to minimize this bias, an energy estimator $E^{'}$

$$E^{'} = p_{T\gamma}^{meas} \cosh(\eta_{jet})\,, \tag{1.8}$$

where η_{jet} is the pseudorapidity of the jet with respect to the primary vertex; and $p_{T\gamma}^{meas}$ and η_{jet} are measured more precisely than jet energy. Once the response in data is measured using equation 1.7, it is fitted with a quadratic logarithmic function of $E^{'}$:

$$R(E^{'}) = p_0 + p_1 \log(E^{'}/E_0) + p_2 \log^2(E^{'}/E_0)\,, \tag{1.9}$$

where $E_0 = 100$ GeV and p_i ($i = 0,\ 1,\ 2$) are the free parameters of the fit.

The statistics of the γ+jets sample limit the direct response measurements in CC to $E' < 350$ GeV. The response above this point needs to be extrapolated up to a point with $\approx$ 600 GeV. Using a direct fit to data to perform the extrapolation would

introduce significant statistical uncertainty. To avoid this high statistical uncertainty, a dedicated Monte Carlo (MC) is used in which the energies are scaled until the fitted response in MC matches the response in data up to the 350 GeV limit. The fitted response is then extended out to $\approx$ 600 GeV. The absolute response including the high energy extrapolation is given in Figure A.3.

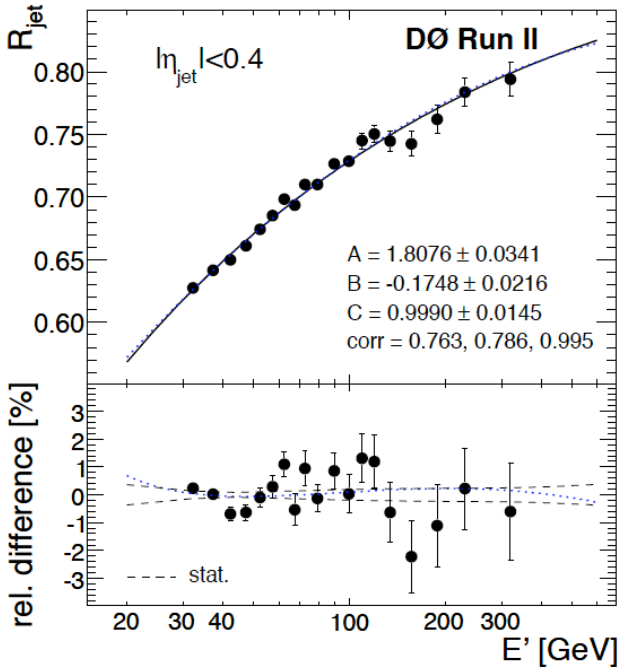

Figure A.3: Absolute response with high energy extrapolation. The solid line represents the high energy extrapolation; the dotted represents the quadratic logarithmic fit.

A.3.3 Relative Response

The relative response correction F_η is a way to correct jets in all η regions by comparing the response of a probe jet to the absolute response correction for the tag object. The same MPF method used to determine the absolute response is used to find the F_η corrections. The relative response correction is measured where the tag

object is a photon, $F_\eta^{\gamma^{meas}+jet}$, or is another jet, F_η^{dijet}. For the $\gamma + jet$ sample the dijet contamination and photon energy scale corrections have not been applied; thus the γ^{meas}.

Once the measurements have been made, both samples are simultaneously fitted using

$$F_\eta(E^{'}; p_1, p_2, p_3, SF_\eta) = \begin{cases} F_\eta^{\gamma+jet}(E^{'}; p_1, p_2, p_3)/k_{R,\eta}^{\gamma}(E^{'}; SF_\eta), & \text{if } \gamma + \text{jet}, \\ SF_\eta\, F_\eta^{\gamma+jet}(E^{'}; p_1, p_2, p_3), & \text{if dijet}, \end{cases} \tag{1.10}$$

where SF_η is a correction factor accounting for the fact that the dijet and $\gamma + jet$ have different relative responses; $F_\eta^{dijet}(E^{'}; p_1, p_2, p_3) = SF_\eta\, F_\eta^{\gamma+jet}(E^{'}; p_1, p_2, p_3)$; $k_{R,\eta}^{\gamma}(E^{'}; SF_\eta)$ has the same meaning as the previously defined $k_{R,CC}^{\gamma}$, but in regions other than the central region; and

$$F_\eta^{\gamma+jet}(E^{'}; p_1, p_2, p_3) = \frac{p_0 + p_1 \log(E^{'}/E_0) + p_2 \log^2(E^{'}/E_0)}{R_{MPF,CC}^{\gamma+jet}(E^{'})} \tag{1.11}$$

The simultaneous fit allows a more accurate fitting for the realtive responses of both the dijet and the γ+jet samples; it also has a similar effect to the high energy extrapolation in the CC region. The relative response corrections including the fits are given in Figure A.4.

A.4 Showering Corrections

The showering correction is requires to correct for a net energy flow across the jet cone boundary which is caused by low momentum particles being bent in the magnetic field, shower development caused by interaction with detector material, etc. Measurement of the showering correction in data starts by studying the energy

distribution in the calorimeter in ringlike strips of increasing radius $\Delta R(y, \phi)$ with respect to the jet axis. This distribution is refered to as the "jet energy profile". This energy distribution is obtained by combining calorimeter cells into towers in the same way as in done in the jet algorithm, and then adding the energy from all towers within a particular ΔR ringlike strip.

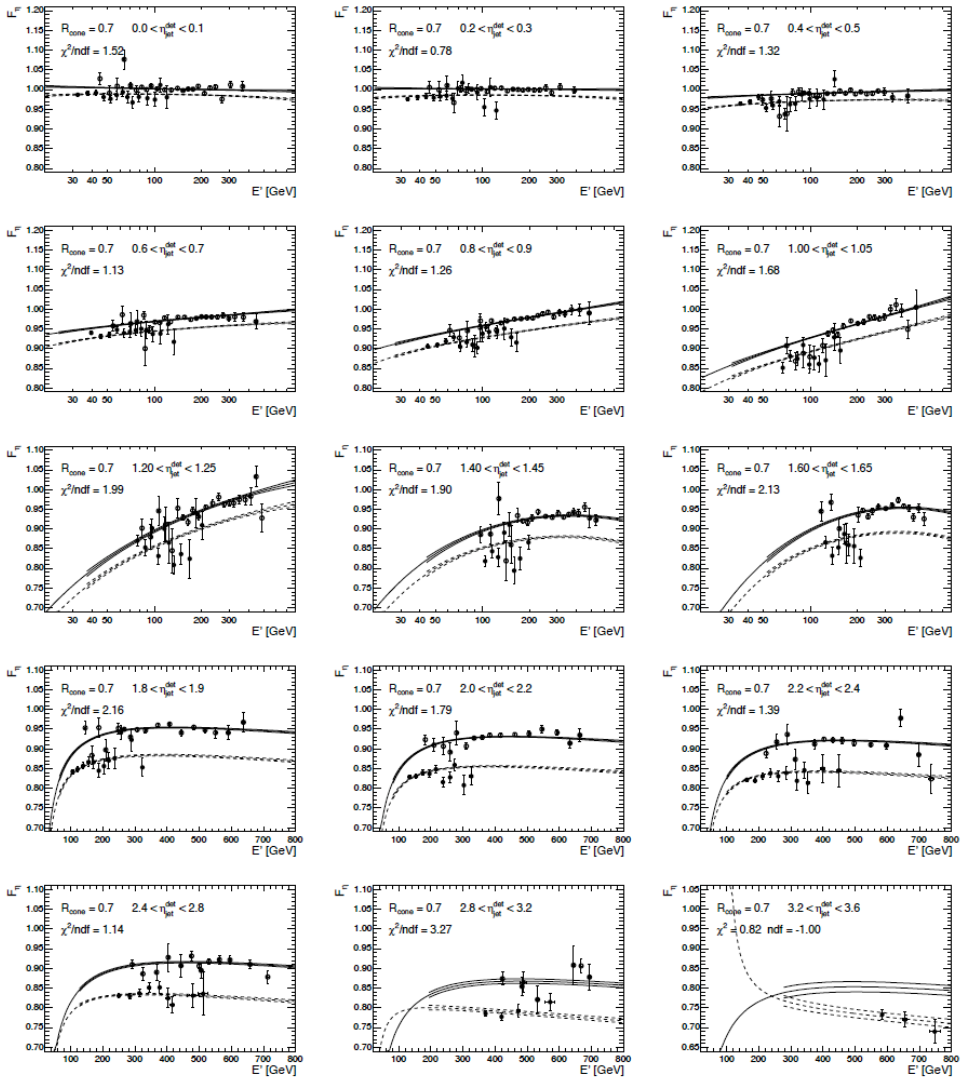

Figure A.4: Relative response for both the γ+jet and dijet samples. The solid (open) circles represent the measurements of the γ+jet (dijet) samples. The dashed (solid) lines represent the fits for the γ+jet (dijet) samples.

In order to obtain the showering correction a linear combination E^{fit} of three jet energy profiles – E^{jet}, $E^{not-jet}$, and E^{offset} – in MC needs to be fitted to the data jet energy profile.

$$E^{fit} = \alpha E^{jet} + \beta E^{not-jet} + E^{offset}\,, \tag{1.12}$$

where E^{jet} is the total energy coming from particles that are from the jet, $E^{not-jet}$ is the total energy coming from particles not from the jet, and E^{offset} is the offset energy. The α and β are fit parameters that are determined by perfoming a χ^2 fit of E^{fit} to the energy profile of data. Once the fit parameters have been determined, the showering correction S is given by

$$S = \frac{\alpha E^{jet(\Delta R<R_{cone})} + \beta E^{not-jet(\Delta R<R_{cone})}}{\alpha E^{jet}}\,, \tag{1.13}$$

where $\Delta R < R_{cone}$ means only the energy that appears inside the jet. Some of the energy inside the jet comes from particles inside the jet and some comes from particles not in the jet. The showering corrections are given in Figure A.5.

A.5 Four Vector Corrections

The standard jet energy scale that has been talked about in the previous sections of this chapter is applied by scaling jet energy and transverse momentum (p_T) by the correction factors which were derived to correct energy and by keeping the direction (rapidity and ϕ) of the jet constant. This will work if the jets are consider massless, *i.e.* $E = p$. However, the jets for Run II are massive, *i.e.* $m \neq 0$ and $E^2 = p^2 + m^2$. Therefore, the same correction cannot be applied to both the p_T and the energy. A suitable correction for the study of massive jets requires that there

be a change in direction (change in rapidity with ϕ constant) of the jet and relative scaling of energy and p_T. The energy, p_T, and rapidity are separately corrected while ϕ is taken to have no need of correction: these four corrections are called the jet four-vector energy scale (J4S).

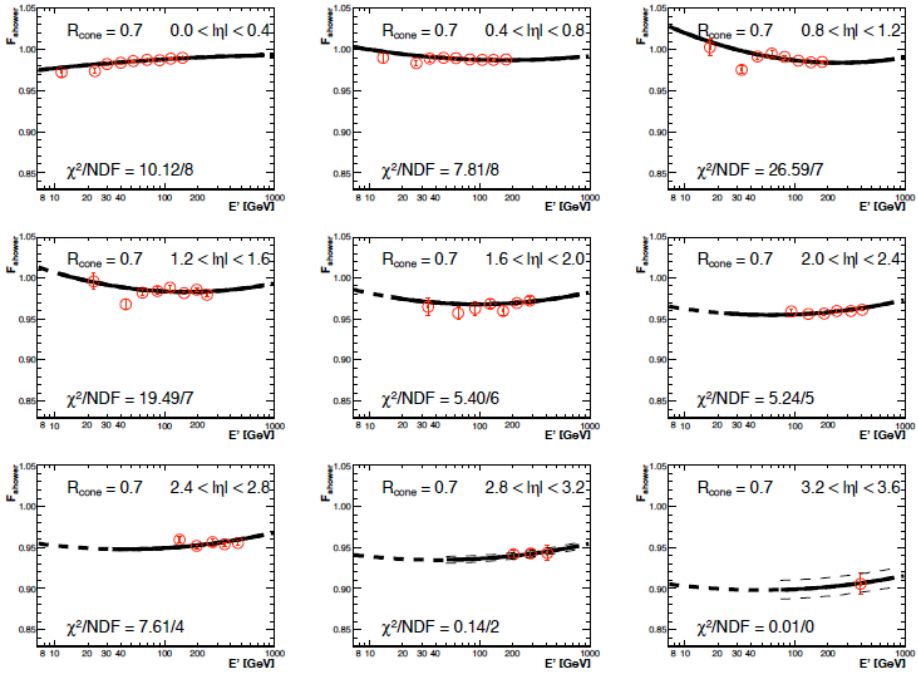

Figure A.5: The showering corrections.

The first step in deriving the J4S is to rederive the standard jet energy scale using dijets instead of γ+jet. The offset energy is taken to be the same as in the standard JES (the one derived using γ+jet). The absolute response for γ+jet is used for dijets because absolute response for dijets cannot be measured directly. To account for this an additional correction

$$k_{sample} = \frac{R_{CC}^{ptcl,dijet}}{R_{CC}^{ptcl.\gamma+jet}} \tag{1.14}$$

is derived. The relative response for dijets F_{η}^{dijet} has already been derived in the standard JES as part of the simultaneous fitting of the γ+jet and dijet samples used in finding $F_{\eta}^{\gamma+jet}$. The k_{bias} corrections are taken to be the same as in the standard JES. The showering correction is rederived for the the dijet sample. These corrections are for the energy.

In finding the correction factors for the p_T, the showering correction needs to be recalculated. The corrections $\frac{p_T^{cal}}{E_{jet}^{cal}}$ and $k_{offset}^{p_T}$ are derived to account for the fact that energy offset corrections are being used instead of computing the p_T offset separately. All other correction factors can be reused from the energy correction for dijets.

APPENDIX B

MC-DATA DIFFERENCE

B.1 Description Of This Correction

This appendix describes a method used to correct MC for the MC-data difference in the jet response. For each calorimeter jet in the MC, we look for a spatially matched particle jet to calculate the correction factor F

$$F = \frac{\sum_i E_i \, R_i^{data}}{\sum_i E_i \, R_i^{MC}} \,, \tag{2.1}$$

where the subscript i runs over the particles in the particle jet, E_i are the energies of the particles, and R_i are the single particle responses in MC or data. This correction factor corrects for the MC-data difference in the jet response and should be applied to the jet energy after the offset correction; *i.e.*

$$E_{jet}^{corr} = (E_{jet}^{raw} - E_{offset}) \cdot F \,, \tag{2.2}$$

where E_{jet}^{raw} is the raw jet energy, E_{offset} is the offset energy derived as part of the jet energy scale (JES), and E_{jet}^{corr} is the corrected jet energy. All other JES corrections should be applied on E_{jet}^{corr} instead of E_{jet}^{raw}.

The single particle MC responses are measured for the following particles: γ, $e^{\pm}$, $\mu^{\pm}$, $\pi^{\pm}$, $K^{\pm}$, K_0^L, K_0^S, $p^{\pm}$, n, and Λ from single particle MC samples. These measurements are made for $0 < |\eta|^{det} < 3.2$ in increments of 0.1. The single particle MC responses are then fitted with

$$\begin{aligned}
R_{\gamma}^{MC} &= 0.25 p_0 \cdot \left[1 + Erf\left(\frac{E+p_1}{\sqrt{2p_2}}\right)\right] \cdot \left[1 + Erf\left(\frac{E+p_3}{\sqrt{2p_4}}\right)\right] + p_5 \\
R_{e^{\pm}}^{MC} &= 0.25 p_0 \cdot \left[1 + Erf\left(\frac{E+p_1}{\sqrt{2p_2}}\right)\right] \cdot \left[1 + Erf\left(\frac{E+p_3}{\sqrt{2p_4}}\right)\right] \\
R_{\mu^{\pm}}^{MC} &= (p_0 + p_1 E) \cdot \text{TMath::Landau}(E, p_2, p_3) \\
R_h^{MC} &= p_0 \cdot \left[1 - p_1 \left(\frac{E}{0.75}\right)^{p_2 - 1}\right],
\end{aligned} \tag{2.3}$$

where $h = \pi^{\pm}$, $K^{\pm}$, K_0^L, K_0^S, $p^{\pm}$, n, or Λ. TMath::Landau is the ROOT function that gives the Landau distribution:

$$\text{Landau}(E, p_2, p_3) = A\left(\frac{E - p_2}{p_3}\right), \tag{2.4}$$

where

$$A(x) = \frac{1}{\pi}\int_0^{\infty} e^{-xt}\, t^{-t}\, \sin(\pi t)\, dt\,. \tag{2.5}$$

Each particle is fitted separately in each of the 32 regions. The values for the fit parameters for each particle in each region are contained in the plots. These fit parameters are what is needed in the later steps of the extraction of the single particle responses in data.

An MC closure test is performed using a γ+jet MC sample in which $\sum_i E_i R_i^{MC}$ is compared to $(E_{raw}^{jet,MC} - E_{offset}) \cdot k_{offset}$, where k_{offset} is the bias correction for E_{offset} and is included in the k_{bias} from the JES in appendix A. The MC closure test is done to check the validity of using the single particle MC responses to to obtain the offset-corrected MC jet energy. Ideally $\sum_i E_i R_i^{MC} = (E_{raw}^{jet} - E_{offset}) \cdot k_{offset}$ or $\frac{(E_{raw}^{jet} - E_{offset}) \cdot k_{offset}}{\sum_i E_i R_i^{MC}} = 1$. Looking at the plots for the MC closure test, it can be seen that the ratio is not one exactly: any difference from one is taken as a systematic uncertainty for the MC-data correction factor, F.

The assumption is made that MC does a good job of describing the single particle responses in data of the γ, $e^{\pm}$, and $\mu^{\pm}$ and that the single particle responses

for the hadrons ($\pi^{\pm}$, $K^{\pm}$, K_0^L, K_0^S, $p^{\pm}$, n, and Λ) are parametrized by A, B, and C:

$$\begin{aligned} R_{\gamma}^{data} &= R_{\gamma}^{MC} \\ R_{e^{\pm}}^{data} &= R_{e^{\pm}}^{MC} \\ R_{\mu^{\pm}}^{data} &= R_{\mu^{\pm}}^{MC} \\ R_{h}^{data} &= C \cdot p_0 \cdot \left[1 - A \cdot p_1 \left(\frac{E}{0.75}\right)^{p_2+B-1}\right], \end{aligned} \tag{2.6}$$

where R^{data} represents the responses of an MC that is tuned so that the MC jet response agrees with response in data.

In the tuning process γ+jet and dijet MC samples and the EMinclusive data sample (which includes γ+jet and dijet background events mixed) are used. The ratio of the transverse momentum of the photon (p_T^{γ}) with

$$p_{T,corr}^{jet} = p_{T,raw}^{jet} \cdot \frac{E_{raw}^{jet} - E_{offset}}{E_{raw}^{jet}} \cdot \begin{cases} F(A,B,C), & \text{if MC,} \\ 1, & \text{if data,} \end{cases} \tag{2.7}$$

is done in data and MC for each event, where $F(A,B,C)$ is from equation 2.1. A, B, and C are tuned so that $\frac{p_{T,corr}^{jet}}{p_T^{\gamma}}$ are consistent between data and MC. The tuning process starts with filling a histogram of $\frac{p_{T,corr}^{jet}}{p_T^{\gamma}}$ versus $E' = \frac{p_T^{\gamma}}{cosh(\eta^{jet})}$. For MC A, B, and C are scanned over. At each set of values a histogram similar to that for data is created and is fitted with a third-order polynomial. This is done for two different event selections simultaneously: tight photon (selects mainly photons) and reverse track isolation (selects mainly dijets). A χ^2 value is then computed between data points and the fitted polynomial in MC for each combination of A, B, and C, simulatenously using the tight photon and the reverse track isolation. The A, B, and

C that gives the smallest χ^2 value is then chosen. These results are shown in the "Extracting Single Particle Data Responses" subsections.

A closure test using the above-chosen A, B, and C is performed separately for the tight photon and the reverse track isolation. This closure test is done to show how well the tuned MC matches data; it also shows how much better the tuned MC is than the default MC. The closure test results are shown in the "Closure Test for MC Tuning to Data" subsections.

B.2 Results for RunIIA

This section contains the results for RunIIA data – single particle MC responses, MC closure test for the single particle responses, extraction of single particle data responses, and closure test for MC tuning to data.

B.2.1 Single Particle MC Responses

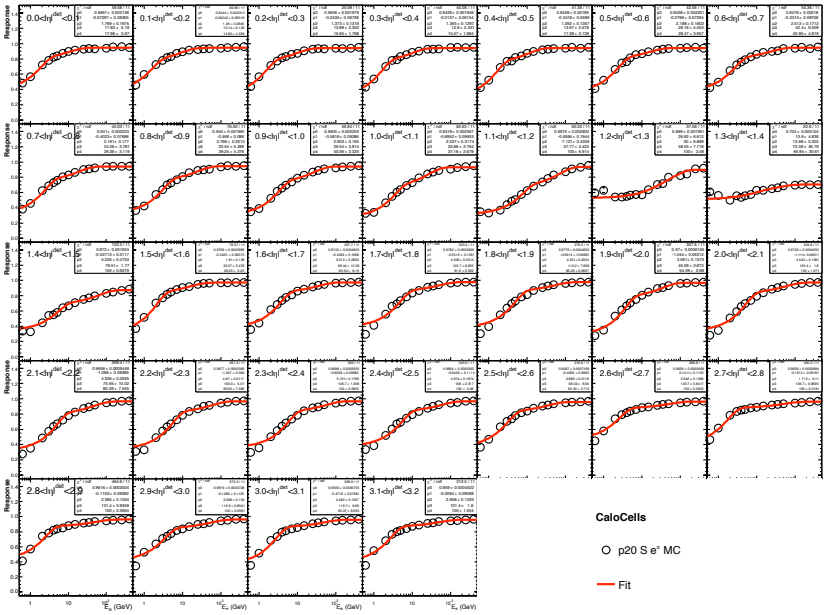

Figure B.1: RunIIA single Particle MC response for the $e^{\pm}$.

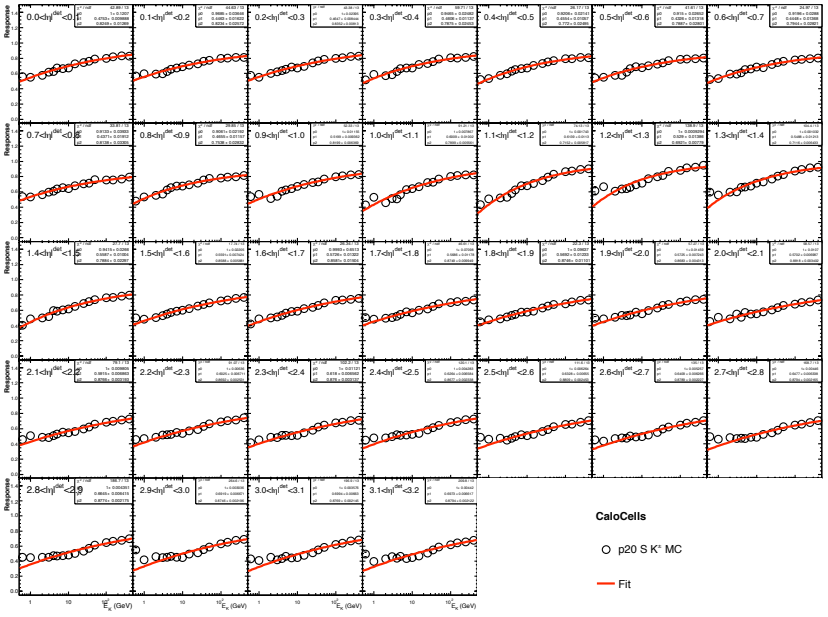

Figure B.2: RunIIA single Particle MC response for the $K^{\pm}$.

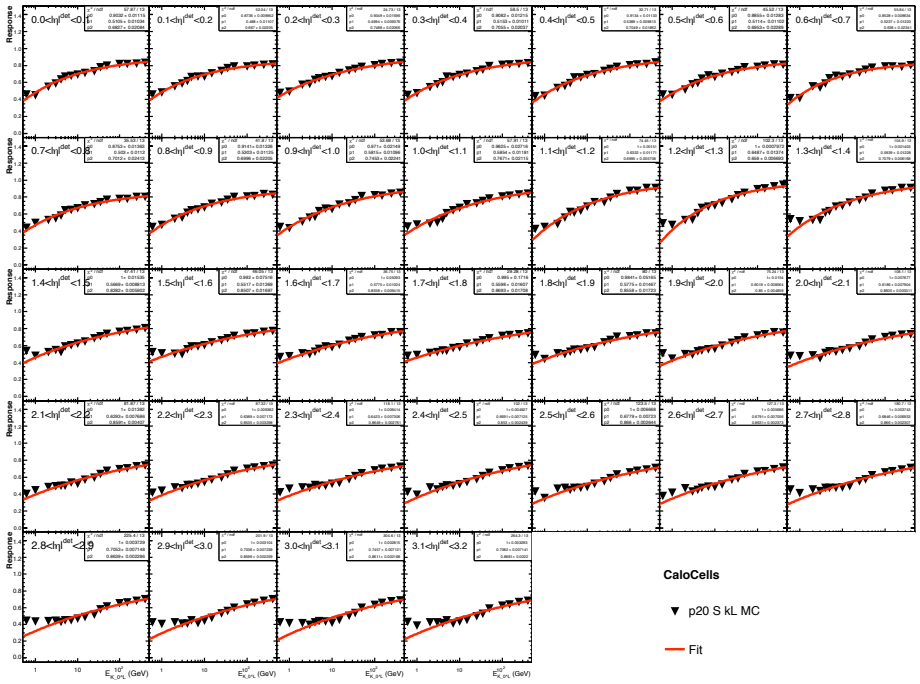

Figure B.3: RunIIA single Particle MC response for the K_L.

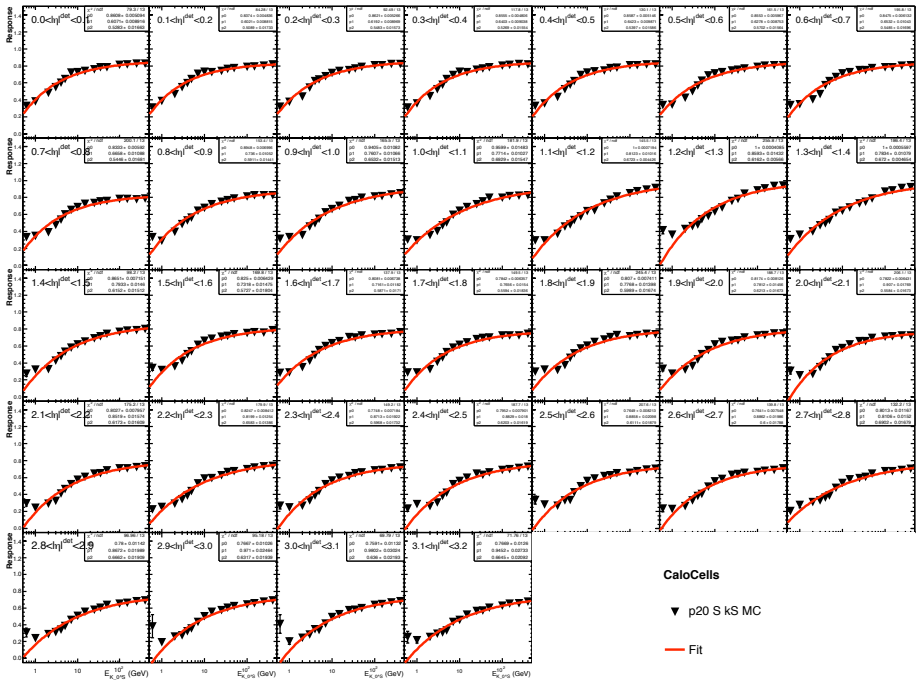

Figure B.4: RunIIA single Particle MC response for the K_S.

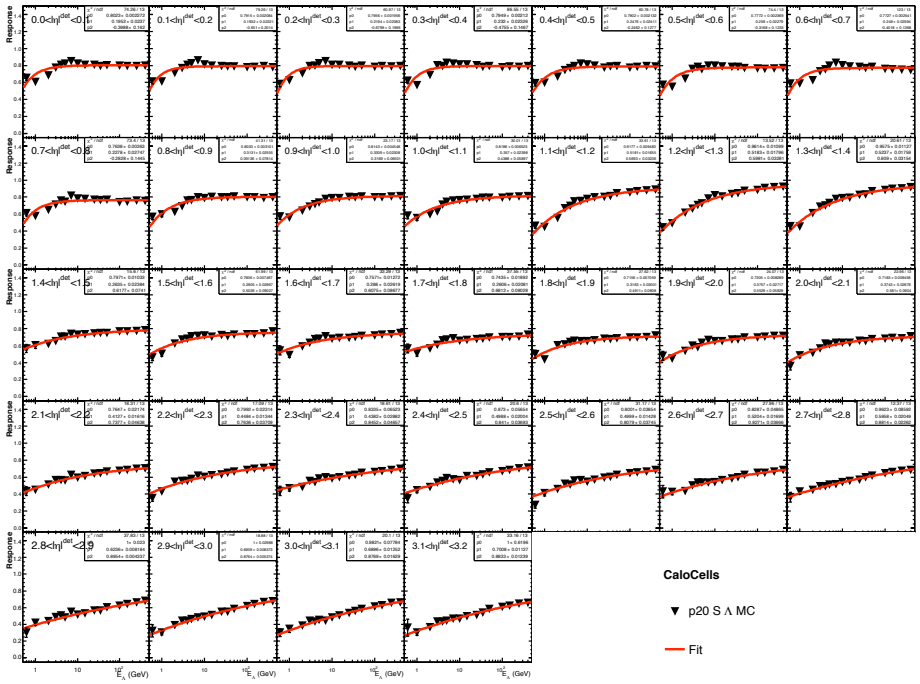

Figure B.5: RunIIA single Particle MC response for the Λ^0.

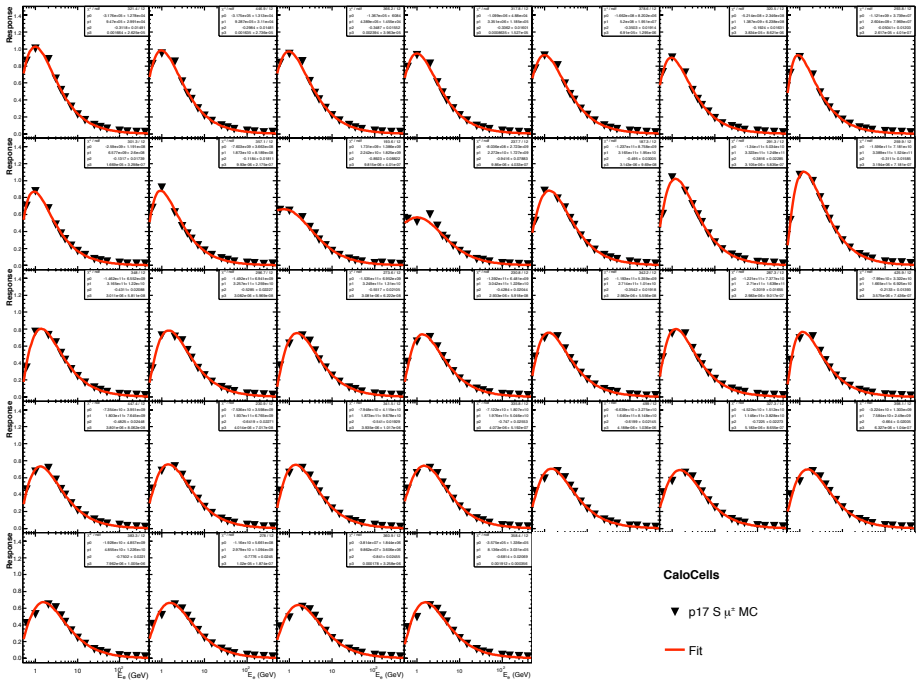

Figure B.6: RunIIA single Particle MC response for the $\mu^{\pm}$.

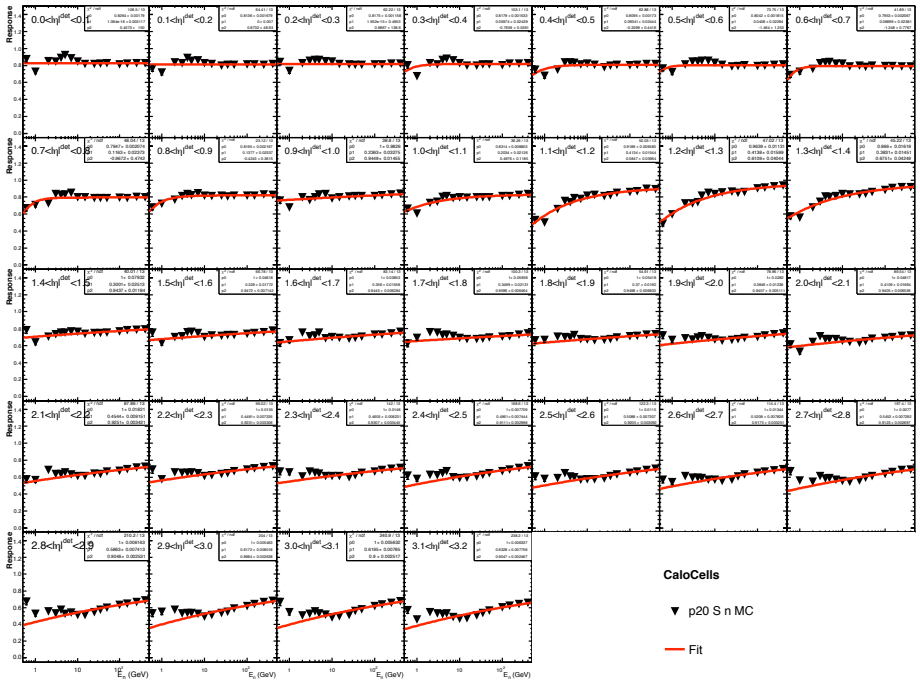

Figure B.7: RunIIA single Particle MC response for the n.

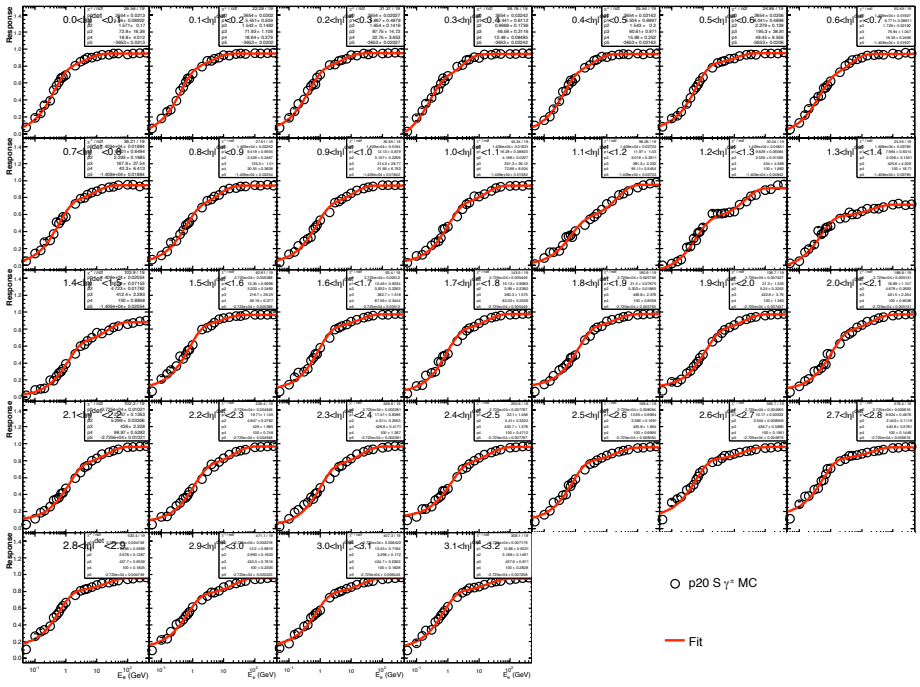

Figure B.8: RunIIA single Particle MC response for the γ.

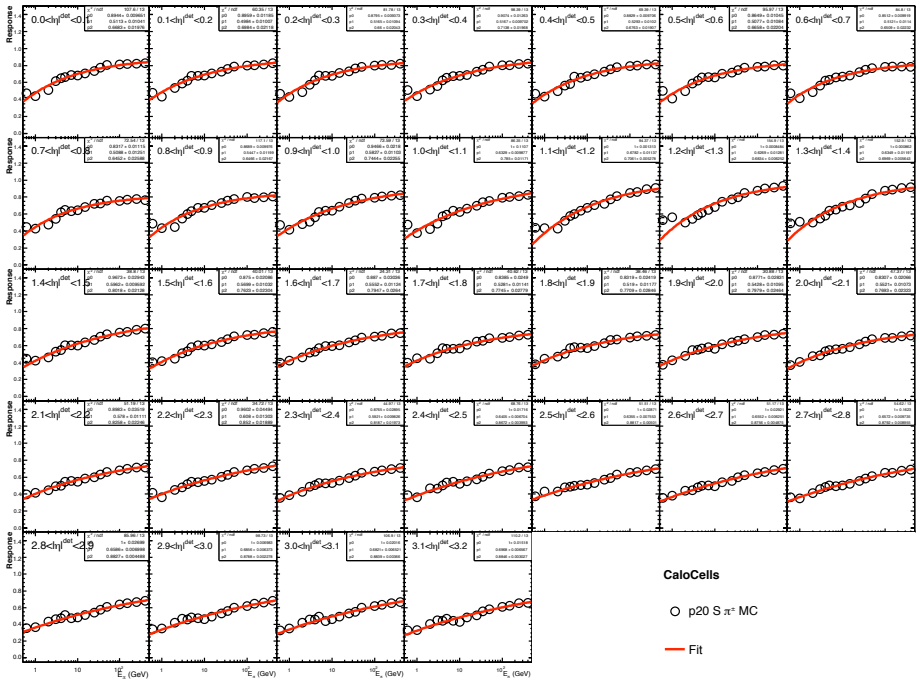

Figure B.9: RunIIA single Particle MC response for the $\pi^{\pm}$.

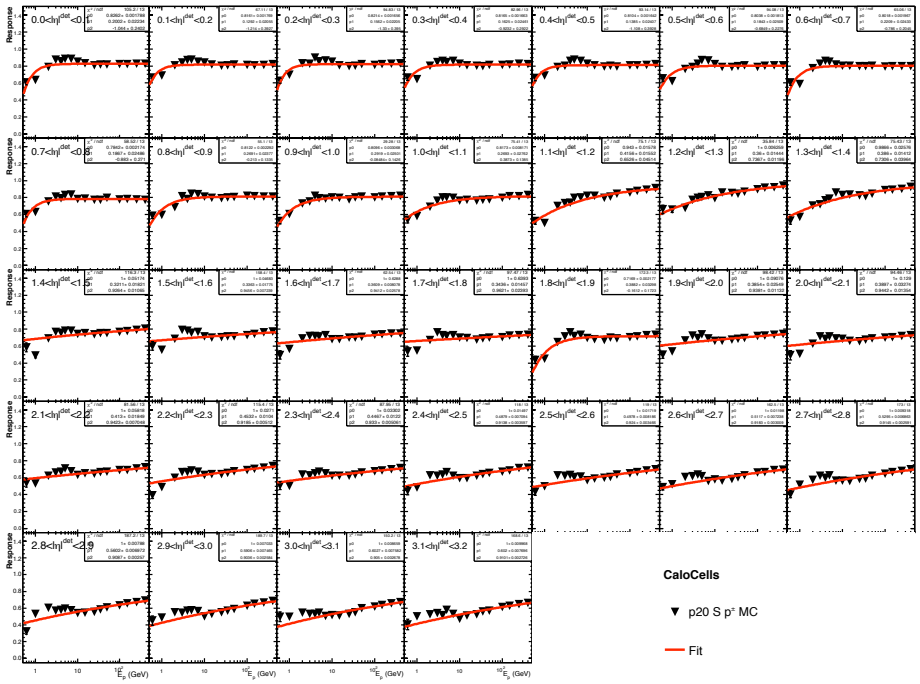

Figure B.10: RunIIA single Particle MC response for the $p^{\pm}$.

B.2.2 MC Closure Test

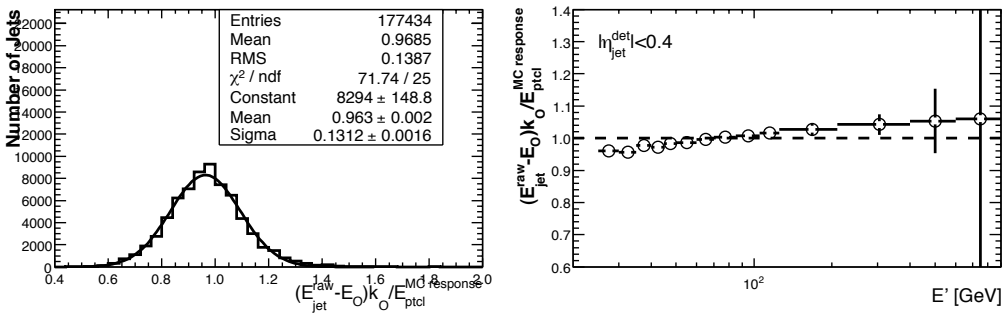

Figure B.11: MC closure test for RunIIA single particle MC, $|\eta_{jet}^{det}| < 0.4$.

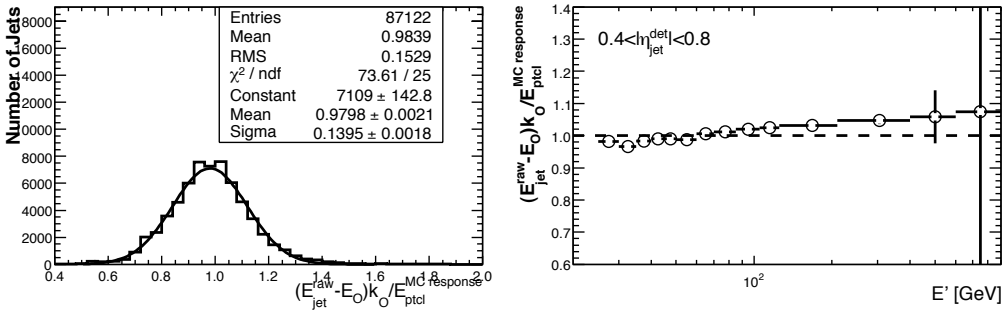

Figure B.12: MC closure test for RunIIA single particle MC, $0.4 < |\eta_{jet}^{det}| < 0.8$.

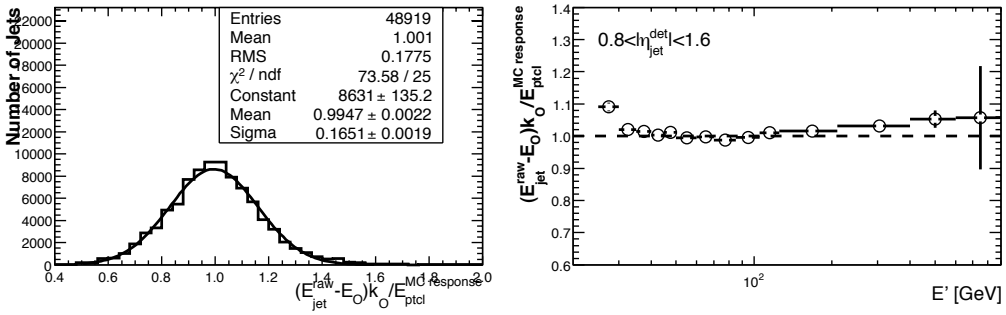

Figure B.13: MC closure test for RunIIA single particle MC, $0.8 < |\eta_{jet}^{det}| < 1.6$.

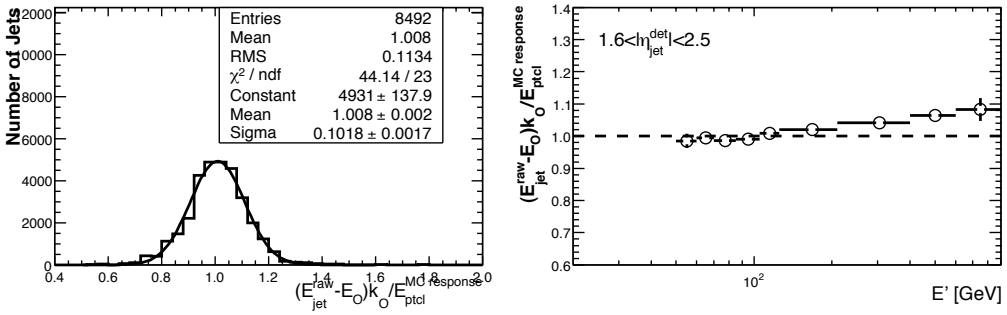

Figure B.14: MC closure test for RunIIA single particle MC, $1.6 < |\eta_{jet}^{det}| < 2.5$.

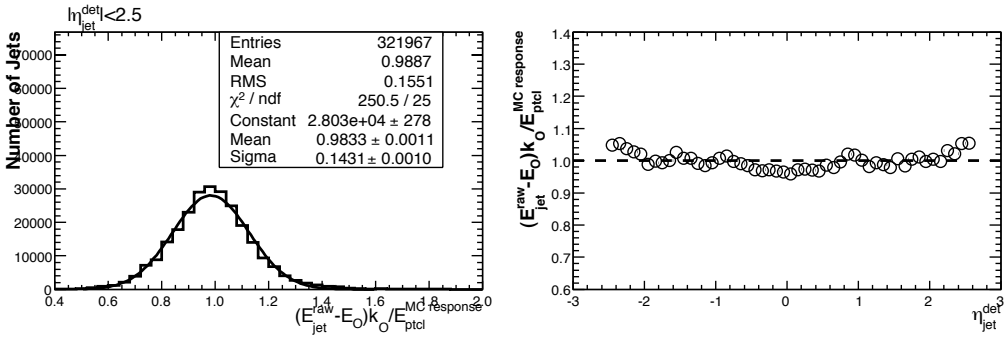

Figure B.15: MC closure test for RunIIA single particle MC, $|\eta_{jet}^{det}| < 2.5$.

B.2.3 Extracting Single Particle Data Responses

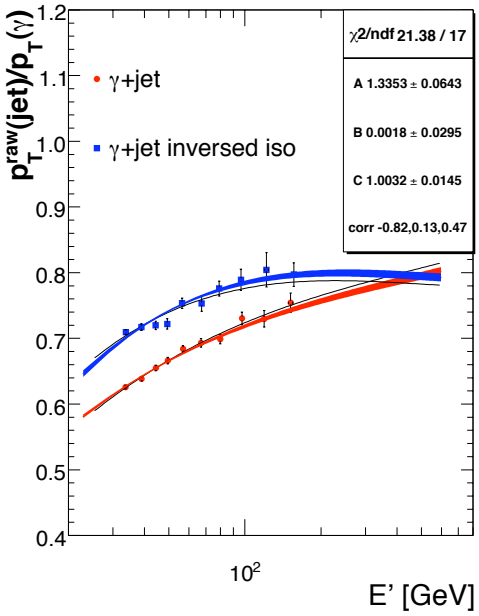

(a) $|\eta_{jet}^{det}| < 0.4$

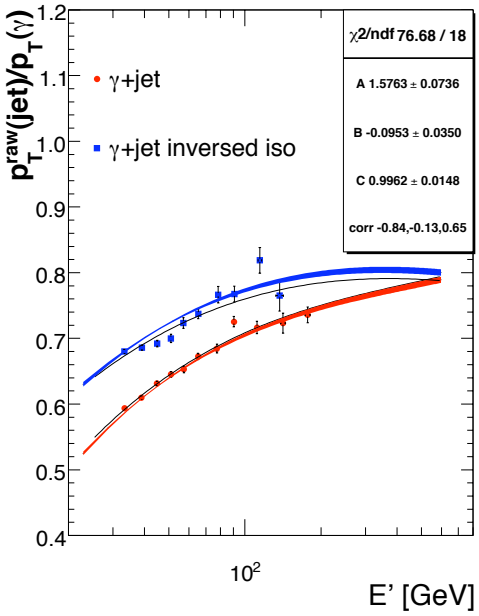

(b) $0.4 < |\eta_{jet}^{det}| < 0.8$

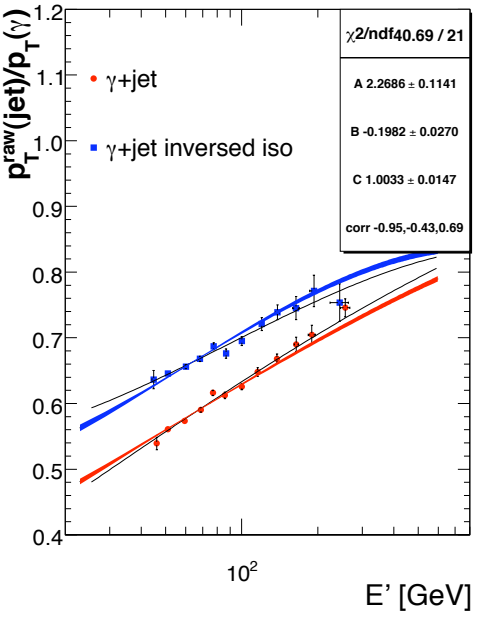

(c) $0.8 < |\eta_{jet}^{det}| < 1.6$

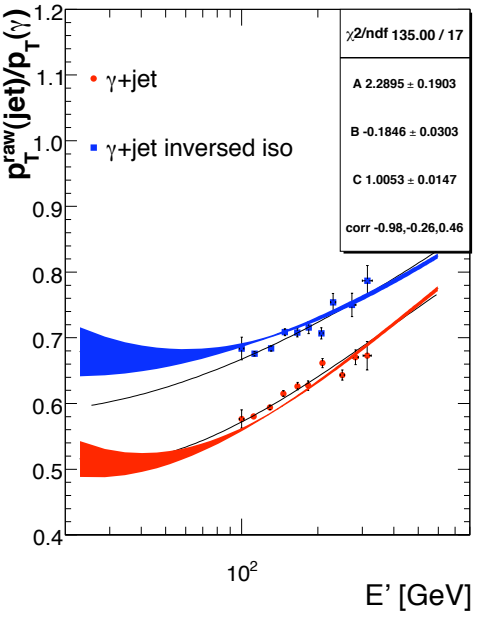

(d) $1.6 < |\eta_{jet}^{det}| < 2.5$

Figure B.16: MC tuning results determining A, B, and C.

B.2.4 Closure Test for MC Tuning to Data

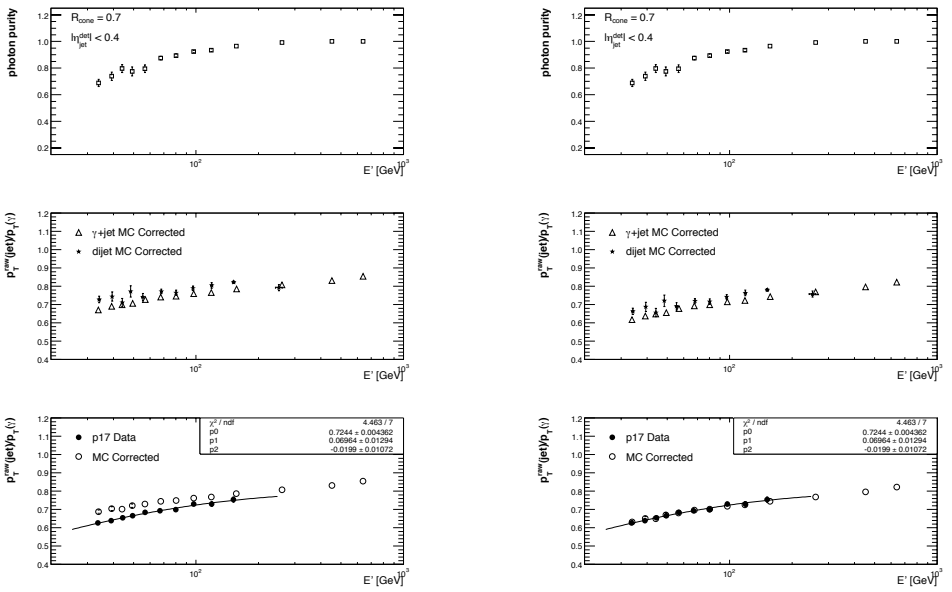

(a) Default MC, A=C=1, B=0 (b) Tuned MC

Figure B.17: RunIIA closure test for tuned MC, tight photon; $|\eta_{jet}^{det}| < 0.4$.

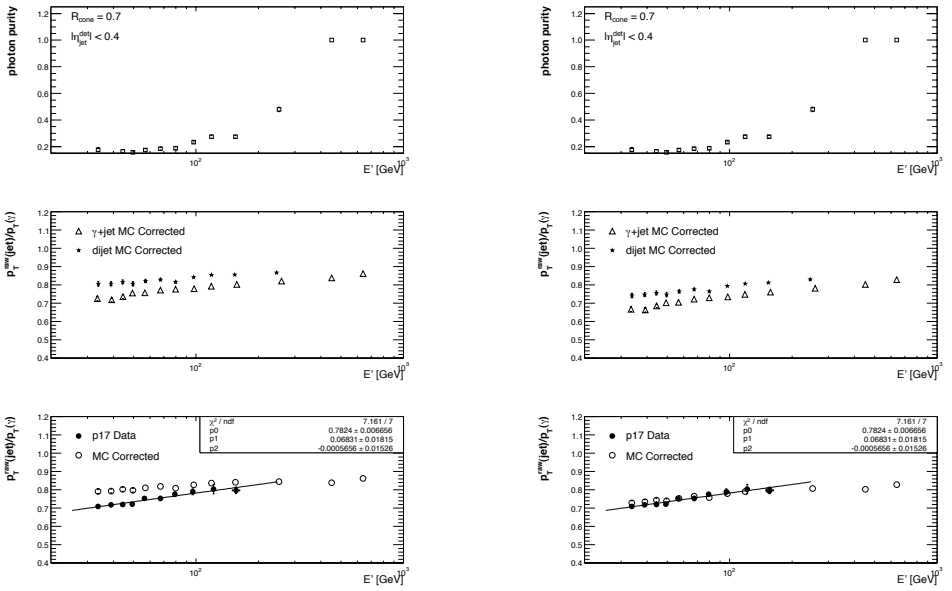

(a) Default MC, A=C=1, B=0 (b) Tuned MC

Figure B.18: RunIIA closure test for tuned MC, reversed photon; $|\eta_{jet}^{det}| < 0.4$.

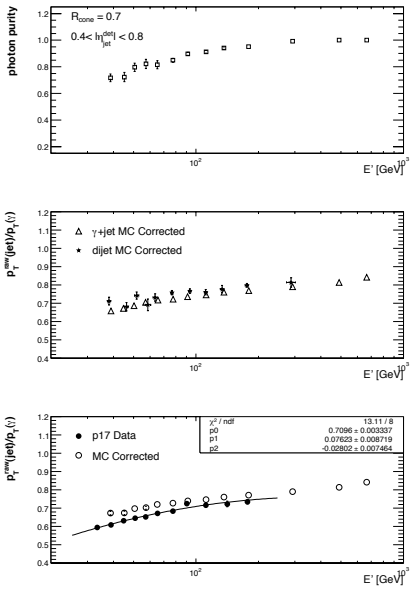

(a) Default MC, A=C=1, B=0

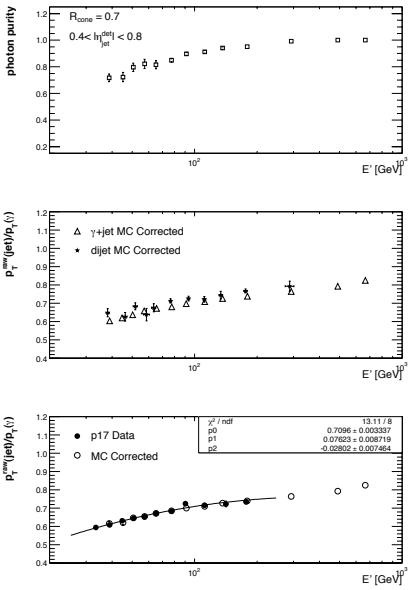

(b) Tuned MC

Figure B.19: RunIIA closure test for tuned MC, tight photon; $0.4 < |\eta^{det}_{jet}| < 0.8$.

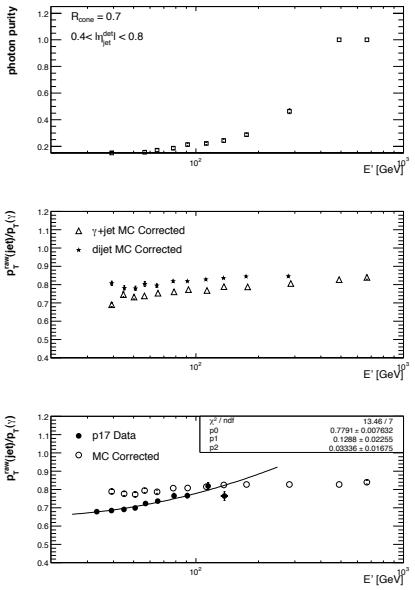

(a) Default MC, A=C=1, B=0

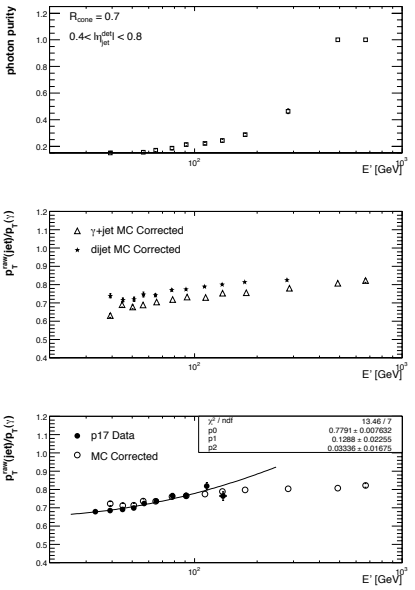

(b) Tuned MC

Figure B.20: RunIIA closure test for tuned MC, reversed photon; $0.4 < |\eta^{det}_{jet}| < 0.8$.

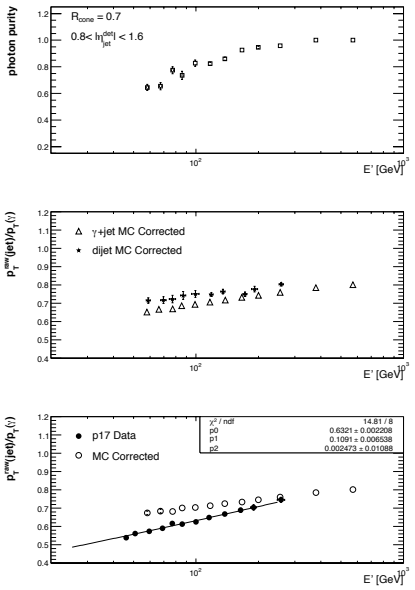

(a) Default MC, A=C=1, B=0

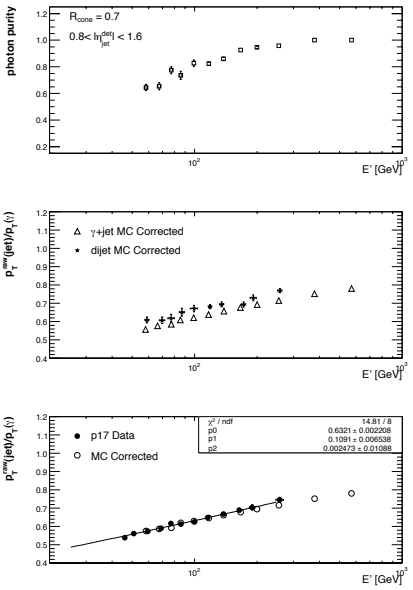

(b) Tuned MC

Figure B.21: RunIIA closure test for tuned MC, tight photon; $0.8 < |\eta_{jet}^{det}| < 1.6$.

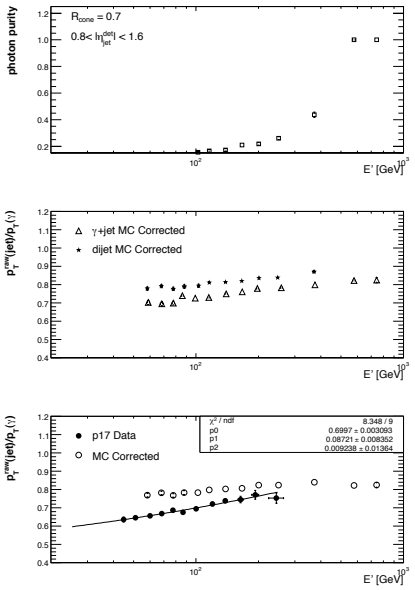

(a) Default MC, A=C=1, B=0

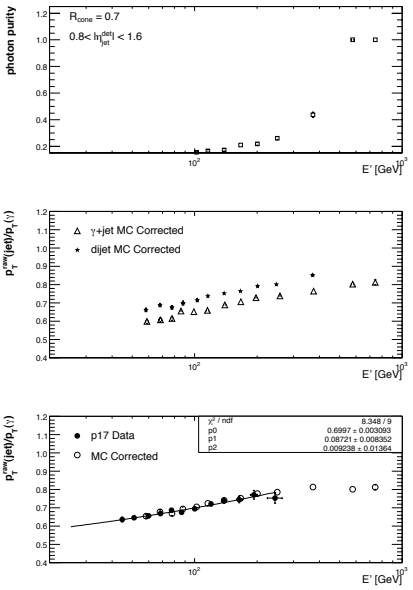

(b) Tuned MC

Figure B.22: RunIIA closure test for tuned MC, reversed photon; $0.8 < |\eta_{jet}^{det}| < 1.6$.

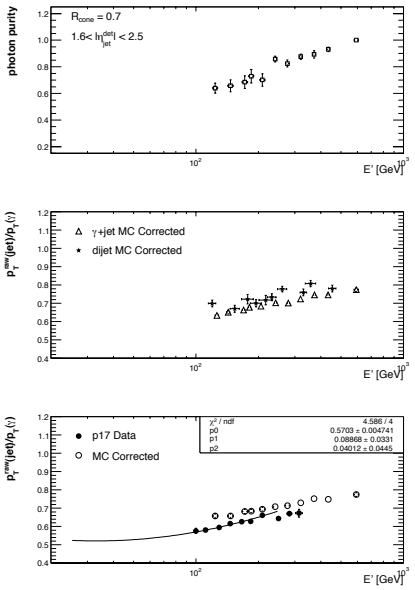

(a) Default MC, A=C=1, B=0

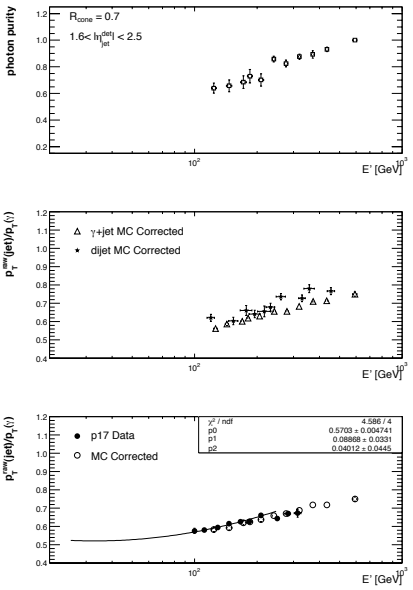

(b) Tuned MC

Figure B.23: RunIIA closure test for tuned MC, tight photon; $1.6 < |\eta_{jet}^{det}| < 2.5$.

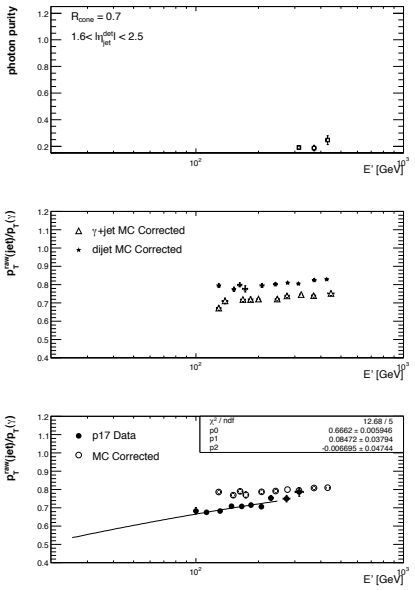

(a) Default MC, A=C=1, B=0

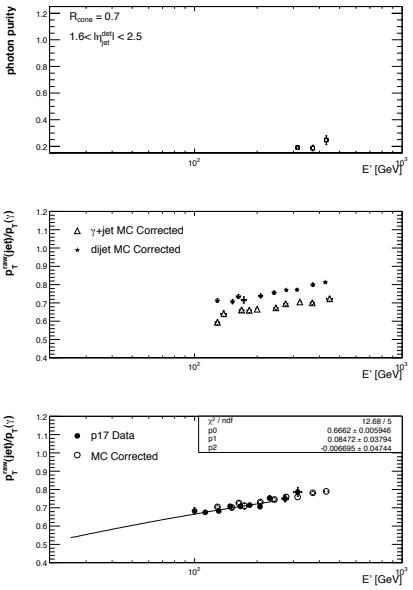

(b) Tuned MC

Figure B.24: RunIIA closure test for tuned MC, reversed photon; $1.6 < |\eta_{jet}^{det}| < 2.5$.

B.3 Single Particle MC Responses for RunIIB

The single particle MC responses that go along with the data taking periods RunIIB-1[1] and RunIIB-2[2] are the same for both periods.

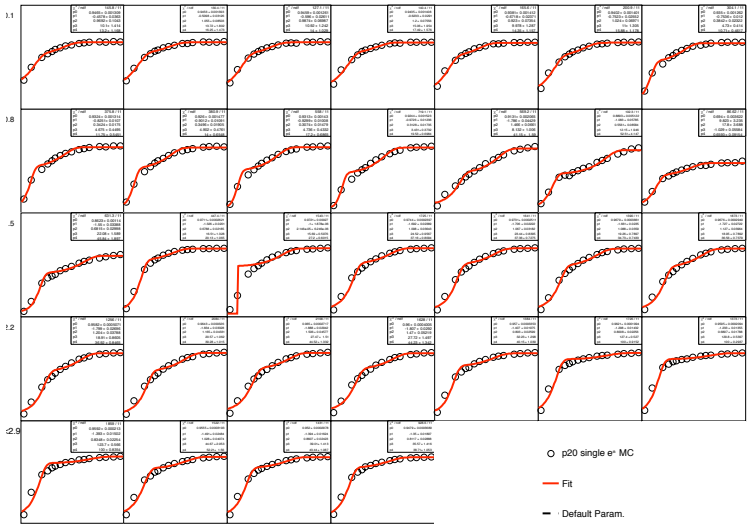

Figure B.25: RunIIB single Particle MC response for the $e^{\pm}$.

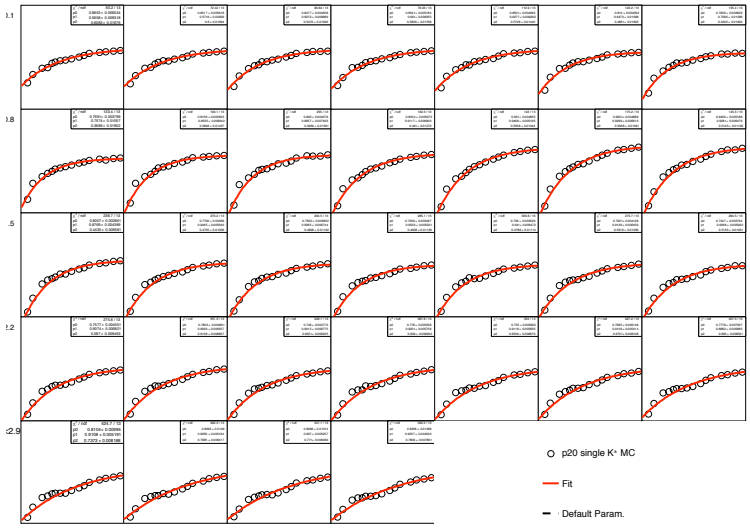

Figure B.26: RunIIB single Particle MC response for the $K^{\pm}$.

[1]RunIIB-1 consists of runs 221698 - 234913 taken from June 2006 to August 2007
[2]RunIIB-2 consists of runs 237342 - 252918 taken from Oct 2007 to June 2009

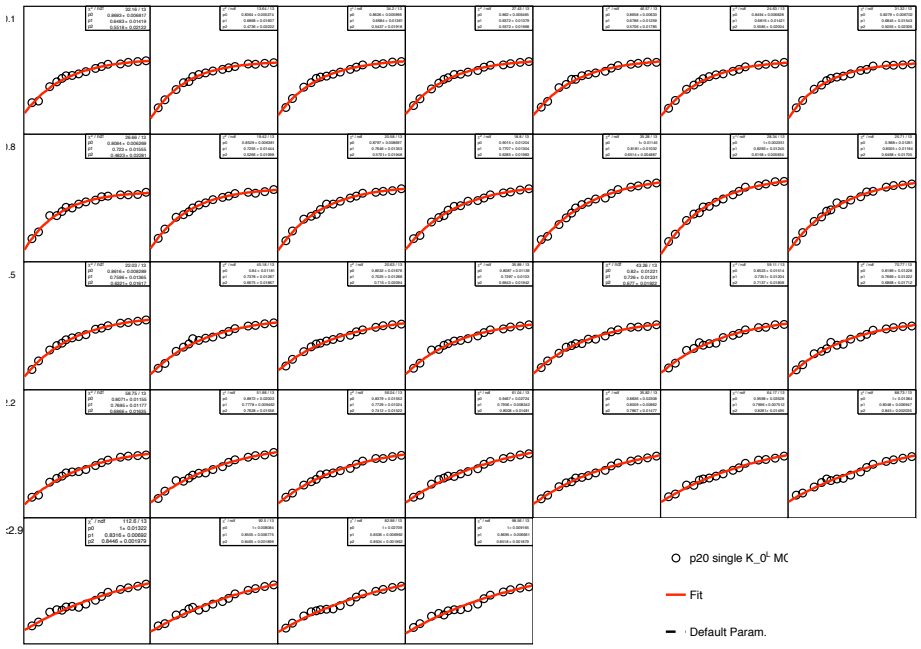

Figure B.27: RunIIB single Particle MC response for the K_L.

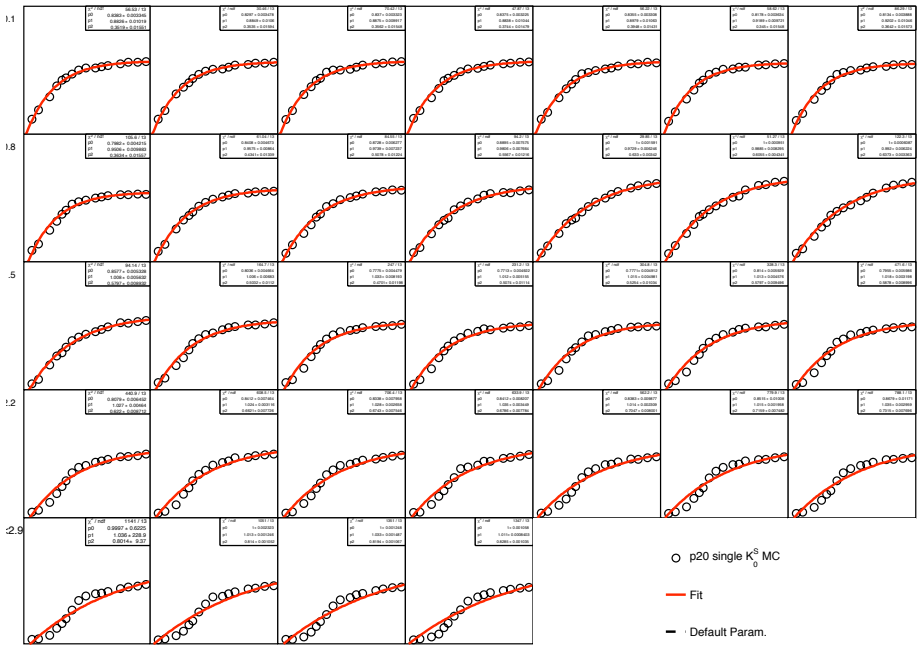

Figure B.28: RunIIB single Particle MC response for the K_S.

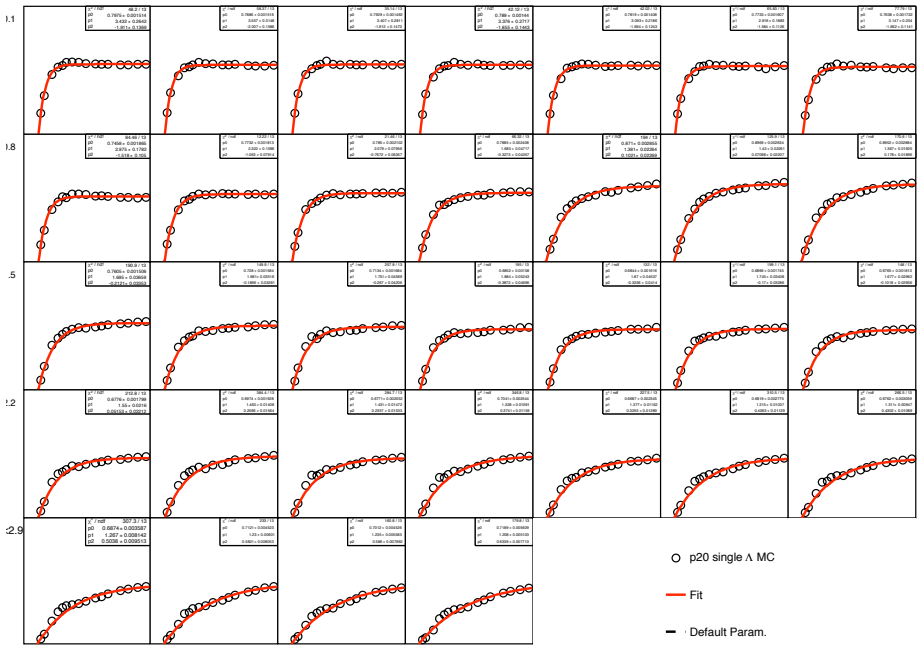

Figure B.29: RunIIB single Particle MC response for the Λ^0.

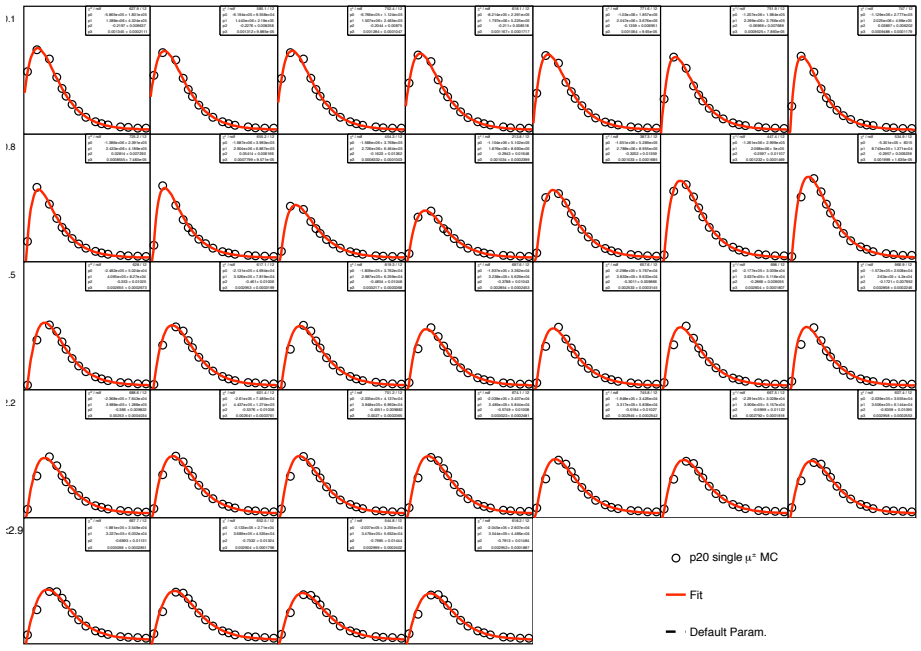

Figure B.30: RunIIB single Particle MC response for the $\mu^{\pm}$.

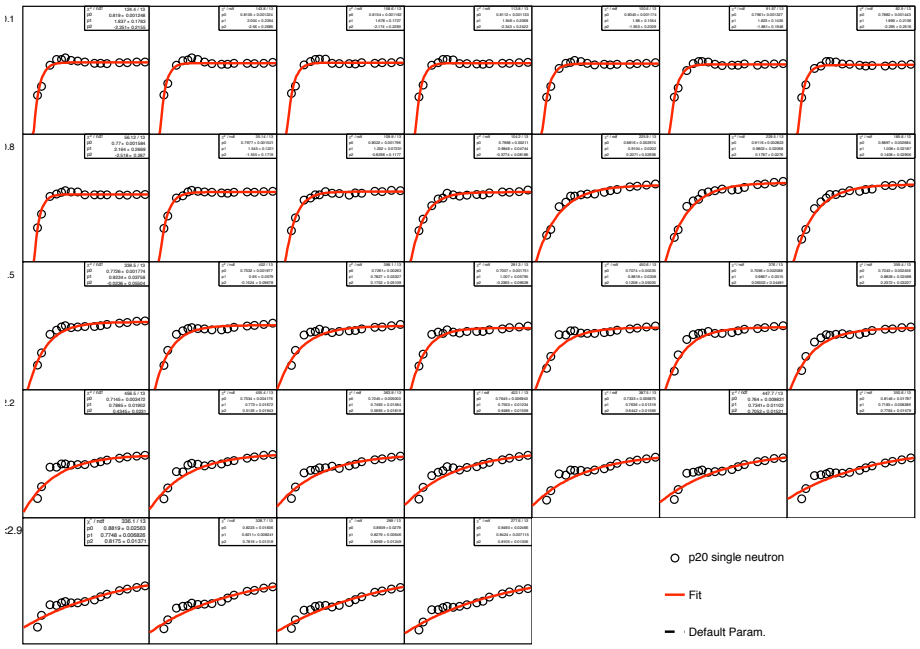

Figure B.31: RunIIB single Particle MC response for the n.

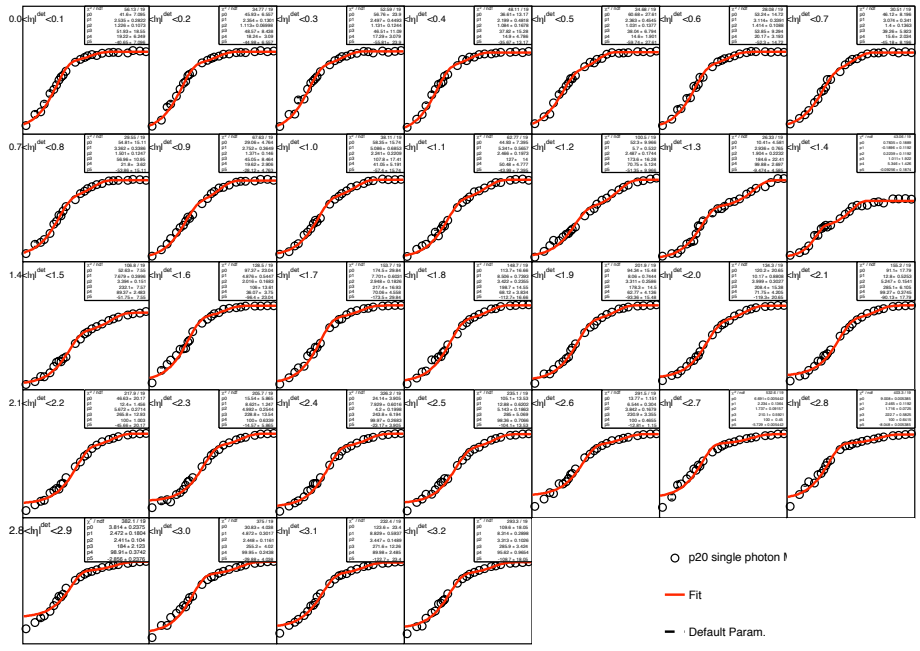

Figure B.32: RunIIB single Particle MC response for the γ.

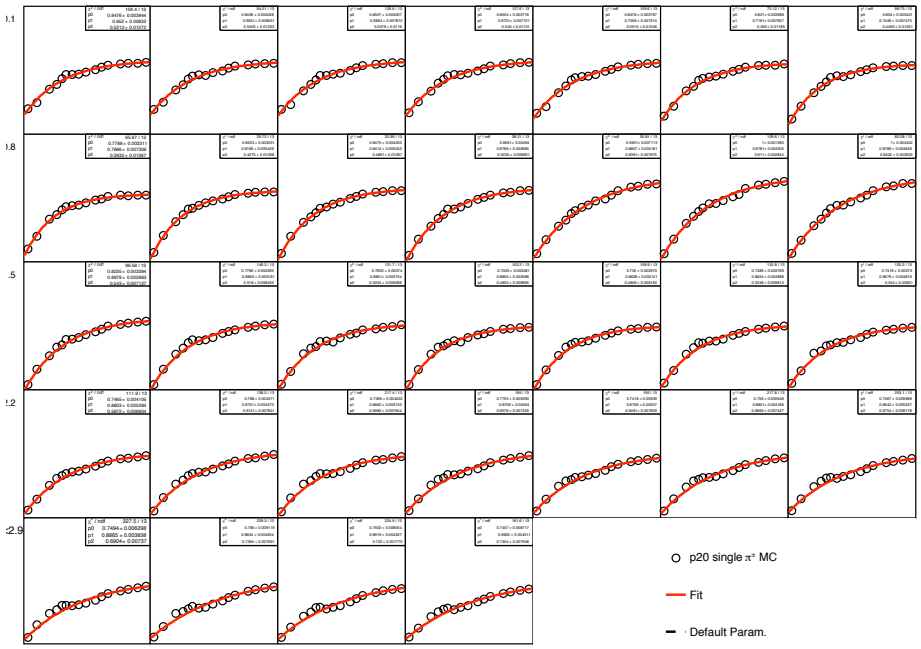

Figure B.33: RunIIB single Particle MC response for the $\pi^{\pm}$.

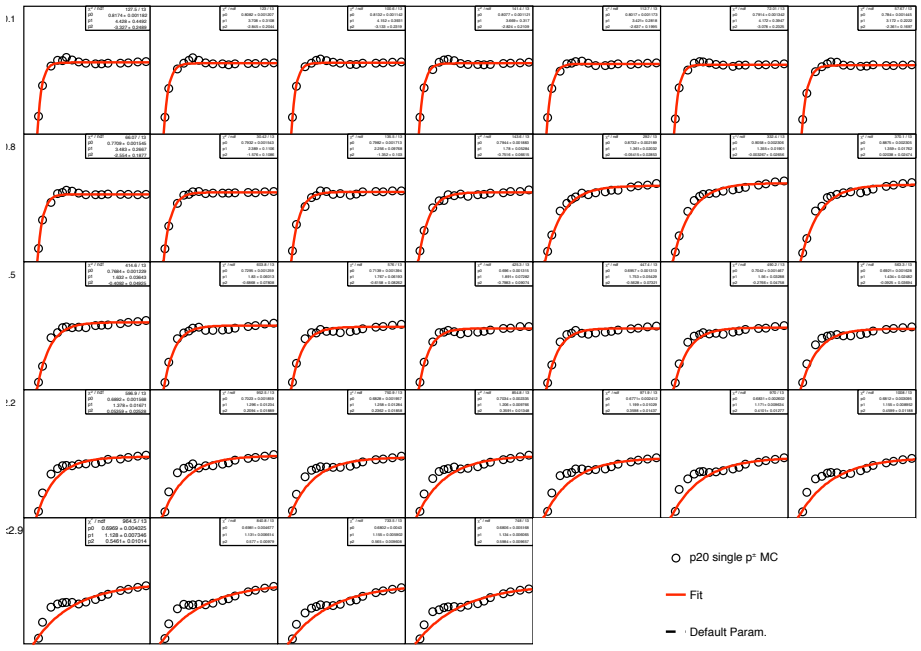

Figure B.34: RunIIB single Particle MC response for the $p^{\pm}$.

B.4 Results for RunIIB-1

This section contains the results for RunIIB-1 data – MC closure test for the single particle responses, extraction of single particle data responses, and closure test for MC tuning to data.

B.4.1 MC Closure Test

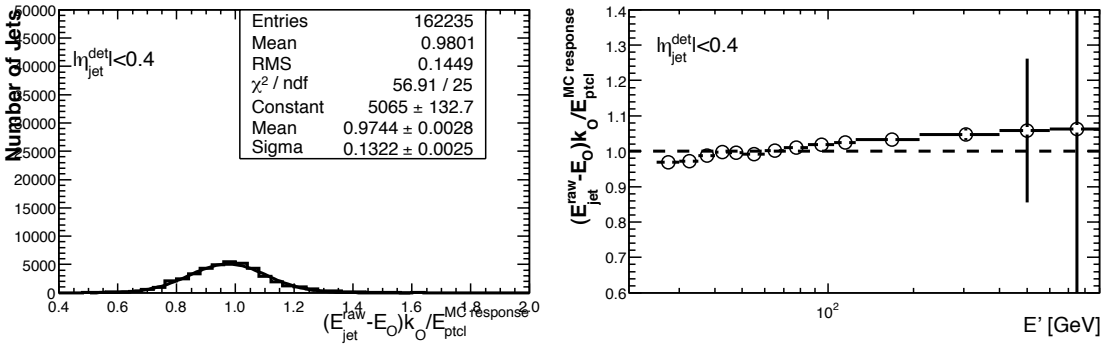

Figure B.35: MC closure test for RunIIB-1 single particle MC, $|\eta^{det}_{jet}| < 0.4$.

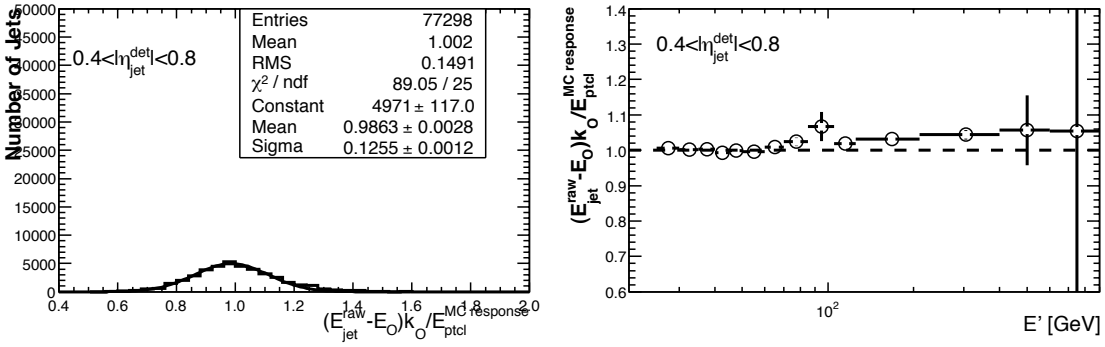

Figure B.36: MC closure test for RunIIB-1 single particle MC, $0.4 < |\eta^{det}_{jet}| < 0.8$.

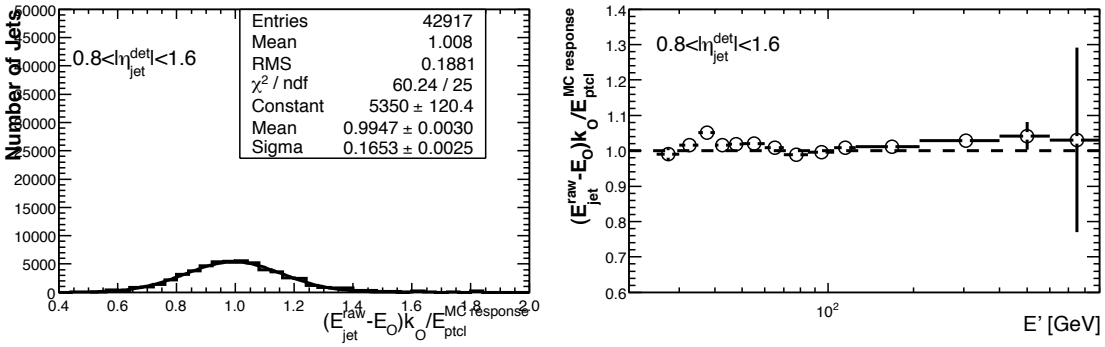

Figure B.37: MC closure test for RunIIB-1 single particle MC, $0.8 < |\eta_{jet}^{det}| < 1.6$.

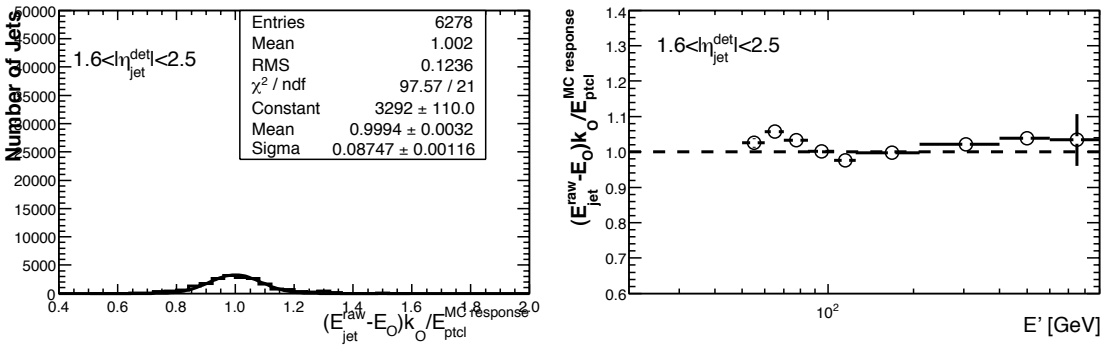

Figure B.38: MC closure test for RunIIB-1 single particle MC, $1.6 < |\eta_{jet}^{det}| < 2.5$.

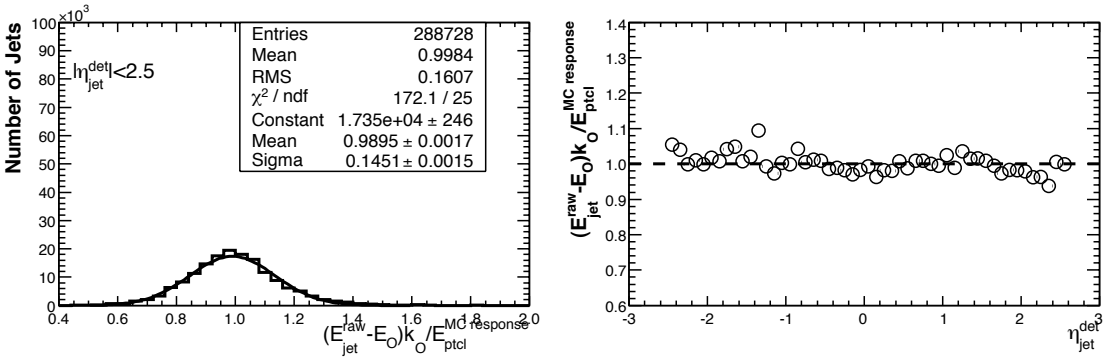

Figure B.39: MC closure test for RunIIB-1 single particle MC, $|\eta_{jet}^{det}| < 2.5$.

B.4.2 Extracting Single Particle Data Responses

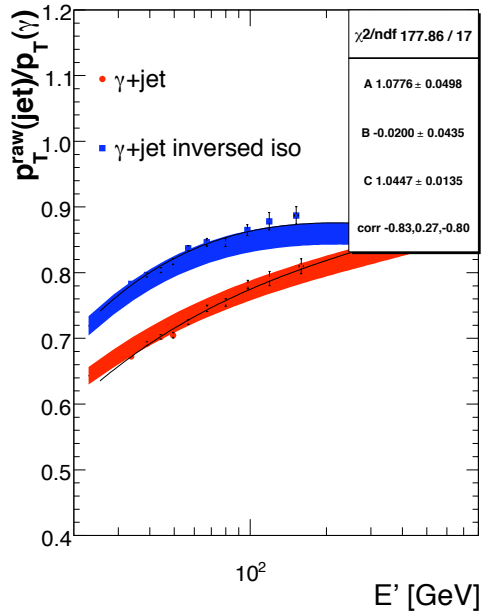

(a) $|\eta_{jet}^{det}| < 0.4$

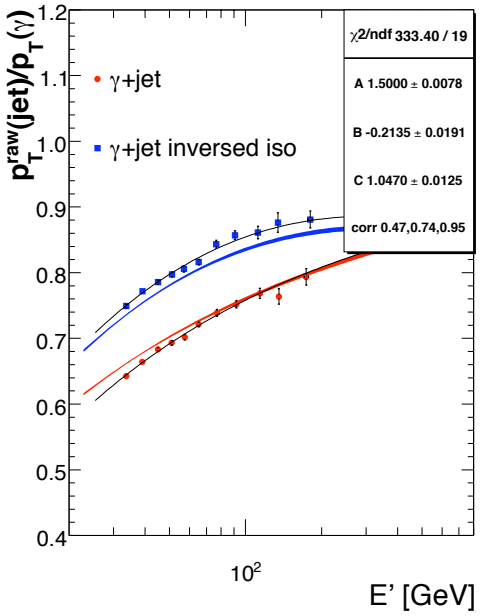

(b) $0.4 < |\eta_{jet}^{det}| < 0.8$

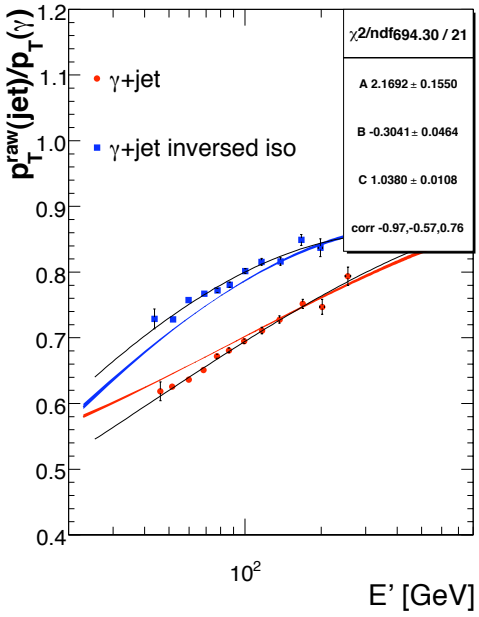

(c) $0.8 < |\eta_{jet}^{det}| < 1.6$

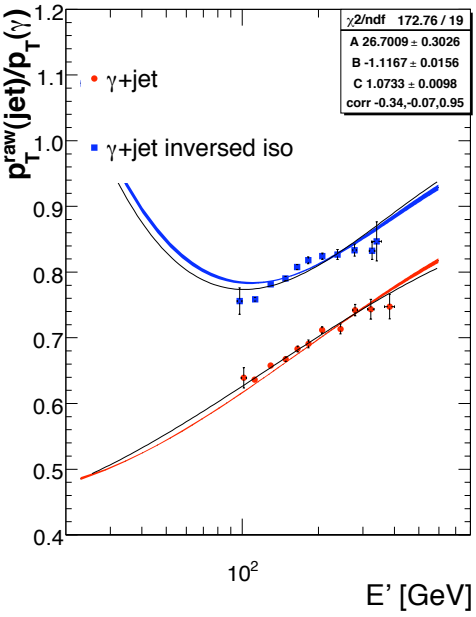

(d) $1.6 < |\eta_{jet}^{det}| < 2.5$

Figure B.40: RunIIB-1 MC tuning results determining A, B, and C.

B.4.3 Closure Test for MC Tuning to Data

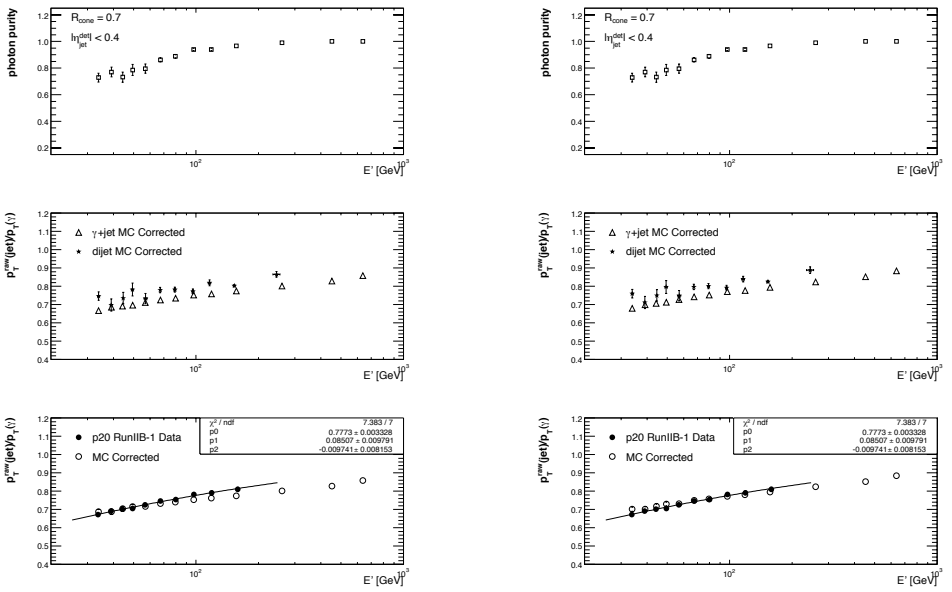

(a) Default MC, A=C=1, B=0 (b) Tuned MC

Figure B.41: RunIIB-1 closure test for tuned MC, tight photon; $|\eta_{jet}^{det}| < 0.4$.

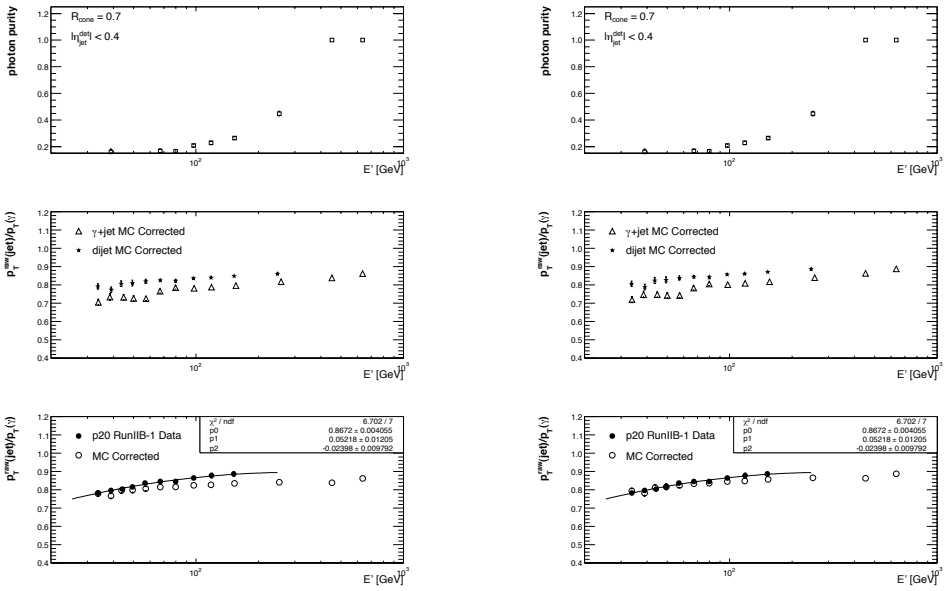

(a) Default MC, A=C=1, B=0 (b) Tuned MC

Figure B.42: RunIIB-1 closure test for tuned MC, reversed photon; $|\eta_{jet}^{det}| < 0.4$.

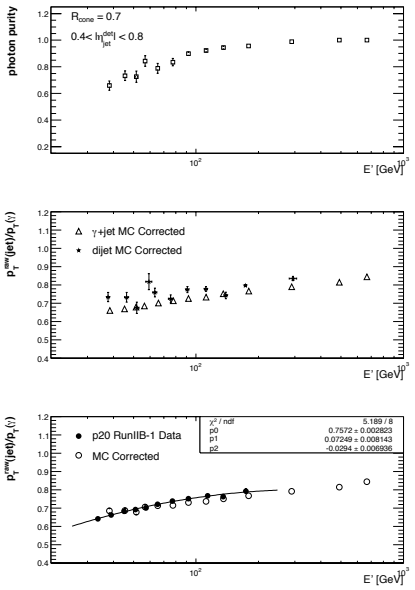

(a) Default MC, A=C=1, B=0

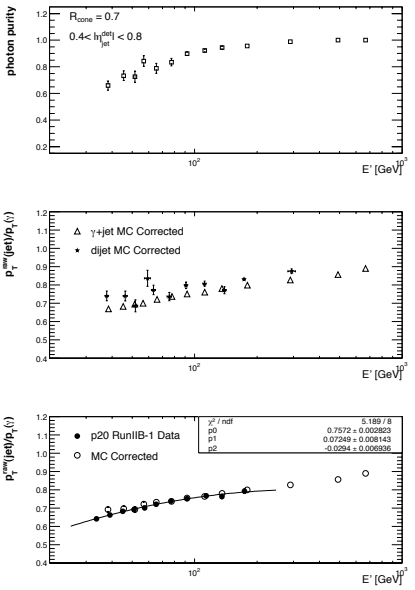

(b) Tuned MC

Figure B.43: RunIIB-1 closure test for tuned MC, tight photon; $0.4 < |\eta_{jet}^{det}| < 0.8$.

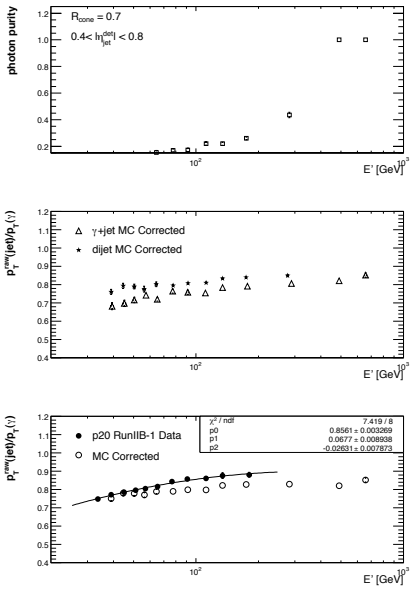

(a) Default MC, A=C=1, B=0

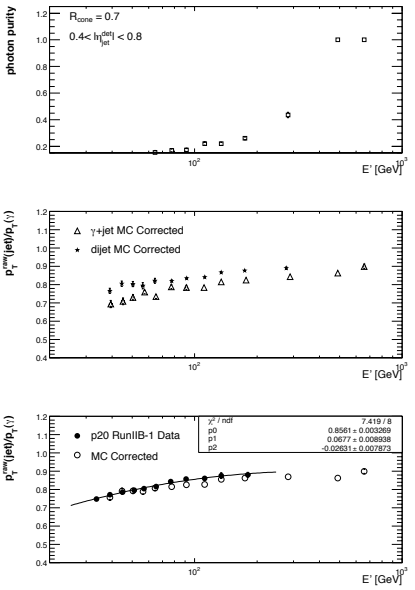

(b) Tuned MC

Figure B.44: RunIIB-1 closure test for tuned MC, reversed photon; $0.4 < |\eta_{jet}^{det}| < 0.8$.

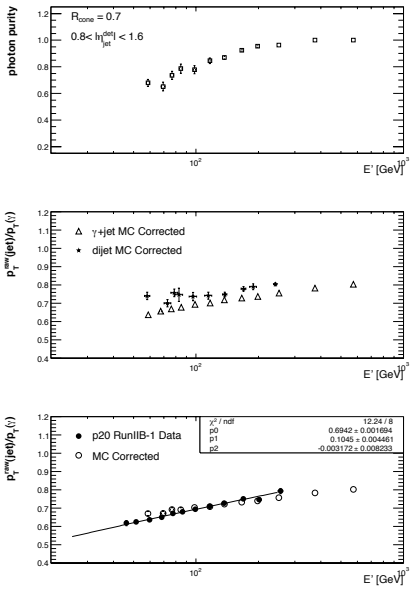

(a) Default MC, A=C=1, B=0

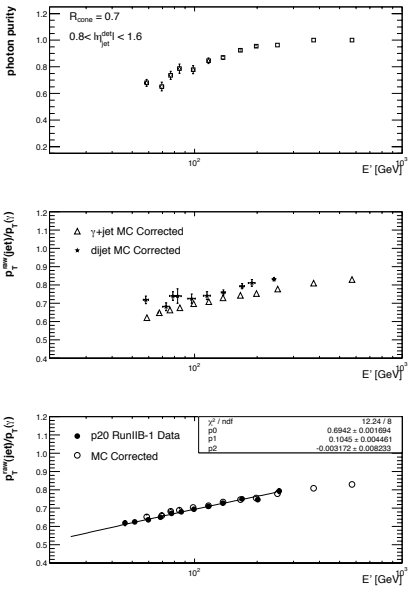

(b) Tuned MC

Figure B.45: RunIIB-1 closure test for tuned MC, tight photon; $0.8 < |\eta_{jet}^{det}| < 1.6$.

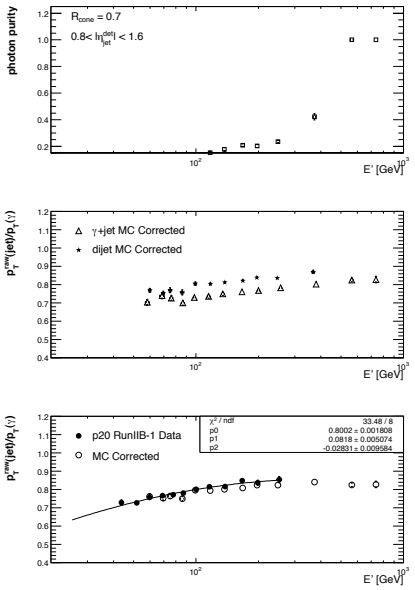

(a) Default MC, A=C=1, B=0

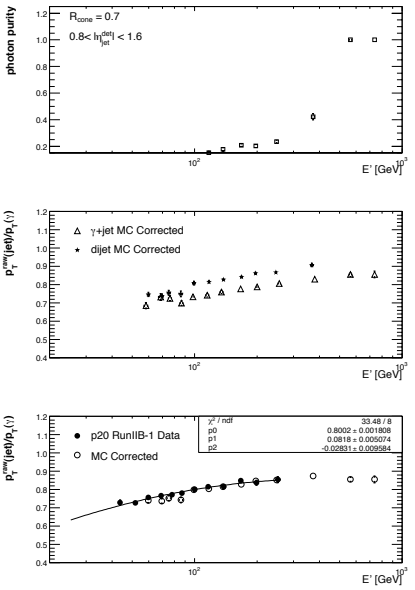

(b) Tuned MC

Figure B.46: RunIIB-1 closure test for tuned MC, reversed photon; $0.8 < |\eta_{jet}^{det}| < 1.6$.

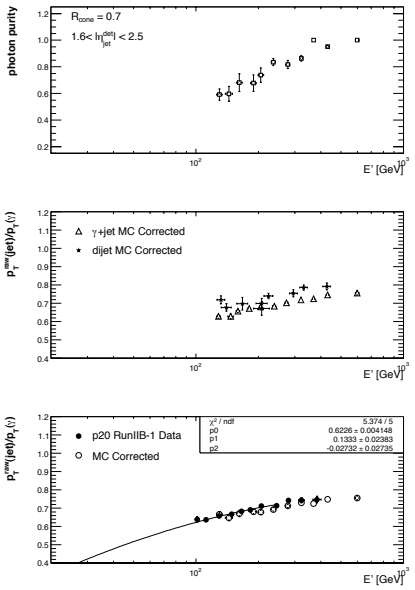

(a) Default MC, A=C=1, B=0

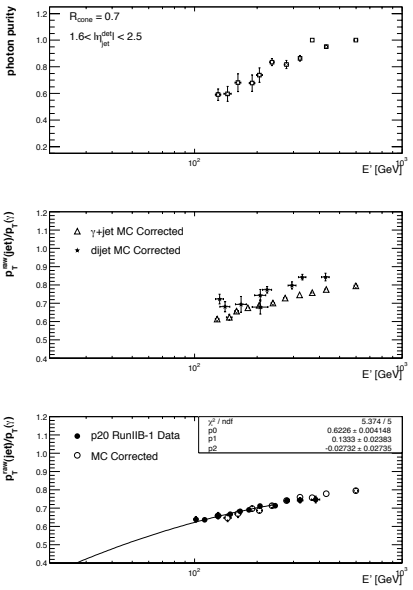

(b) Tuned MC

Figure B.47: RunIIB-1 closure test for tuned MC, tight photon; $1.6 < |\eta^{det}_{jet}| < 2.5$.

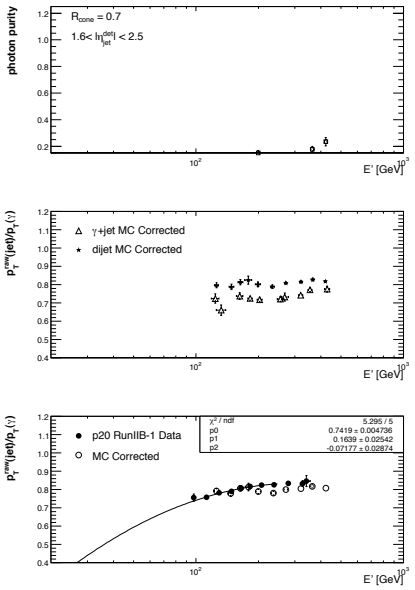

(a) Default MC, A=C=1, B=0

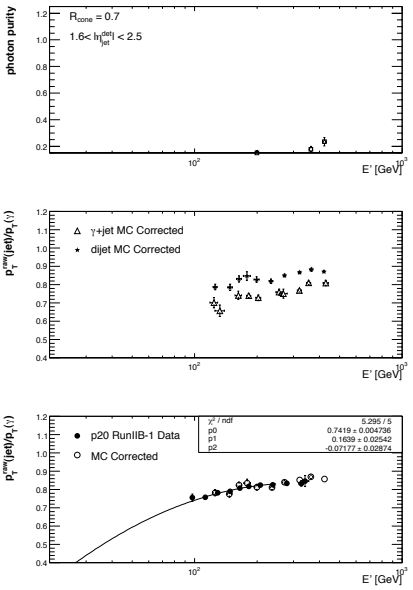

(b) Tuned MC

Figure B.48: RunIIB-1 closure test for tuned MC, reversed photon; $1.6 < |\eta^{det}_{jet}| < 2.5$.

B.5 Results for RunIIB-2

This section contains the results for RunIIB-2 data – MC closure test for the single particle responses, extraction of single particle data responses, and closure test for MC tuning to data.

B.5.1 MC Closure Test

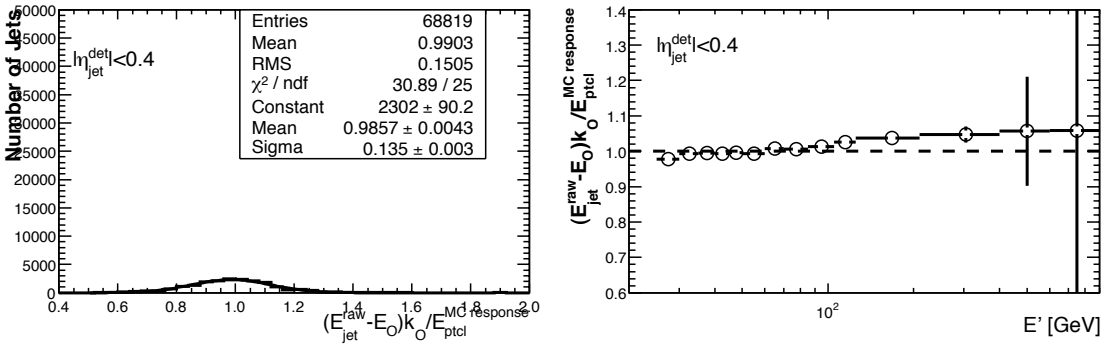

Figure B.49: MC closure test for RunIIB-2 single particle MC, $|\eta^{det}_{jet}| < 0.4$.

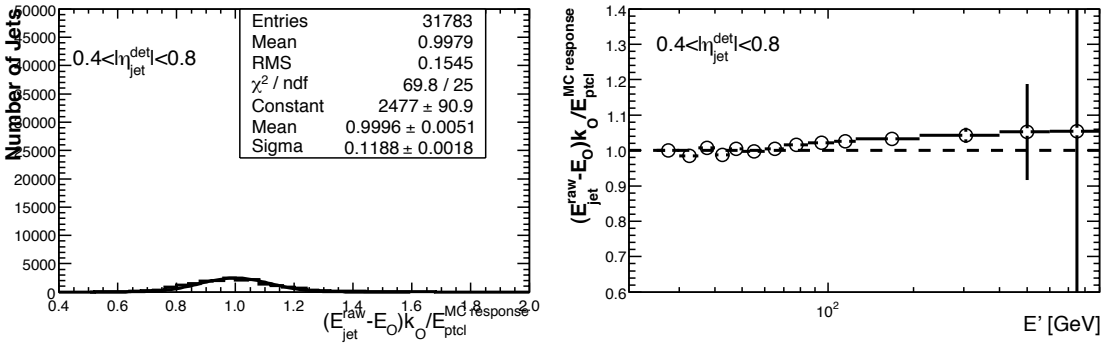

Figure B.50: MC closure test for RunIIB-2 single particle MC, $0.4 < |\eta^{det}_{jet}| < 0.8$.

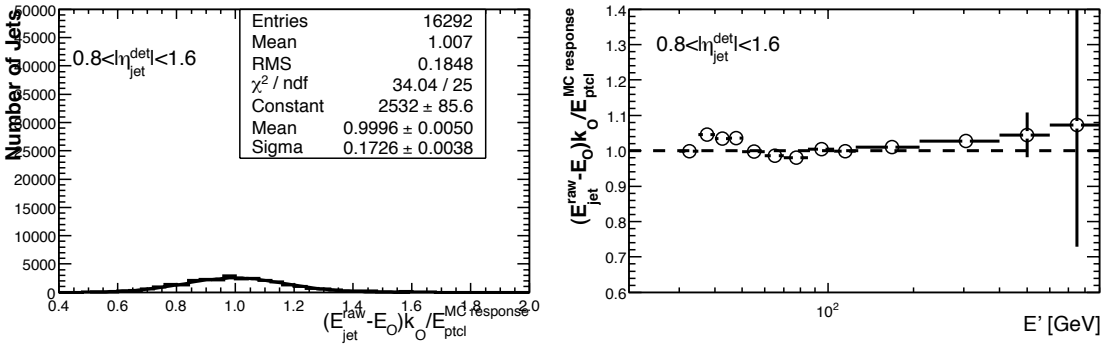

Figure B.51: MC closure test for RunIIB-2 single particle MC, $0.8 < |\eta^{det}_{jet}| < 1.6$.

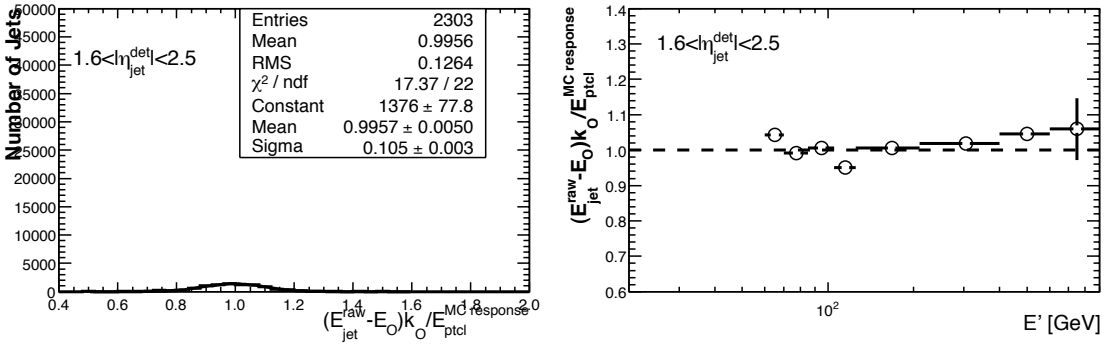

Figure B.52: MC closure test for RunIIB-2 single particle MC, $1.6 < |\eta^{det}_{jet}| < 2.5$.

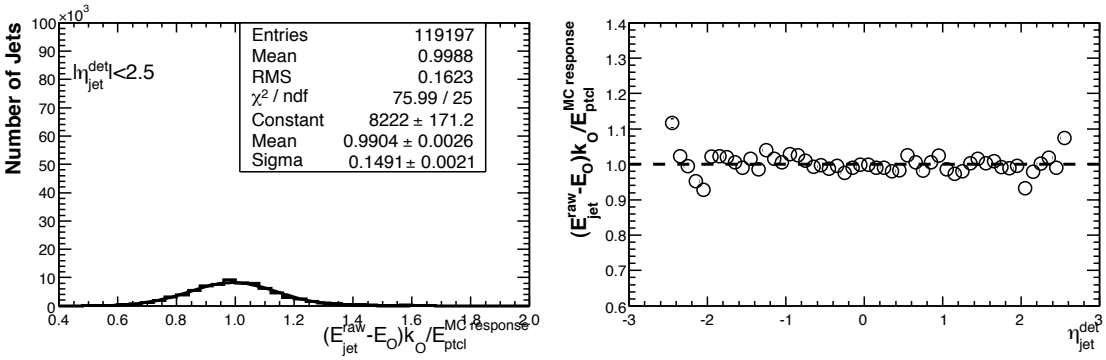

Figure B.53: MC closure test for RunIIB-2 single particle MC, $|\eta^{det}_{jet}| < 2.5$.

B.5.2 Extracting Single Particle Data Responses

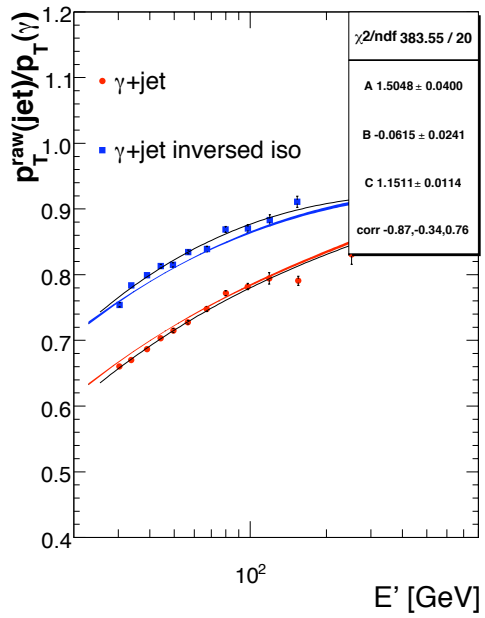

(a) $|\eta_{jet}^{det}| < 0.4$

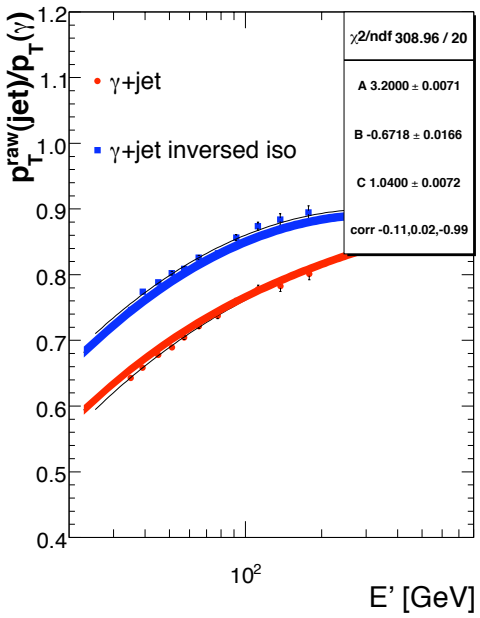

(b) $0.4 < |\eta_{jet}^{det}| < 0.8$

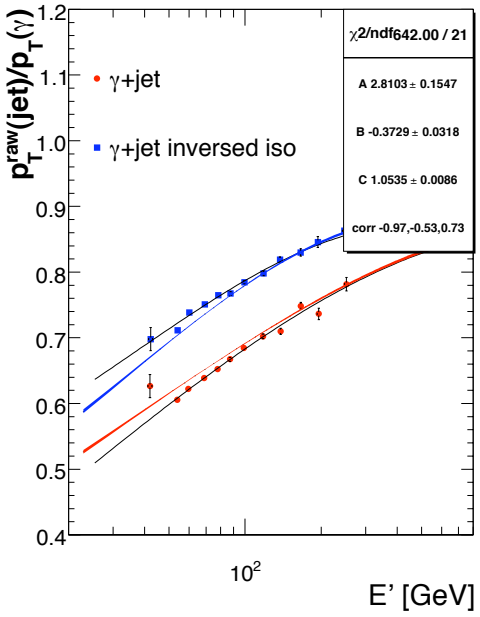

(c) $0.8 < |\eta_{jet}^{det}| < 1.6$

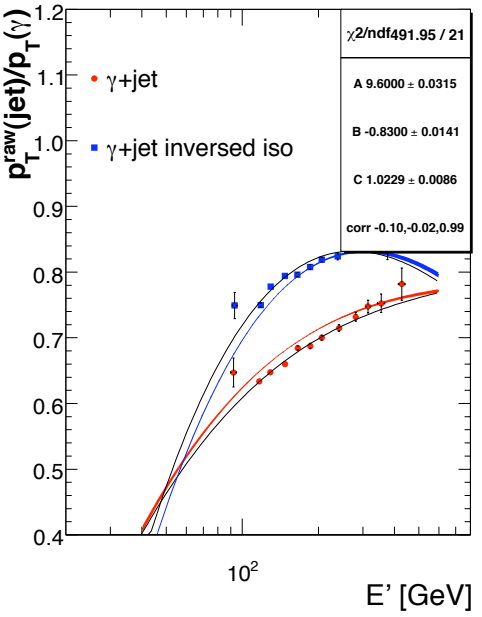

(d) $1.6 < |\eta_{jet}^{det}| < 2.5$

Figure B.54: RunIIB-2 MC tuning results determining A, B, and C.

B.5.3 Closure Test for MC Tuning to Data

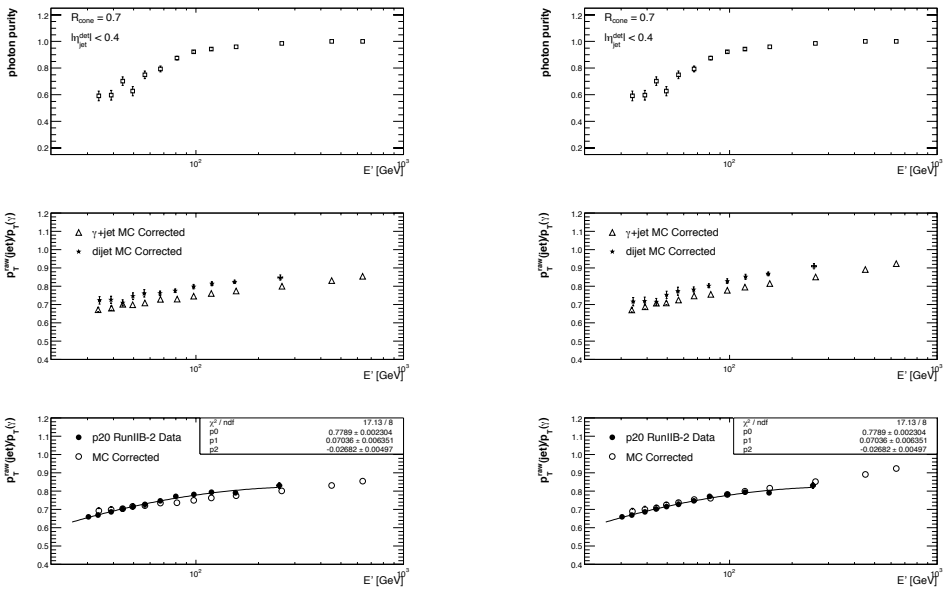

(a) Default MC, A=C=1, B=0 (b) Tuned MC

Figure B.55: RunIIB-2 closure test for tuned MC, tight photon, $|\eta_{jet}^{det}| < 0.4$.

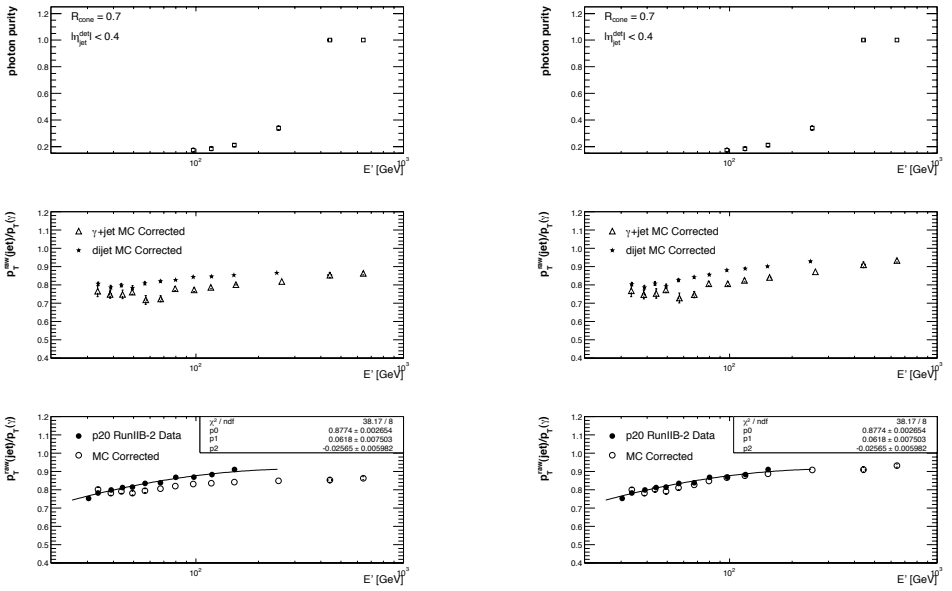

(a) Default MC, A=C=1, B=0 (b) Tuned MC

Figure B.56: RunIIB-2 closure test for tuned MC, reversed photon, $|\eta_{jet}^{det}| < 0.4$.

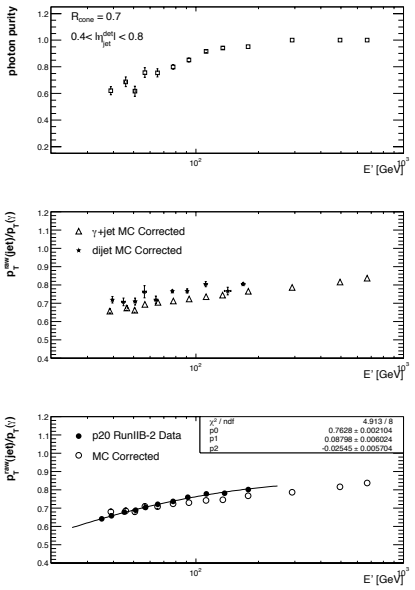

(a) Default MC, A=C=1, B=0

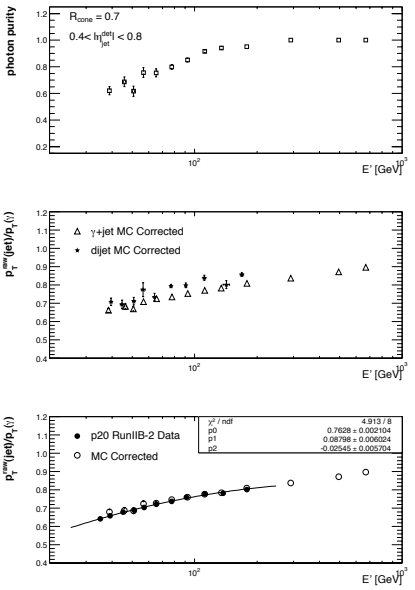

(b) Tuned MC

Figure B.57: RunIIB-2 closure test for tuned MC, tight photon, $0.4 < |\eta_{jet}^{det}| < 0.8$.

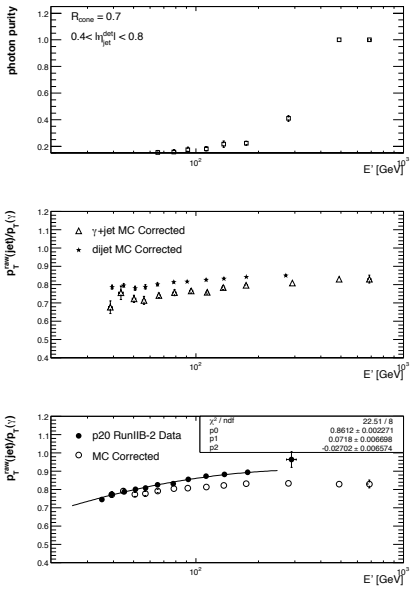

(a) Default MC, A=C=1, B=0

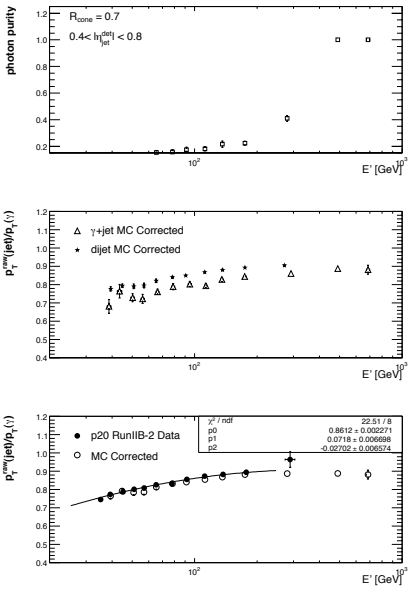

(b) Tuned MC

Figure B.58: RunIIB-2 closure test for tuned MC, reversed photon, $0.4 < |\eta_{jet}^{det}| < 0.8$.

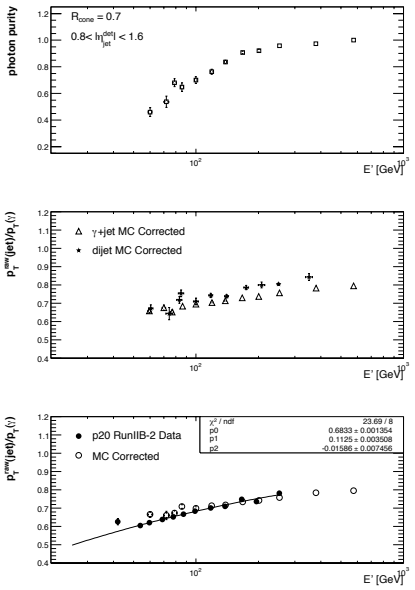

(a) Default MC, A=C=1, B=0

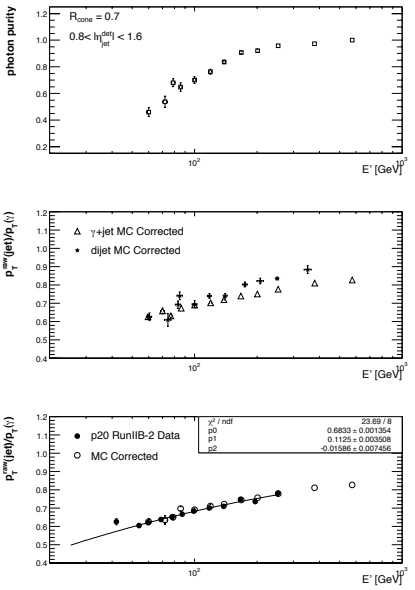

(b) Tuned MC

Figure B.59: RunIIB-2 closure test for tuned MC, tight photon, $0.8 < |\eta_{jet}^{det}| < 1.6$.

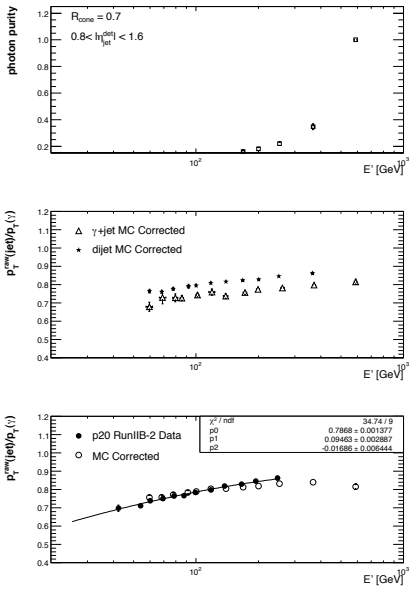

(a) Default MC, A=C=1, B=0

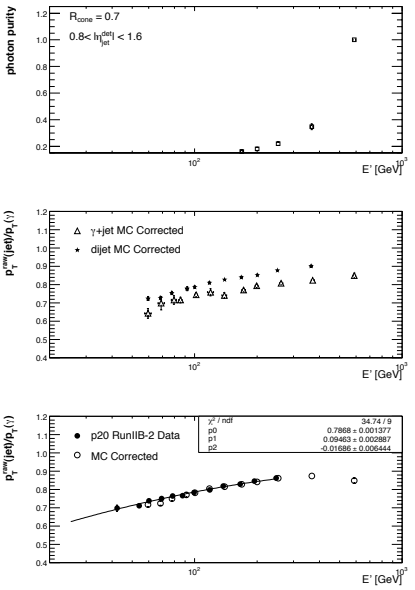

(b) Tuned MC

Figure B.60: RunIIB-2 closure test for tuned MC, reversed photon, $0.8 < |\eta_{jet}^{det}| < 1.6$.

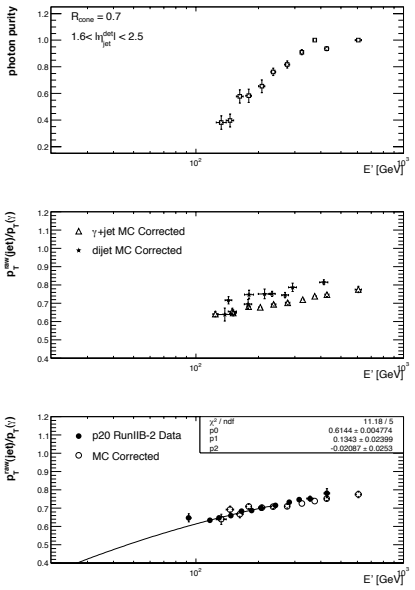

(a) Default MC, A=C=1, B=0

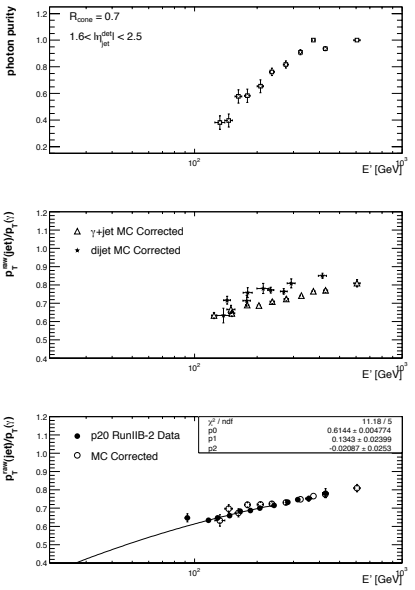

(b) Tuned MC

Figure B.61: RunIIB-2 closure test for tuned MC, tight photon, $1.6 < |\eta_{jet}^{det}| < 2.5$.

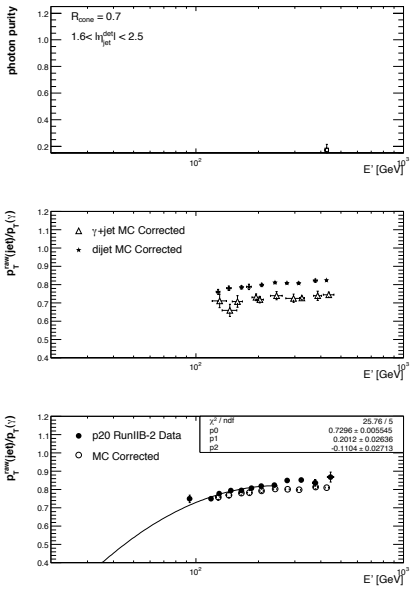

(a) Default MC, A=C=1, B=0

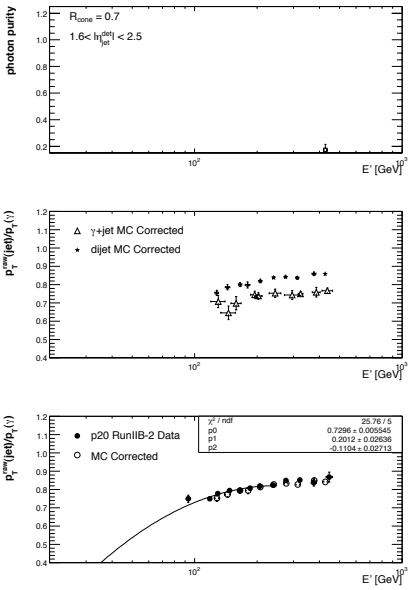

(b) Tuned MC

Figure B.62: RunIIB-2 closure test for tuned MC, reversed photon, $1.6 < |\eta_{jet}^{det}| < 2.5$.

APPENDIX C

TRIGGER TURNON STUDIES

C.1 Trigger Turnon Curves: Why and How

In the process of data taking (see last section in Chapter 4) many different physics objects are formed, including jets. DØ has seven different single jet triggers that fire on jets: JT8, JT15, JT25, JT45, JT65, JT95, and JT125, where the number is the minimum transverse momentum on which the triggers fire. For this analysis only JT45, JT65, JT95, and JT125 (and indirectly JT25) are used. In order to have the most accurate analysis, it needs to be determined when these triggers are nearly 100% (99% for this analysis) efficient.

In this analysis two different quantities are studied: normalized differential distributions of event shapes and average event shapes. The first plots $\frac{1}{\sigma}\frac{d\sigma}{dX}$ vs X (X being the event shape) in four different H_T regions, associated with the above-mentioned jet triggers: JT45, JT65, JT95, and JT125. Before choosing these regions, the 99% efficient point needs to be obtained. The second plots $\overline{X}$ vs H_T, where the plot is subdivided into four different parts, each part being associated with one of the above-mentioned jet triggers: JT45, JT65, JT95, and JT125. Before the subdivisions are determined, the 99% efficient point needs to be found.

To determine the H_T value at which the 99% point occurs, the plots of N vs H_T need to be obtained for JT25, JT45, JT65, JT95, and JT125. For this analysis the range for H_T, when determining the 99% point, was set at 80 GeV - 1000 GeV with a bin size of 10 GeV. These plots can then be used to find the cross section plots $\frac{d\sigma}{dH_T}$ vs H_T by scaling each bin of N vs H_T by $\frac{1}{L\epsilon * dH_T}$, where L is the luminosity for the jet trigger, ϵ is the vertex efficieny for each jet trigger, and dH_T is the width of the bin.

The trigger efficiency for a particular single jet trigger as a function of H_T is obtained by comparing it to the lower threshold trigger which is assumed to be fully efficient – e.g. $\frac{K_{JT65}}{K_{JT45}}$, where $K = \frac{d\sigma}{dH_T}$. This method works because the JT8 trigger is shown to be fully efficient by studying an event sample which was obtained independently using a muon trigger [25]. After this is known, the ratio of cross sections can be used to bootstrap all of the other efficiencies. An efficiency found by using ratios of cross sections is called the relative efficiency. Trigger turnon values for the four triggers that are used for this analysis are found for two-jet and three-jet events separately.

C.2 Finding The 99% Efficiency Value Using Steffensen's Method

Once the trigger turnon plots are found they need to be fitted with the following function:

$$F(p) = 0.5 * \left[1 + Erf\left(\frac{p-a}{b + c * log(p)}\right)\right], \tag{3.1}$$

where $p = \frac{H_T}{1GeV}$; a, b, and c are the fit parameters; and Erf is the error function. The H_T values are those at the bin centers. Once these parameters are known, to find the H_T that gives 99% efficiency let $F(p) = H$, where $H = 0.99$ in this analysis. This gives

$$\begin{aligned} H &= 0.5 * \left[1 + Erf\left(\frac{p-a}{b + c * log(p)}\right)\right] \\ 2 * H - 1 &= Erf\left(\frac{p-a}{b + c * log(p)}\right) \\ Erf^{-1}(2 * H - 1) &= \frac{p-a}{b + c * log(p)} \\ p &= a + M * [b + c * log(p)], \end{aligned} \tag{3.2}$$

where Erf^{-1} is the inverse error function; $M = Erf^{-1}(2 * H - 1)$; and the last equation is the one that needs to be solved to find the value of $p = \frac{H_T}{1GeV}$ that gives 99% efficiency.

Steffensen's method [18] is a way of numerically solving an equation of the form $p = g(p)$, for this analysis $g(p) = a + M * [b + c * log(p)]$. It generates a sequence whose members get progressively closer to the solution of the equation $p = g(p)$:

$$
\begin{array}{ccc}
 & p_0^{(0)} & \\
p_1^{(0)} = g(p_0^{(0)}) \quad p_2^{(0)} = g(p_1^{(0)}) & p_0^{(1)} = p_0^{(0)} - \dfrac{(p_1^{(0)} - p_0^{(0)})^2}{p_2^{(0)} - 2 * p_1^{(0)} + p_0^{(0)}} & \\
p_1^{(1)} = g(p_0^{(1)}) \quad p_2^{(1)} = g(p_1^{(1)}) & p_0^{(2)} = p_0^{(1)} - \dfrac{(p_1^{(1)} - p_0^{(1)})^2}{p_2^{(1)} - 2 * p_1^{(1)} + p_0^{(1)}} & \\
 & \vdots & \\
p_1^{(i)} = g(p_0^{(i)}) \quad p_2^{(i)} = g(p_1^{(i)}) & p_0^{(i+1)} = p_0^{(i)} - \dfrac{(p_1^{(i)} - p_0^{(i)})^2}{p_2^{(i)} - 2 * p_1^{(i)} + p_0^{(i)}} . &
\end{array}
\tag{3.3}
$$

The initial approximation to the solution is $p_0^{(0)}$, and the successively closer answers are the $p_0^{(i+1)}$. This sequence is continued until an answer is found that is close enough to the correct answer. Closeness is determined by checking to see if $|p_0^{(i+1)} - p_0^{(i)}|$ is less than some tolerance. The algoirthm for Steffensen's method takes an initial guess as to what the solution is and then interates until a solution is found: each iteration is a line in the above-listed sequence. The C++ code used to implement Steffensen's method is given by

```
double htCut;
double minEff = 0.99;
double solErf = TMath::ErfInverse(minEff/0.5 - 1.0);

double p0 = Eff->GetBinCenter(binLoc5+2); // initial guess
double p1, p2;
```

```
double TOL = TMath::Power(10,-4);
int MAX_ITER = 20;
bool metTOL = false;

a = modErfFit->GetParameter("a");
b = modErfFit->GetParameter("b");
c = modErfFit->GetParameter("c");

cout << endl << "Starting Steffensen's Method" << endl;

int numIter = 0;
while (!metTOL) {
        if (numIter > MAX_ITER) {break;}
        p1 = a + solErf*(b + c*TMath::Log(p0));
        p2 = a + solErf*(b + c*TMath::Log(p1));
        htCut = p0 - TMath::Power(p1-p0,2)/(p2-2*p1+p0);

        if (TMath::Abs(htCut-p0) < TOL) {metTOL = true;}
        else {numIter++; p0 = htCut;}
}

cout << "Ending Steffensen's Method" << endl;

htCut = TMath::Ceil(htCut);
cout << "final htCut = " << htCut << endl << endl;
```

C.3 Trigger Turnon Curves: Results

The plots for the trigger turnon study are given in Figure C.1 for two-jet events and Figure C.2 for three-jet events. These plots include the portion of the efficiency plots where the turnon occurs, the line that describes the fit to the data, horizontal lines for 0.98 and 1.0, a vertical line at the location of the 99% point, and the value of the 99% point.

The values used in this analysis for the start of each trigger region are required to be greater than or equal to both the 2-jet turnon and the 3-jet turnon. Table C.1 gives a summary of the H_T values (in GeV) for: the 99% turnon values for the 2-jet

and 3-jet events and the values used for both the normalized differential distributions and the average event shapes.

Table C.1: Summary of the H_T values (in GeV) at 99% efficiency for 2-jet and 3-jet events. The last two columns give the actual values used for the normalized differential distributions and for the average event shapes.

Trigger	2-jet turnon	3-jet turnon	Norm. Diff	Ave. ES
JT45	175	177	180	180
JT65	245	267	300	310
JT95	350	358	450	415
JT125	440	455	675	530

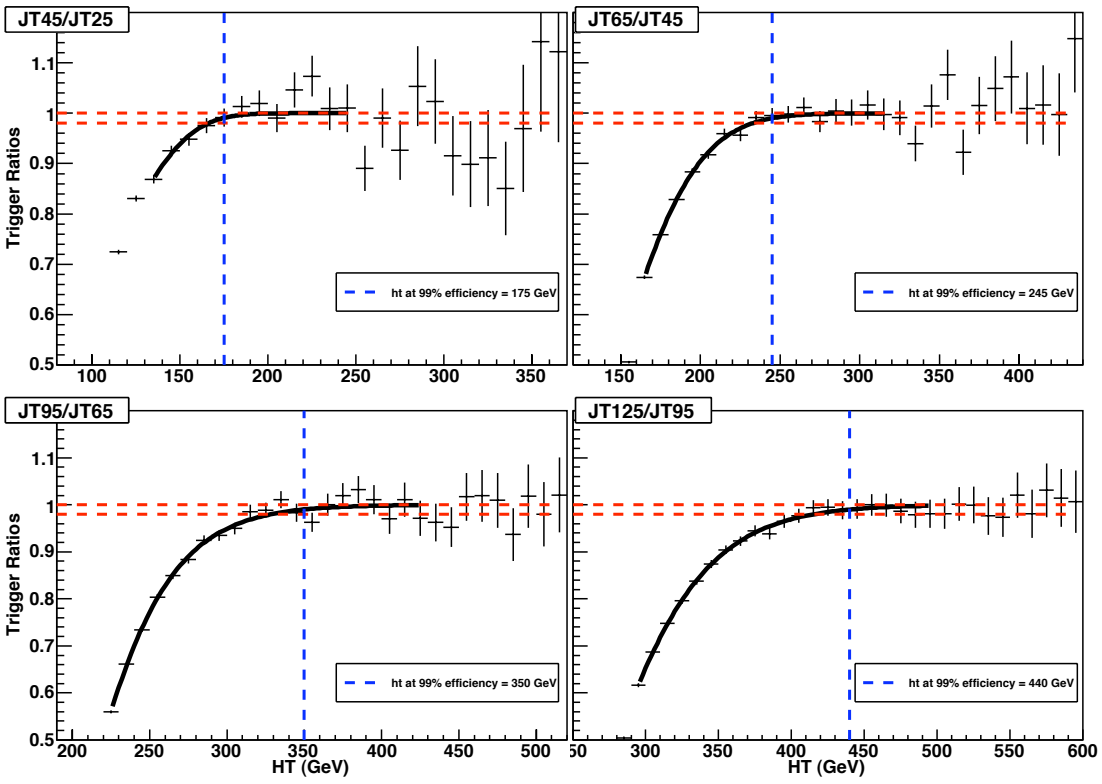

Figure C.1: Trigger turnon curves fitted to determine the 99% efficiency value, for 2 jet events

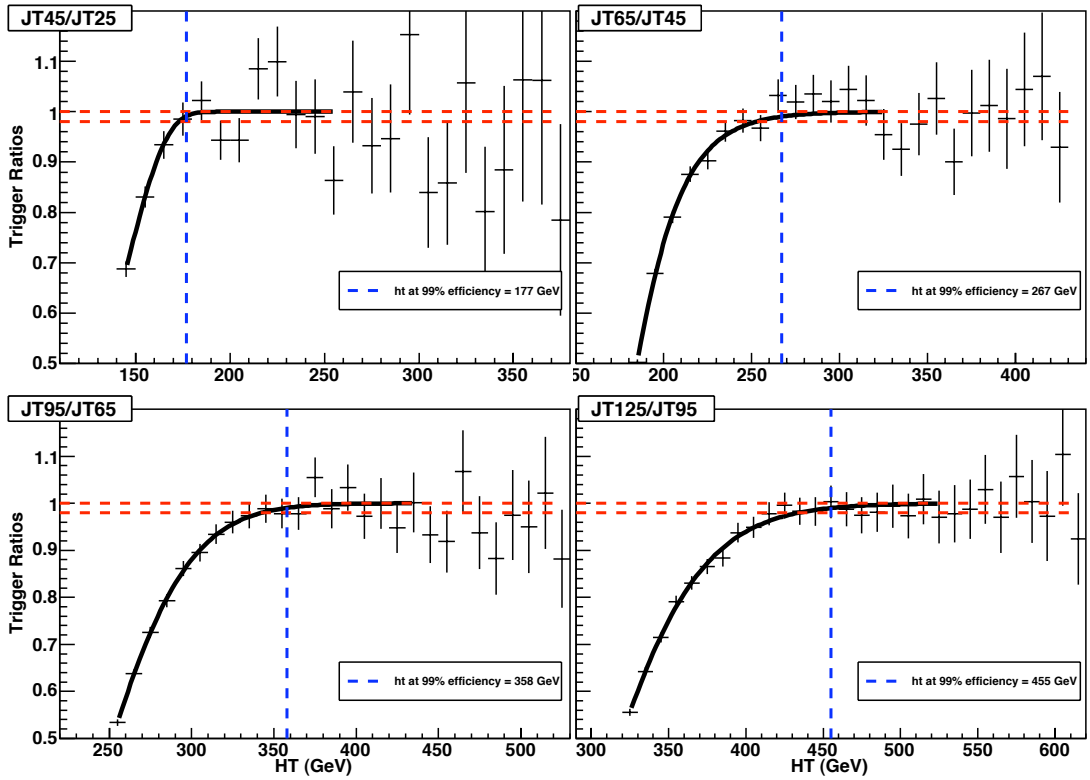

Figure C.2: Trigger turnon curves fitted to determine the 99% efficiency value, for 3 jet events

APPENDIX D

CONTROL PLOTS

When events from Monte Carlo (MC) simulation, whether SHERPA or PYTHIA, have been reweighted to describe the primary experimental observable, checks have to be made to see that the reweighted MC describes other quantities reasonably accurately. The MC used for the event shape analysis is the one that was reweighted to describe the ratio of 3-jet cross section to 2-jet cross section ($R_{3/2}$). Control plots were generated for a minimum tranverse momentum of 30 GeV ($p_{Tmin} = 30$ GeV).

There are 15 quantities for which control plots were made. Table D.1 lists the 15 quantities and whether they were for 2-jet events, 3-jet events, or both. The control plots were done for the four jet triggers – JT45, JT65, JT95, and JT125. From looking at the results of the control plots, it can be seen that SHERPA in general gives a better description than PYTHIA.

Table D.1: Control plot quantities.

Quantity	Description	2 or 3 jets
z_{vtx}	z component of the vertex	2, 3
y_1	rapidity of the leading jet	2, 3
y_2	rapidity of the second jet	2, 3
$\frac{y_3 y_2}{\lvert y_2 \rvert}$	signed rapidity of the third jet	2, 3
$\frac{y_4 y_3}{\lvert y_3 \rvert}$	signed rapidity of the fourth jet	3
p_{T2}	transverse momentum of the second jet	2, 3
p_{T3}	transverse momentum of the third jet	2, 3
p_{T4}	transverse momentum of the fourth jet	3
$\frac{p_{T3}}{p_{T2}}$	ratio of third to second jet momentum	2
$\frac{p_{T4}}{p_{T3}}$	ratio of fourth to third jet momentum	3
η_{det1}	detector pseudorapidity for leading jet	2, 3
η_{det2}	detector pseudorapidity for second jet	2, 3
η_{det3}	detector pseudorapidity for third jet	3
$\Delta\phi_{12}$	difference in ϕ for leading and second jets	2
ΔR_{min}	min. dist. $y - \phi$ space for first three jets	3

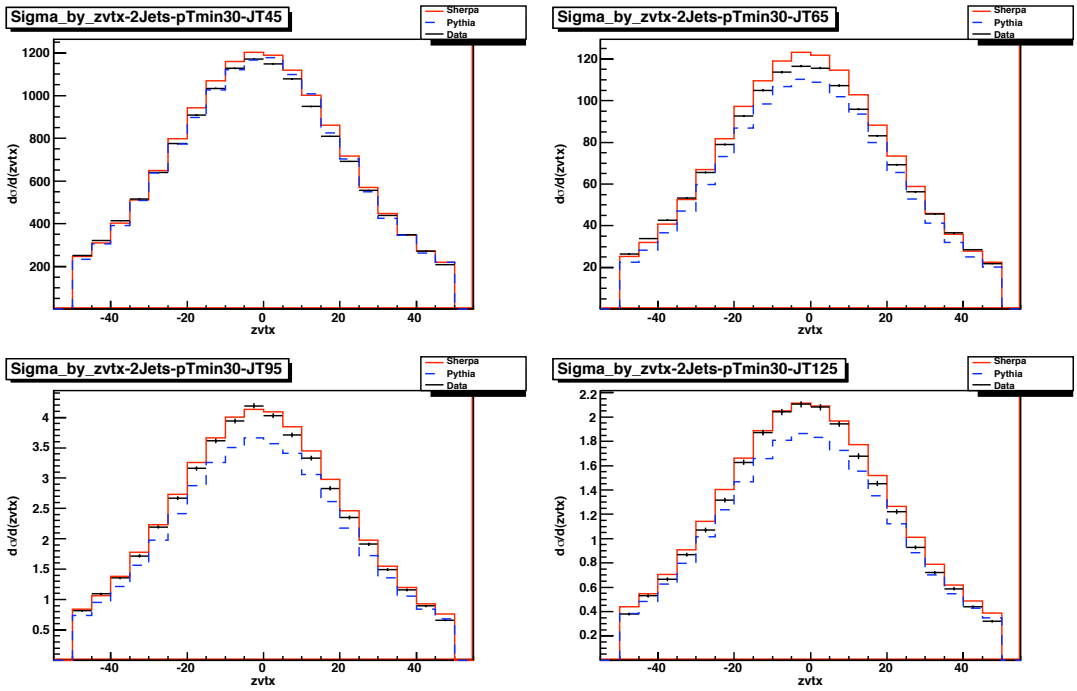

Figure D.1: The z vertex, 2 jet event.

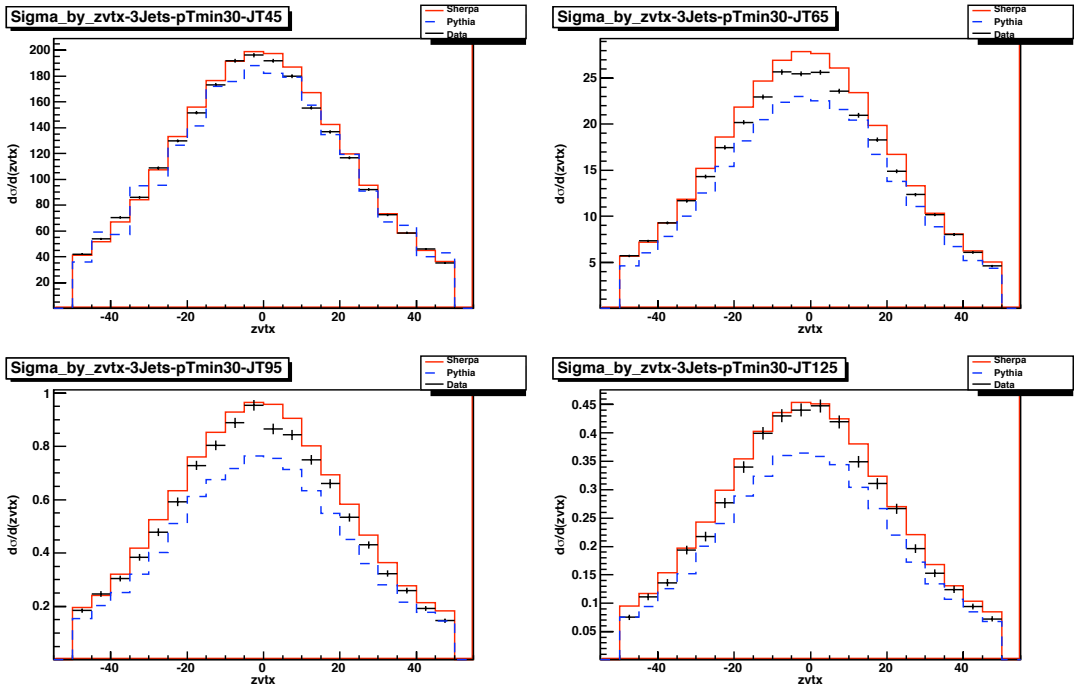

Figure D.2: The z vertex, 3 jet event.

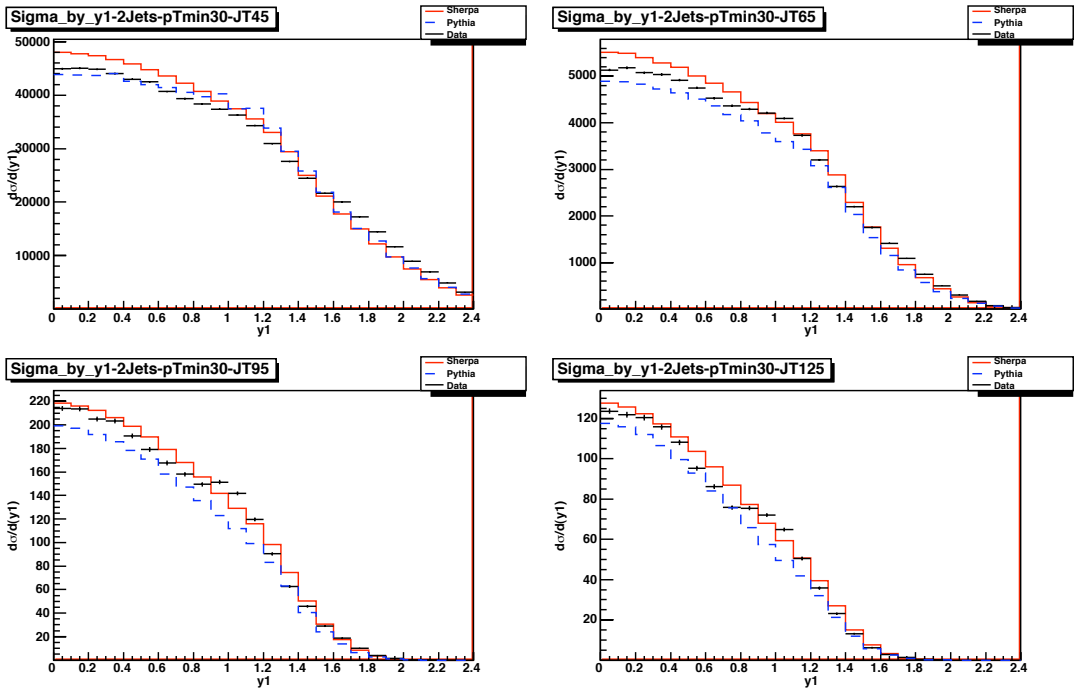

Figure D.3: The leading jet rapidity, 2 jet event.

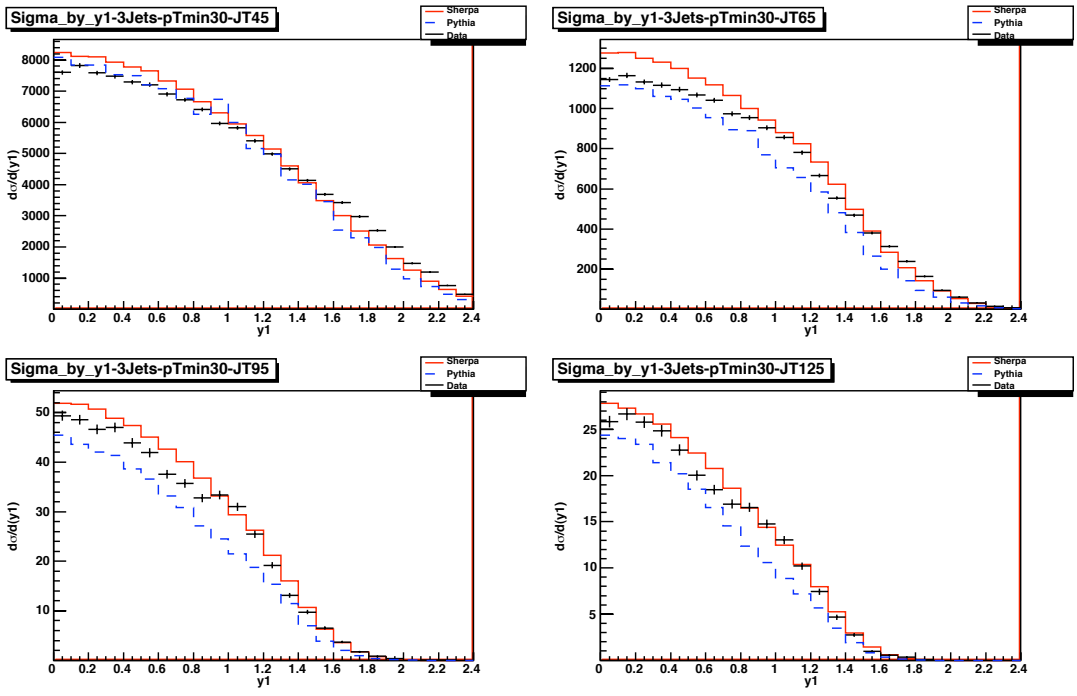

Figure D.4: The leading jet rapidity, 3 jet event.

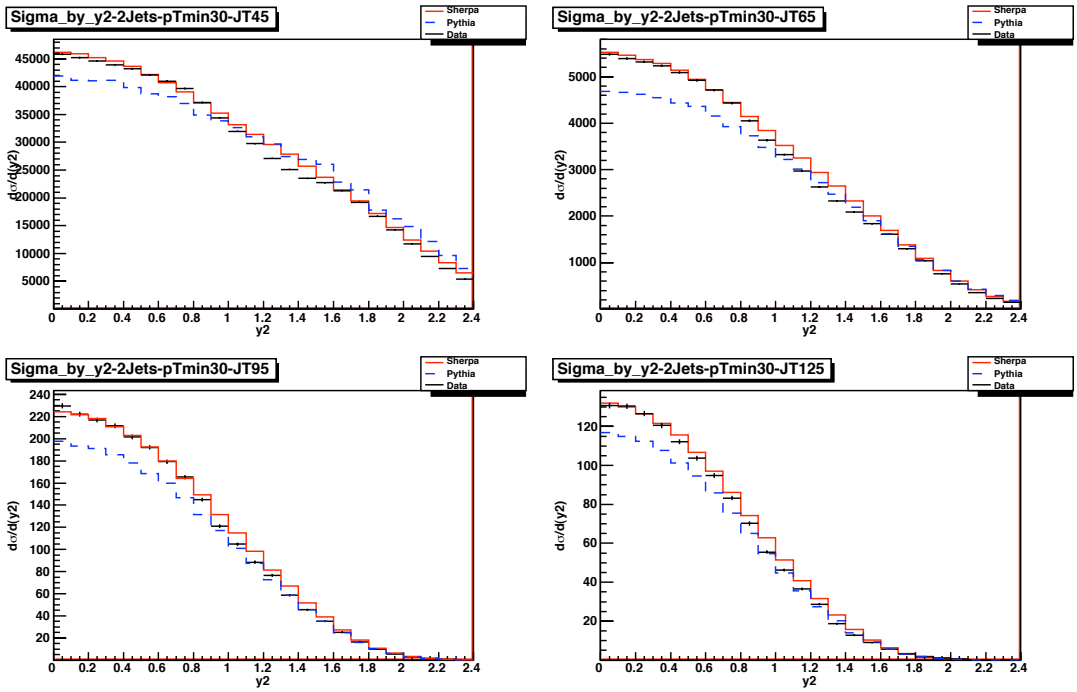

Figure D.5: The second jet rapidity, 2 jet event.

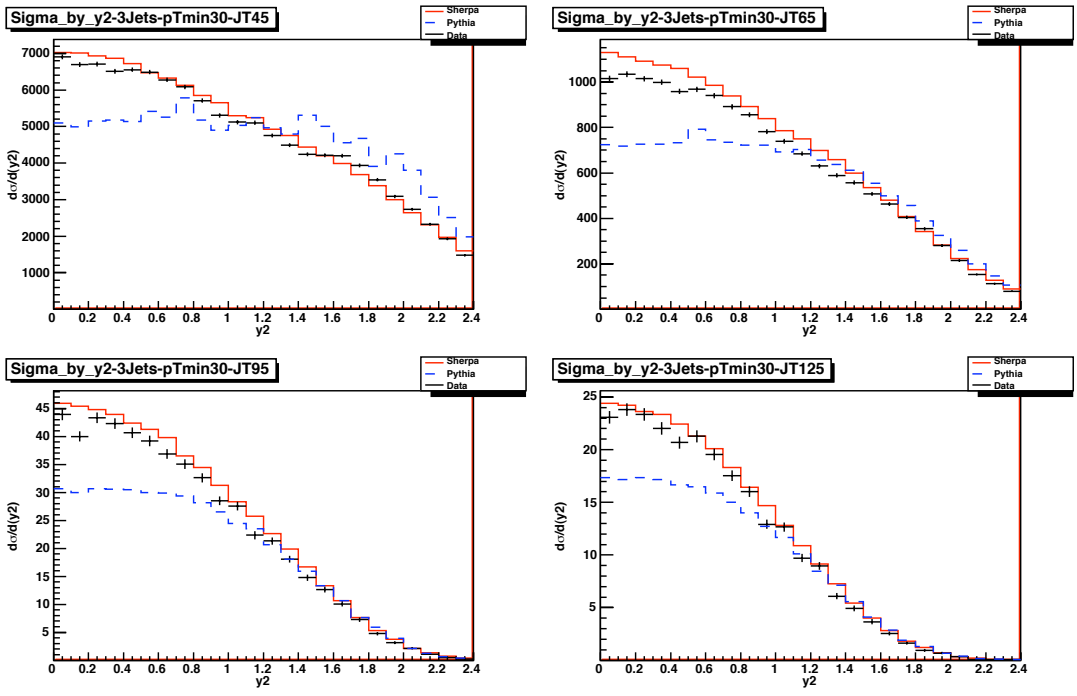

Figure D.6: The second jet rapidity, 3 jet event.

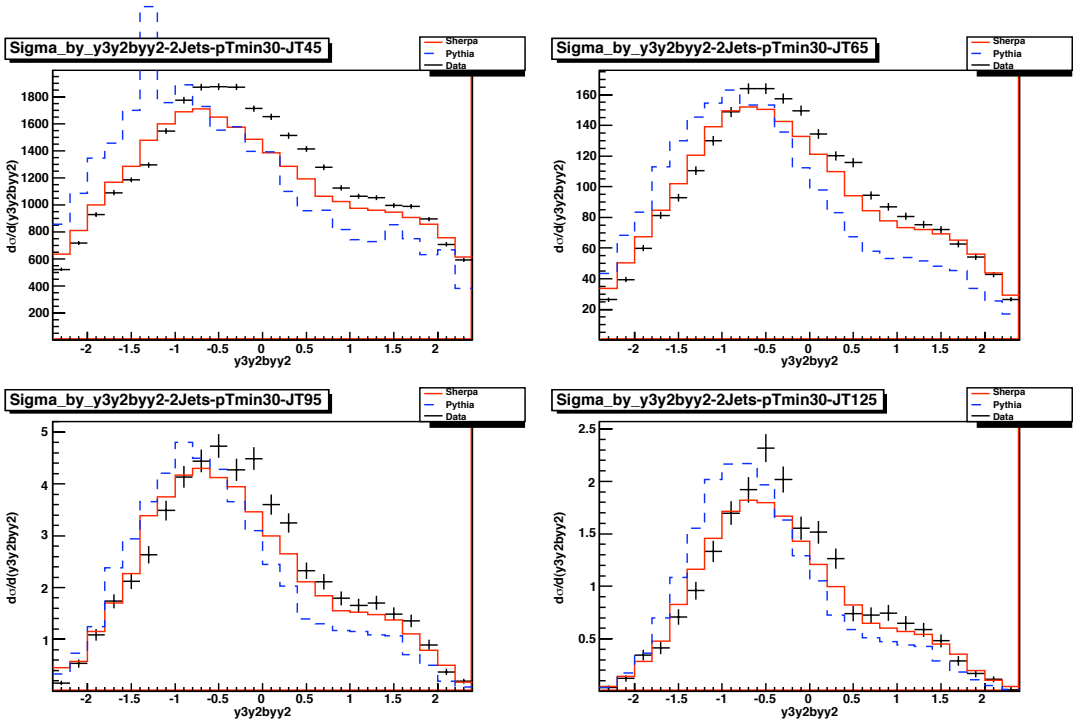

Figure D.7: The third jet signed rapidity, 2 jet event.

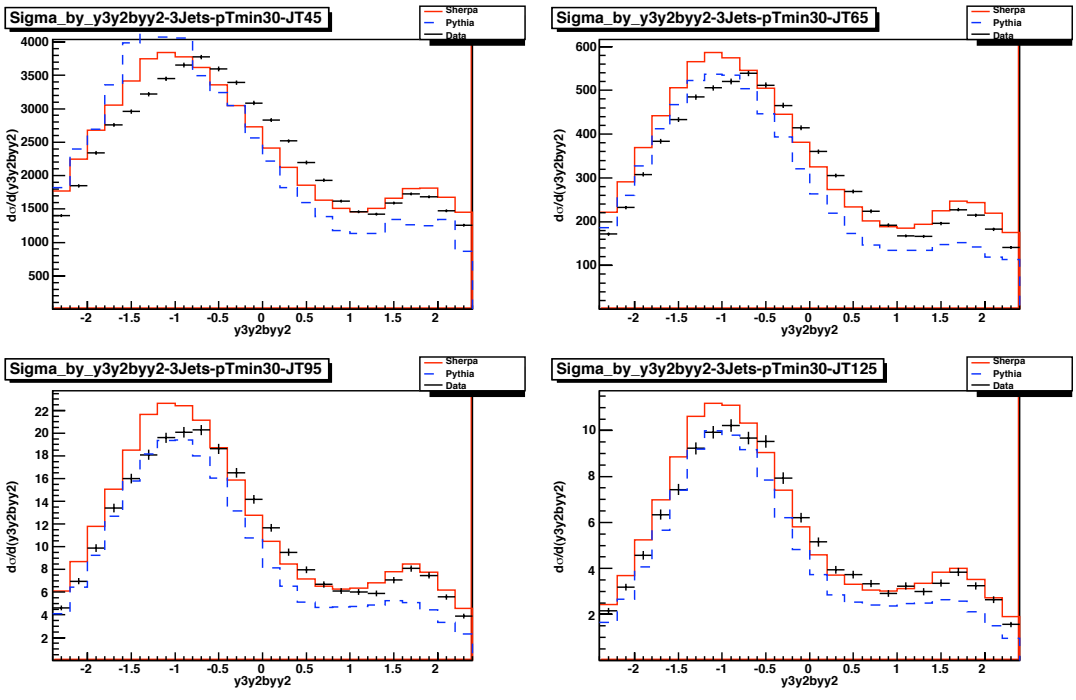

Figure D.8: The third jet signed rapidity, 3 jet event.

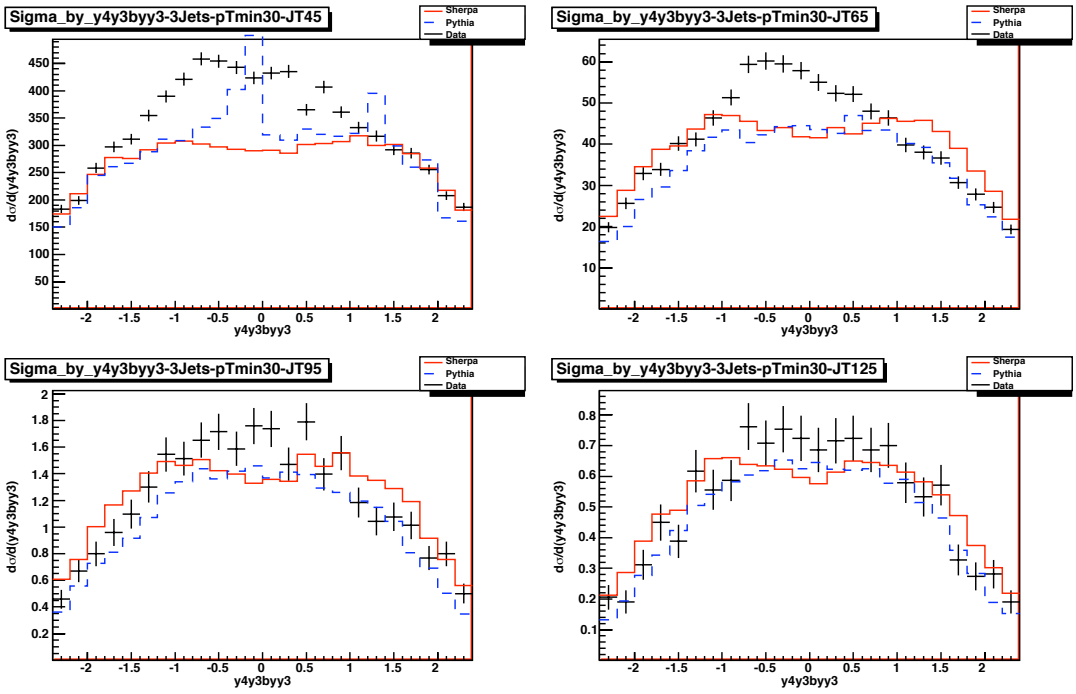

Figure D.9: The fourth jet signed rapidity, 3 jet event.

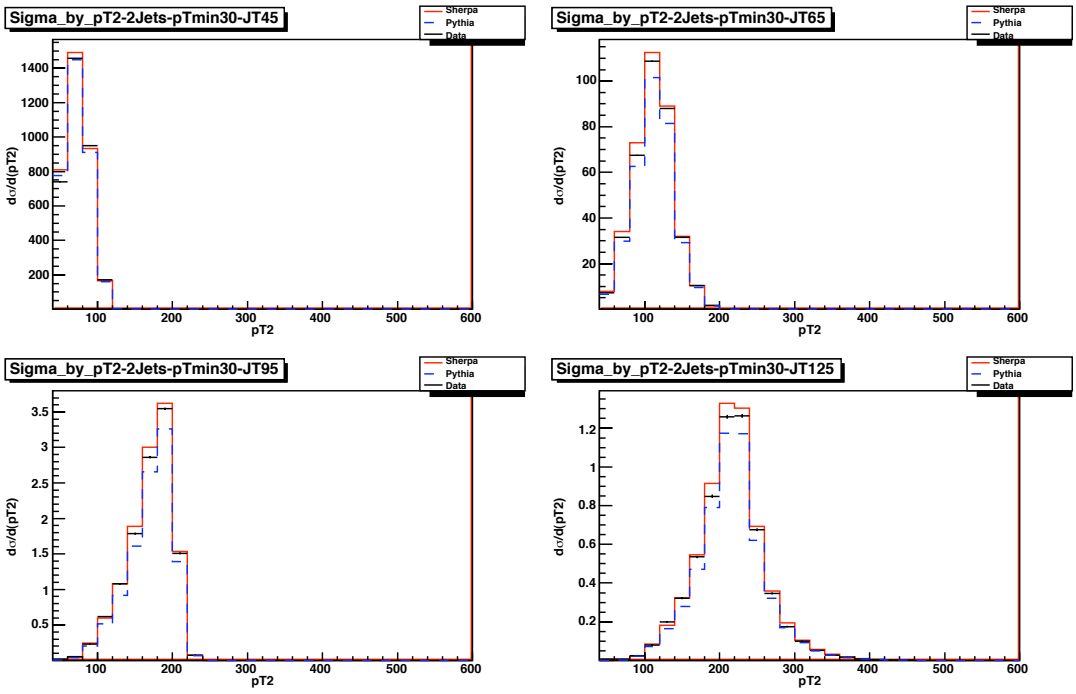

Figure D.10: The second jet transverse momentum, 2 jet event.

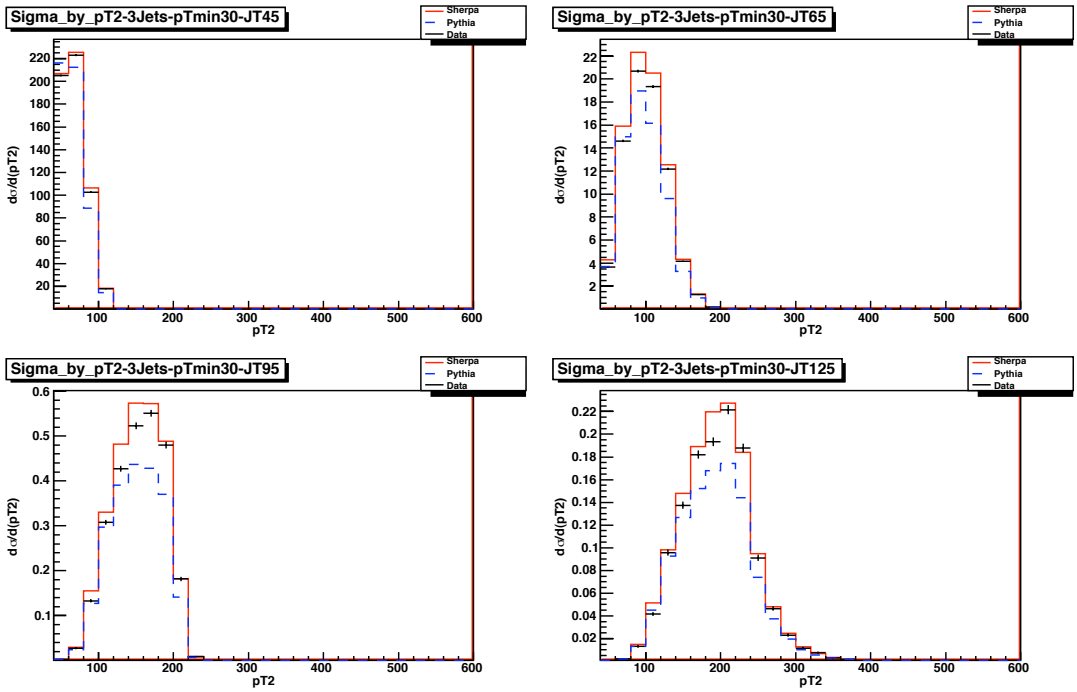

Figure D.11: The second jet transverse momentum, 3 jet event.

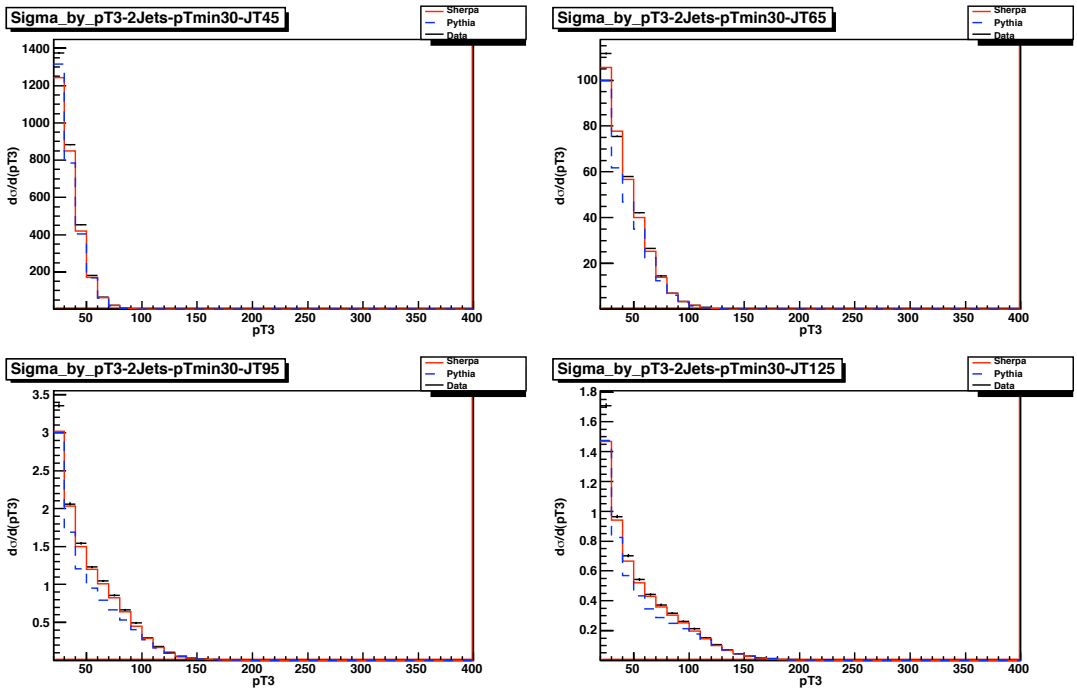

Figure D.12: The third jet transverse momentum, 2 jet event.

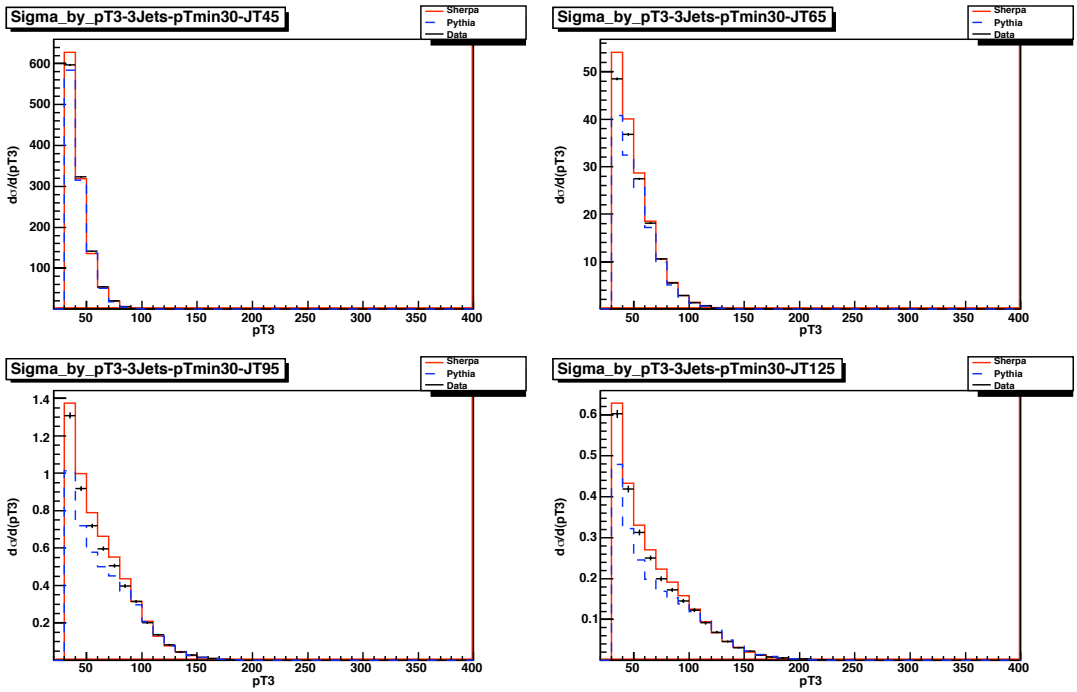

Figure D.13: The third jet transverse momentum, 3 jet event.

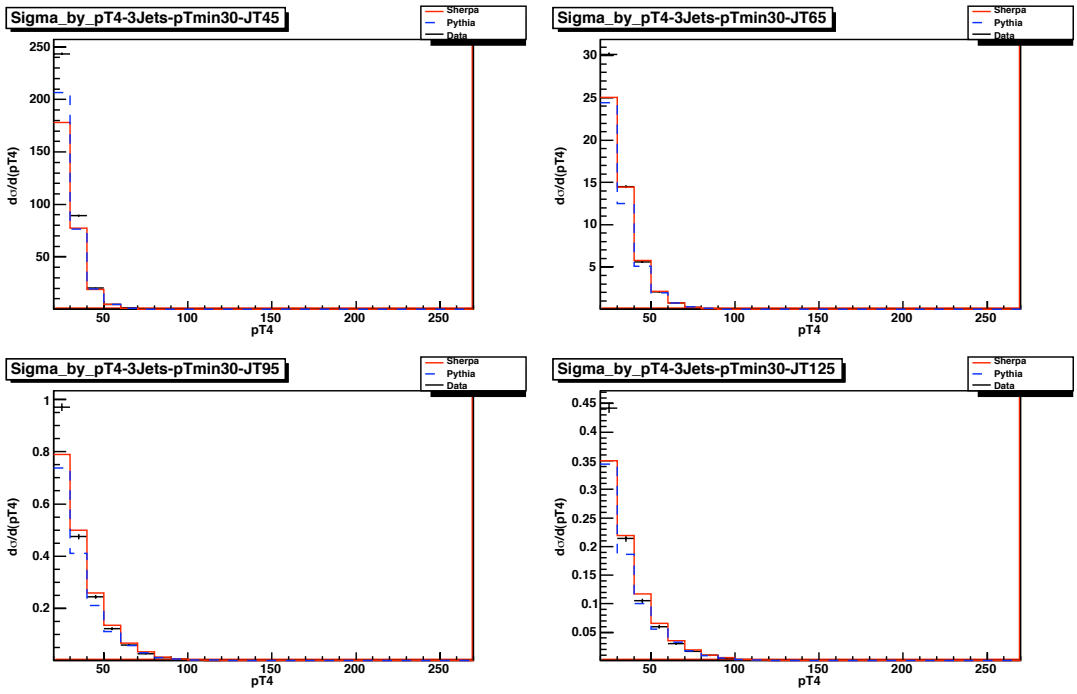

Figure D.14: The fourth jet transverse momentum, 3 jet event.

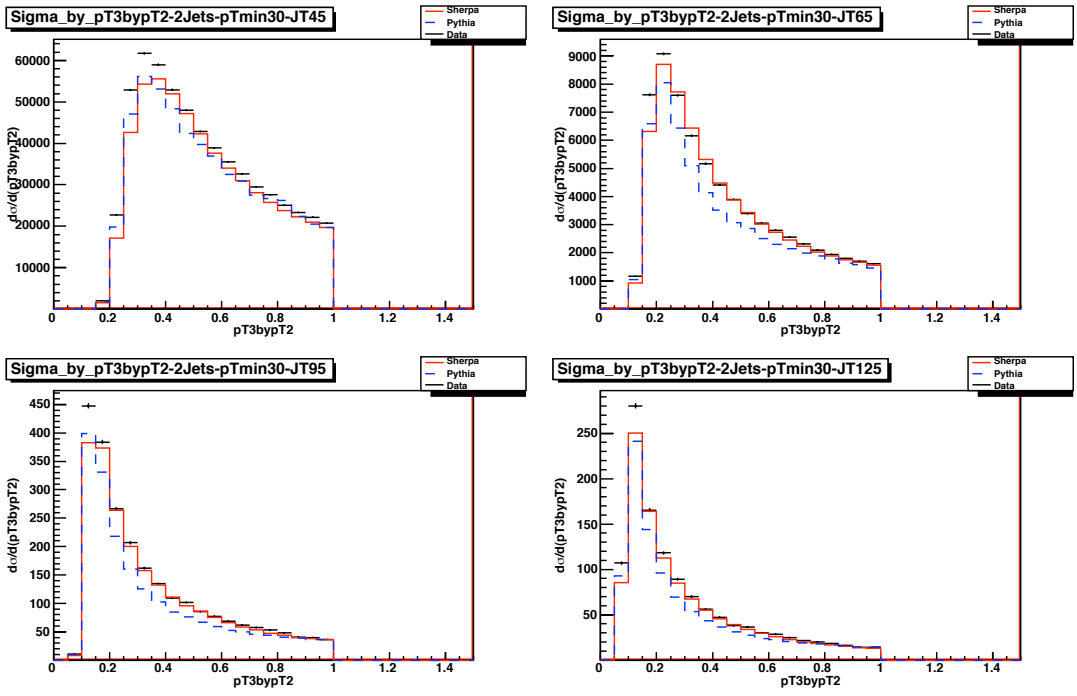

Figure D.15: The ratio of the transverse momenta of the 3^{rd} and 2^{nd} jets, 2 jet event.

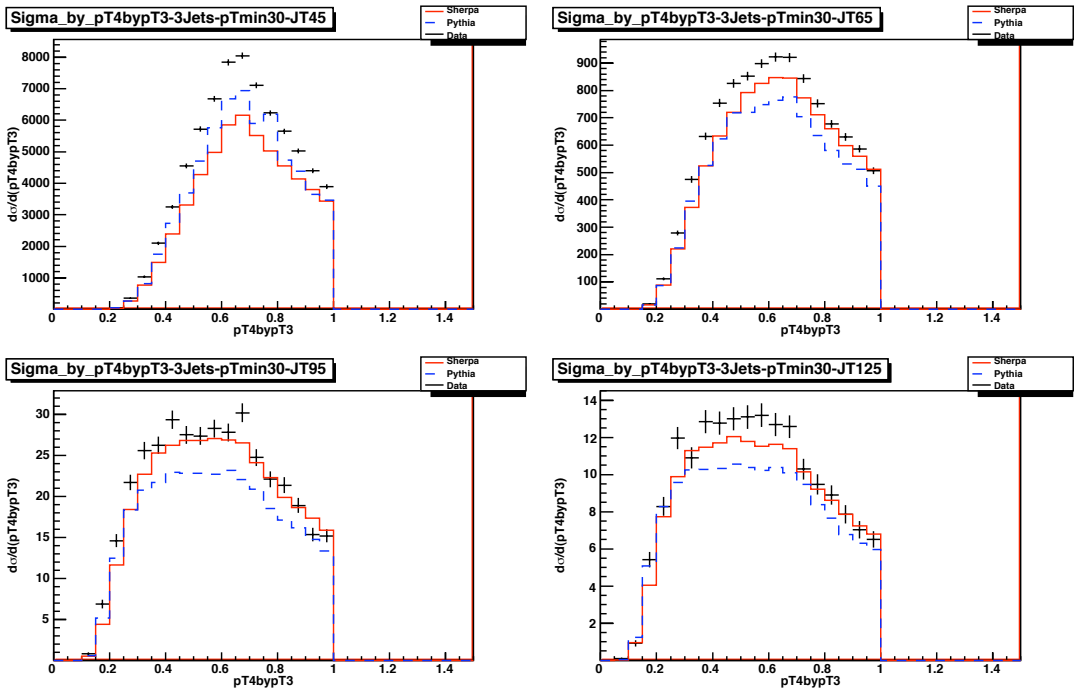

Figure D.16: The ratio of the transverse momenta of the 4^{th} and 3^{rd} jets, 3 jet event.

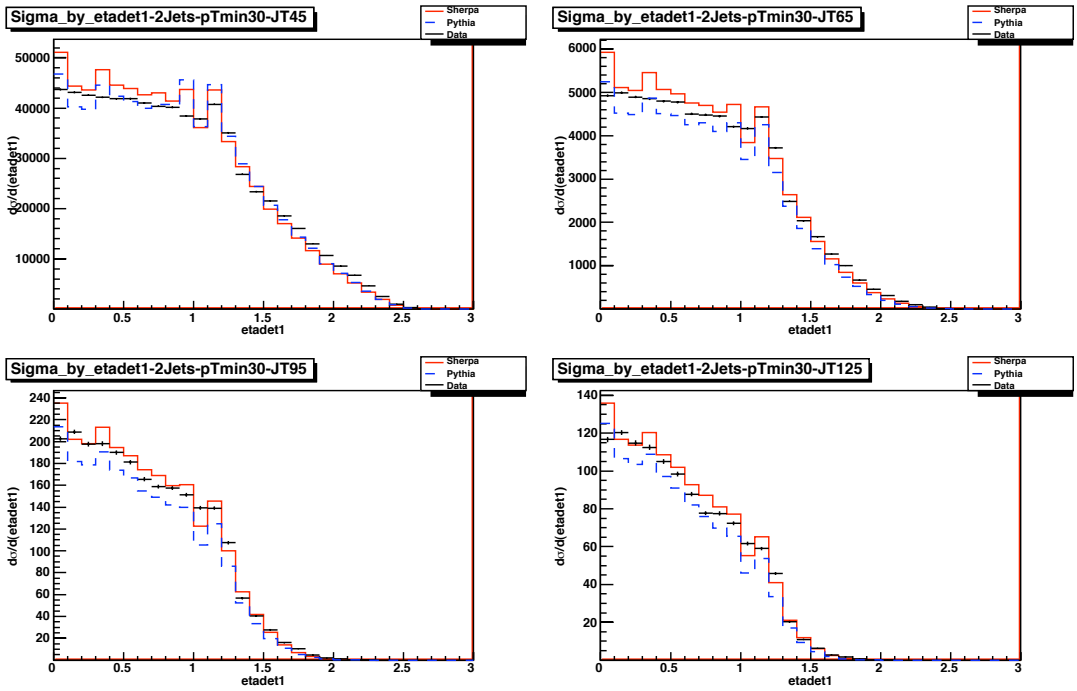

Figure D.17: The leading jet detector pseudorapidity, 2 jet event.

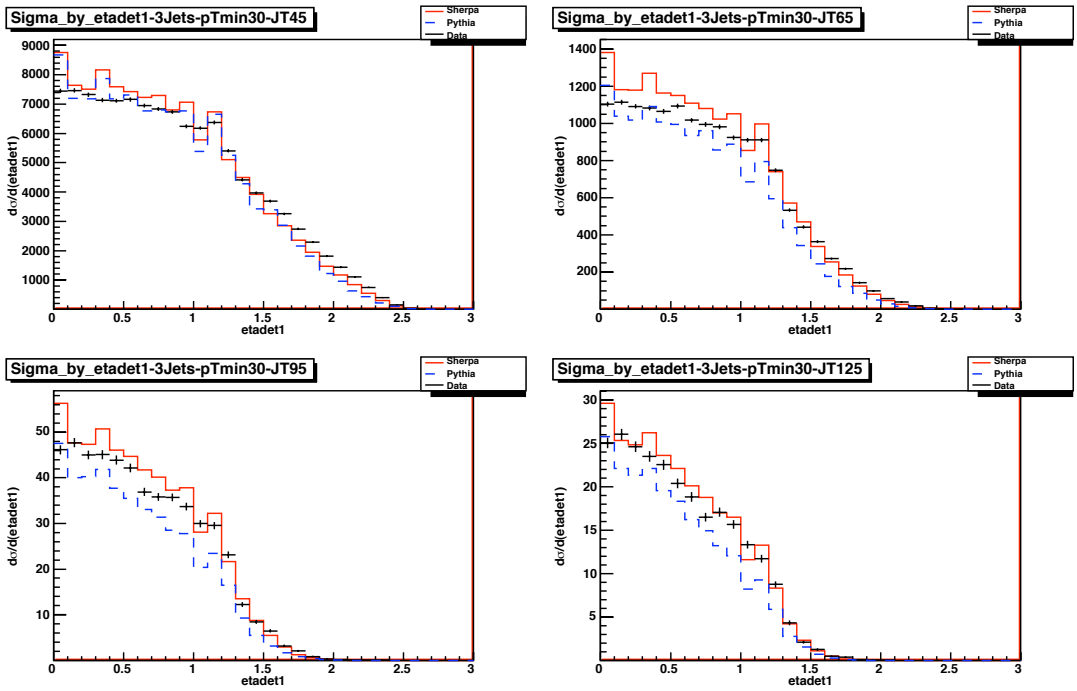

Figure D.18: The leading jet detector pseudorapidity, 3 jet event.

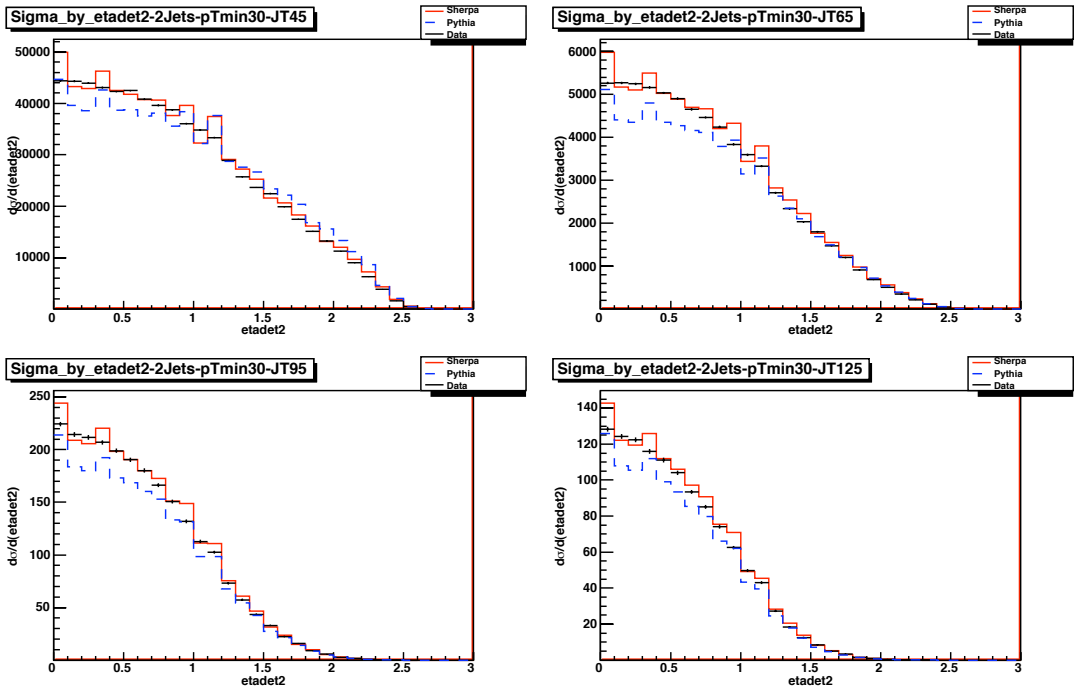

Figure D.19: The second jet detector pseudorapidity, 2 jet event.

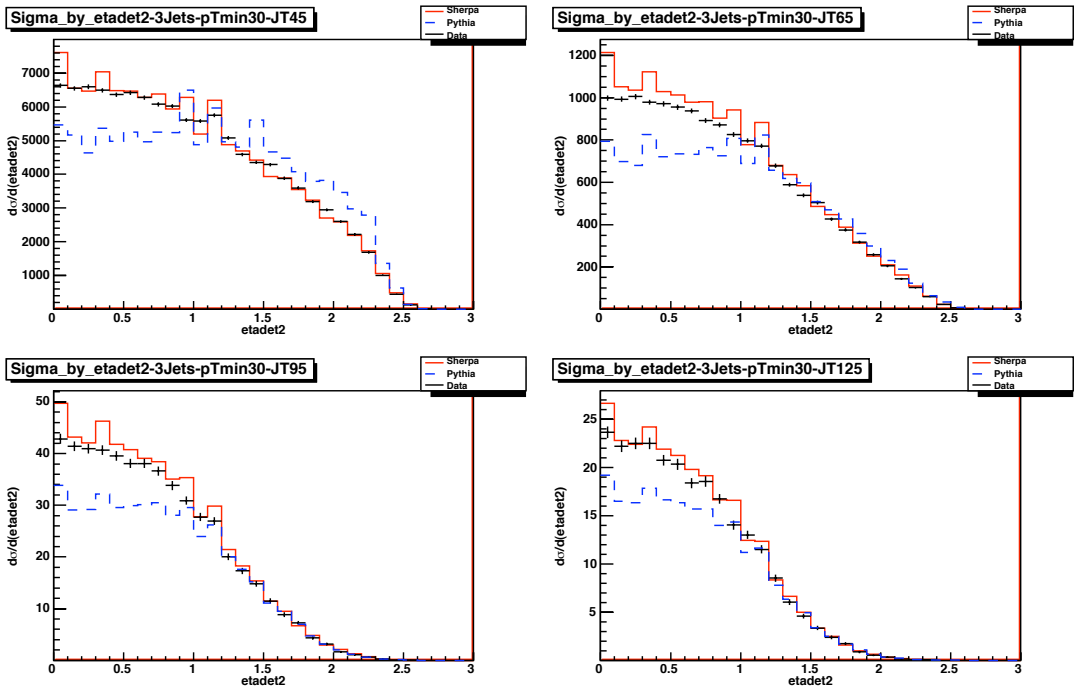

Figure D.20: The second jet detector pseudorapidity, 3 jet event.

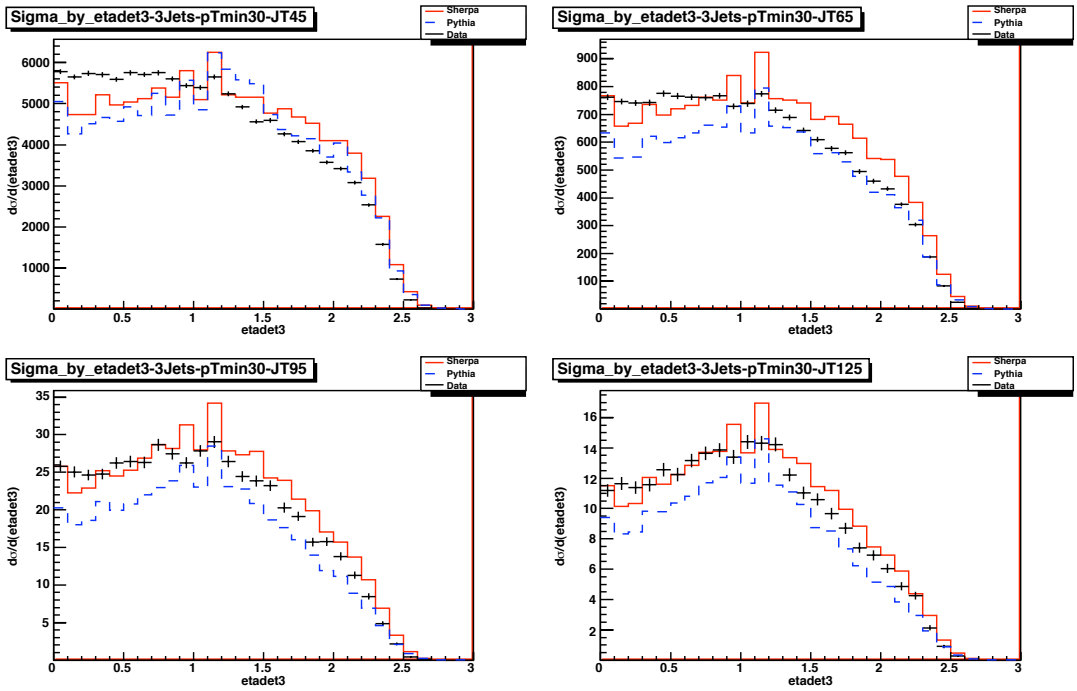

Figure D.21: The third jet detector pseudorapidity, 3 jet event.

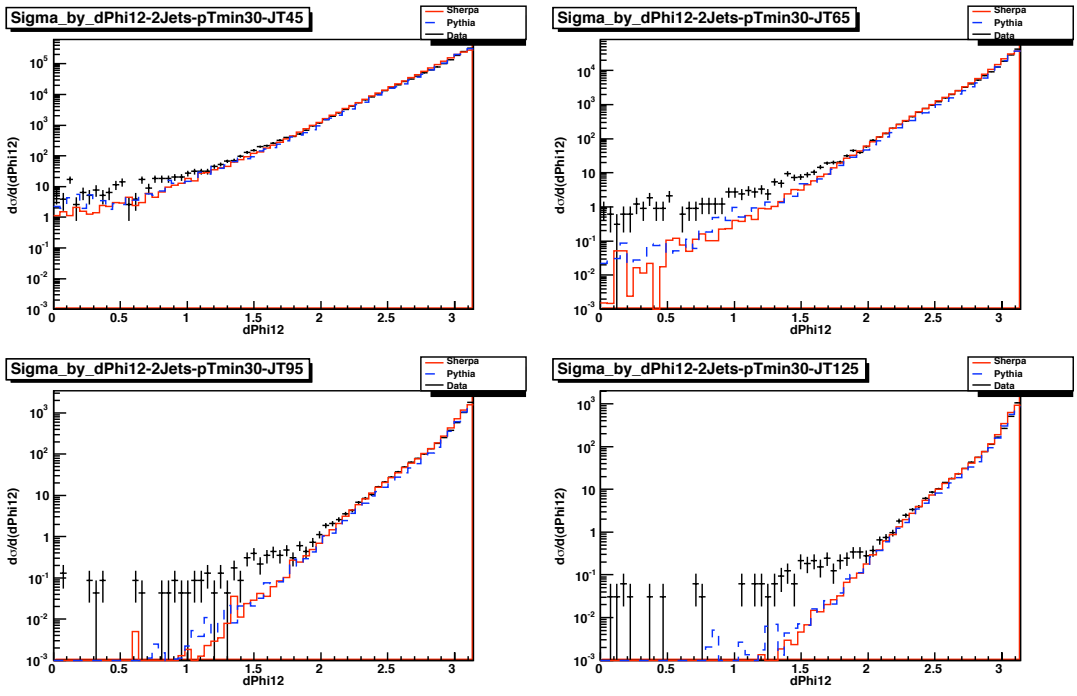

Figure D.22: The difference in phi for the leading and second jets, 2 jet event.

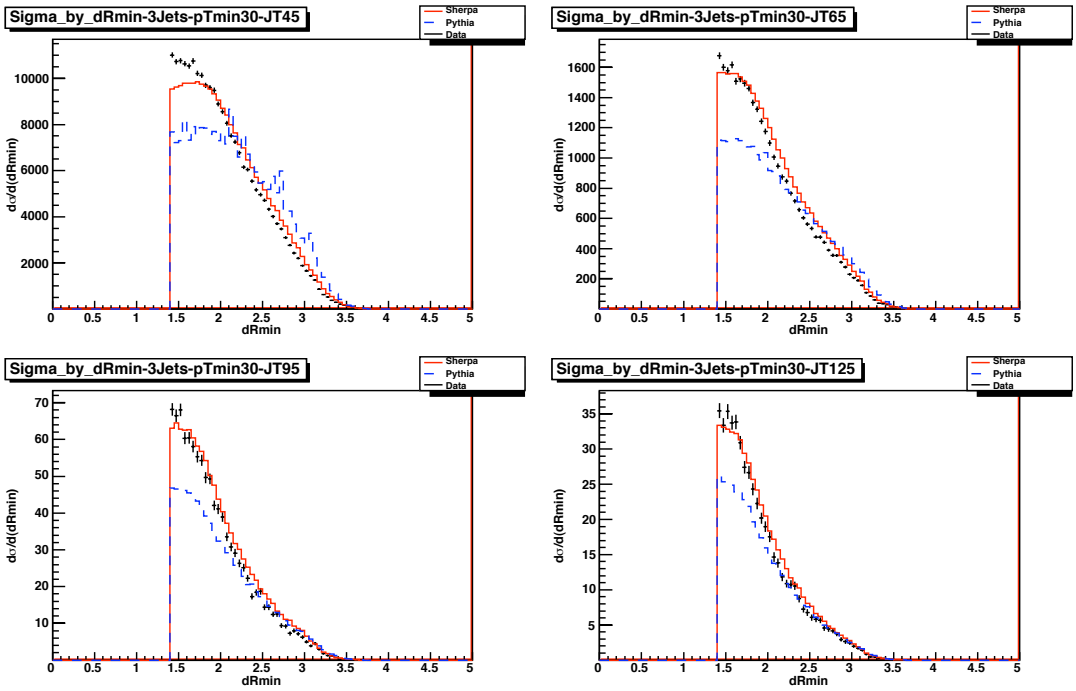

Figure D.23: The minimum distance between jets, 3 jet event.

APPENDIX E

UNCERTAINTIES

E.1 JES Uncertainty Sources

Table E.1: JES unceratinty sources.

Comp.	Description	Comp.	Description
jes_{000}	EM energy scale	jes_{025}	η fit in EC
jes_{001}	Dead material	jes_{026}	Zero suppression bias
jes_{002}	Photon enregy scale	jes_{027}	ZSb number of vertices
jes_{003}	Photon sample purity	jes_{028}	ZSb jet matching
jes_{004}	EM-jet background	jes_{029}	MPF method bias (MPFb)
jes_{005}	High-p_T extrapolation	jes_{030}	MPFb Pythia vs. Herwig
jes_{006}	PDF uncertainty at high p_T	jes_{031}	MPFb scaling
jes_{007}	Time stability	jes_{032}	MPF jet matching p_T
jes_{008}	Fit in CC kRjetCCStat0	jes_{033}	Detector showering (Shw)
jes_{009}	Fit in CC kRjetCCStat1	jes_{034}	Shw sample purity
jes_{010}	Fit in CC kRjetCCStat2	jes_{035}	Shw scaling
jes_{011}	η-intercalibration in CC	jes_{036}	Shw jet matching
jes_{012}	η-intercalibration in IC	jes_{037}	Shw template fits
jes_{013}	η-intercalibration in IC	jes_{038}	Shw Tune A vs. Tune DW
jes_{014}	η-intercalibration in EC	jes_{039}	Closure
jes_{015}	η-intercalibration in EC	jes_{040}	MPFb for dijets
jes_{016}	η-intercalibration in EC	jes_{041}	MPFb for dijets
jes_{017}	η-intercalibration in EC	jes_{042}	Dijet CC response
jes_{018}	JES resolution bias	jes_{043}	Dijet CC response
jes_{019}	η fit in CC	jes_{044}	Dijet CC response
jes_{020}	η fit in IC	jes_{045}	Dijet CC response
jes_{021}	η fit in IC	jes_{046}	Inclusive jet response
jes_{022}	η fit in EC	jes_{047}	Offset
jes_{023}	η fit in EC	jes_{048}	Offset systematics
jes_{024}	η fit in EC	jes_{049}	empty placeholder

E.2 p_T Resolution Uncertainty Sources

Table E.2: p_T resolution unceratinty sources.

Component	Description	Component	Description
$ptres_{00}$	Fit uncertainty	$ptres_{08}$	statistical CC1
$ptres_{01}$	Soft correction	$ptres_{09}$	statistical CC2
$ptres_{02}$	Ptcl-level p_T imbalance	$ptres_{10}$	statistical IC1
$ptres_{03}$	Noise CC	$ptres_{11}$	statistical IC2
$ptres_{04}$	Noise IC	$ptres_{12}$	statistical EC1
$ptres_{05}$	Noise EC	$ptres_{13}$	statistical EC2
$ptres_{06}$	Noise forward	$ptres_{14}$	statistical forward
$ptres_{07}$	Closure		

APPENDIX F

DETERMINATION OF OPTIMAL BINNING

F.1 Average Event Shapes

The binning in H_T for the average event shapes is taken to be the same as in the dijet azimuthal decorrelation study [17].

F.2 Differential, Normalized Distributions

In order to have the best results possible for the normalized differential event shape distributions a determination of the optimal binning needs to be performed using a MC study. These studies are performed for each event shape in each H_T region. For each event shape distribution migration study plots are created – plotting particle-level event shape value on the y-axis and detector-level event shape value on the x-axis for a particular event. The range of the x and y axes are from zero to one with one negative bin also included for each axis to account for events where the particle-level event and detector-level event are not in the same H_T region.

Each of the migration study plots also includes a diagonal line which indicates events where the particle-level and detector-level values for the event shape are in the same bin. Using these migration study plots, the efficiency (eff_i) and purity (pur_i) for each bin i in the event shape distribution can be determined by using

$$\begin{aligned} eff_i &= \frac{diag_i}{\sum_j x_{j,i}} \\ pur_i &= \frac{diag_i}{\sum_j y_{i,j}}\,, \end{aligned} \tag{6.1}$$

where $diag_i$ is the number of events where the detector-level and particle-level values are in the same range (a value along the above-mentioned diagonal); $\sum_j x_{j,i}$ sums all

of the events that have a particle-level value in a bin i; and $\sum_j y_{i,j}$ sums all of the events that have a detector-level value in a bin i.

The results of the migration study plots and efficiency and purity plots for the chosen optimal binning are given for each event shape in each of the four H_T regions. Plots of the normalized differential event shape distributions are given for data using the optimal binning and for data and MC using a bin size of 0.02. These show that the structure of the distribution is not lost by using the optimal binning.

F.2.1 Thrust

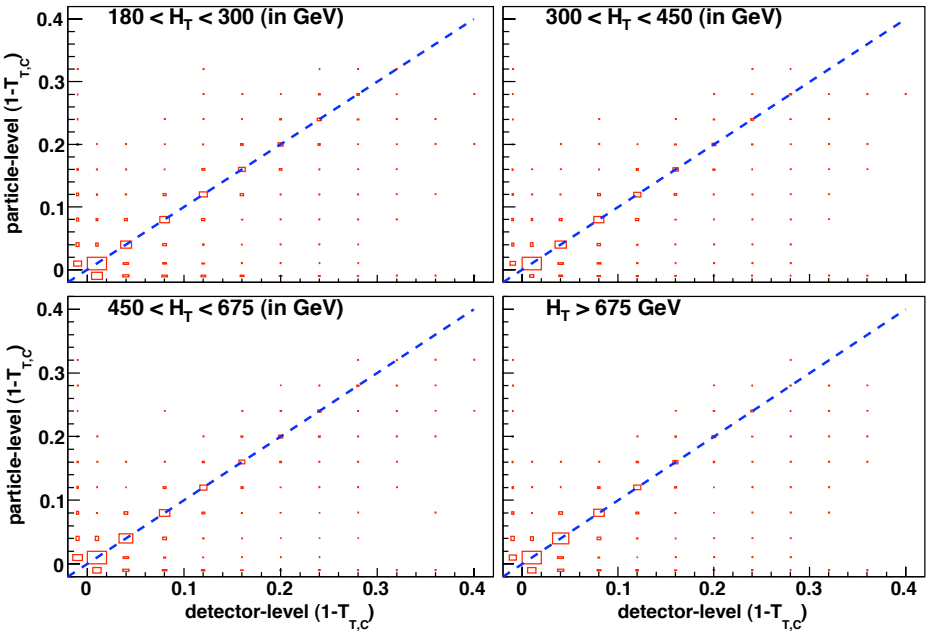

Figure F.1: Migration plots for the thrust

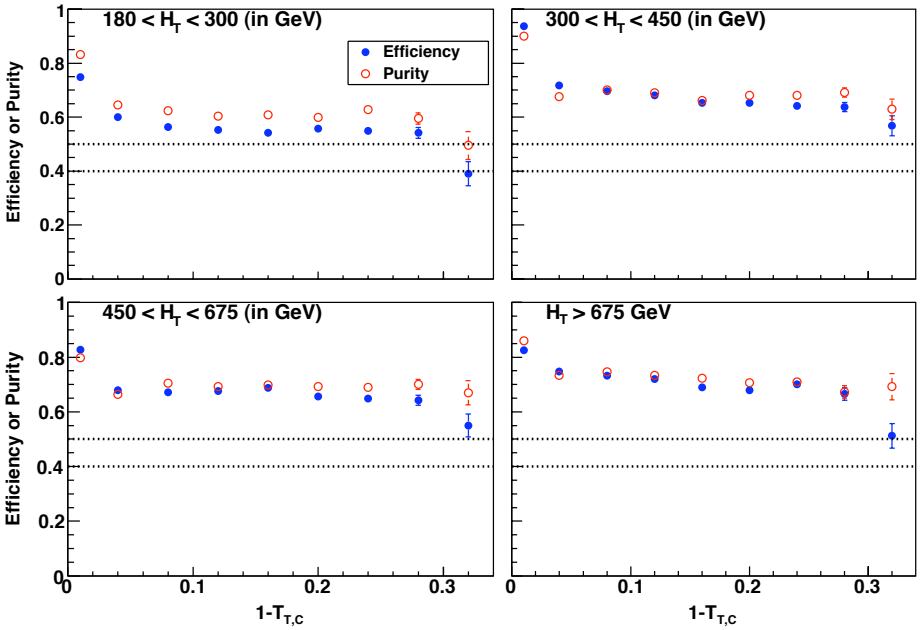

Figure F.2: Efficiency and purity plots for the thrust

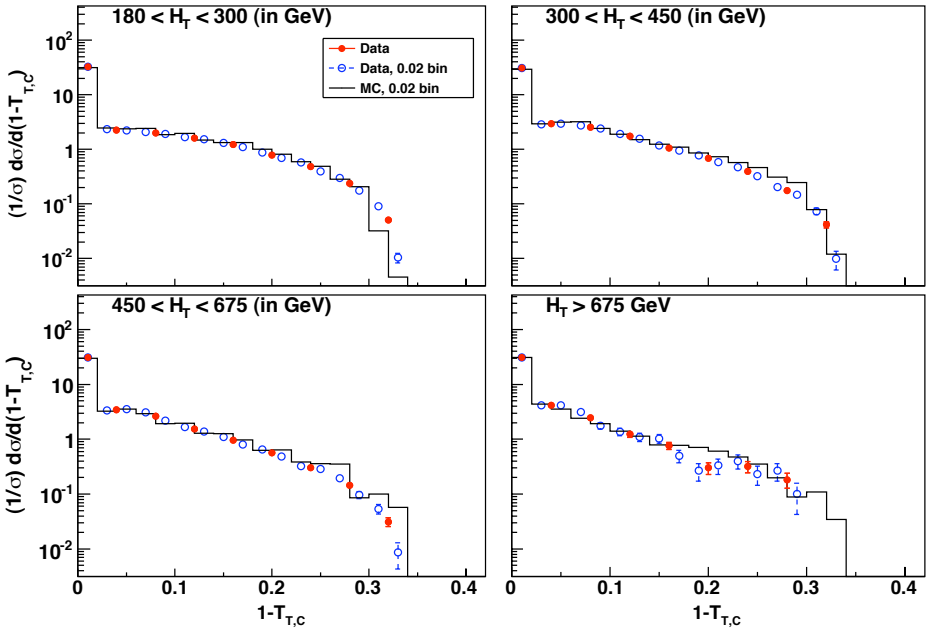

Figure F.3: Differential, normalized distribution plots for thrust, data with optimized binning and data/MC with bin size of 0.02

F.2.2 Thrust Minor

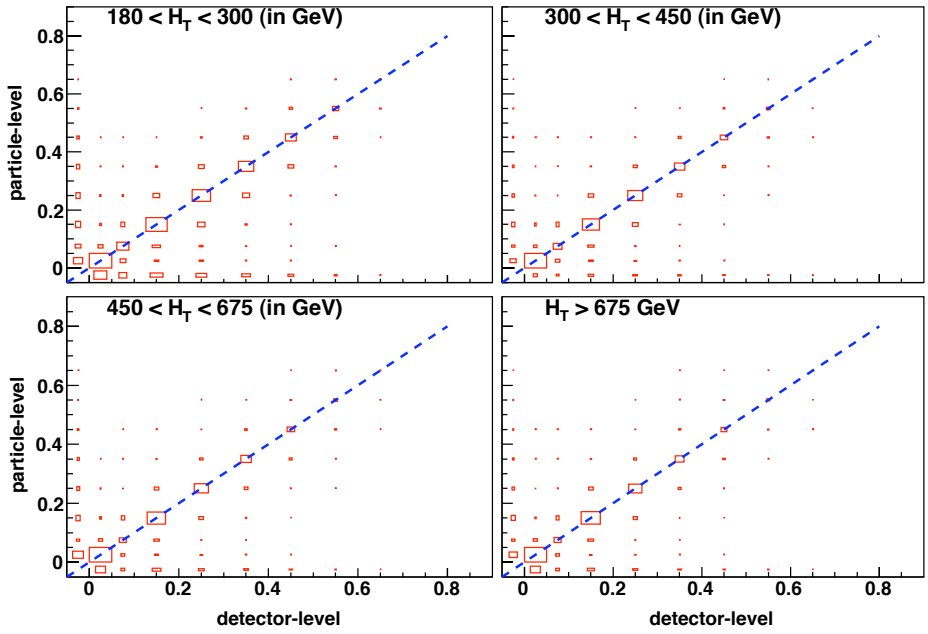

Figure F.4: Migration plots for the thrust minor

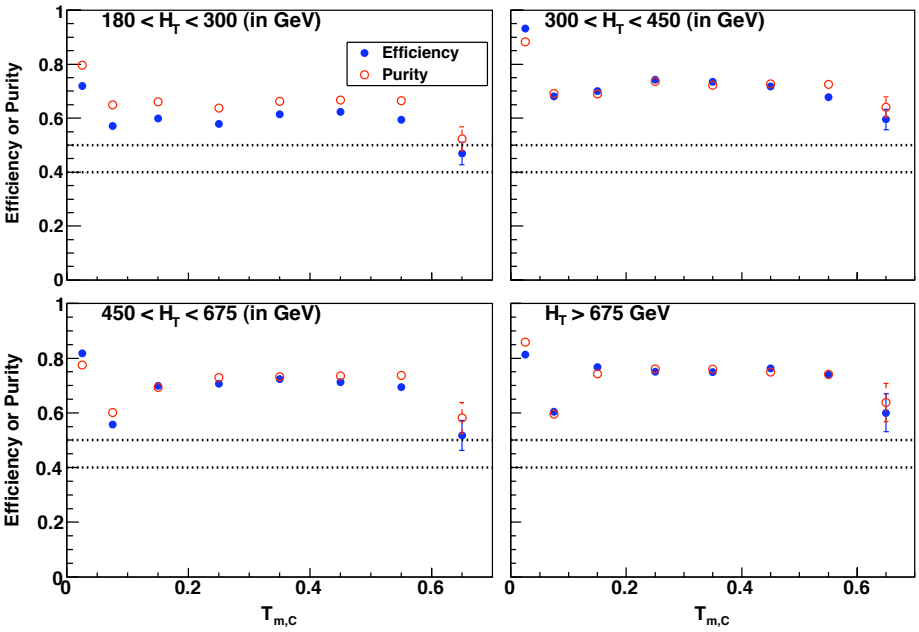

Figure F.5: Efficiency and purity plots for the thrust minor

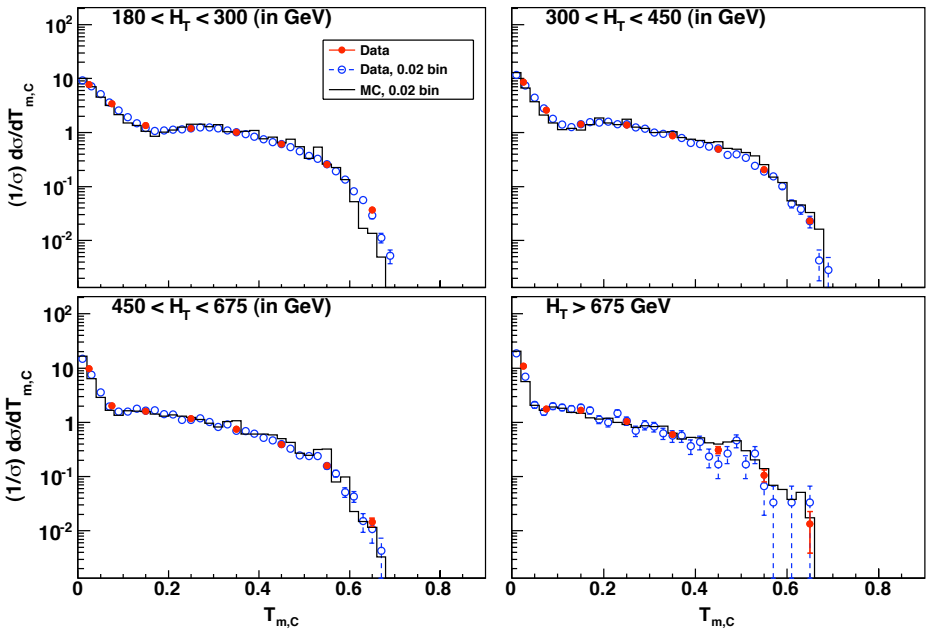

Figure F.6: Differential, normalized distribution plots for thrust, data with optimized binning and data/MC with bin size of 0.02

F.2.3 Sum of Masses

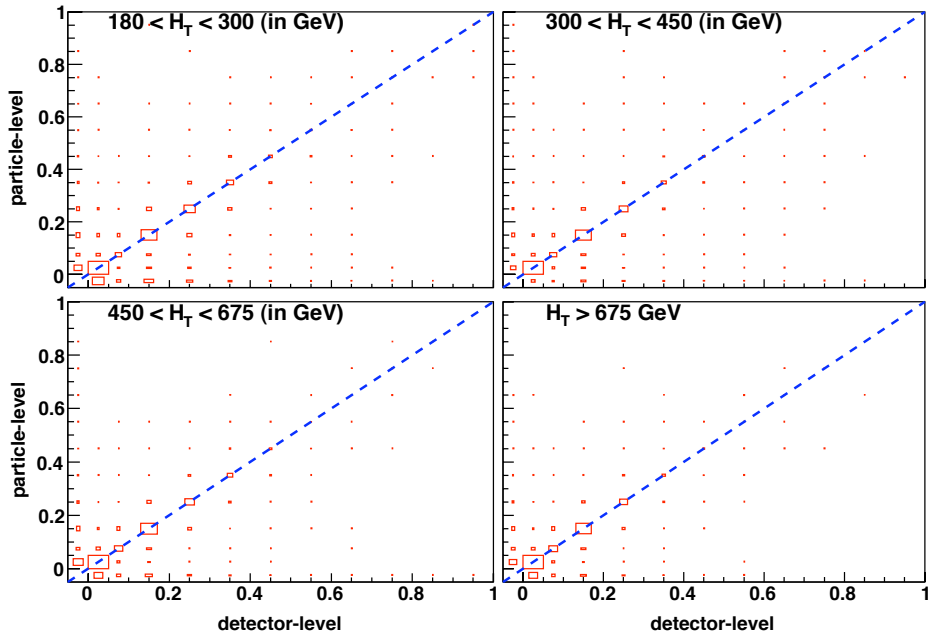

Figure F.7: Migration plots for the sum of masses

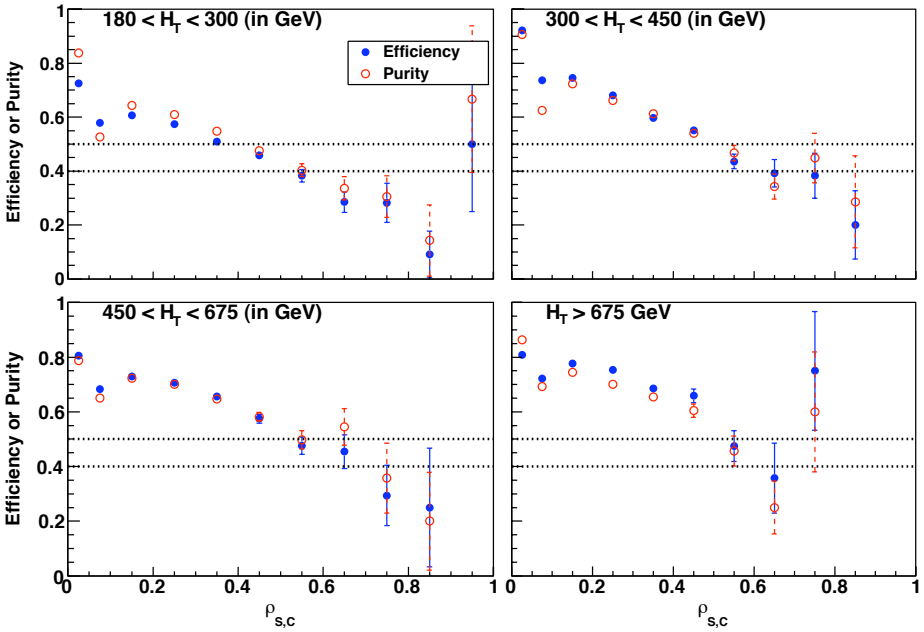

Figure F.8: Efficiency and purity plots for the sum of masses

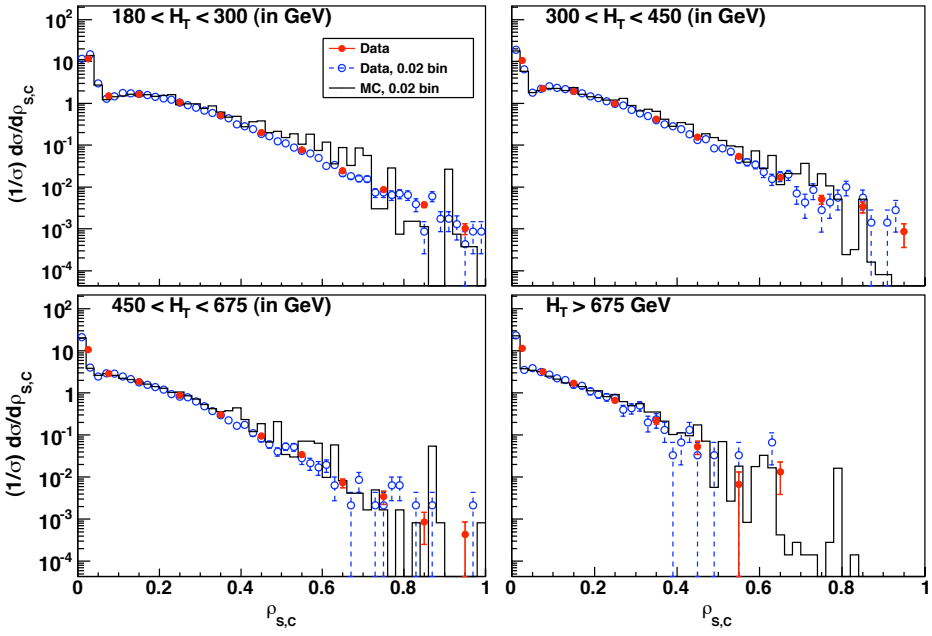

Figure F.9: Differential, normalized distribution plots for sum of masses, data with optimized binning and data/MC with bin size of 0.02

F.2.4 Heavy Mass

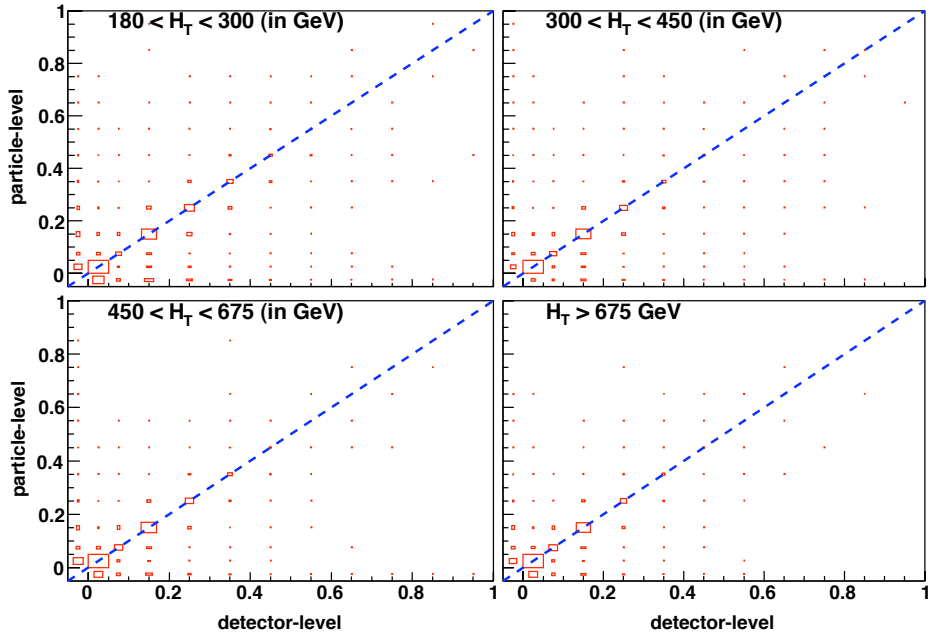

Figure F.10: Migration plots for the heavy mass

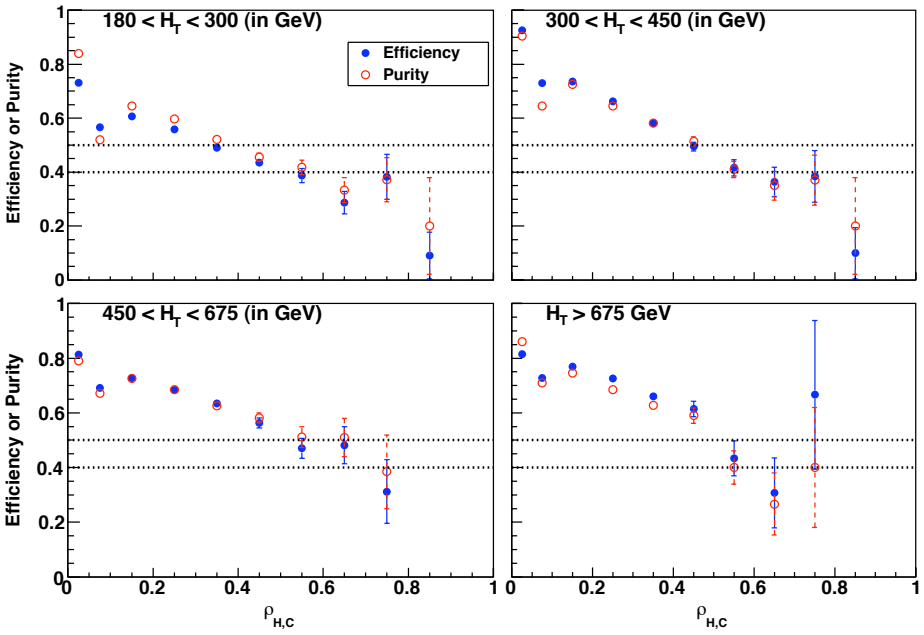

Figure F.11: Efficiency and purity plots for the heavy mass

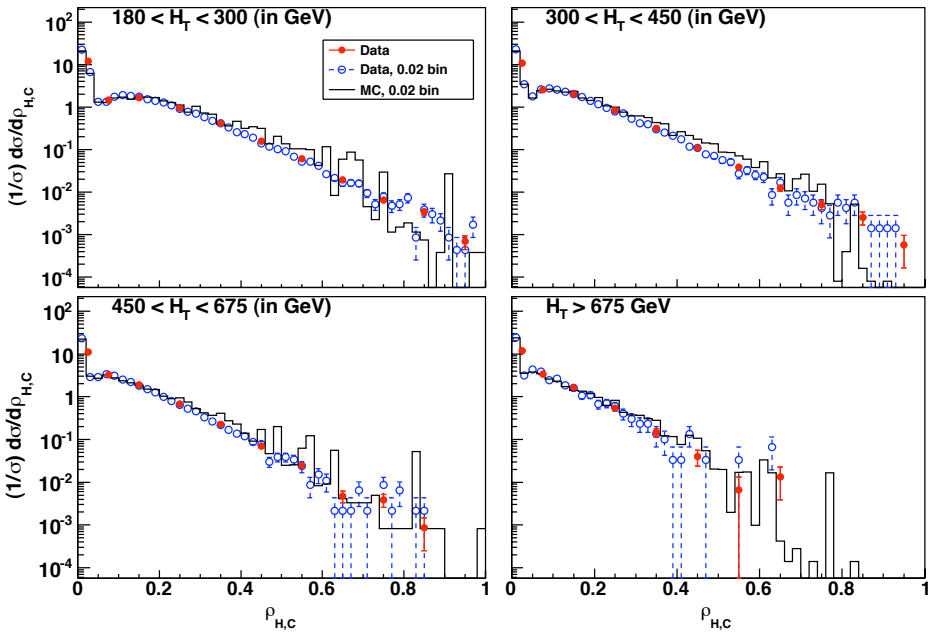

Figure F.12: Differential, normalized distribution plots for heavy mass, data with optimized binning and data/MC with bin size of 0.02

F.2.5 Total Broadening

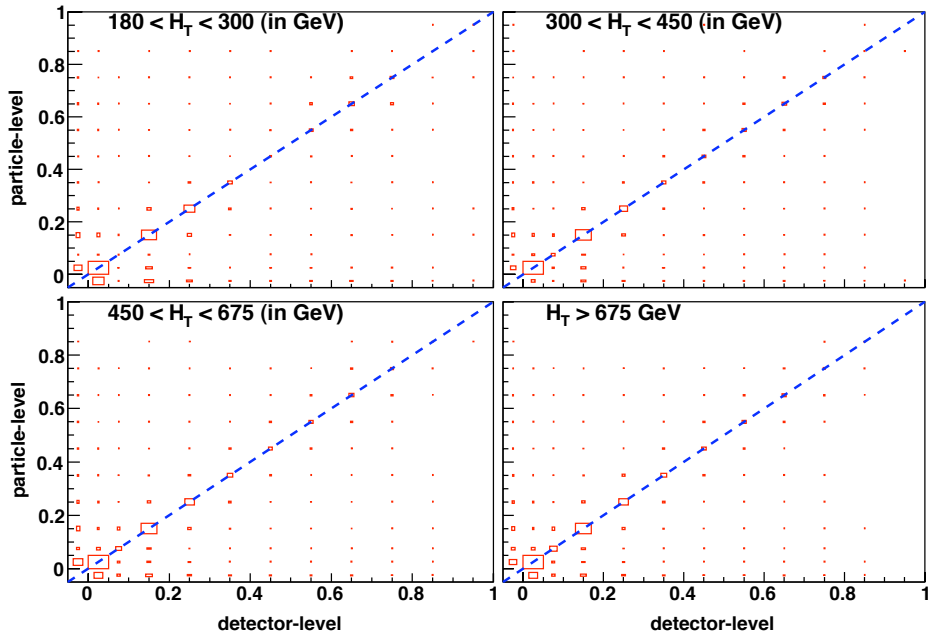

Figure F.13: Migration plots for the total broadening

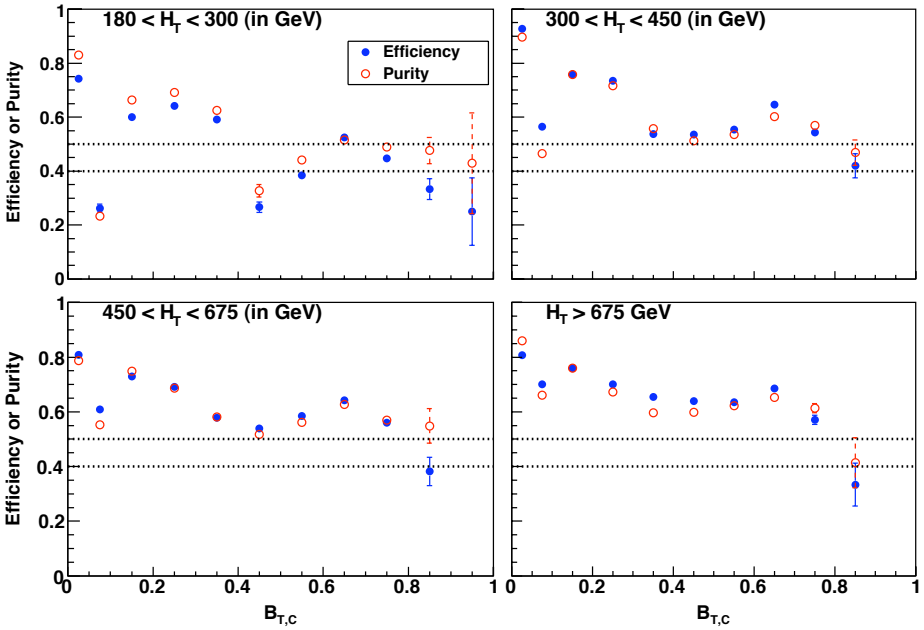

Figure F.14: Efficiency and purity plots for the total broadening

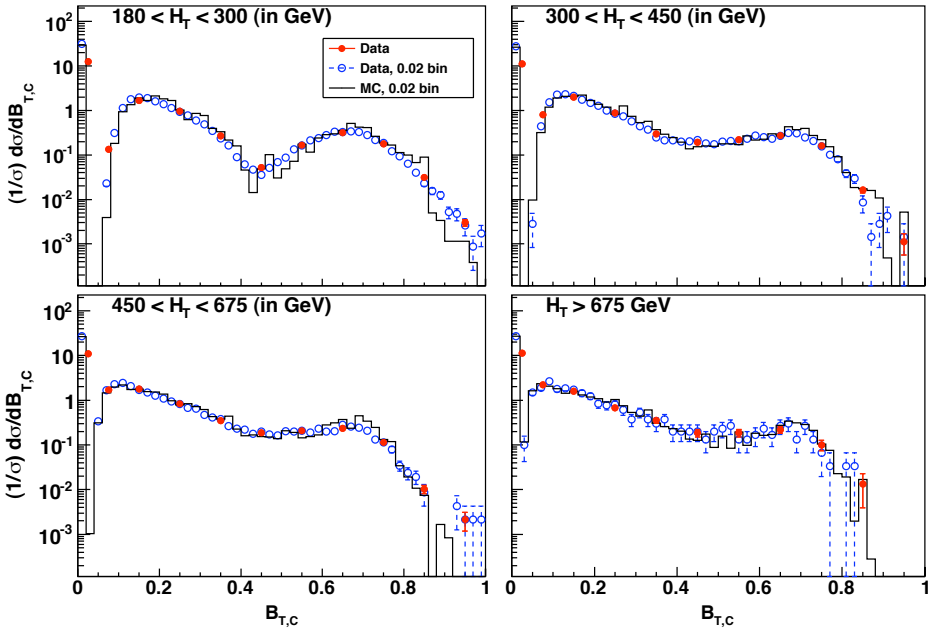

Figure F.15: Differential, normalized distribution plots for total broadening, data with optimized binning and data/MC with bin size of 0.02

F.2.6 Wide Jet Broadening

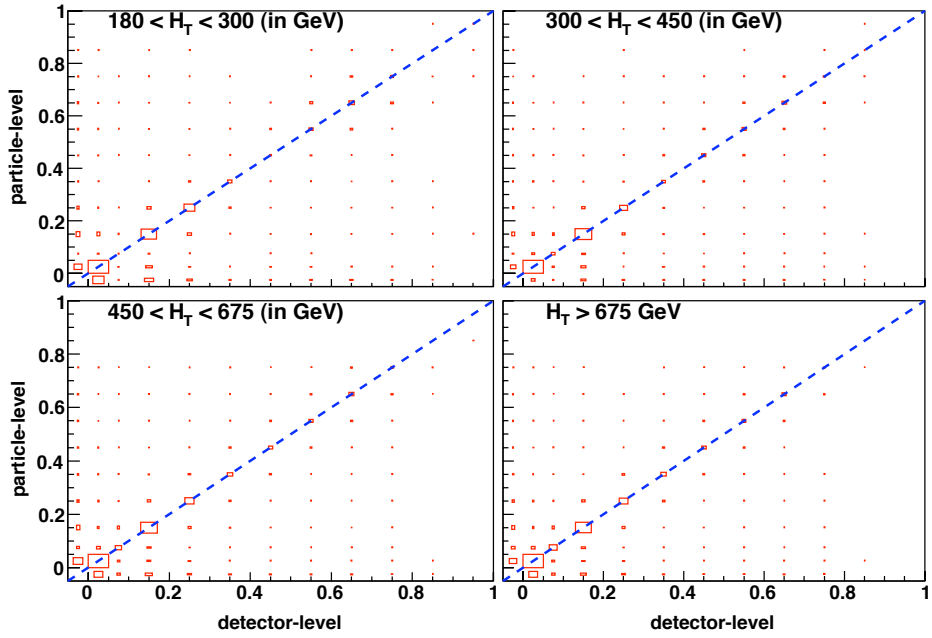

Figure F.16: Migration plots for the wide jet broadening

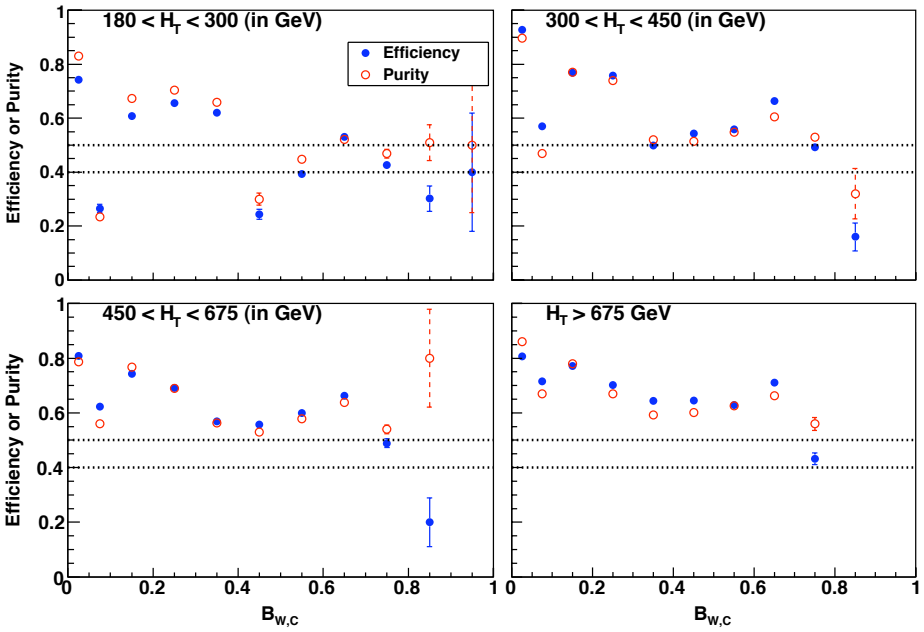

Figure F.17: Efficiency and purity plots for the wide jet broadening

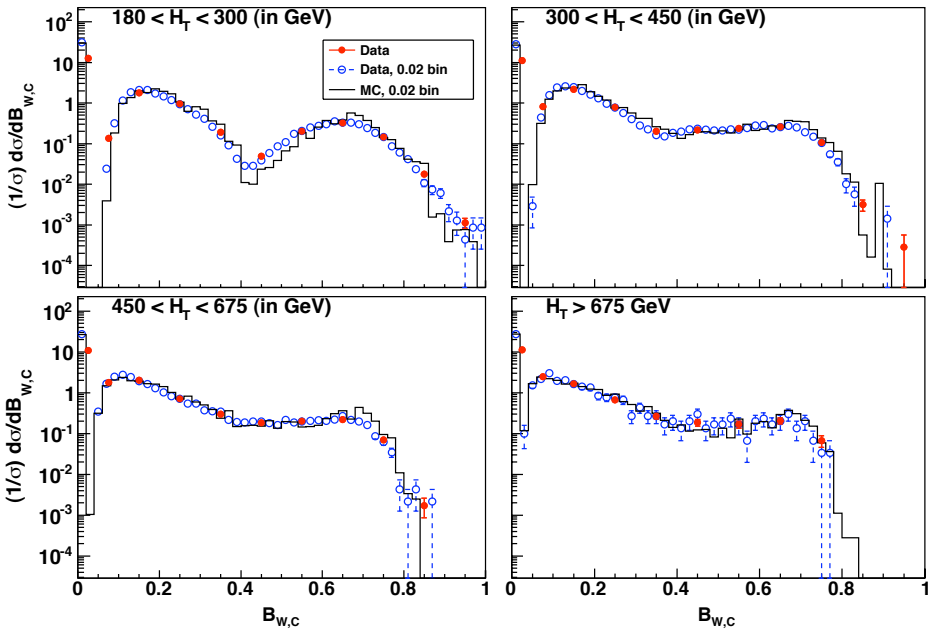

Figure F.18: Differential, normalized distribution plots for wide jet broadening, data with optimized binning and data/MC with bin size of 0.02

F.2.7 F-parameter

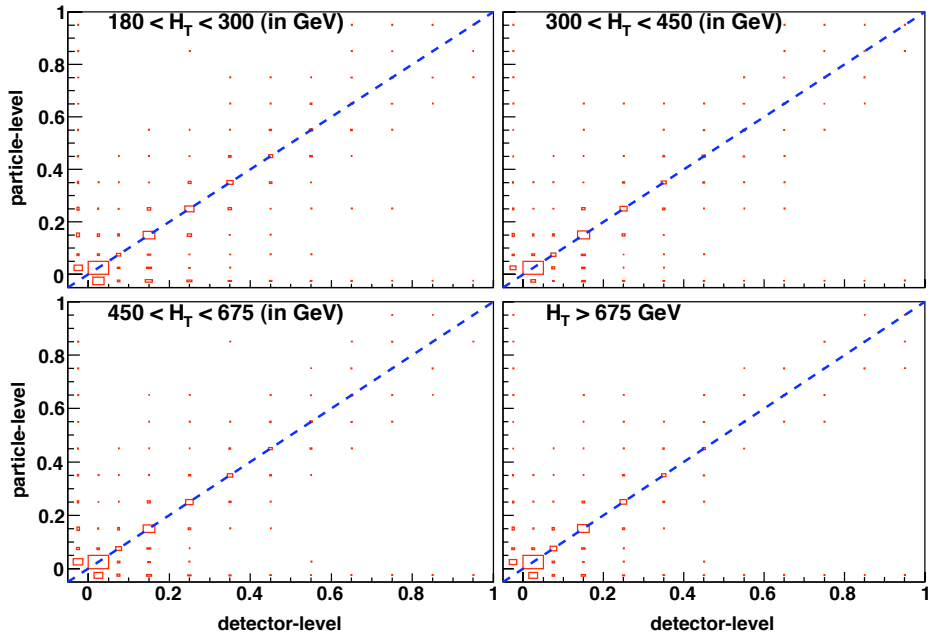

Figure F.19: Migration plots for the F-parameter

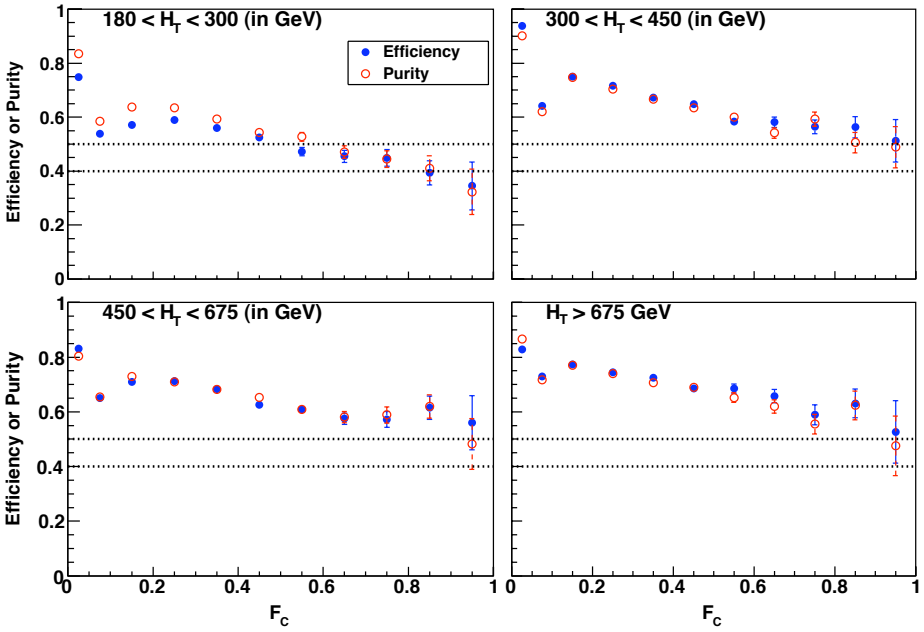

Figure F.20: Efficiency and purity plots for the F-parameter

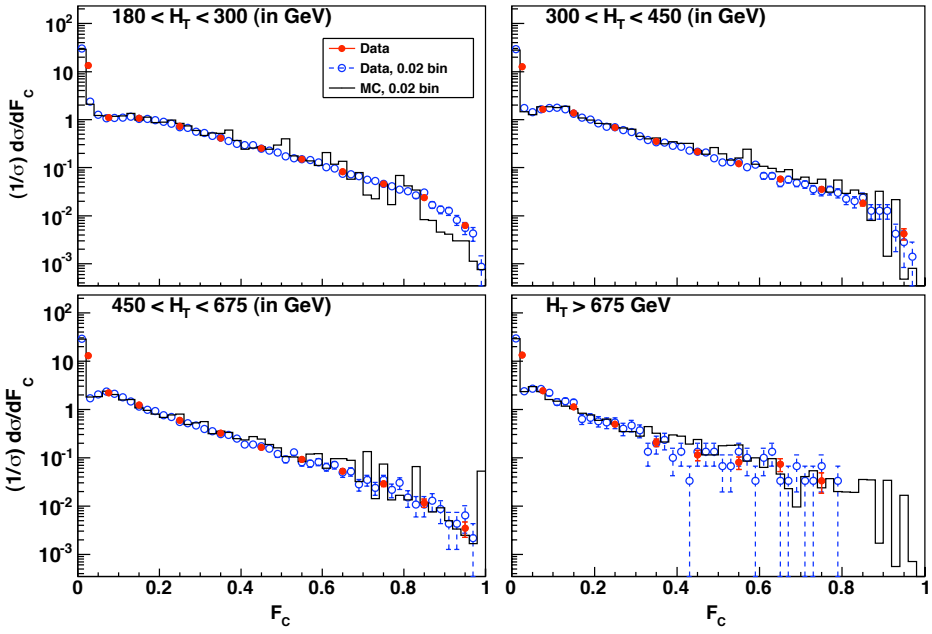

Figure F.21: Differential, normalized distribution plots for F-parameter, data with optimized binning and data/MC with bin size of 0.02

F.2.8 Spherocity

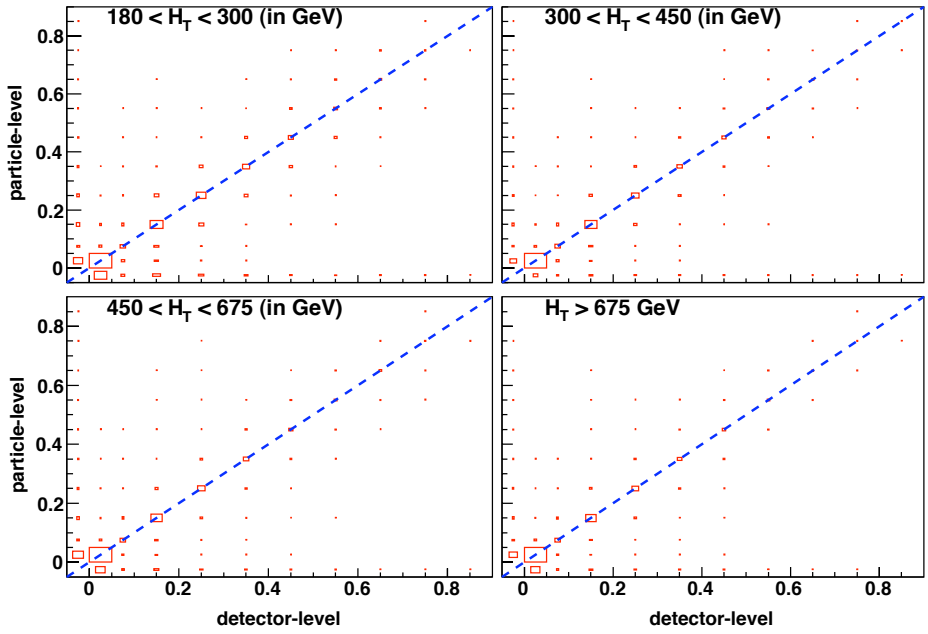

Figure F.22: Migration plots for the spherocity

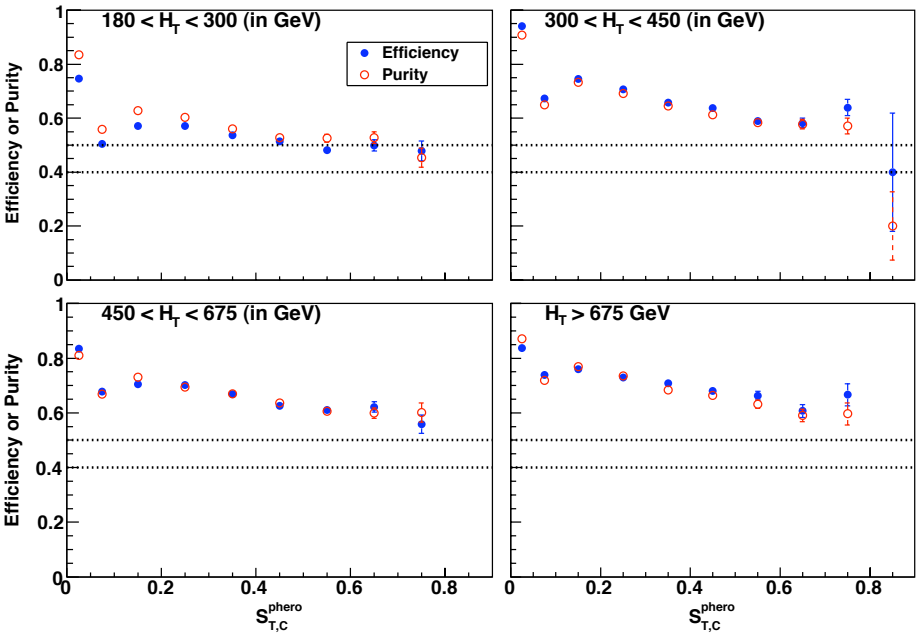

Figure F.23: Efficiency and purity plots for the spherocity

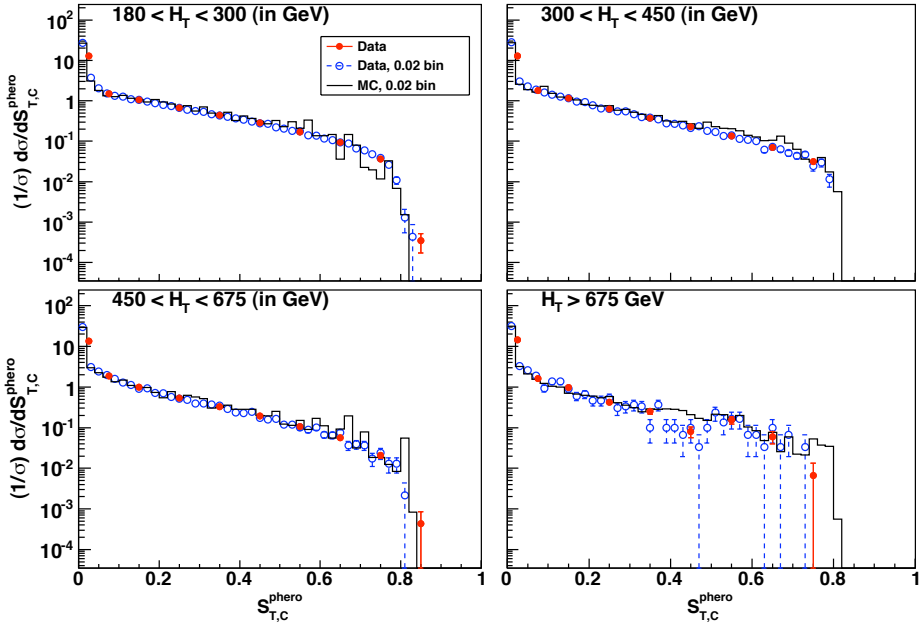

Figure F.24: Differential, normalized distribution plots for spherocity, data with optimized binning and data/MC with bin size of 0.02

F.2.9 Sphericity

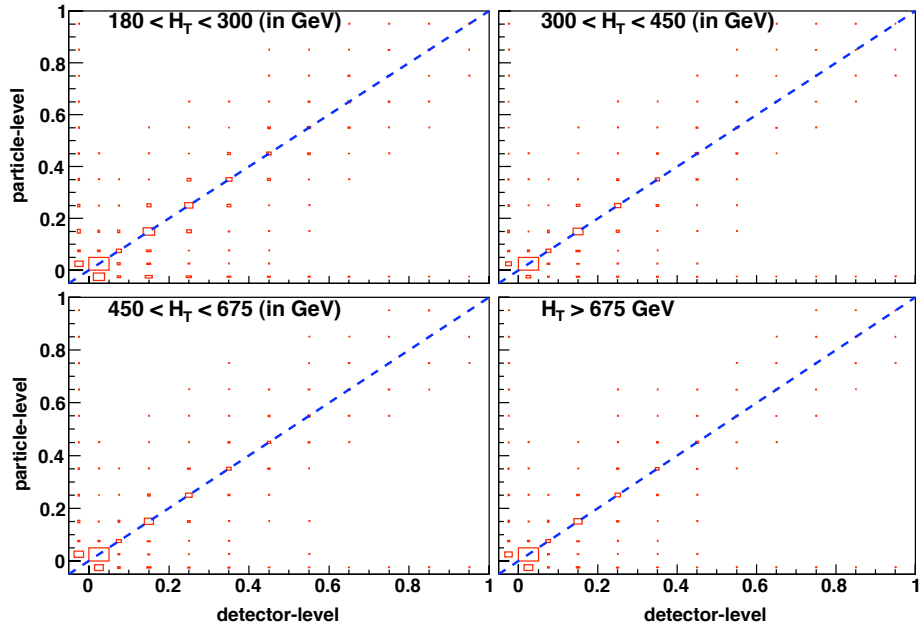

Figure F.25: Migration plots for the sphericity

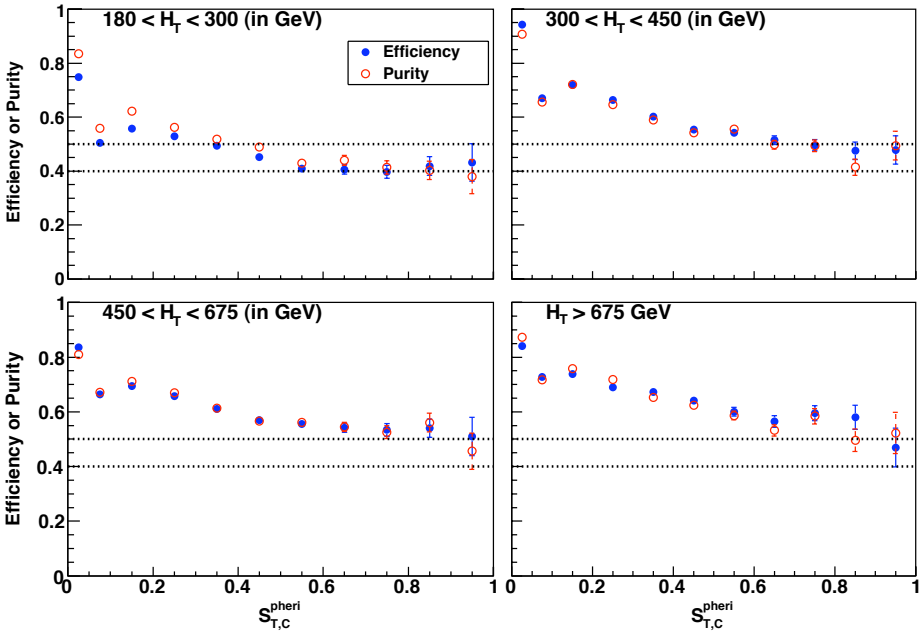

Figure F.26: Efficiency and purity plots for the sphericity

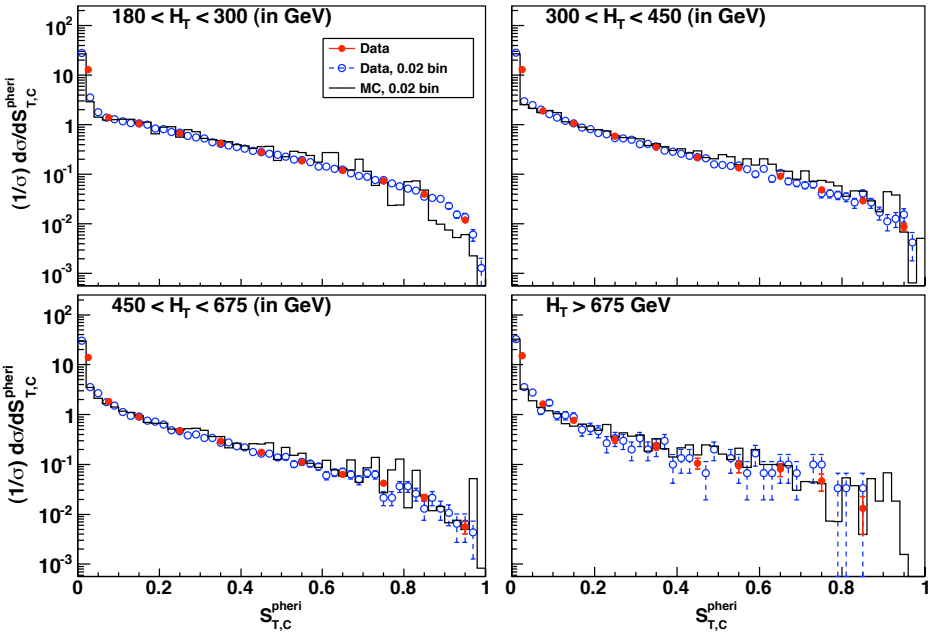

Figure F.27: Differential, normalized distribution plots for sphericity, data with optimized binning and data/MC with bin size of 0.02

APPENDIX G

MINIMUM NUMBER OF EVENTS

In order to make any reliable conclusions from the data for the normalized differential distributions, each bin of the measurement needs to have enough statistics, taken to be 20 for this dissertation.

The first step is to plot events/bin vs X for all event shapes in each of the four H_T regions, drawing a horizontal line at 20 events; these plots are shown in section G.0.10. Looking at these plots from left to right, find the first data point that falls below this line: the last data point used in the analysis is the one right before this one. Normalized differential distribution plots are shown in section G.0.11, where a vertical line is drawn indicating the bins used in the analysis (to the left of the vertical line).

G.0.10 Number of Events/Bin

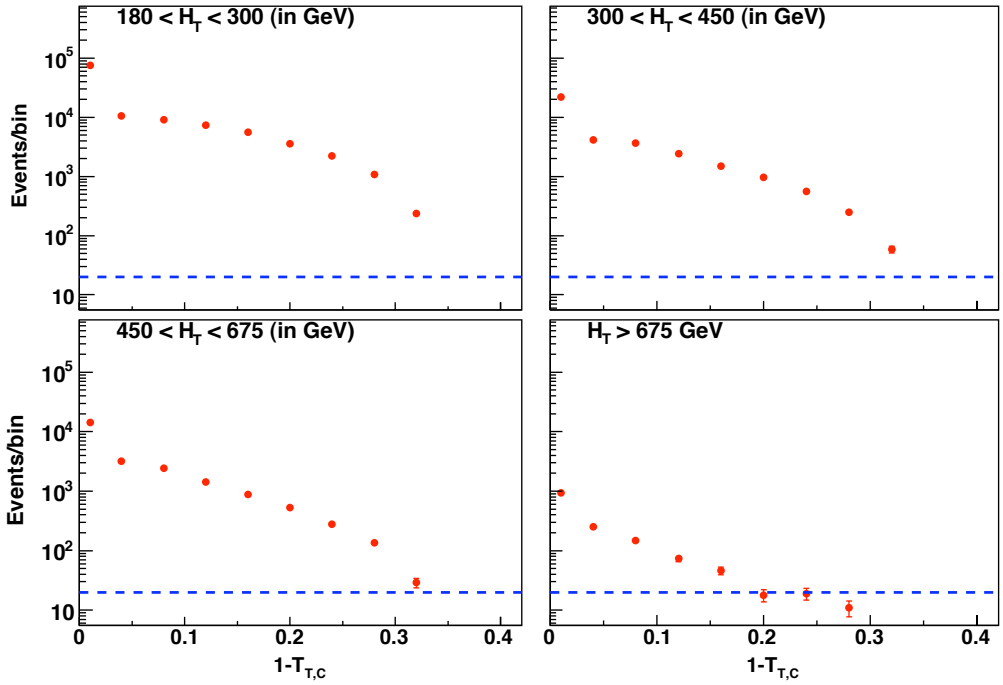

Figure G.1: Thrust: bins with the number of events ≥ 20

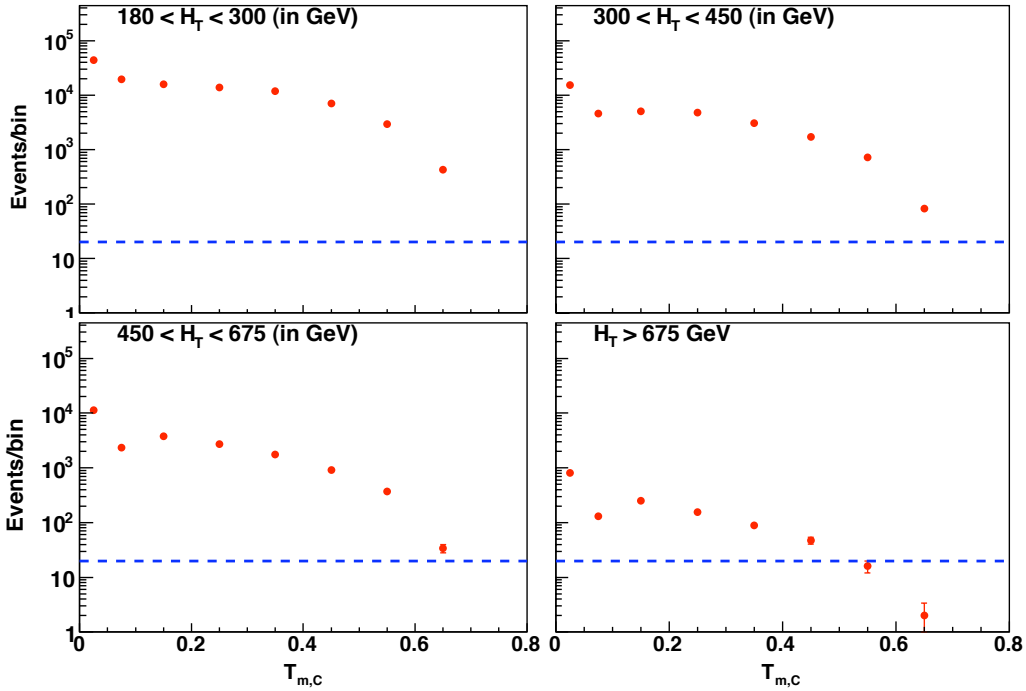

Figure G.2: Thrust Minor: bins with the number of events ≥ 20

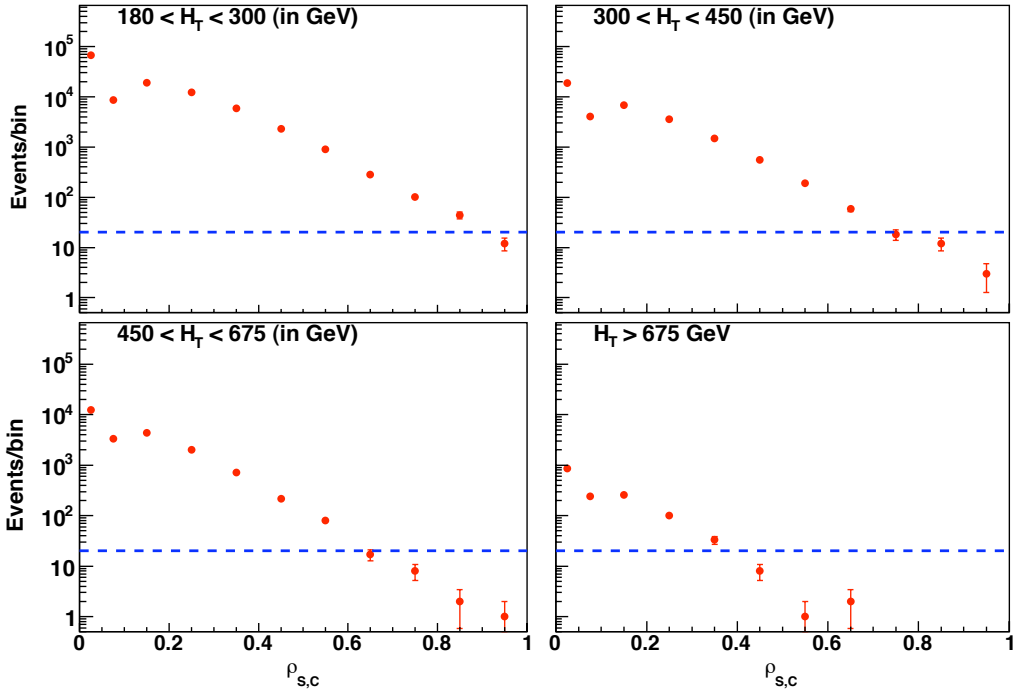

Figure G.3: Sum of Masses: bins with the number of events ≥ 20

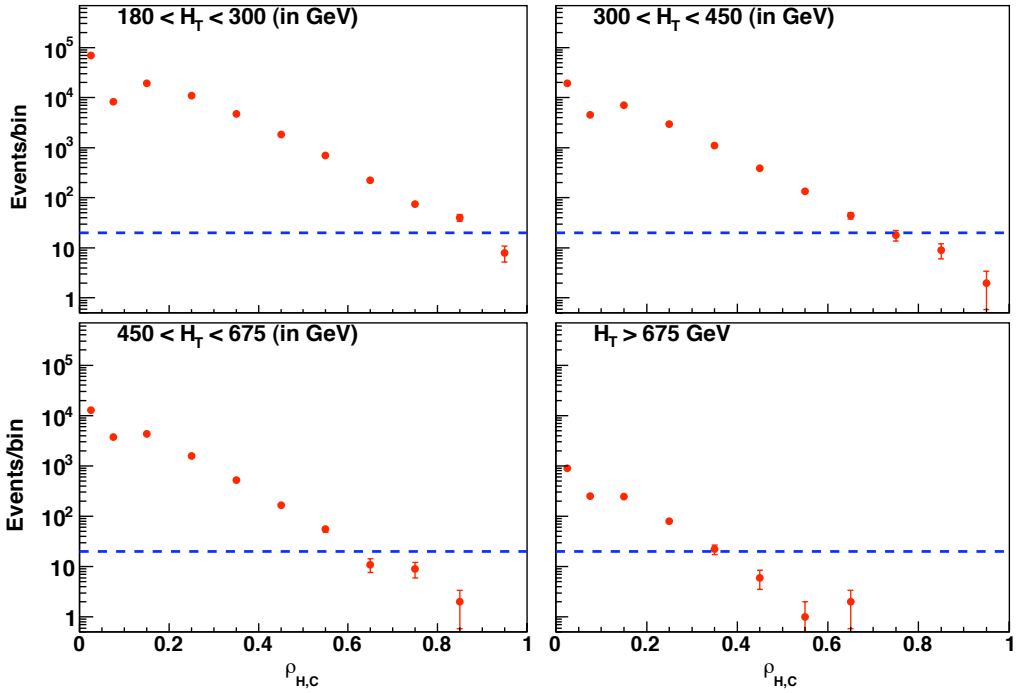

Figure G.4: Heavy Mass: bins with the number of events ≥ 20

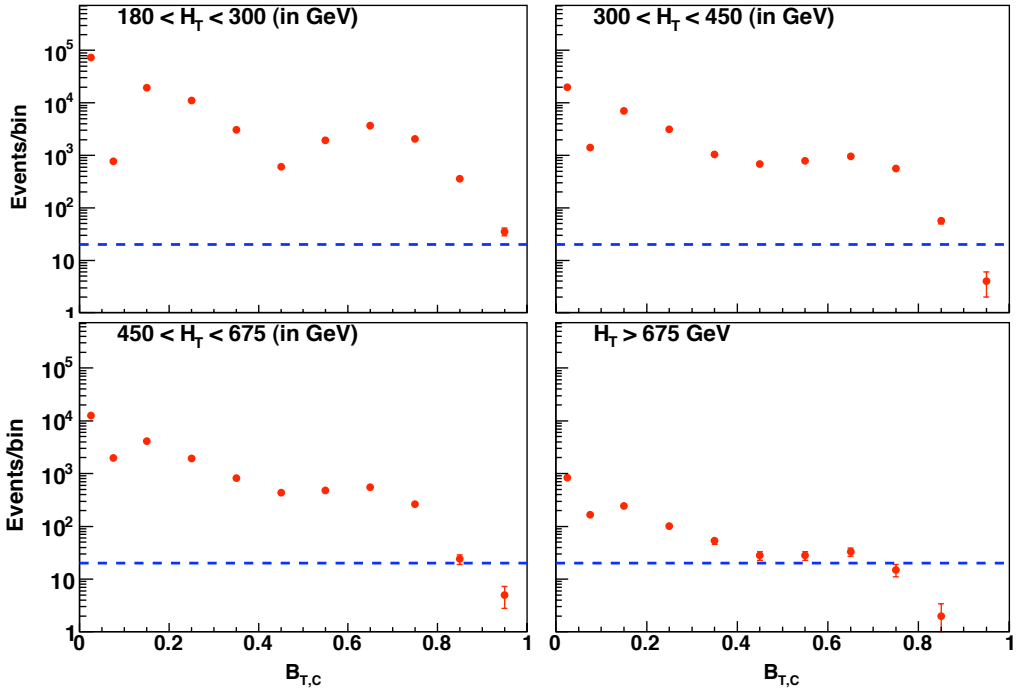

Figure G.5: Total Broadening: bins with the number of events ≥ 20

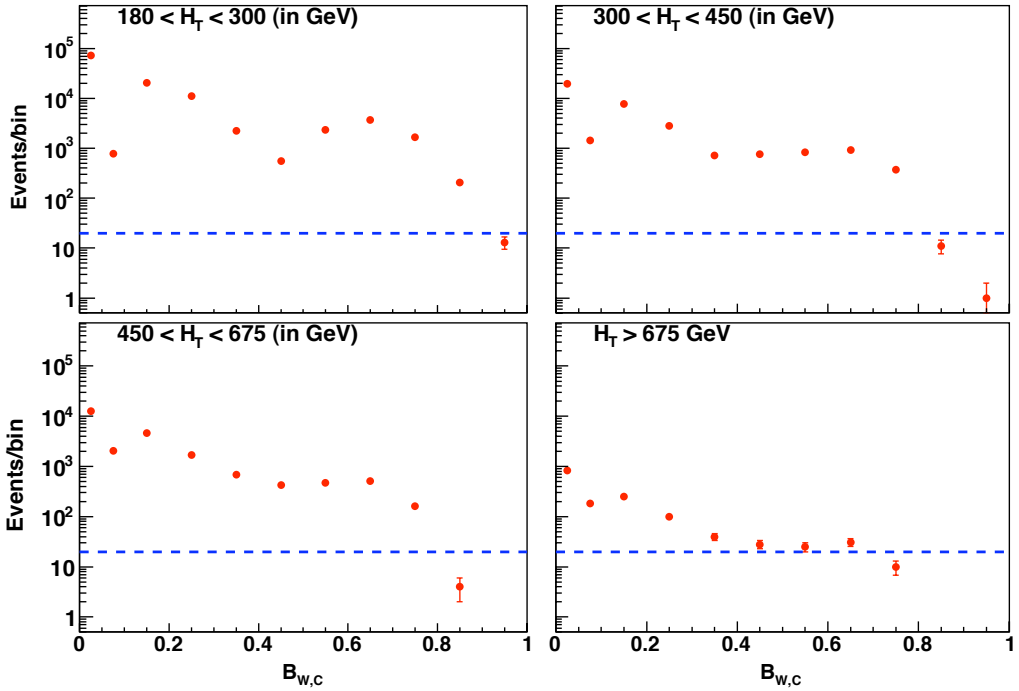

Figure G.6: Wide Jet Broadening: bins with the number of events ≥ 20

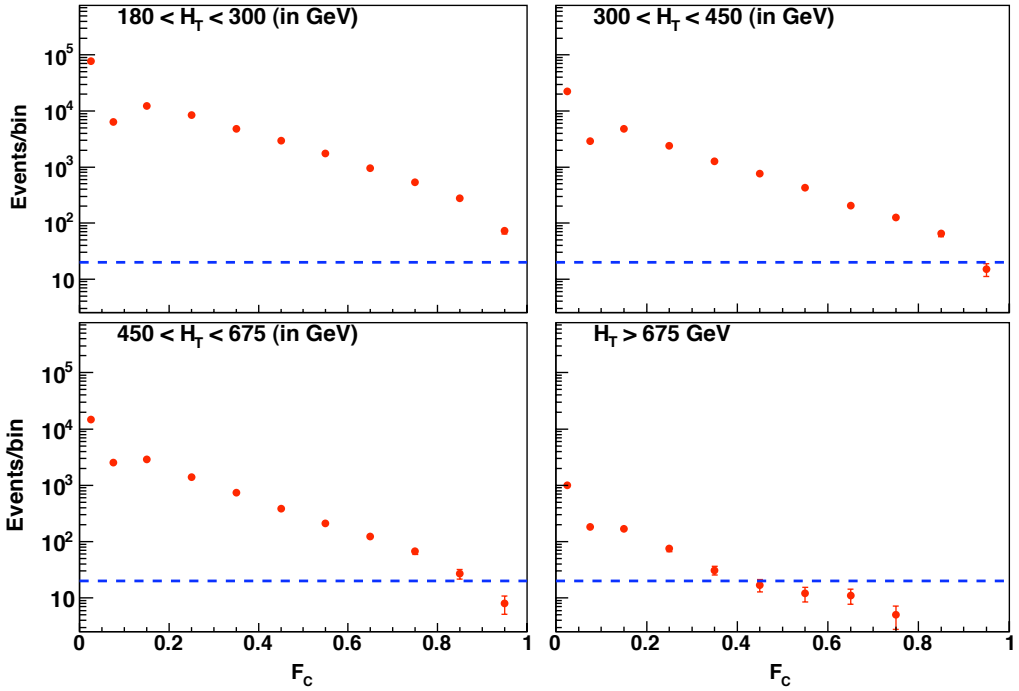

Figure G.7: F-parameter: bins with the number of events ≥ 20

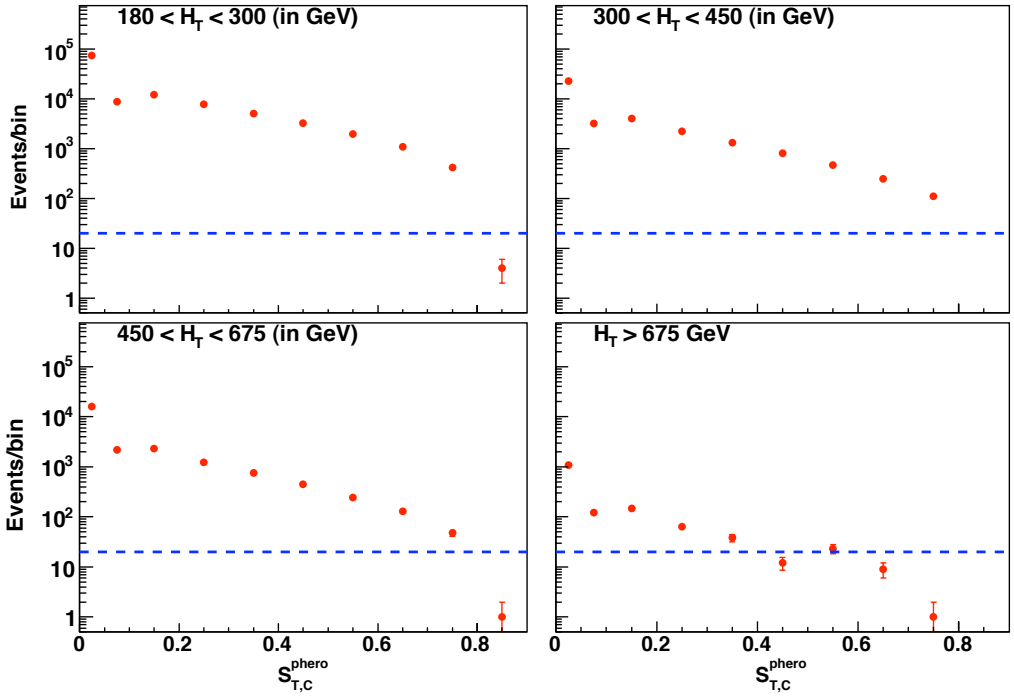

Figure G.8: Spherocity: bins with the number of events ≥ 20

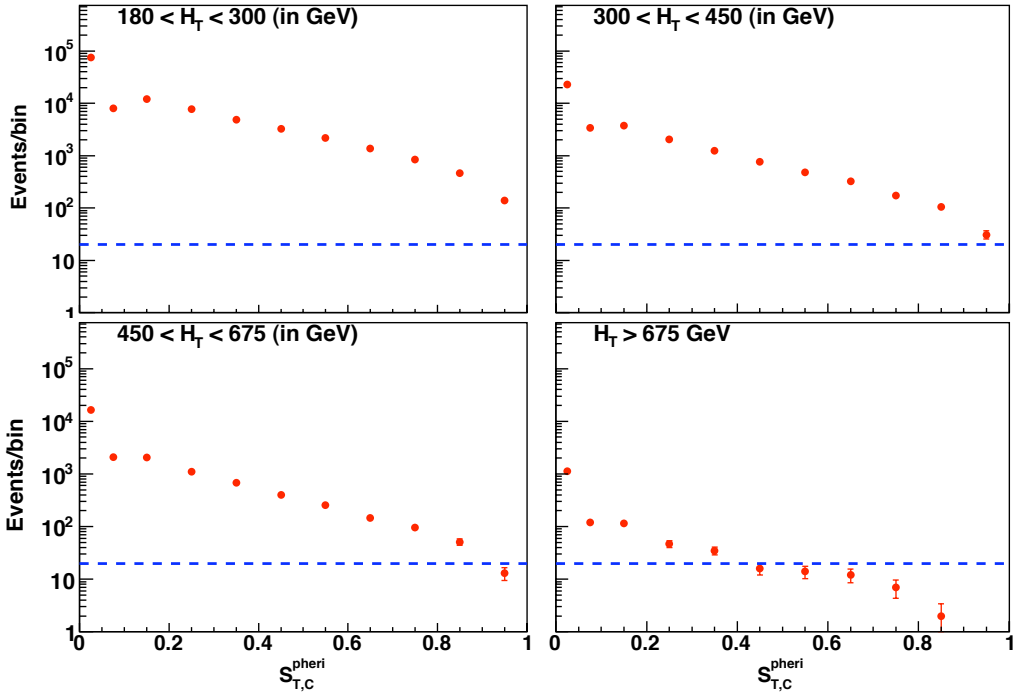

Figure G.9: Sphericity: bins with the number of events ≥ 20

G.0.11 Normalized Differential Distributions, Bins With $\geq$ 20 Events

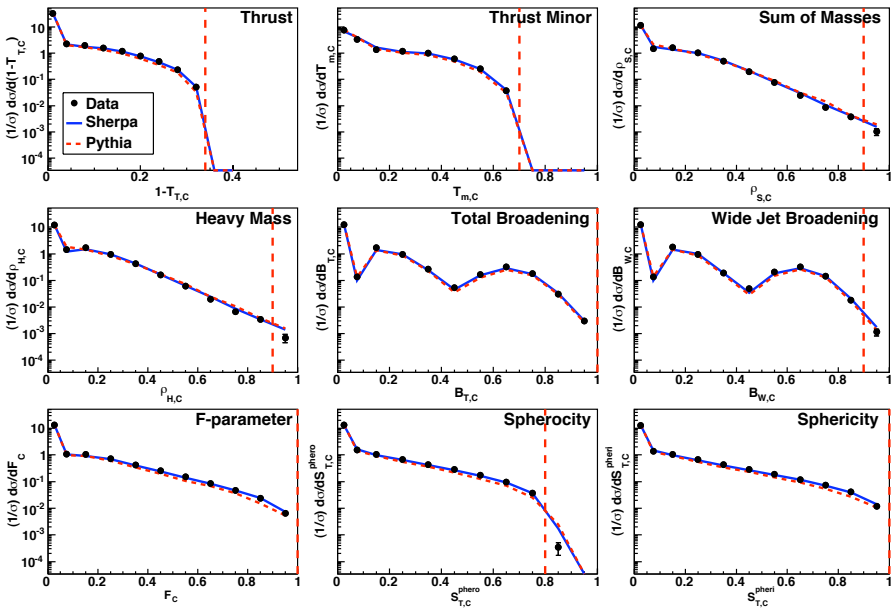

Figure G.10: Normalized differential distribution with $180 \geq H_T < 300$ (in GeV) showing bins with the number of events ≥ 20, left of the red line.

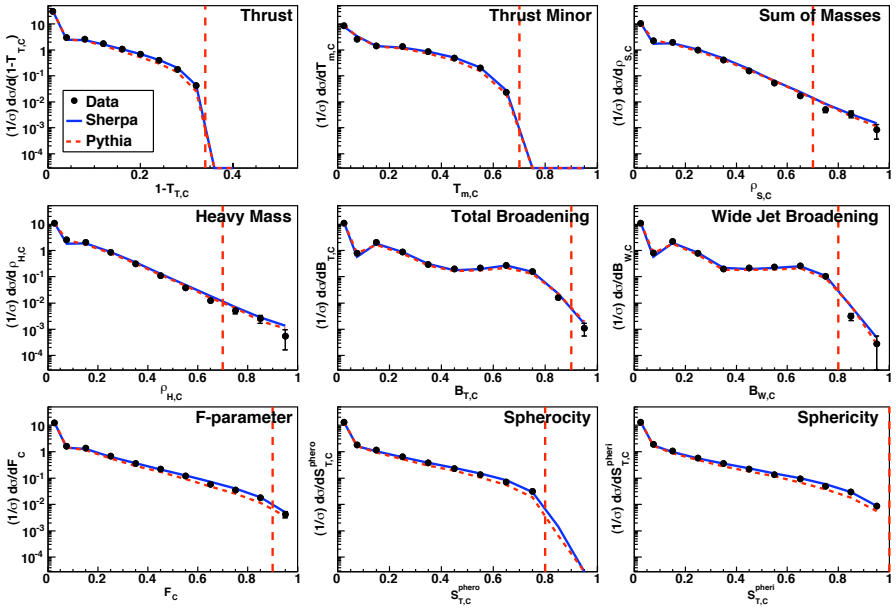

Figure G.11: Normalized differential distribution with $300 \geq H_T < 450$ (in GeV) showing bins with the number of events ≥ 20, left of the red line.

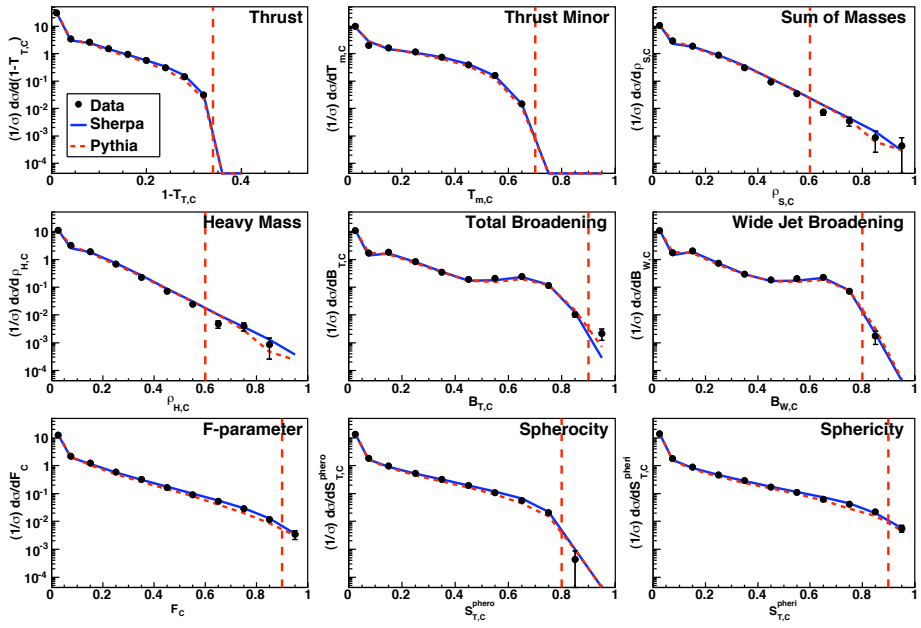

Figure G.12: Normalized differential distribution with $450 \geq H_T < 675$ (in GeV) showing bins with the number of events ≥ 20, left of the red line.

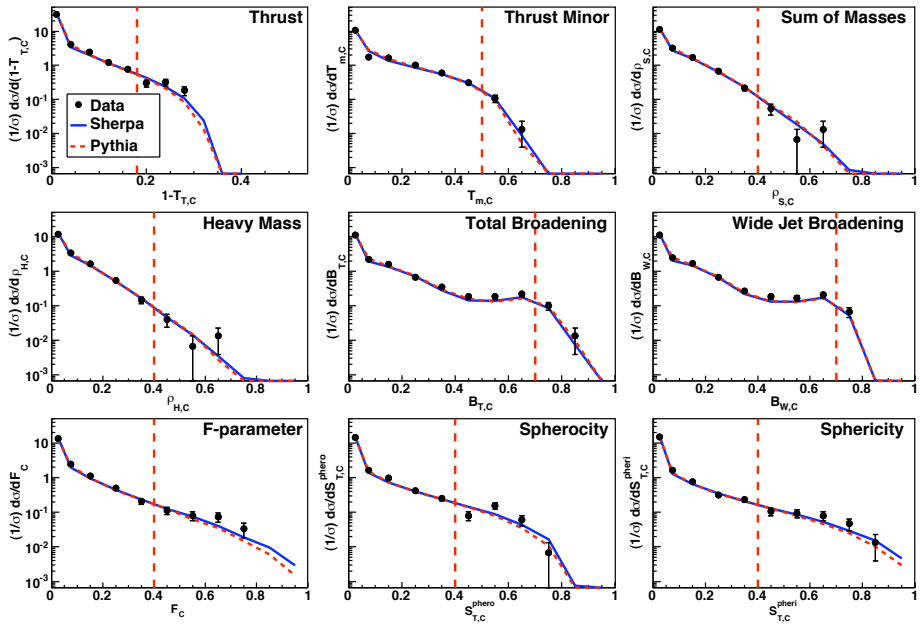

Figure G.13: Normalized differential distribution with $675 \geq H_T$ (in GeV) showing bins with the number of events ≥ 20, left of the red line.

APPENDIX H

COORDINATE SYSTEM AND DEFINITIONS

H.1 Coordinate System Used By DØ

At DØ a right-handed coordinate system (see Figure H.1) is used in which the z-axis points along the proton beam, the y-axis points up, and the x-axis points toward the center of the Tevatron ring: ϕ is the azimuthal angle, θ is the polar angle, and r is the distance perpendicular to the beam pipe.

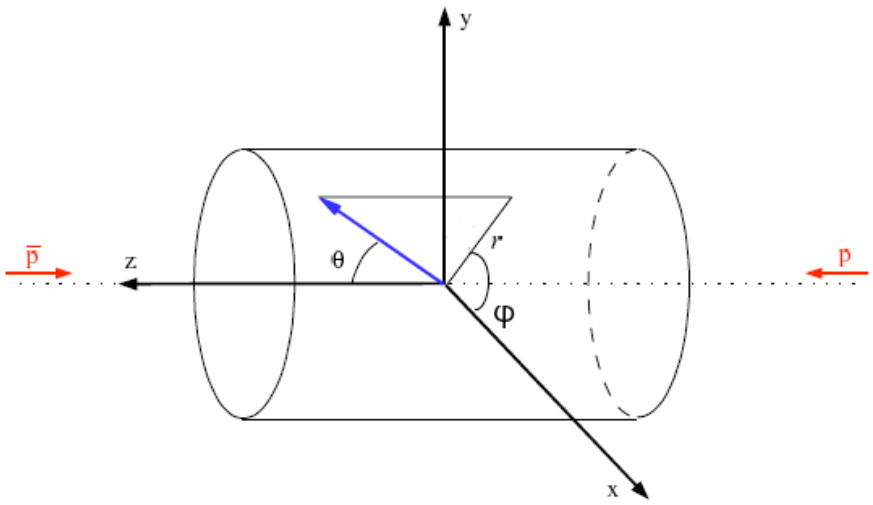

Figure H.1: Diagram showing the right-handed coordinate system used DØ.

H.2 Definitions

As is common in high energy physics, natural units are used in which $\hbar = c = 1$. In this unit system, p, E, and m all have the same units, eV.

Table H.1: Definitions used.

polar angle	θ	$\arctan(\sqrt{x^2+y^2}/z)$
azimuthal angle	ϕ	$\arctan(y/x)$
rapidity	y	$0.5\ln[(E+p_z)/(E-p_z)]$
pseudorapidity	η	$-0.5\ln[\tan(\theta/2)]$
transverse momentum	p_T	$p_T = \sqrt{p_x^2+p_y^2}$
distance in ϕ	$\Delta\phi_{ij}$	$\Delta\phi_{ij} = \min(\lvert\phi_1-\phi_2\rvert, 2\pi-\lvert\phi_1-\phi_2\rvert)$
distance in $y-\phi$ space	ΔR	$\Delta R_{ij} = \sqrt{(y_i-y_j)^2+(\Delta\phi_{ij})^2}$
center-of-mass energy	$\sqrt{s}$	$\sqrt{s} = E_{CM} = E_p + E_{\overline{p}} = 1.96$ TeV
energy of jet	E	
transverse energy	E_T	$E_T = E/\cosh(\eta)$
	H_T	$H_T = \sum_{i\in C} p_{Ti}$
	y^*	$y^* = \lvert y_1 - y_2\rvert/2$
	y^{boost}	$y^{boost} = (y_1+y_2)/2$
cross section	σ	
(instantaneous) luminosity	$\mathcal{L}$	
integrated luminosity	L	$L = \int \mathcal{L}\,dt$
electron volt	eV	1.602×10^{-19} J
	MeV	10^6 eV
	GeV	10^9 eV
	TeV	10^{12} eV
unit of cross section	barn	barn $= 10^{-28}\,\mathrm{m}^2$
	pb^{-1}	$\mathrm{pb}^{-1} = 10^{40}\,\mathrm{m}^{-2}$
	fb^{-1}	$\mathrm{fb}^{-1} = 10^{43}\,\mathrm{m}^{-2}$

APPENDIX I

RAPIDITY PLOTS FOR EACH JET

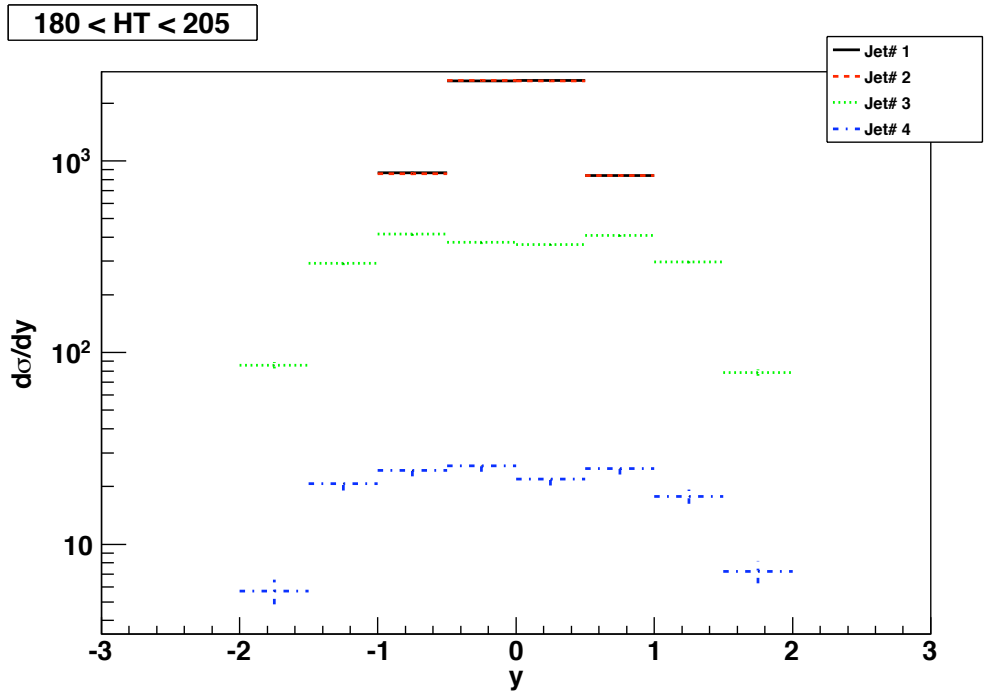

Figure I.1: Differential cross section for each jet in $180 < H_T < 205$ GeV.

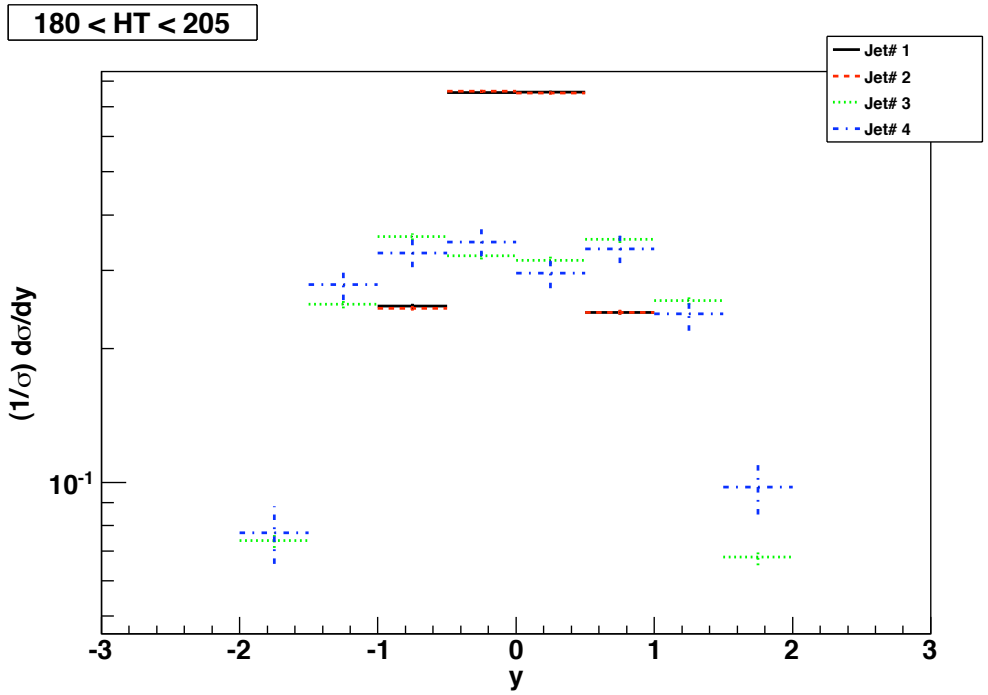

Figure I.2: Normalized differential cross section for each jet in $180 < H_T < 205$ GeV.

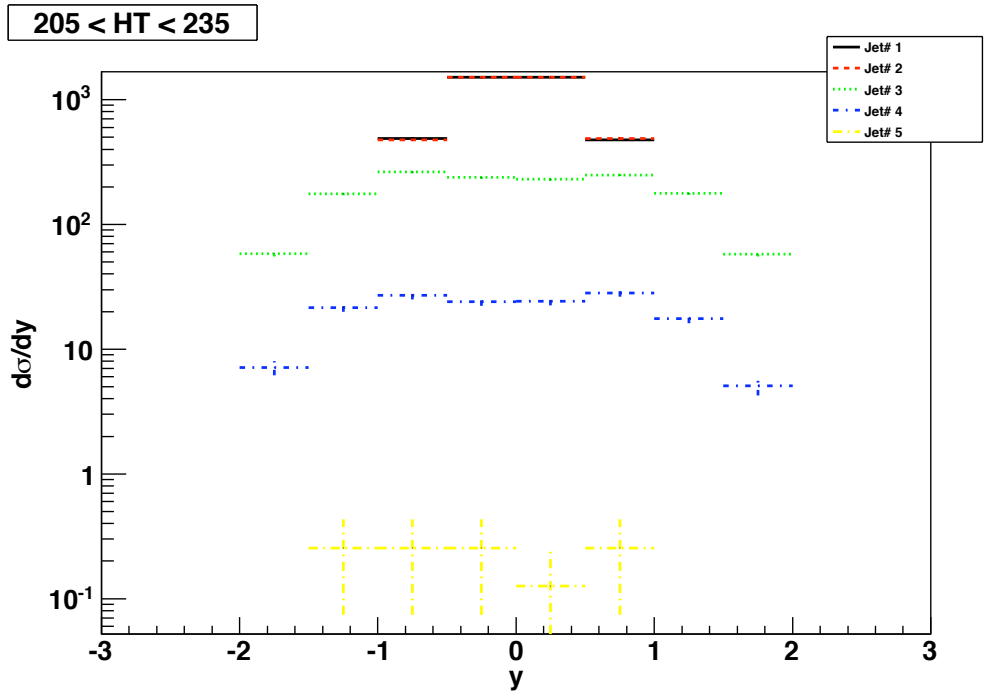

Figure I.3: Differential cross section for each jet in $205 < H_T < 235$ GeV.

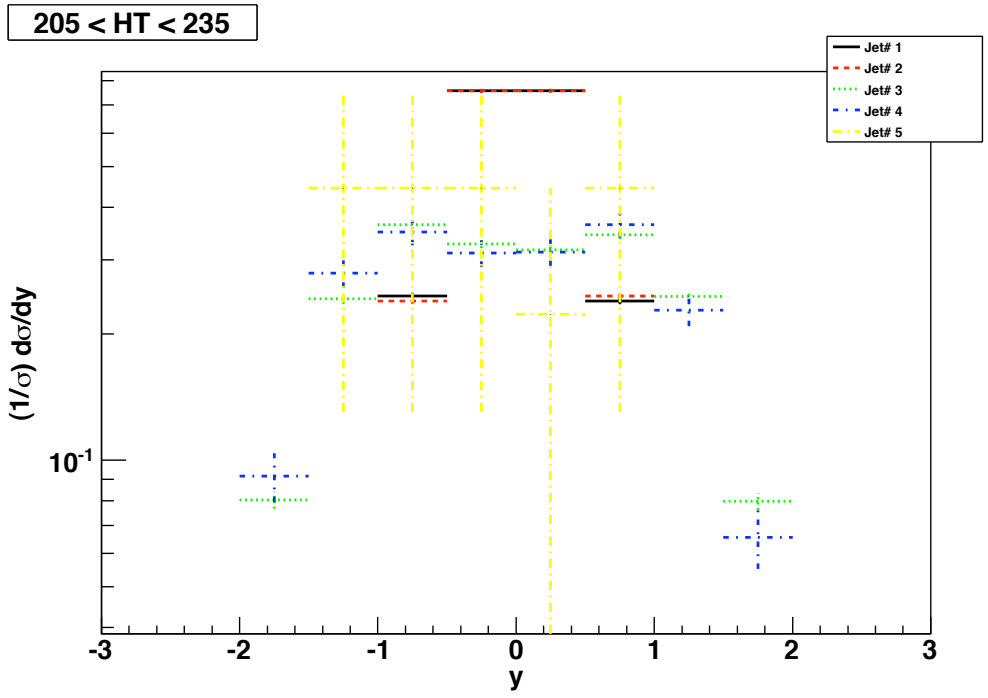

Figure I.4: Normalized differential cross section for each jet in $205 < H_T < 235$ GeV.

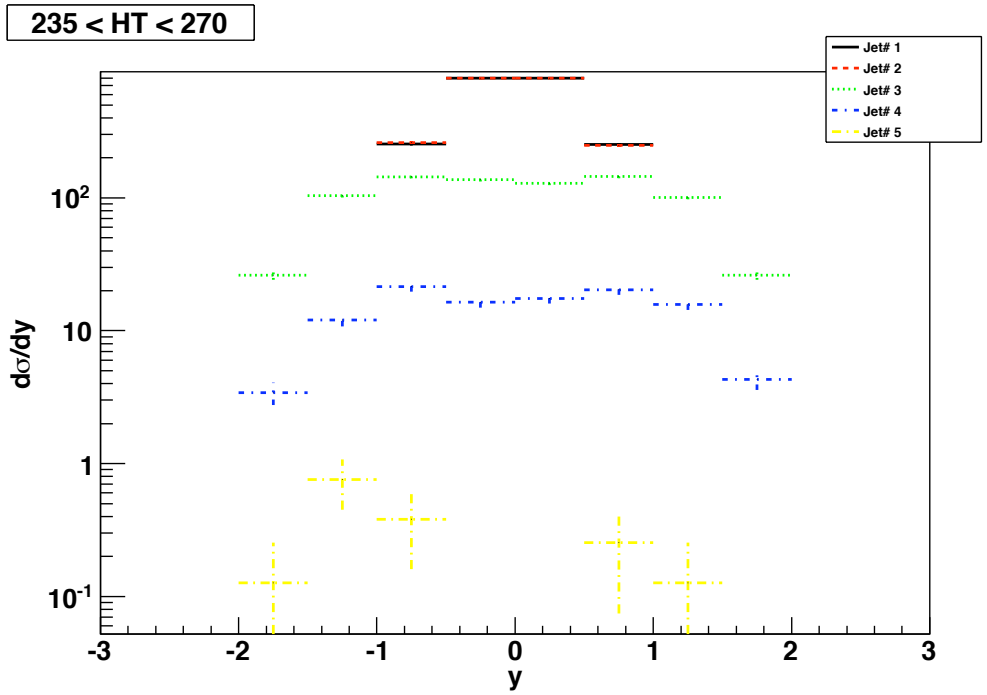

Figure I.5: Differential cross section for each jet in $235 < H_T < 270$ GeV.

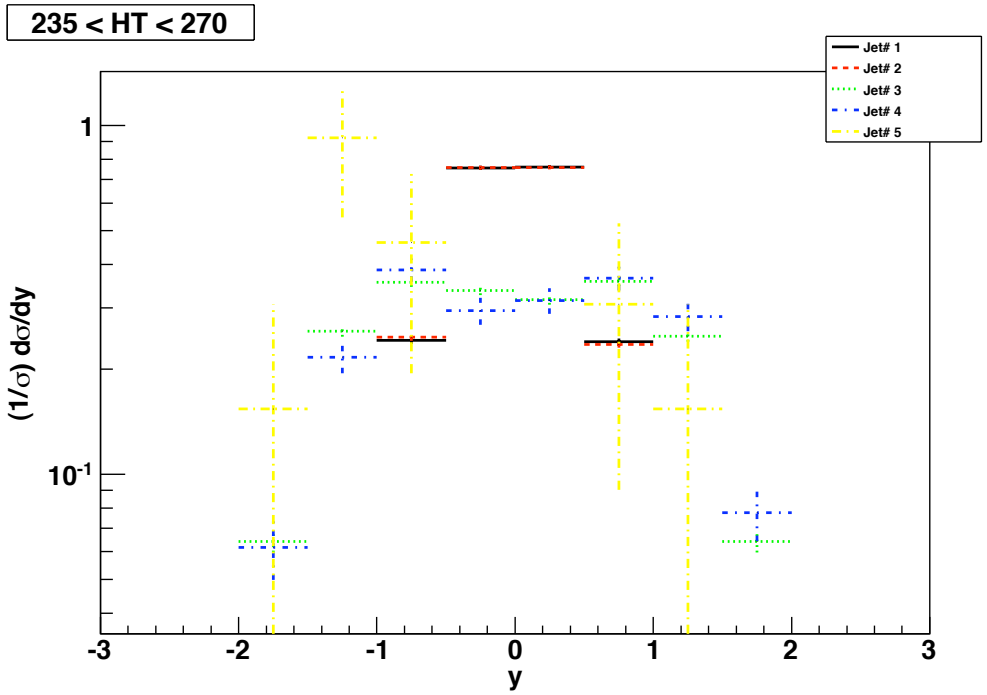

Figure I.6: Normalized differential cross section for each jet in $235 < H_T < 270$ GeV.

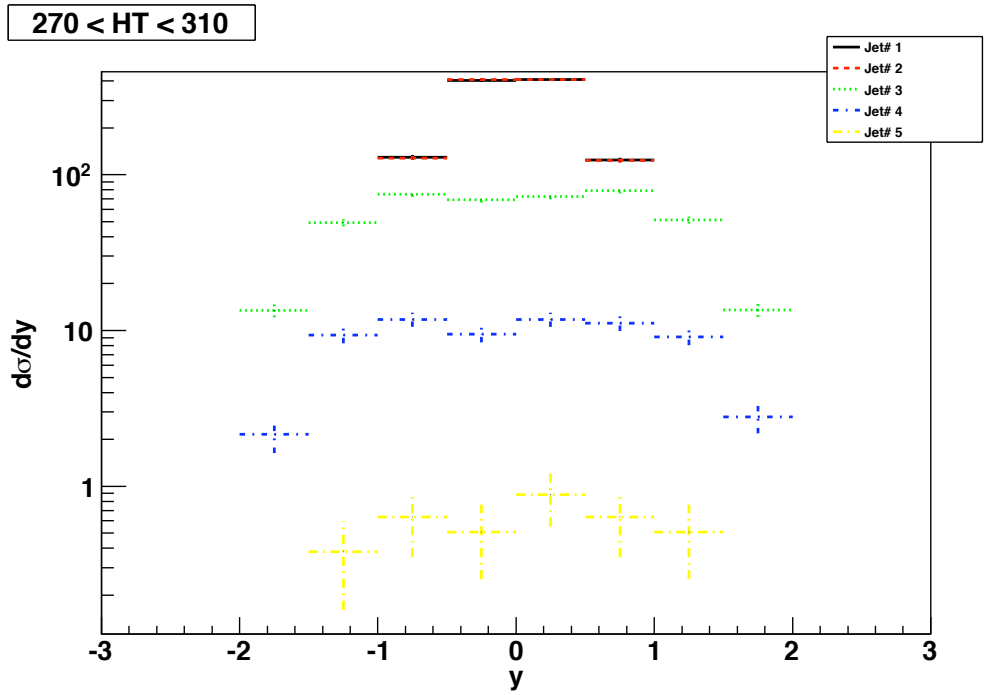

Figure I.7: Differential cross section for each jet in $180 < H_T < 205$ GeV.

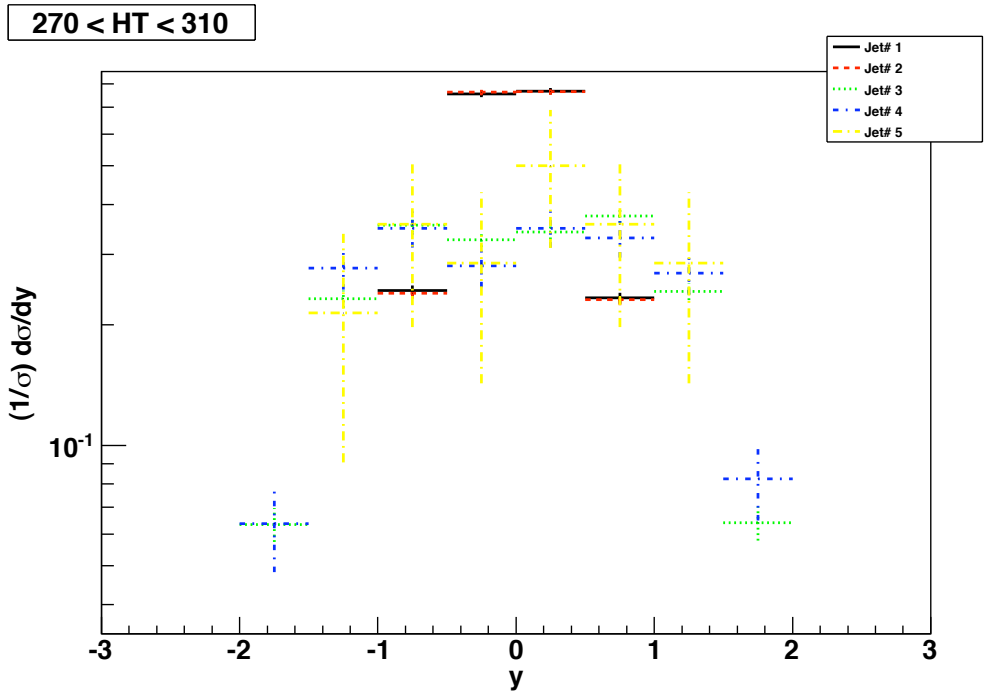

Figure I.8: Normalized differential cross section for each jet in $270 < H_T < 310$ GeV.

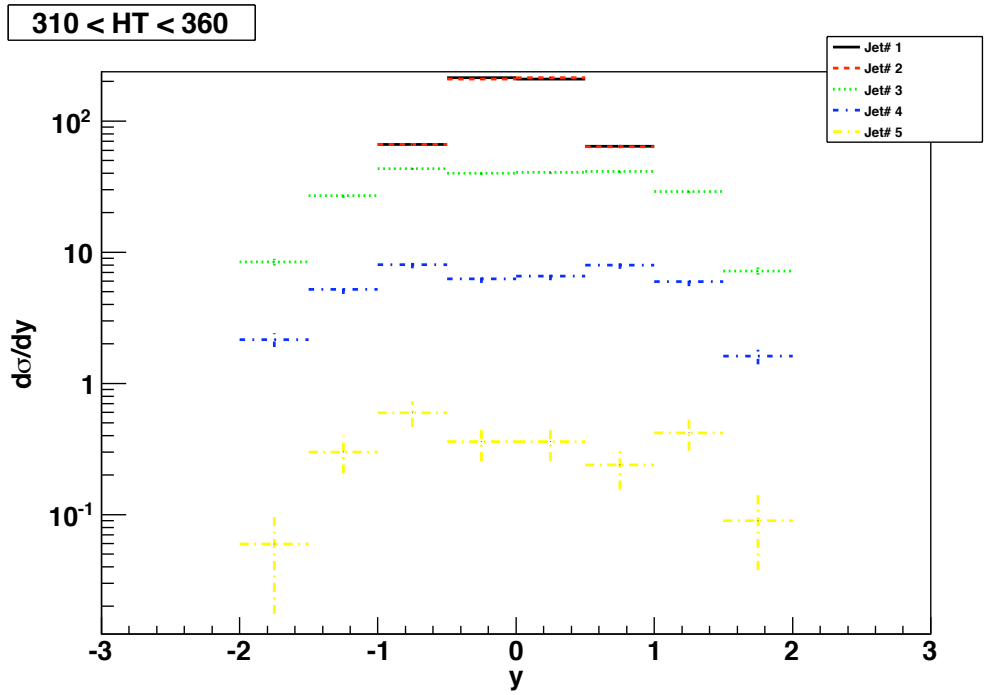

Figure I.9: Differential cross section for each jet in $310 < H_T < 360$ GeV.

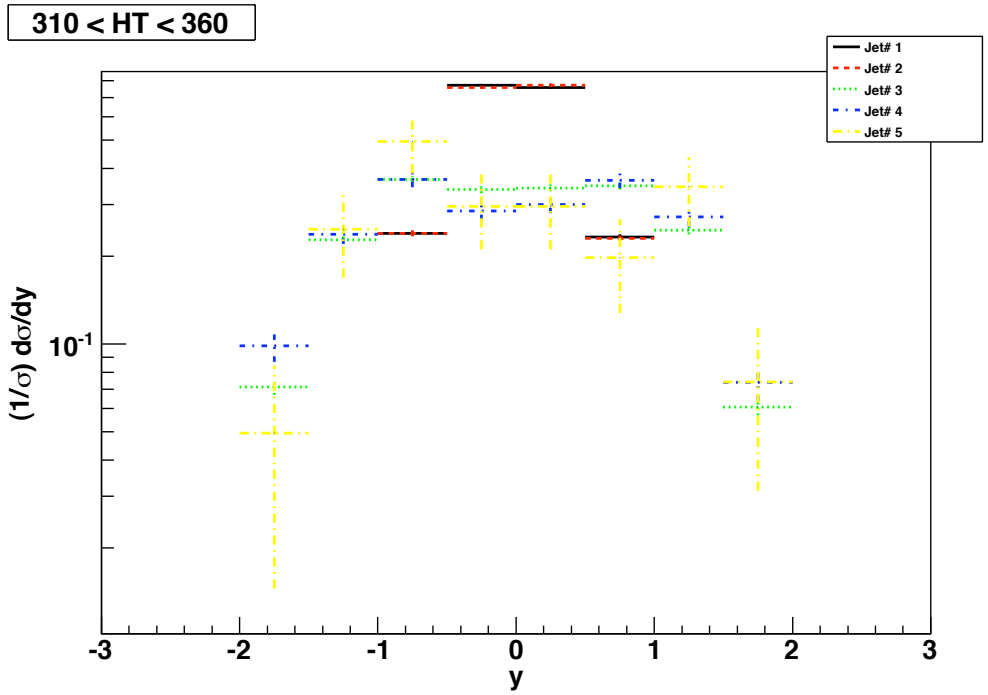

Figure I.10: Normalized differential cross section for each jet in $310 < H_T < 360$ GeV.

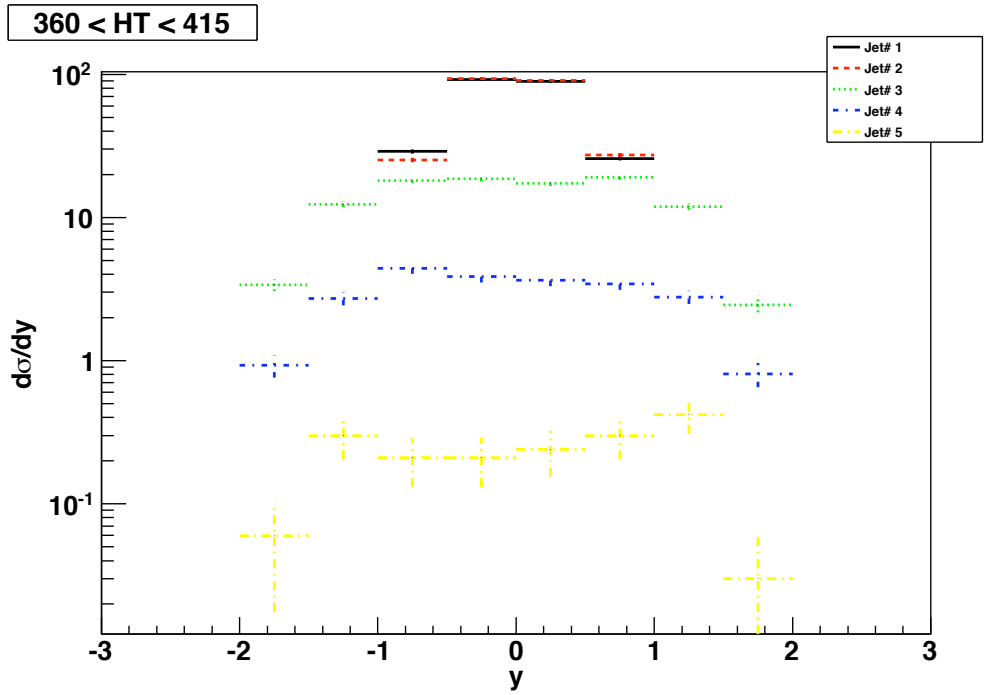

Figure I.11: Differential cross section for each jet in $360 < H_T < 415$ GeV.

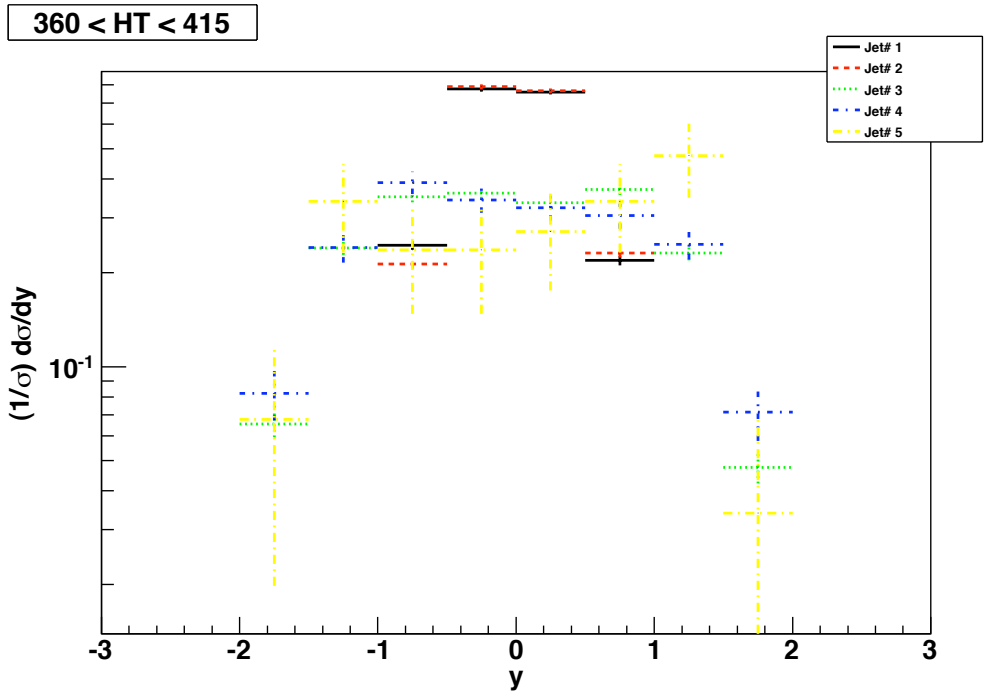

Figure I.12: Normalized differential cross section for each jet in $360 < H_T < 415$ GeV.

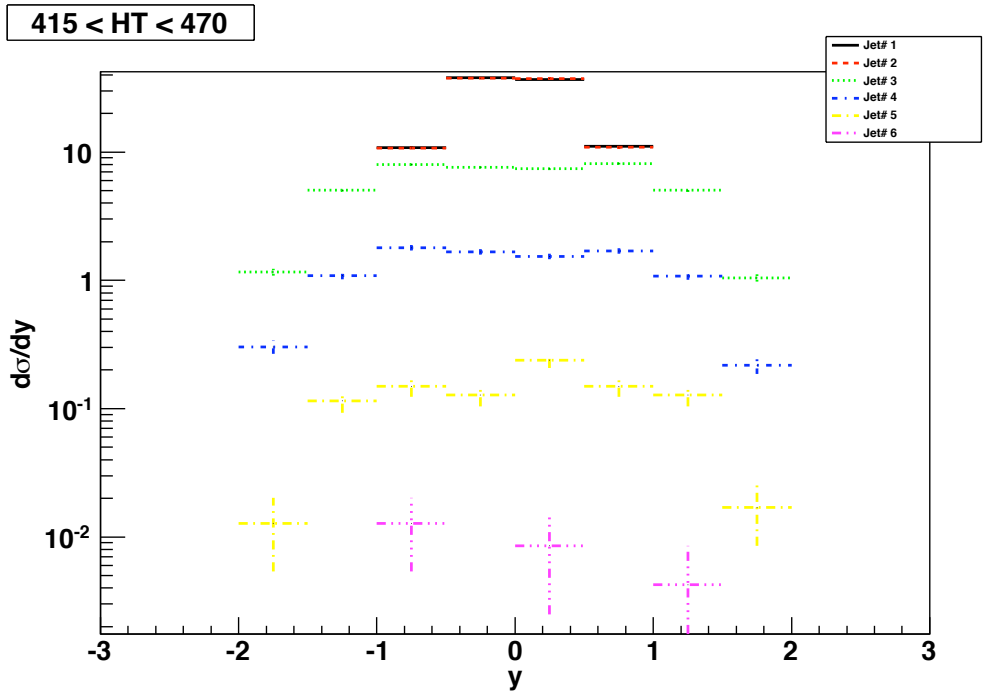

Figure I.13: Differential cross section for each jet in $415 < H_T < 470$ GeV.

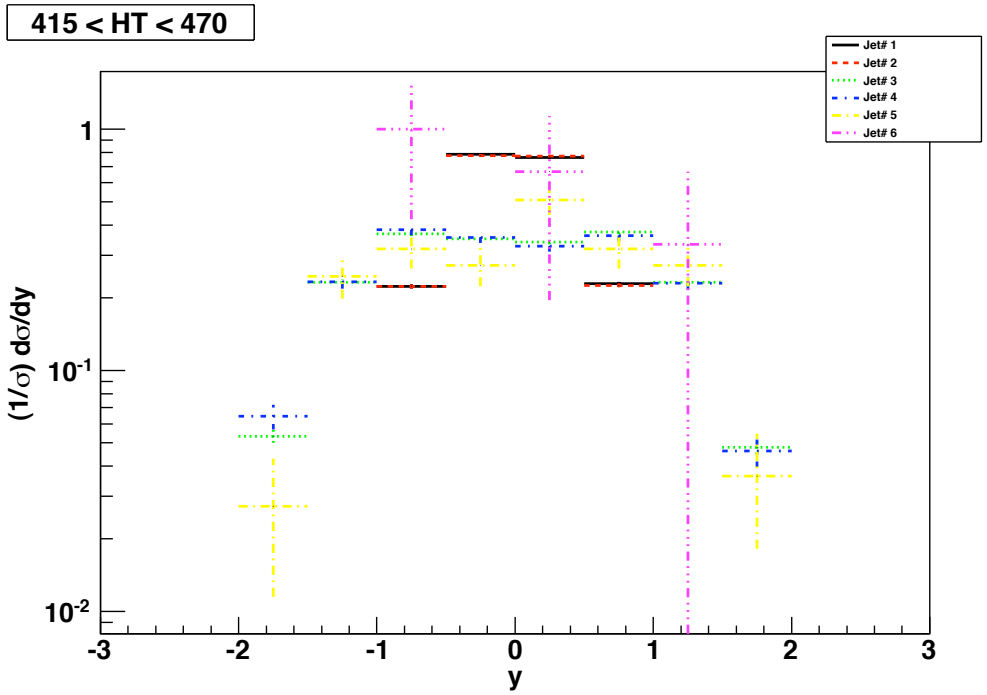

Figure I.14: Normalized differential cross section for each jet in $415 < H_T < 470$ GeV.

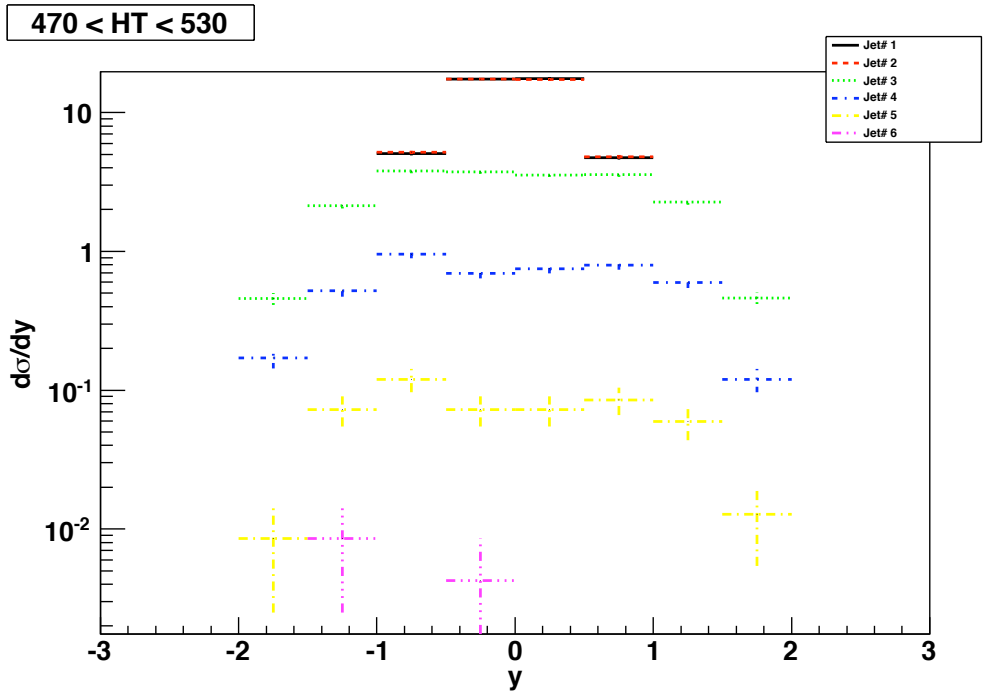

Figure I.15: Differential cross section for each jet in $470 < H_T < 530$ GeV.

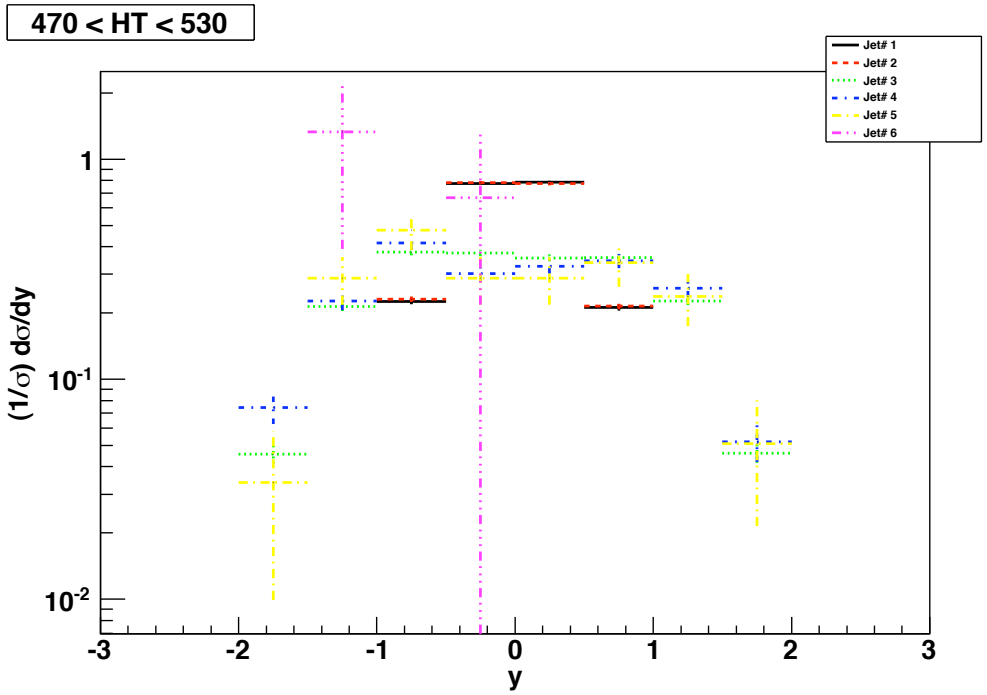

Figure I.16: Normalized differential cross section for each jet in $470 < H_T < 530$ GeV.

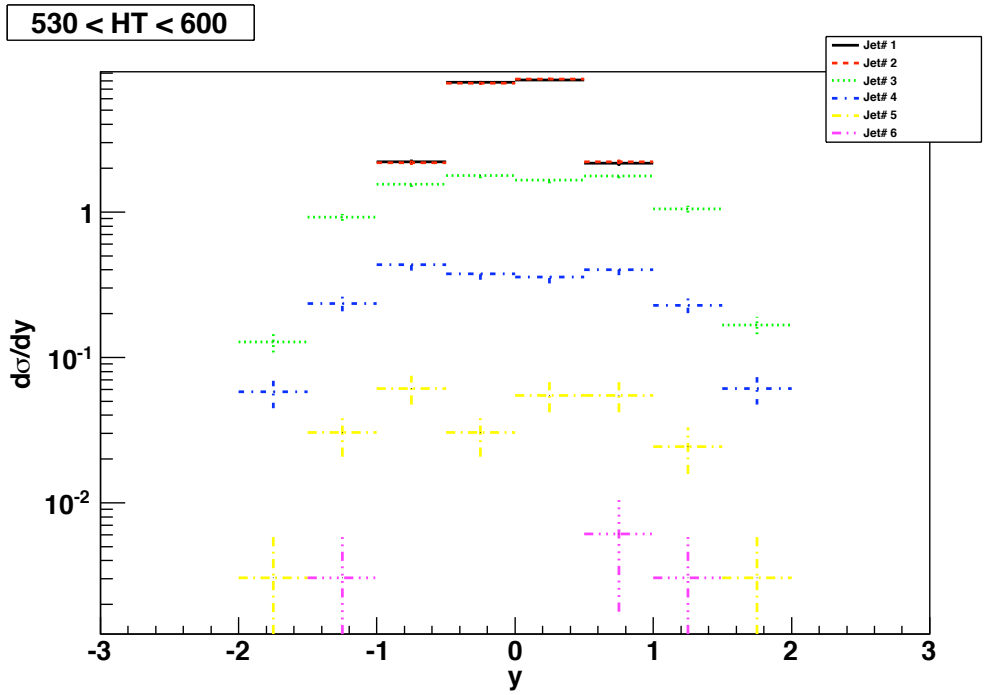

Figure I.17: Differential cross section for each jet in $530 < H_T < 600$ GeV.

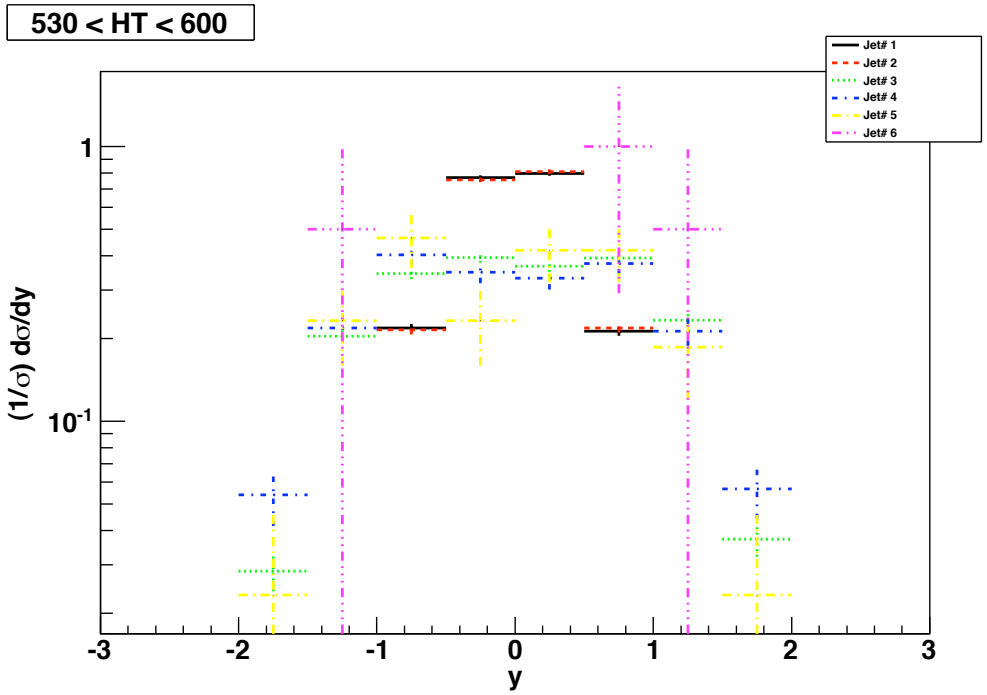

Figure I.18: Normalized differential cross section for each jet in $530 < H_T < 600$ GeV.

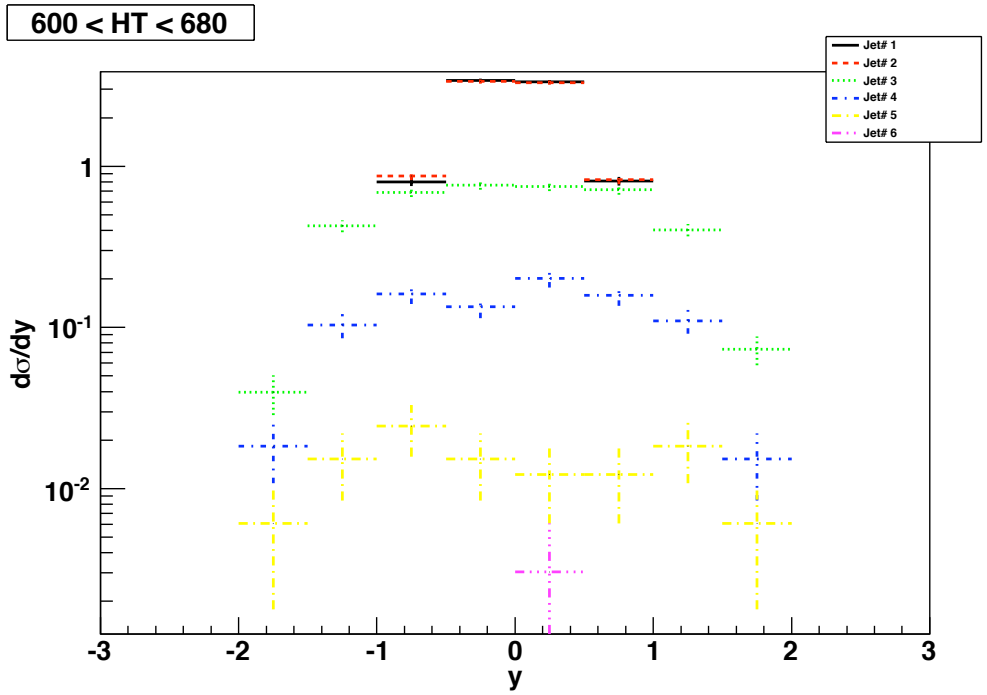

Figure I.19: Differential cross section for each jet in $600 < H_T < 680$ GeV.

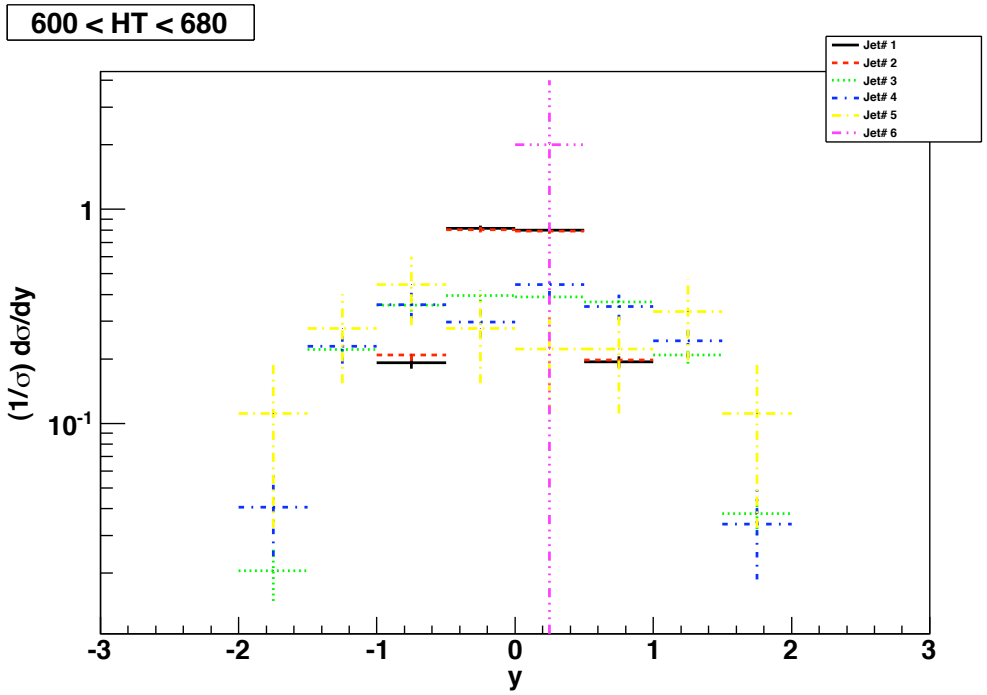

Figure I.20: Normalized differential cross section for each jet in $600 < H_T < 680$ GeV.

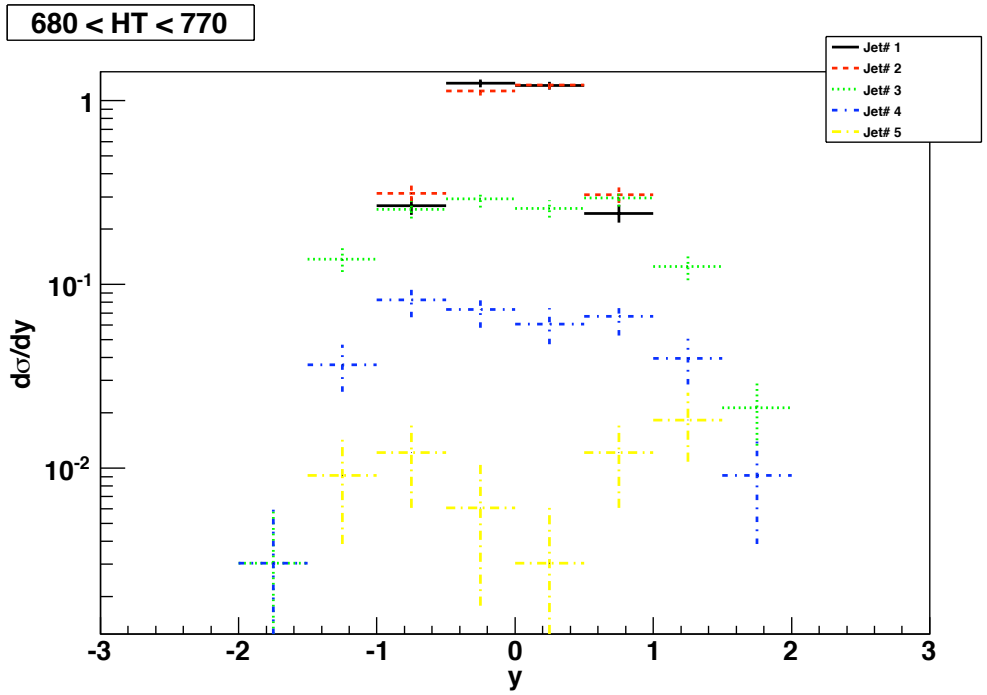

Figure I.21: Differential cross section for each jet in $680 < H_T < 770$ GeV.

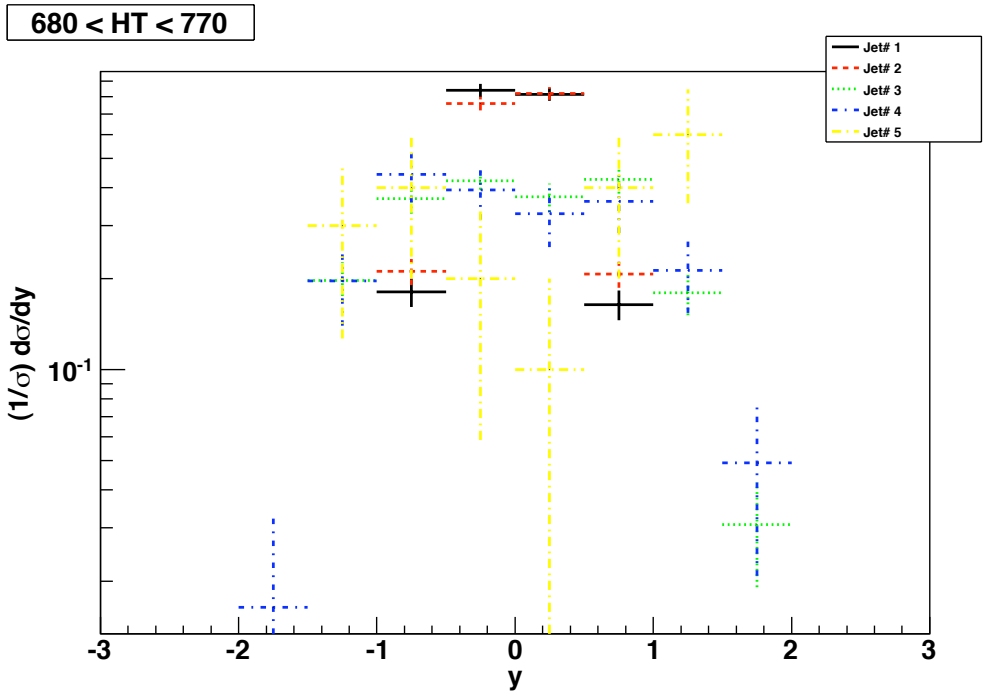

Figure I.22: Normalized differential cross section for each jet in $680 < H_T < 770$ GeV.

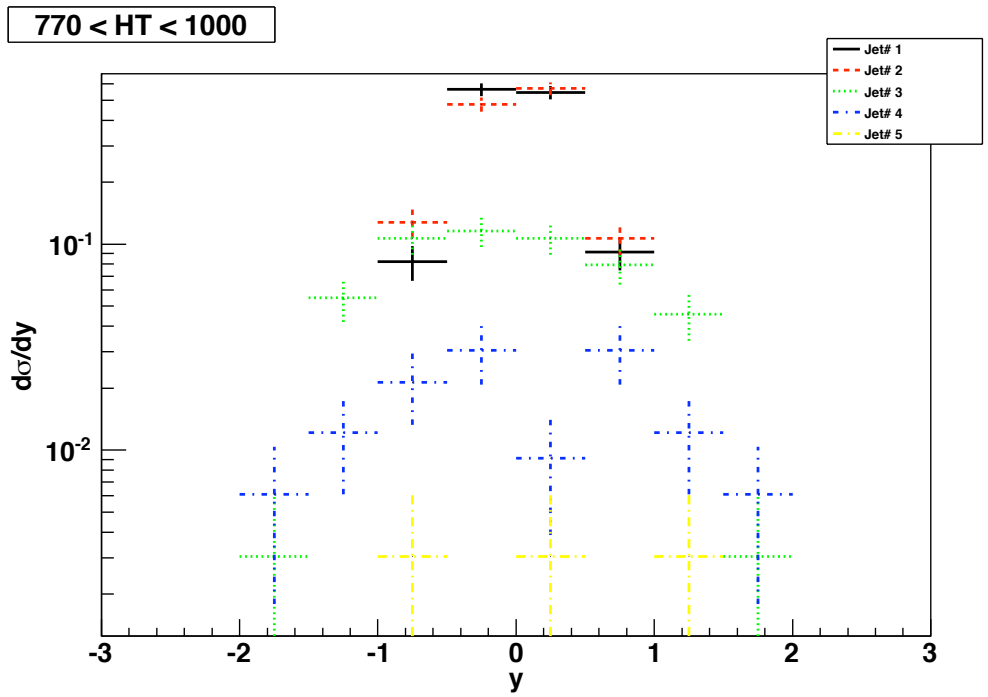

Figure I.23: Differential cross section for each jet in $770 < H_T < 1000$ GeV.

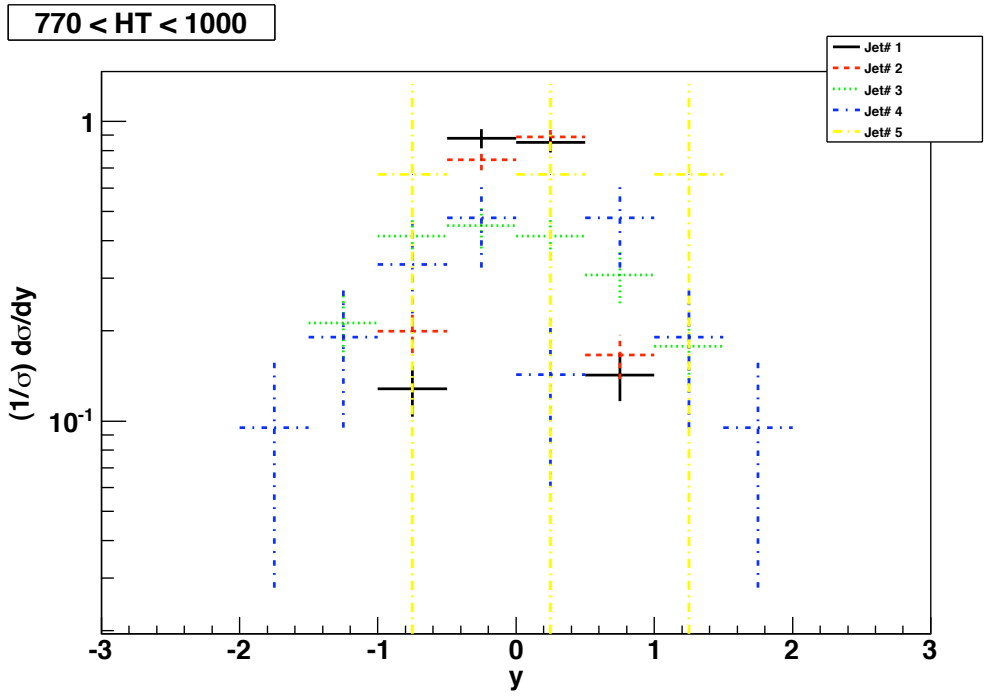

Figure I.24: Normalized differential cross section for each jet in $770 < H_T < 1000$ GeV.

BIBLIOGRAPHY

[1] R. Cahn and G. Goldhaber, *The Experimental Foundations of Particle Physics (2^{nd} ed)*, Cambridge, (2009).

[2] E.D. Bloom, *et al*, "High Energy Inelastic *e-p* Scattering at 6 deg and 10 deg." Phys. Rev. Lett., 23, p. 930 (1969).

[3] G. Hanson, *et al*, "Evidence for Jet Structure in Hadron Production by e^+e^- Annihilation", Phys. Rev. Lett., 35, p. 1609 (1975).

[4] TASSO Collaboration, R. Brandelik, *et al.*, "Evidence for Planar Events in e^+e Annihilation at High Energies.", Phys. Lett., 86B, 243 (1979).

[5] A. Banfi, G.P. Salam, and G. Zanderighi, "Phenomenology of event shapes at hadron colliders", JHEP, V 2010, No 6, (2010).

[6] CMS Collaboration, "First measurement of hadronic event shapes in pp collisions at $\sqrt{s} = 7$ TeV", Phys. Lett. B, 699, 48 (2011).

[7] T. Gleisberg, *et al*, "Event generation with SHERPA 1.1", JHEP02, 007 (2009).

[8] T. Sjöstrand, S. Mrenna, and P. Skands, "PYTHIA 6.4 Physics and Manual", JHEP05, 026, (2006).

[9] R.P. Feynman, "The theory of positrons", Phys. Rev., 76, p. 749 (1949a).

[10] M. Voutilainen, "Mearsument of the inclusive jet cross section in $p\overline{p}$ collisions at $\sqrt{s} = 1.96$ TeV", Ph. D. thesis (2008).

[11] E. Busato and B. Andrieu, "Jet Algorithms in the DØ Run II Software: Description and User's Guide", DØ internal note [4457], (2004).

[12] J.-C. Winter, F. Krauss, and G. Soff, "A modified cluster-hadronisation model", Eur. Phys. J., C36, (2004).

[13] B. Andersson, *The Lund model*, Camb. Monogr. Part. Phys. Nucl. Phys. Cosmol., 7, (1997).

[14] DØ Collaboration, "The Upgraded DØ Detector", Nuclear Instruments and Methods in Physics Research, A 565, p. 463 (2006).

[15] ROOT, http://root.cern.ch/drupal/ (2012).

[16] DØ Collaboration, "Measurement of Ratios of Multi-Jet Cross Sections in ppbar collisions at sqrts = 1.96 TeV", DØ conference note [6032], (2010).

[17] K. Chakravarthula and M. Wobisch, "Measurement of the Rapidity Dependence of Dijet Azimuthal Decorrelations", DØ internal note (in preparation).

[18] R.L. Burden and J.D. Faires, *Numerical Analysis (8^{th} ed)*, Thomson Brooks/Cole, (2005).

[19] A. Harel, "Jet ID Optimization", DØ internal note [4919] (2005).

[20] M. Wobisch, *et al*, "DØJetSim - A Parameterized Detector Simulation for Jet Physics", DØ internal note [5703] (2008).

[21] JES Group, "Jet Energy Scale Determination at D0 Run II (final p17 version)", DØ internal note [5382], (2007).

[22] M. Voutilainen and JES Group, "Jet Four-vector Scale Determination for Dijets in D0 Run IIa (final p17 version)", DØ internal note [5550], (2007).

[23] S. Atkins, *et al*, "Correction for the MC-Data Difference in the Jet Response at DØ", DØ internal note [6143], (2011).

[24] S. Atkins, *et al*, "Correction for the MC-Data Difference in the Jet Response at DØ for RunIIB", DØ internal note [6144], (2011).

[25] M. Voutilainen, "Jet Trigger Efficiencies for RunIIa", DØ internal note [5549] (2006).